SYNTHESIS OF SPRAY PYROLYSED TRANSITION AND RARE EARTH METAL OXIDES (Co_3O_4, MnO_2, WO_3, CeO_2) THIN FILMS AND THEIR CHARACTERIZATION
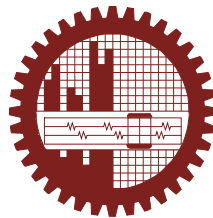
by

MST. MUSLIMA ZAHAN

Roll No : 1015144003F

Session : October, 2015

DOCTOR OF PHILOSOPHY IN PHYSICS
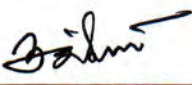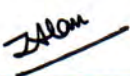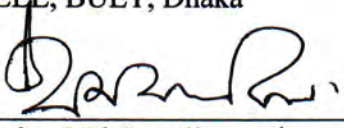
Department of Physics

BANGLADESH UNIVERSITY OF ENGINEERING AND TECHNOLOGY

DHAKA-1000, BANGLADESH

March, 2021

The thesis titled **"Synthesis of Spray Pyrolysed Transition and Rare Earth Metal Oxides (Co$_3$O$_4$, MnO$_2$, WO$_3$, CeO$_2$) Thin Films and Their Characterization"** submitted by Mst. Muslima Zahan, Roll No.: 1015144003F, Registration No.: 1009143017, Session: October, 2015, has been accepted as satisfactory in partial fulfillment of the requirement for the degree of Doctor of Philosophy (Ph.D) in Physics on March 31, 2021.

BOARD OF EXAMINERS

1. _____
   Prof. Dr. Jiban Podder
   Department of Physics, BUET, Dhaka

   Chairman
   (Supervisor)

2. _____
   Prof. Dr. Md. Rafi Uddin
   Head
   Department of Physics, BUET, Dhaka

   Member
   (Ex-Officio)

3. _____
   Prof. Dr. A. K. M. Akther Hossain
   Department of Physics, BUET, Dhaka

   Member

4. _____
   ·Prof. Dr. Md. Mostak Hossain
   Department of Physics, BUET, Dhaka

   Member

5. _____
   Prof. Dr. A. B. M. Obaidul Islam
   Department of Physics, University of Dhaka, Dhaka

   Member

6. _____
   Prof. Dr. Mohammad Jahangir Alam
   Department of EEE, BUET, Dhaka

   Member

7. _____
   Prof. Dr. Abu Bakar Md. Ismail
   Department of Applied Physics & Electronic Engineering
   University of Rajshahi, Rajshahi

   Member
   (External)

Candidate's Declaration

It is hereby declared that this thesis or any part of it has not been submitted elsewhere for the award of any degree or diploma.

_____

MST. MUSLIMA ZAHAN

Roll No.: 1015144003F

Session: October, 2015

Dedicated
To
My Parents

Acknowledgements

Abstract

Semiconducting metal oxide based nano-materials play a very important role in the various fields of sensing materials for gas sensor and bio sensors due to rich physical and chemical stability. In this thesis, Iron (Fe) and Copper (Cu) doped cobalt oxide (Co_3O_4), manganese dioxide (MnO_2), tungsten oxide (WO_3) and cerium dioxide (CeO_2) nanostructured thin films have been synthesized via spray pyrolysis deposition technique to explore their suitable morphological, structural, optical and electrical properties, pre-requisite for glucose sensing abilities. The presence of low concentration of Fe and Cu (about 4 to 6 at.%) strongly influenced the crystallite size of Co_3O_4, MnO_2, WO_3 and CeO_2, as analyzed by field emission scanning electron microscope (FESEM) and X-ray diffraction (XRD). Elemental analysis by energy dispersive X-ray spectroscopy (EDX) confirmed the stoichiometry and homogeneity of the films. XRD patterns of the deposited films showed spinel cubic, body centered tetragonal, monoclinic and face centered cubic crystal structure of Co_3O_4, MnO_2, WO_3 and CeO_2, respectively, which well agrees with the JCPDS data. Crystallite sizes of Co_3O_4, MnO_2, WO_3 and CeO_2 were obtained 29 nm, 24nm, 13 nm and 15 nm respectively, measured by Scherer relation. Optical band gaps calculated using Tauc relation were found 2.02 eV, 3.81eV, 2.72 eV and 3.44 eV for Co_3O_4, MnO_2, WO_3 and CeO_2 films respectively and were tuned by Fe and Cu concentration. The dc electrical resistivity was obtained in the order of 10^4 Ω-cm and confirmed the semiconducting behavior of the films. p-type carrier of Co_3O_4, MnO_2, and n-type carrier of WO_3, CeO_2 were obtained by Hall Effect measurements. Glucose ($C_6H_{12}O_6$) sensing performance of MnO_2 and Fe doped MnO_2 were carried out using electrical four point probe method. The highest glucose-sensing response was recorded about 29% at 5 minutes for 4 at% Fe: MnO_2. The sensing performance of 4 at% Fe: MnO_2 was found higher than undoped MnO_2 sample under the same glucose concentration. Thus, Fe and Cu dopant is expected to improve the sensing properties of Co_3O_4, MnO_2, WO_3 and CeO_2, and could be suitable candidate for biosensor developments.

Contents

List of Contents

List of Figures

List of Tables

List of Abbreviations

FESEM	Field emission scanning electron microscope
EDX	Energy dispersive X-ray spectroscopy
XRD	X-ray Diffraction
FWHM	Full Width at Half Maxima
UV-Vis	Ultra Violet Visible Spectroscopy
λ	Wave length
θ	Bragg angle
d_{hkl}	Interplanar spacing
D	Crystallite size
δ	Dislocation density
β	Full width at the half maximum
TC(hkl)	Texture coefficient
Eg	Optical band gap
ν	Frequency
h	Planck's constant
d	Thickness
α	Absorption coefficient
T	Transmittance
ρ	Electrical resistivity
V	Voltage
I	Current
S	Probe distance
n_c	Carrier concentration
μ	Carrier mobility

CHAPTER 1

INTRODUCTION

CHAPTER 1 INTRODUCTION

1.1 Introduction to Metal Oxides

Metal oxides are an important class of materials from both scientific and technological point of view. There are several types of metal oxides such as transition metal oxides (TiO_2, MnO_2, NiO, Co_3O_4 etc.), pretransition metal oxides (Al_2O_3, MgO etc.), Post-transition metal oxides (ZnO, SnO_2 etc.) alkaline earth metal oxides (CaO, MgO etc.), rare earth metal oxides (Sm_2O_3, CeO_2, Nd_2O_3, Ce_2O_3 etc.).They found huge interesting applications in different technological fields. Oxide semiconductors are gaining interest as new materials that may challenge the supremacy of silicon. Metal oxide thin films are known for many years ago due to the industrial interest on their unique properties. Research on metal oxides has been started at 19's and it actually has drawn the interest of scientists after the invention of metal oxides semiconductor field effect transistor in the year 1960 [1-2]. Metal oxides semiconductors are noticeable dissimilar to conventional inorganic semiconductors like silicon with respect to materials design concepts, electronic structure, transport properties and optoelectronic properties. The physicochemical properties of metal oxide thin layers are closely related to preparation processes and operating conditions. Indeed, it is possible to obtain thin films having an amorphous or crystalline structure. Thereafter, films structural, electrical and optical properties can be tailored by varying the condition and the deposition process. Control of film properties is therefore key parameters of metal oxide films preparation to be used in wide applications such as: fabrication of microelectronic circuits, sensors, piezoelectric devices, fuel cells, coatings against corrosion, and as catalysts. Metal oxides thin films have wide applications in the field of mechanics, electronics, optoelectronics, solar cells and bio sensing devices. Thin film science is one of the most important fields which have greatly contributed to the flourishing of human civilization [3-6]. Although a large number of studies have been performed on the metal oxides thin films, yet transition metal oxides have vast demand for opto electronics and bio sensing devices based applications. The heart of the periodic table is the transition metals. Another important metals are rare earth. The transition and rare earth metal oxides exhibit a great diversity of structural, optical, electrical and magnetic properties with both scientific interest and practical applications. Now a day's thin film emerges as an important branch in science and technology. For the

development of fundamental and applied research and consequently to enrich knowledge in this field it is necessary to do research and analysis. Therefore it is very important to take this research work to gather more knowledge in this field. From this viewpoint, more available and common transition and rare earth metal oxides (Co_3O_4, MnO_2, WO_3, CeO_2) are discussed in this chapter to be suitable for biosensor devices.

1.2 Transition Metal Oxides

Transition metals have s, p, d, and f unfilled orbital's electrons. The transition metals have multiple potential oxidation states which are related to the number of electrons that an atom loses, gains, or appears to use when joining with another atom in compounds.[7-10]. Transition metals have the highest number of unpaired valence electrons. The oxidation states would be the highest of the transition metals. The phenomena of oxidation states are dependent on the unpaired d-orbital electrons bond. Since 3d orbital is located to 4s orbital, the unpaired d-orbital electrons are added to the 2s orbital electrons. Most of the transition metals such as Sc, Ti, V, Cr, Mn, Fe, Co ,Ni, Cu, Zn, Zr, Nb, Mo, Ag, Cd etc. are known as d-block elements and their oxides are compounds composed of oxygen atoms bound to these transition metals. The bulk electronic band structure of transition metal oxides consists of overlapping 2p orbital from oxygen atoms, forming the lower energy, highly populated valence band, higher energy conduction band consists of overlapping d orbital of the transition metal cation. Transition metal oxides are also able to undergo photo assisted adsorption and desorption to control their semi conductivity. They are commonly utilized for their catalytic activity and semi conductive properties. Transition metal oxides semiconductor thin films show a large optical band gap when the crystallite size becomes less than the Bohr exciton radius. Transition metal oxides are an important group of materials because of their wide variety of structures, interesting physical and chemical properties, and numerous applications. From a chemical point of view, the most common family of transition metal oxides (Co_3O_4, MnO_2,WO_3) play an important role in catalysis, organic and inorganic synthesis, corrosion and energy conversion.

1.2.1 Cobalt Oxides (Co_3O_4)

Cobalt oxides are one of the most important transition metal oxides which has huge interest in several fields. Bulk cobalt oxide crystals appear in two stable crystallographic structures, the rock salt-type CoO and the normal-spinel-type Co_3O_4. CoO phase has a

high chemical stability but it easily oxidized to Co_3O_4 in the open air atmosphere. Among the family of transition metal oxides, Co_3O_4 is one of the versatile oxide material, a p-type semiconductor with an optical band gap of 2.0- 2.4 eV [11-12]. In the Co-O bonding system, Co_3O_4 possess more stable phase than CoO at low temperature (773 K). Above 1073 K, CoO is thermodynamically a stable phase in the air. The most stable phase of Co_3O_4 thin films display a mixed valence compound with a normal spinel structure having Co^{2+} and Co^{3+} placed at tetrahedral and octahedral sites, respectively. All the oxygen atoms are in equivalent sites in the Co_3O_4 spinel with Co-O bond lengths for Co^{2+} and Co^{3+} of 1.99 Å and 1.89 Å, respectively [13]. Spinel Co_3O_4 thin films have given extensive interest because of their diverse properties and wide applications in the field of batteries, fuel cells, and electrolytes. **Fig.** 1.1 shows the cubic normal spinel structure of Co_3O_4 (space group Fd $\overline{3}$ m) containing cobalt ions in two different oxidation states, Co^{2+} (light purple) and Co^{3+} (dark purple) and red ball represents oxygen atoms.
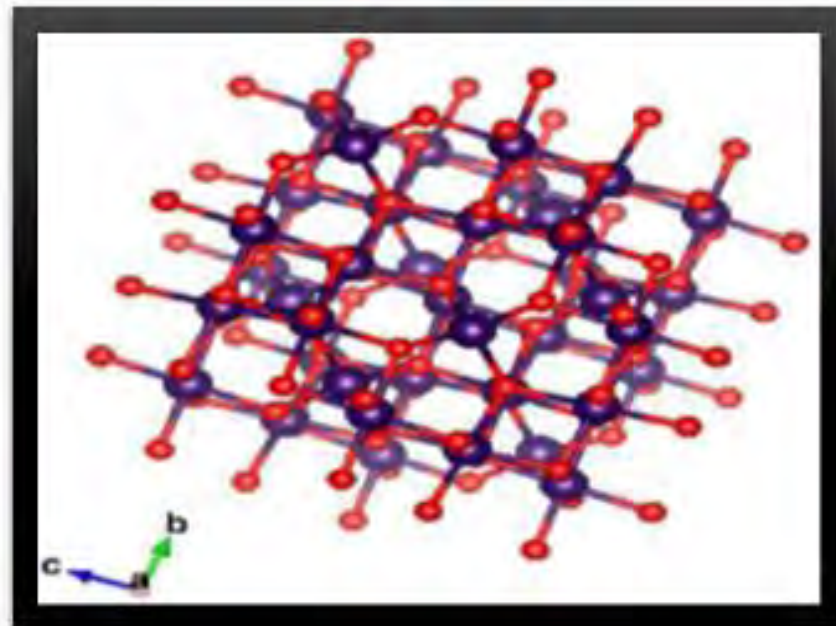
Fig. 1.1 Crystal structure of spinel cubic Co_3O_4.

1.2.2 Manganese Dioxides (MnO₂)

Manganese oxide (MnO_2) is one of the most interested nanoparticles and common transition metal oxides due to multiple valences, high capacitance, natural abundance and environmental friendliness containing p-type charge carriers especially in the bio sensing devices. Manganese is a grey white metal with an atomic radius about 1.4 Å. It is a hard metal and is very brittle, fusible with difficulty but easily oxidized. MnO_2 has multiple

phases including α, β, γ and δ, whose structural framework consists of [MnO$_6$] octahedral subunits sharing vertices and edges [14-15]. α-MnO$_2$ is thermodynamically a most stable semiconductor among these manganese oxides. α-MnO$_2$ exhibits high proton conductivity than β-MnO$_2$ and provide additional adsorption sites to accept cations. In α-MnO$_2$ interstitial cations induce charge-switching states through stabilization of Mn-O antibonding orbitals from the α-MnO$_2$ conduction band and cations stabilize high energy dangling O 2p bonds resulting from Mn vacancies. α- MnO$_2$ can easily formed composed of spherical aggregates of nanoparticles which is suitable for biosensor devices. The structure has tetragonal symmetry with space group I$_4$/m. **Fig.** 1.2 shows the tetragonal α-MnO$_2$ containing Mn ions in blue colors and red ball represents oxygen atoms.
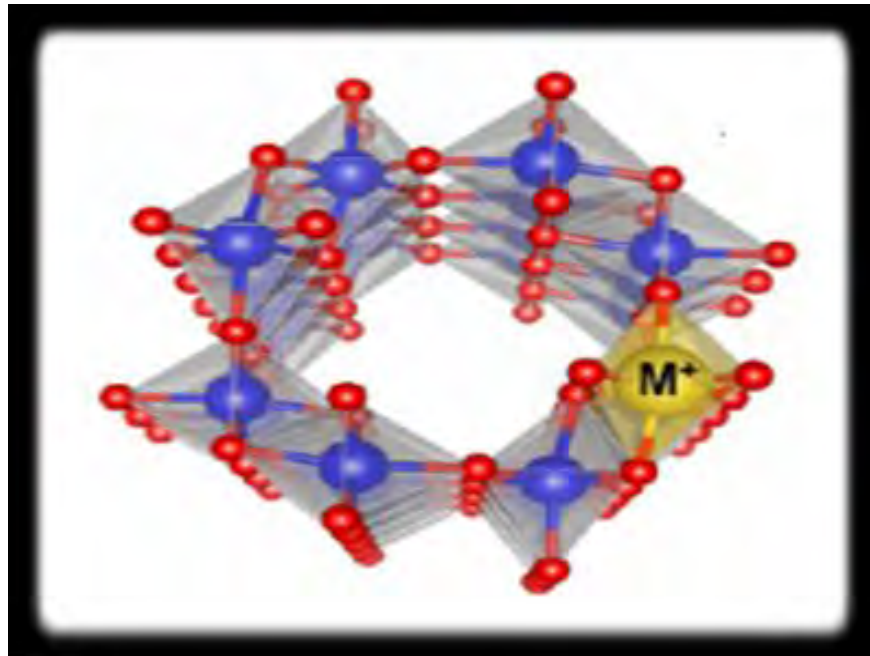
Fig. 1.2 Crystal structure of tetragonal α- MnO$_2$.

1.2.3 Tungsten Oxides (WO$_3$)

In the recent years, the benefits of transition metal oxides have been exploited in many challenging fields of information science, nano and micro-electronics, computer science, energy, transportation, safety engineering, military technologies, optoelectronic, electro chromic devices etc. [16-17]. Among them one of the most interesting and novel properties of tungsten oxide (WO$_3$) is applied in advanced technological applications, because of a unique physical and chemical properties, structural transformation and sub stoichiometric phase transitions and a wide band gap oxide semiconductor properties. It

attracted the more attention of researchers to explore their applications in the fields of in electrochromic devices, semiconductor gas sensors and pholtocatalysis and biosensor devices [18-19]. Nanostructured tungsten trioxide, WO_3 (TO) is temperature dependent. It is tetragonal at temperatures above 740°C, orthorhombic from 330 to 740°C, monoclinic from 17 to 330°C, and triclinic from 50 to 17 °C. The most common structure of WO_3 is monoclinic. The monoclinic WO_3, on the other hand, is completely oxidized, and therefore has a better catalytic activity [20-21] Tungsten trioxide is used for many purposes in everyday life. It is frequently used in industry to manufacture tungstate for x-ray screen phosphors, for fireproofing fabrics and in gas sensors. Due to its rich yellow color, WO_3 is also used as a pigment in ceramics and paints. TO has attracted a great deal of interest in the last few years for bio sensing applications. TO is a n-type semiconducting material with a wide band gap. Its band gap energy has been mainly measured by optical absorption, varying from about 2.6 to 3.0 eV [22-23]. The band gap of WO_3 is certainly of interest for both applied and fundamental aspects. **Fig.** 1.3 shows the monoclinic WO_3 crystal structure with space group $2_1/c$ containing W ions in blue colors and red ball represents oxygen atoms.
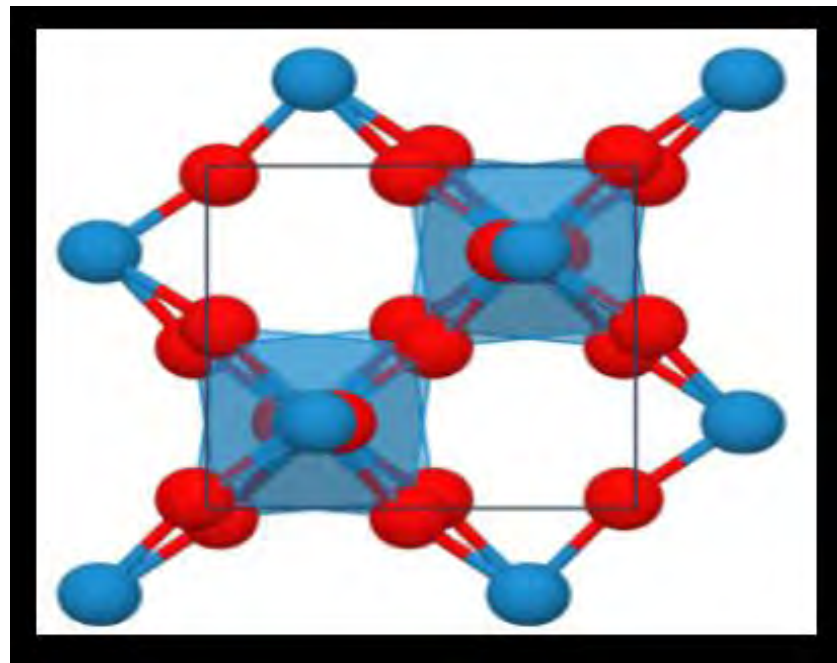
Fig. 1.3 Crystal structure of monoclinic WO_3.

1.3 Rare Earth Metal Oxides (Cerium Dioxide, CeO_2)

The rare earth metals are the elements of lanthanide group in the periodic table. These elements such as La, Ce, Pr, Nd, Pm, Sm, Eu, Gd etc possess strong correlations among

their 4f electrons. The 4f electrons in the rare-earths are highly localized. The delocalized f electrons would then be able to participate in bonding. Cerium is a most common lanthanide series rare earth element and can exist in either the free metal or oxide form. It can cycle between the cerous, cerium (III), and ceric, cerium (IV) oxidation states [24]. Both oxidation states of cerium strongly absorb ultraviolet light and have two characteristic spectrophotometric absorbance peaks (230-260 and 300-400 nm) [25]. In the recent years, development of lanthanide compounds (Z=57-71) such as ceria (CeO_2) nanomaterial's among the rare earth metal oxides, have been paid much attention.

Nanoscale ceria materials can rapidly formed redox Ce^{4+}/Ce^{3+} sites into their 4f shell of ions; assisting industrial and medical applications [26-28]. Since such small dimensions possess specific surface areas and have excellent fundamental technological consequences. Ceria is associated with rich oxygen vacancies and higher redox ability between Ce^{3+} and Ce^{4+}. Cerium oxide has low toxicity and close lattice parameter matching with silicon. It shows fascinating optical properties, such as high refractive index, good transmission in the visible and IR regions, high absorption in UV region with a wide band gap 3.2 eV.8. It exhibits two structures mainly cubic fluorite cerium dioxide, Cerium (IV) oxide, CeO_2 or ceria (due to tetravalent Ce) and a hexagonal sesquioxide Cerium (III) oxide, Ce_2O_3 (due to trivalent Ce). Cerium oxide is a notable functional material with an extraordinary capacity to store and release oxygen without losing its fluorite cubic structure. Cerium oxide (CeO_2) having cubic structure is the most important oxide due to its extraordinary chemical properties (acid-base and oxidation-reduction behavior), thermal stability and oxygen mobility. Cerium oxide is a very useful base material used as catalyst supports, ion conductors, and gas and bio sensors. The principal application of ceria is for polishing, especially chemical mechanical planarization (CMP) CeO_2 is used to decolorize glass by converting green tinted ferrous impurities to nearly colorless ferric oxides [29]. Nanoscale ceria materials can rapidly formed redox Ce^{4+}/Ce^{3+} sites into their 4f shell of ions; assisting industrial and medical applications [26-28]. Since such small dimensions possess specific surface areas and have excellent fundamental technological consequences. Ceria is associated with rich oxygen vacancies and higher redox ability between Ce^{3+} and Ce^{4+}. Cerium oxide has low toxicity and close lattice parameter matching with silicon. It shows fascinating optical properties, such as high refractive index, good transmission in the visible and IR regions, high absorption in UV region with a wide band gap 3.2 eV.8. It exhibits two structures mainly cubic fluorite

cerium dioxide, Cerium (IV) oxide, CeO_2 or ceria (due to tetravalent Ce) and a hexagonal sesquioxide Cerium (III) oxide, Ce_2O_3 (due to trivalent Ce). Cerium oxide is a notable functional material with an extraordinary capacity to store and release oxygen without losing its fluorite cubic structure. Cerium oxide (CeO_2) having cubic structure is the most important oxide due to its extraordinary chemical properties (acid-base and oxidation-reduction behavior), thermal stability and oxygen mobility. Cerium oxide is a very useful base material used as catalyst supports, ion conductors, and gas and bio sensors. The principal application of ceria is for polishing, especially chemical mechanical planarization (CMP) CeO_2 is used to decolorize glass by converting green tinted ferrous impurities to nearly colorless ferric oxides [29].

Fig. 1.4 Crystal structure of cubic CeO_2.

Cerium oxide has found use in infrared filters, as an oxidizing species in catalytic converters and as a replacement for thorium dioxide in incandescent mantles. Catalysis The interconvert ability of CeO_x materials is the basis of the use of ceria for an oxidation catalyst. One small but Ceria has been used as a sensor in catalytic converters in automotive applications, controlling the air exhaust ratio to reduce NO_x and carbon monoxide. Ceria is of interest as a material for solid oxide fuel cells (SOFCs) because of its relatively high oxygen ion conductivity. Semiconducting oxide materials owing to high ionic conductivity, capacitive action, catalytic properties and high isoelectric point (IEP)

have gained considerable interest in the fields of biosensors as alternate matrices. The excellent electronic conductivity makes CeO_2 an attractive matrix for biosensor application. Cerium oxide is an important oxide material used to prepare high and low index films to have multi-layer optical thin film devices due to its desirable properties like refractive index, excellent optical transmission in the visible and near infrared region, good adhesion, environmental stability, etc. **Fig.** 1.4 shows the face centered cubic CeO_2 crystal structure with space group $Fm\bar{3}m$, containing Ce ions in white colors and red ball represents oxygen atoms Table 1.1 shows the basic information of some common transition and rare earth metal oxides (Co_3O_4, MnO_2, WO_3 and CeO_2).

Table 1. 1 Basic information of some common metal oxides

Properties	Co_3O_4	MnO_2	WO_3	CeO_2
Molar Mass (g/mol)	240.80	86.94	231.84	172.12
Density (g/cm^3)	6.11	05.03	7.16	7.22
Melting Point (ºC)	895	535	1473	2400
Boiling point (ºC)	900	1042	1700	3500
Oxidation number	+2, +3	+4	+5, +6	+3, +4

1.4 Applications of Thin Films

Among the various transition metal oxides, nanostructured Co_3O_4, MnO_2, WO_3 and CeO_2 have many advantages such as large surface area, high surface reaction activity, independence of oxygen and strong adsorption ability to immobilize biomolecules, which might promote the development of thin film electrodes. Nanostructured oxides thin films have experienced a rapid development due to their potential applications in a wide variety of technologies such as electronics, catalysis, ceramics, magnetic data storage, structural components, optoelectronic devices, display devices, biomaterials, antimicrobials, photonic and electronic devices [30-32], gas/bio sensors etc. [33-34]. **Fig**. 1.5 shows the images of several fields where metal oxides thin films are used.

1.4.1 Glucose bio sensing applications of thin films

Sensing of bio components and chemical species are increasing significantly now a days. In the case of chemical species sensing, it is essential to distinguish sensing devices that is crucial to simplify a better life. Diabetes mellitus is the major causes of death and

disability in the world. It is effectively controlled by regular monitoring of physiological blood glucose levels. Glucose sensing for diabetes monitoring is crucial because it is a chronic disease. About 200 million people in the world are afflicted with diabetes mellitus. This figure is expected to rise up to more than three hundred million by 2030 [35]. Glucose is playing an important role of human lifeblood. Frequently and accurately detection of glucose is of considerable sense in life. Thus, due to the importance of glucose in the fields of medicine, biotechnology, nutrition, and environmental science, the study of glucose detection has drawn tremendous attention [36-37].
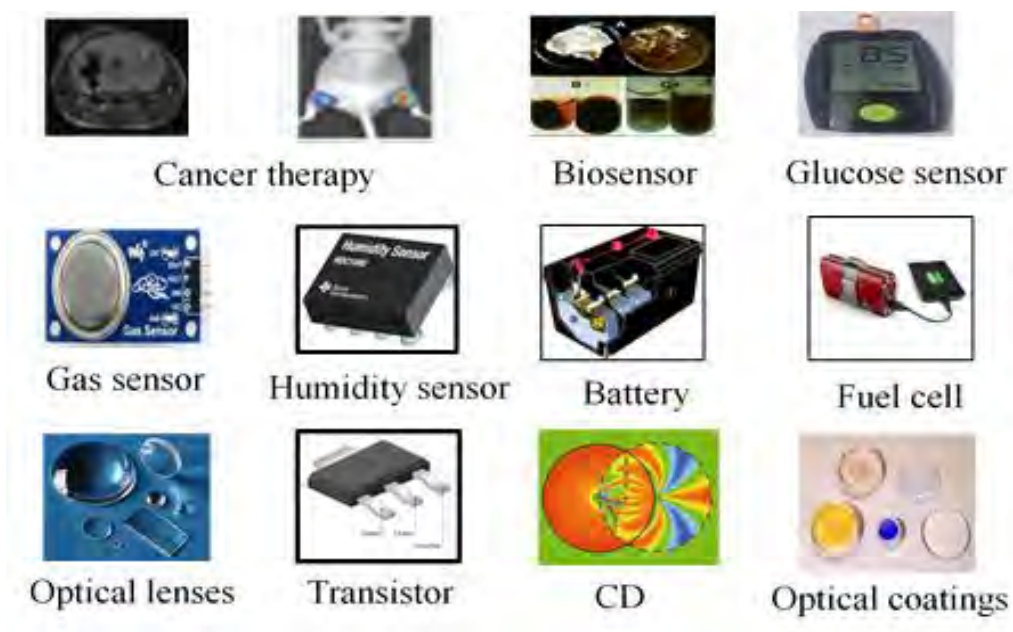
Fig 1.5 Applications of metal oxides thin films.

Traditional glucose sensors are enzymatic micro sensors; which utilizes glucose oxidase (GO_x) on the film surface to oxidize glucose. The main point of view is to oxidize glucose on electrode surface without any enzyme. Among numerous metal oxides, the transition and rare earth metal oxides have drawn more interest in sensing abilities for non-enzymatic glucose sensors as they possess good catalytic properties, large surface area and fast electron transfer which can make the ideal detection elements like glucose. The historical commencement of biosensors was in 1960s with the pioneering work of Clark and Lyons [38], and the first enzyme-based glucose sensor commenced by Updike and Hicks in 1967 [39]. Since then, an extensive research have been done on the glucose biosensors based on the GO_x [40-42].Therefore, the development of highly selective, sensitive, inexpensive, reliable and fast enzymatic/nonenzymatic glucose sensor is still imperatively needed. In recent years, an increasing number of researchers have explored

the production of novel nano-scale metal oxides, noble metal-doped metal oxides, and metal oxide nano composites. Novel analytical devices based on nanostructured metal oxides are cost-effective, highly sensitive due to the granularity, porosity large surface-to-volume ratio of the nanostructure, and additionally show excellent selectivity when coupled to bio recognition molecules with simple design [43-45].

Numerous processes have been developed for creating new glucose biosensors such as electrochemical methods, colorimetry, conductometry, optical methods, and fluorescent spectroscopy. Among them, the electrochemical glucose sensors have attracted the most attention over the last 40 years because of their unbeaten sensitivity and selectivity. Additionally, electrochemical techniques show lower detection limit, faster response time, better long term stability and inexpensiveness. Nanostructured metal oxides thin films have been used as a substrate or catalyst for glucose oxidation reaction in non-enzymatic glucose sensor development. The high hole mobility and excess of oxygen atoms in the metal oxide structure demonstrate its high conductivity for electrochemical technique applications [46]. In recent years progressive attempts have been made to determine the glucose without any enzyme for the reliable fast determination. Most enzyme less electrochemical glucose sensors rely on the properties of the electrode materials, on which the glucose is oxidized directly. Considering the importance of glucose detection in the fields of biotechnology, a method has been affected in the present work that may be an efficient method for the fast and precise determination of sensing current and glucose concentration response.

1.5 Iron (Fe) and Copper (Cu) as Dopants

Element doping is a common and effective way to change the properties of materials. The presence of the dopants plays a crucial role in improving the chemical and physical properties of transition and rare earth metal oxides thin films.In order to improve the electrical conductivity, transmission stability and feasibility for the practical use, various processes like changing substrate temperature, doping, annealing and aging are employed. Among these methods, doping is one of the excellent ways to improve the above mentioned properties. In recent years, to fabricate nanostructured transition and rare earth metal oxides with tunable physical and chemical properties for broad range of applications several efforts have been devoted, among which transition metal doping is a promising and efficient route to improve the optical absorption and the electrical behavior. A good number of research work have been done on the synthesis and characterization of

transition and rare earth metal oxide (Co_3O_4, MnO_2, WO_3 and CeO_2) thin films doping with various cations such as K^+, NH_4^+, Ba^{2+}, Fe^{3+}, Cr^{3+}, Cu^{2+}, Ag^+, etc. Supplementary to these metals, Fe and Cu have a great deal of diligence dopants because of low cost, good electrical conductivity, non-toxicity and environmentally friendly nature [47-50].

Copper (Cu) ions have long recognized for human health. Cu doped TMO (TM: transition metal) attracts much attention because of displayed potentials due to spin frustration and thermo electrics. The monovalent Cu cations are linearly coordinated with two O ions and the parallel O-Cu-O chains connect TM^{3+} cations forming two-dimensional sheets of edge-sharing TMO_6 octahedrons. Accordingly, Cu:TMO can be regarded as a natural super lattice composed of TM oxide magnetic layers and cuprous oxide semiconducting layers. Therefore, strong or unconventional coupling between spin and exciton can be expected in Cu: TMO. In addition, carrier doping into Cu: TMO is possible; thus interplay among spin, exciton, and charge carrier could be expected. Copper is considered ideal for cationic doping into TMO and rare earth metal oxides to improve catalytic, sensing and electrochemical properties.

Fe doped TMO (Fe: TMO) show diverse properties, like proper crystal structure, suitable particle size, appropriate optical band gap, moderate magnetizations, high coercivities, single domain effects, and so on which leads to impressive industrial and biological applications. The additional Fe cations perform an important stabilization function for the structure of TMO and influence its corresponding properties at the same time. Fe also improve the catalytic properties of rare earth metal oxide (CeO_2). Hence Fe acts as donor containing n-type charge carrier and Cu acts as p-type acceptor. **Fig**. 1.6 shows the position of carrier type due to doping in semiconductor. The addition of dopants, which can generate electrons or holes, known as n-type and p-type semiconductors respectively are responsible to alter the Fermi level which lies within the band gap in semiconductors. If a material is doped with impurities which serve to increase the number of electrons within the semiconductor material then the Fermi level is raised near the top of the band gap, such that extra electrons can easily be excited into the conduction band. If a material is doped with impurities which serve to increase the number of holes (acceptors) just above the valence band, this shifts the Fermi level down to just above the valence band. Thus, nanostructured metal oxides thin films may suitable candidate for developing glucose biosensors by changing optical, structural and electrical parameters of the thin films by doping transition metal into metal oxides [51-52].
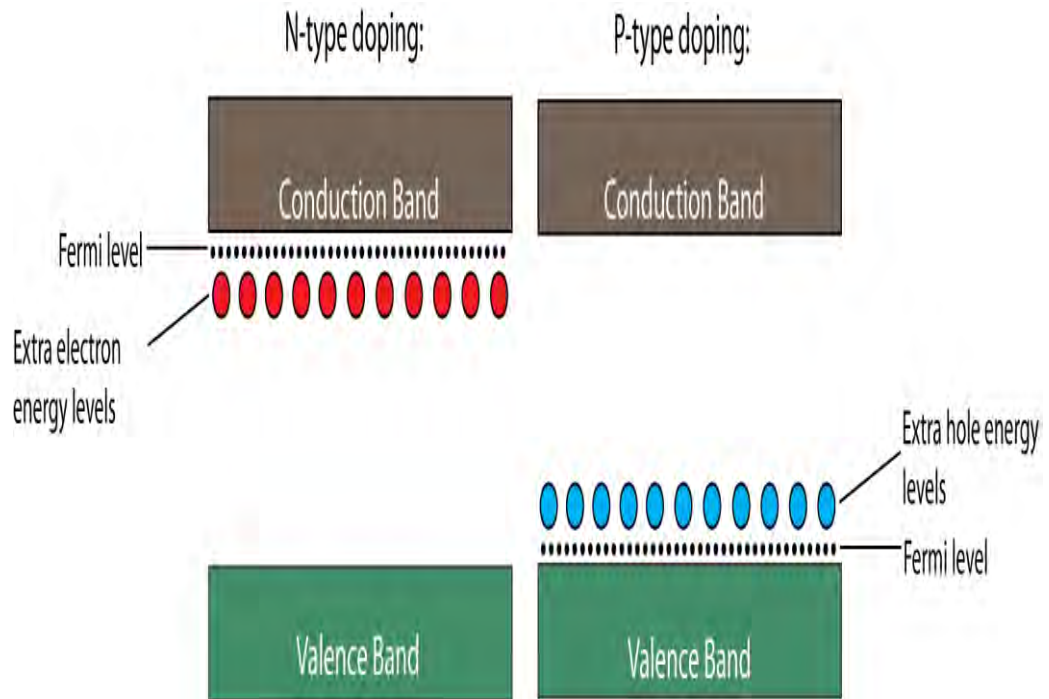
Fig. 1.6 Doping in semiconductors.

1.6 Motivations of The Present Research Work

A lot of researchers have explored the production of novel nano-scale metal oxides, noble metal-doped metal oxides, transition metal oxides, rare earth metal oxides and rare earth metal doped metal oxides. Novel analytical devices based on nanostructured metal oxides are cost-effective, highly sensitive due to the large surface-to-volume ratio of the nanostructure, and additionally show excellent selectivity when coupled to bio recognition molecules with simple design. Metal oxides show excellent biocompatibility and easy synthetic procedure for nanostructure that enables reliable immobilization of Glucose oxidase (GO_x). Metal-oxide based sensors are very sensitive, relatively inexpensive and have the advantage of rapid response associated with specific nanostructures such as nanowire, nanorod, nanotube, nanoparticle, nanofiber, and so on. Among the various types of nanomaterial that have been developed, nanostructured metal oxides have recently aroused much interest as immobilizing matrices for biosensor development Nanostructured metal oxides have been found to exhibit interesting nano morphological, functional biocompatible, non-toxic and catalytic properties. These materials also exhibit enhanced electron-transfer kinetics and strong adsorption capability, providing suitable microenvironments for the immobilization of biomolecules and resulting in enhanced electron transfer and improved bio sensing characteristics. The catalytic ability of

transition and rare earth metal oxides such as Co_3O_4, MnO_2, WO_3, and CeO_2 of nonenzymatic direct electro oxidation of glucose is one of the attractive properties in glucose detection allowing minimum fabrication cost and stable glucose sensors. With a view to such applications, an attempt has been made to prepare Co_3O_4, MnO_2, WO_3 and CeO_2 thin films doped with Cu and Fe via spray pyrolysis method. From technological point of interest, such transition and rare earth metal oxides semiconductor thin films will be deposited on glass substrate. These oxides thin films with different thickness and molar concentration of dopant (Cu, Fe) are to be synthesized in aqueous solution. The effects of dopant (Cu, Fe) concentration on structural, optical and electrical properties of the Co_3O_4, MnO_2, WO_3 and CeO_2 thin films are to be studied in details. A good homogenous and stoichiometric thin film with high efficiency is expected to be grown by taking the advantage of this low cost technology and also more expected to be grown by using the advantages of this low cost technique. By varying the pH of the aqueous solutions, density of ion concentration or the substrate temperature, the deposition of thin film can be controlled easily. Such good controllability of the thin films from aqueous solutions has great advantages of economy, convenience and capacity of large area deposition for production design. A suitable morphology, crystallite size, optical band gap and electrical conductivity are expected for nanocrystalline semiconducting metal oxides thin films which will provide information for their suitability of biosensor fabrication.

1.7 Objectives of The Present Work

The goal of the present investigation is to grow and characterization of Co_3O_4, MnO_2, WO_3, and CeO_2 thin films, and the effect of Fe and Cu doping. Objectives of this research are:

(i). To deposit Co_3O_4, MnO_2, WO_3, and CeO_2 thin films by doping Fe and Cu separately at different molar concentrations.

(ii). To study the surface morphology, elemental composition and structural parameters of deposited films.

(iii). To determine the optical transmittance and absorbance of undoped and doped metal oxide films with respect to wavelength and to see electronic band gap tunability.

(iv). To study the electrical conductivity, carrier concentration, Hall mobility etc. of the films

(v). To measure the C_2H_5OH, CH_4, NH_3 etc. gas sensitivity and to study the bio (glucose) sensing effect of the deposited films.

1.8 Significance of Study

In this study, spray pyrolysis deposition technique is used to obtain nanostructured metal oxides (Co_3O_4, MnO_2, WO_3 and CeO_2) thin films with consistent particle sizes and morphologies. Spray pyrolysis deposition technique shows much better surface of thin films compare to the conventional methods. It is easy in term of experimental setup as well as cost effective than others. The size and morphologies of Co_3O_4, MnO_2, WO_3, and CeO_2 thin films depend upon different synthesis methods and deposition parameters such as change in substrate temperature, annealing, aging, doping etc. The properties of Co_3O_4, MnO_2, WO_3, and CeO_2 thin films such as surface morphological, structural, optical and electrical are strongly affected by the Fe and Cu doping concentrations.

1.9 Thesis Layout

This thesis is organized in chapter wise. The outlines of the present thesis are arranged as following:

In chapter 1, the general introduction containing transition and rare earth metal oxides (Co_3O_4, MnO_2, WO_3 and CeO_2) and applications areas of metal oxides thin films are described. In addition, the motivation and objectives and expected outcomes of the present thesis are presented on why we chose Co_3O_4, MnO_2, WO_3 and CeO_2 thin films.

In chapter 2, some earlier literature survey on (Cu, Fe): (Co_3O_4, MnO_2, WO_3 and CeO_2) thin films infightings upon their different properties and applications are provided.

In chapter 3, a brief description on the different thin film deposition techniques and growth mechanism of nanostructured thin films are carried out. Also, details on the different characterization techniques with theoretical knowledge and basic working principles are highlighted. In addition, a detailed description of the actual materials and synthesis process carried out in the deposition of the nanostructured (Co_3O_4, MnO_2, WO_3 and CeO_2) thin films doped with Fe and Cu separately at different molar concentration are presented.

In chapter 4, the results of the deposited nanostructured thin films obtained from different characterization techniques are reported with discussion in details.

In chapter 5, conclusion of the present thesis work is presented in brief. Also a future outlook for continued research in this direction is highlighted.

CHAPTER 2

LITERATURE REVIEW

2.1   Literature Review on Fe and Cu Doped Co_3O_4 Thin Films

2.2   Literature Review on Fe and Cu Doped MnO_2 Thin Films

2.3   Literature Review on Fe and Cu Doped WO_3 Thin Films

2.4   Literature Review on Fe and Cu Doped CeO_2 Thin Films

CHAPTER 2 LITERATURE REVIEW

A large number of researchers all over the world in the nook and corner are searching for new invention in this field and findings are publishing in national and international journals. For many years, Metal oxides thin films have been studied extensively because of a wide range of technical applications, for instance as transparent electrodes in photovoltaic and display devices, gas sensors, and chemical sensors, biosensors and so on. We may now discuss in brief review of some common transition and rare earth metal oxides (Co_3O_4, MnO_2, WO_3, CeO_2) thin films doped with Fe and Cu as bellow.

2.1 Literature Review on Fe and Cu Doped Co_3O_4 Thin Films

Spinel type Fe:Co_3O_4 (0, 5 and 10% of Fe) thin films were prepared on stainless steel substrate using the thermal decomposition method by **Laouini, E., et al. [53].** No parasitic phases were detected and all the peaks, exhibited by the patterns, were characteristic of spinel type oxides, regardless of the oxide composition and support. The X-ray diffract gram for the oxide with 5% of Fe showed the broad and less defined diffraction lines due to weak crystallinity. An enhancement of the electro catalytic activity, towards the oxygen evolution, was observed with the increase of iron content in the cobalt oxide.

Pulsed spray evaporation chemical vapor deposition was employed for the synthesis of cobalt-based spinel oxide thin films, $Co_{3-x}Fe_xO_4$ with x = 0-1.56 by **Naoufal, B., et al. [54].** XRD analysis showed that the normal spinel structure was retained for $0 \leq x \leq 0.65$ by the selective insertion of Fe^{3+} in the octahedral sites. The spinel inversion was noticed above this range. The room-temperature electrical resistivity of the thin films was controlled between 9 and 0.007 Ω cm by the adjustment of iron doping concentration. The controlled iron doping was demonstrated to be an efficient strategy to tune the reactivity and the selectivity of CO of the cobalt-based spinel oxide.

Hans, A. G., et al. [55] reported on optical and structural properties of α-Fe_2O_3 and Co_3O_4 thin films, grown by direct oxidation of pure metal films deposited on soda-lime glass. Structural characteristics and morphology of the films were investigated by X-ray diffraction and scanning electron microscopy. Linear optical absorption, and linear refraction as well as nonlinear optical properties were investigated. XRD pattern exhibited

a diffraction peak at 2θ= 33:18°corresponding to crystalline hematite (α-Fe$_2$O$_3$) where the pattern corresponding to Co$_3$O$_4$, observed after the oxidation process is complete, corresponds to the (311) plane of Co$_3$O$_4$ with a diffraction peak at 2h ¼ 36:88. The intercept of the straight line for the α-Fe$_2$O$_3$ film shows that Eg = 2.3 eV at 541 nm while the Co$_3$O$_4$ sample presents two band gaps of direct allowed transitions, one band gap of 1.56 eV at 798 nm and another of 2.22 eV at 561 nm.

Tobias, G., et al. [56] studied that when the Co$_3$O$_4$ is doped with small amount of iron (Co/Fe atomic ratio of 64/1), the surface area of the sample does not change significantly. However, the pore volume of the sample is increased to 0.31 cm3/g. This indicated a noticeable change in porous structure of the materials. All iron doped samples had a higher pore volume (in the range of 0.30−0.37 cm^3/gm.) than undoped Co$_3$O$_4$. In addition, the effect of diverse structural properties was investigated through electrochemical water splitting, showing enhanced catalytic activities when iron species were distributed in the Co$_3$O$_4$ structure. Compared with noble metal catalysts, iron incorporated mesoporous Co$_3$O$_4$ showed prominent electrochemical activity, and therefore this type of transition metal based mesostructured material with high surface area could be used as an alternative electro catalyst for water oxidation.

Pure and Fe-doped cobalt oxide thin film electrodes are successfully prepared by nebulizer spray pyrolysis technique by **Manickam, M., et al. [57].** Single phase polycrystalline cubic structure with (220) plane orientation are observed in the XRD analysis for pure and Fe-doped cobalt oxide films. From the optical analysis, two band gaps are observed in the range 1.366-1.713 eV and 2.846-2.925 eV for lower and higher energy regions respectively. HR-SEM images revealed the formation of well covered and spherical shaped particles in the formed films. The increased of electrical conductivity with Fe doping concentration were confirmed at room temperature. The maximum specific capacitance value was observed in the 2.5 wt% of Fe doped Co$_3$O$_4$ thin film electrode at the scan rate of 2 mV/s. Cobalt oxide (Co$_3$O$_4$) and copper-doped cobalt oxide (Cu$_x$Co$_{3-x}$O$_4$) thin films were prepared by **Rosa, T. A. L., et al. [58]** onto titanium substrate using thermal decomposition method. They studied that SEM micrographs showed a granular and highly porous surface. The surface morphology became gradually more porous and rough as the copper content increased. XRD analysis showed that the Ti/Cu$_x$Co$_{3-x}$O$_4$

electrodes displayed a similar diffraction pattern corresponding to a monophasic Cu-Co mixed spinel oxide.

Yamada, Y., et al. [59] studied Cu/Co_3O_4 nanoparticles as catalysts for Hydrogen evolution from Ammonia borane by hydrolysis. They investigated a series of nanosized Co_3O_4 particles in which Cu was loaded on the surface were examined as robust catalysts for hydrogen evolution by ammonia borane hydrolysis. Their catalytic activity was dependent on the shape and size of nanosized Co_3O_4. The shape of nanosized Co_3O_4 was cube, hexagonal sheet, or uncontrolled. Among these, the Co_3O_4 in the shape of hexagonal sheet showed the highest catalytic activity.

Mehrabadi, Z. S., et al [60] studied on nanostructured Cu doped cobalt oxide(Co_3O_4) thin films by sol gel technique with different mole ratios of Cu/Co ranging from 0.05 to 0.15. From XRD studies, the polycrystalline structure of Co_3O_4 with cubic phase ($a = 8.08400$ Å) in all the samples were identified. The main XRD peak in the preferred orientation corresponded to (311) plane and peak intensities did not change with Cu doping. They also demonstrated that no other peak were created in samples with different Cu/Co molar ratio which confirmed that the formed phases were stable and that their formation was independent of copper quantity. The mean size of Cu–Co oxide nanoparticles at different mole ratios of Cu/Co were between 24nm to 28nm and that gradually decreased with increasing Cu/Co ratios. They also studied methane gas sensing properties. The gas sensing measurements revealed that Cu as a dopant improved the sensing properties of Co_3O_4 and sensitivity increased with Cu concentration. The best sensing properties were found at the Cu/Co mole ratio of 0.125 and 0.15.

Amri, A., et al [61] prepared copper-cobalt oxide thin films with different copper/cobalt molar ratios, of [Cu]/ [Co] = 0.5, 1, and 2 on aluminum substrates via a simple and cost-effective dip-coating method. Field emission scanning electron microscopy (FESEM) studies showed that the surfaces of both [Cu]/[Co] = 0.5 and 1 samples consisted primarily of fine granular nanoparticles, whereas the [Cu]/[Co] = 2 had a smoother surface. The XRD result showed that $Cu_xCo_{3-x}O_4$, known as copper−cobalt spinel, was cubic and had Fd$\overline{3}$m (227) space group with lattice parameter a ≈ 8.11 Å.

Spray pyrolysed Cu doped Co_3O_4 thin films were prepared by **Hassan, A. I., et al.[62]** on silicon substrate. X-ray diffraction results revealed that all films consist of single Co_3O_4

phase with preferred orientation (111) and cubic spinel structure. the grain size decrease with increasing Cu doping. After systematically investigated, they concluded that the doping of Cu ions on Co_3O_4 nanostructures played a crucial role in improving the detector performance. The 9wt% Cu:Co_3O_4 based as detector showed a highest responsivity than pure Co_3O_4 nanostructures. These results demonstrated that Cu doping Co_3O_4 thin films might promising for fabricating high performance photo detector working for visible region.

The non-enzymatic glucose sensing ability of elemental Cu doped Co_3O_4 thin films deposited on FTO substrate by **Harry, M., et al. [63]** using a facile chemical solution method. No hole or crack is observed from the SEM image, highlighting the consistency of the film thickness through the entire geometrical area. Sample also exhibited the fcc crystal structure of Co_3O_4.There was a small expansion of the average lattice constant regardless to the Cu doping. Introduction of Cu resulted in increased electrical conductivity, charge career density and decreased charge transfer resistance in Co_3O_4. The as prepared Cu doped Co_3O_4 thin film sensor, showed very high sensitivity of 1850 μAcm-$2Mm^{-1}$ with a limit detection of 0.153μM and, was used successfully to measure glucose concentration in human serum sample.

2.2 Literature Review on Fe and Cu Doped MnO_2 Thin Films

Xiongfei, S., et al. [64] studied sol gel-assisted nanostructured Fe-doped manganese oxide. Characterization of the samples over a wide range of Fe-doping levels ($0 \leq$ Fe/Mn$\leq$1/2) was carried out using a variety of experimental techniques. SEM images revealed that the morphology changed from nano needle to nanorod after Fe doping. Using conventional CuKα XRD, each samples were indexed on the tetragonal I4/m structure for Fe/Mn $\leq$ 1/2. XRD demonstrated that the Fe ions replaced the Mn ions in the crystal structure, particularly in the (211) planes, and resulted in a lattice expansion along the c axis.

The addition of iron (Fe) in order to improve the super capacitive properties of MnO_2 electrodes using galvanostatic mode **Dubal, D. P., et al. [65]** studied Fe:MnO_2 thin films grown on SS substrates with different Fe concentrations ranging from 0.5 to 4 at%. There was no difference between XRD patterns of MnO_2 and Fe: MnO_2, which meaned that Fe oxide could be amorphous and did not change the amorphous nature of deposited MnO_2.

Here the surface of MnO_2 became slightly nanocrystalline, whereas as Fe doping concentration increased to 1 at%, the surface of MnO_2 became slightly compact and spongy. Further as the Fe concentration in the plating solution continuously increased to 2.0 at%, the spongy surface of MnO_2 was converted into more nanocrystalline. Due to Fe addition, the surface of the MnO_2 electrode became nanocrystalline. However, the nano crystallinity began to decrease as the Fe addition in the plating solution was further increased. The surface became compact and even smoother than the plain MnO_2. Thus the results indicated that up to 2at% the Fe addition modified the surface of the MnO_2 electrode. This type of amorphous and nanocrystalline structure was expected to produce high super capacitance values.

Yue, M., et. al. [66] studied iron doped manganese oxides by a nanocasting method followed by controlled calcination. The amount of iron doping was optimized to provide the best balance of electronic and ionic wiring effects. Electrochemical measurements showed that the Fe-doped manganese composite had the best overall performance: a large reversible capacity, good rate capability and outstanding cycle life which suggested that it had the potential to be a candidate anode material for the next-generation.

Yang, P., et al. [67] fabricated nanostructured MnO_2 and Fe_2O_3 for Low-Cost High-Performance Solid-State Asymmetric Supercapacitors (ASCs) via a facile scalable method. They demonstrated excellent stability in a large potential window of 1.6 V and exhibited excellent energy density of 0.55 mWh/cm^3. They also showed good flexibility and high rate capability. Moreover, an application of high-performance ASCs in effectively switching colors of electrochromic systems was demonstrated, promoting low-cost high-performance solid-state ASCs to be a highly promising candidate for next-generation energy storage systems.

Fe doped MnO_2 thin films grown on stainless steel substrates were studied by **Ruting Huang et al. [68].** XRD peaks of 10 wt% Fe/M-MnO_2 were observed at $2\theta = 37.1, 42.5, 56.1,$ and $66.6°$. No peaks assigned to iron species in Fe/M-MnO_2 with different Fe concentrations ranging from 5 to 30 wt% Careful observations indicated that the diffraction peaks of Fe/M-MnO_2 had slight right deviation. Elemental analysis showed the homogeneity of Fe in Fe/M-MnO_2. EDX spectrometry confirmed the presence of Fe, Mn and O in Fe/M-MnO 2.35. The elemental composition analysis determined that only 6.58wt% Fe has been loaded in Fe/M-MnO_2, which agreed with Fe content (7.14 wt%).

The morphologies of numerous sub microspheres with thorns on the surface were observed by SEM images.

Chodankar, N. R., et al. [69] prepared nanostructured MnO_2 and Fe_2O_3 thin films on stainless steel by electro deposition method. The SEM images of the thin films showed porous surface. The SEM images also confirmed spongy balls like structure with ultrathin nanoflake. The average size of spongy balls for were about 200–300 nm. At higher magnification, it can be seen that the ultrathin nanoflake with spongy balls of MnO_2 provided the electronic transfer channel, which was expected to improve the conductivity and rate capacity of the obtained MnO_2 nanostructure.

Hiraga, H., et al. [70] studied $CuMnO_2$ thin films on $MgAl_2O_4$ (111) substrates by pulsed laser deposition method. X-ray diffraction revealed that the films had high crystalline quality with epitaxial relationship of $CuMnO_2$ (001) / $MgAl_2O_4$ (111) and $CuMnO_2$ (100)/ $MgAl_2O_4$ (11-2). XRD results also showed the monoclinic structure of $CuMnO_2$. The ultraviolet-visible optical response revealed a distinct absorption peak at 4.5 eV presumably with excitonic nature and broad peaks at 3.0 and 3.7 eV.

Copper manganese oxides (CMOs) were synthesized using a co-precipitation method with different precursors and precipitants for carbon monoxide oxidation by Li-**Na Cai et al. [71].** The as-synthesized catalysts were characterized by powder X-ray diffraction (XRD). The crystalline phase of copper manganese oxides obtained using strong electrolyte (OH^-) as the precipitant were mainly spinel $Cu_{1.5}Mn_{1.5}O_4$, while the catalysts prepared with weak electrolyte (CO_3^{2-}) as the precipitant mostly comprised of $MnCO_3$, Mn_2O_3 and CuO, and showed a much higher CO oxidation activity than that of the $Cu_{1.5}Mn_{1.5}O_4$. Keeping the same precipitant while changing the precursor caused a change in the H2 consumption which influenced the CO oxidation activity. A suitable combination of precipitant and precursor resulted in the most efficient CO oxidation catalyst.

Falahatgar, S. S., et al.[72] reported on nanostructured copper manganese oxide (CMO) thin films deposited by sol gel dip-coating technique. The prepared thin films exhibited uniform distribution of nanograins with faceted particles observed by FESEM. The EDX of CMO thin films revealed the presence of manganese, copper and oxygen. The samples exhibited the mixed copper manganese oxide corresponding to $CuMn_2O_4$ together with

Mn_3O_4 obtained by XRD analysis. The optical band gaps of CMO thin films were determined by Tauc plot and obtained between 2.68 and 3.01 eV.

MnO_2 and copper doped MnO_2 nanocrystals were synthesized by a chemical precipitation method reported **by Poonguzhali, R., et al [73]**. The tetragonal crystal structure of α-MnO_2 was confirmed through XRD analysis. The incorporation of Cu was confirmed from XPS patterns. The influence of copper doping on electrochemical capacitor performance of MnO_2 was investigated by cyclic voltammetry and galvanostatic charge–discharge studies. Among the various concentrations of doping, the 0.1M of Cu doped MnO_2 showed a very high specific capacitance.

Cu-doped nanostructured MnO_2 thin films were studied. The thin films were prepared by spin-coating technique on glass substrates by **Falahatgar, S. S., et al. [74].** The XRD patterns revealed the orthorhombic phase of MnO_2 (Ramsdellite). The FESEM images showed the size of nanograins and porosity of surfaces of the films. The refractive index and extinction coefficient dispersion and optical band gap were calculated by Forouhi-Bloomer model using the fitting process of the measured transmission data. The optical band gap of the films increased with increasing cu doping.

Shan Xu et al. [75] Cu-doped MnO_2 was synthesized by a hydrothermal synthesis methods. It was found that hydrothermal temperature and Cu doping had much influence on the morphologies and electrochemical performance of the products. The results showed that the morphology of the products presents the transformation from microspheres composed of nanorods to dispersed nanorods with the increase of the hydrothermal temperature. The XRD patterns indicated the tetragonal system α-MnO_2. No peaks related to Cu or other impurities were noted up to 0.075 M of Cu (7.5% Cu^{2+}). EDX elemental mapping showed the distribution of Mn, Cu, and O. The Cu-doped MnO_2 showed the smallest charge transfer resistance, the highest conductivity.

2.3 Literature Review on Fe and Cu Doped WO_3 Thin Films

Mixed tungsten and iron oxide thin films were prepared by **Comini, E., et al [76].** SEM analyses revealed a compact layer for the thin films with a fine morphology. The film thickness, measured with a profilometer, was 300 nm approximately. The electrical response of thin films of W-Fe oxides toward CO, NO_2, ozone and ethanol was investigated. Iron addition always increased the response towards ozone, carbon

monoxide and ethanol. For nitrogen dioxide, the introduction of iron concentrations lower than 10% produced an enhancement in the response.

Dongqin, B., et al. [77] synthesized iron-containing WO_3 (FeW) through thermal decomposition method. XRD analysis showed monoclinic WO_3 phase. No crystalline phases of iron oxides was found, probably due to the low content (0.30 wt %) of Fe. In the UV-vis diffuse reflectance spectra all samples displayed a wide absorption band in the region from 200 to 500 nm. The spectral onset was around 480 nm, corresponding to a band gap energy of about 2.6 eV. They also showed that WO_3 was an efficient photo catalyst for organic degradation only in the presence of H_2O_2. It was proposed that the electron transfer from the conduction band of WO_3 to Fe_2O_3 clusters was responsible for the observed improvement in photo catalytic activity.

Nanostructured WO_3 thin films doped with Fe was reported by **Ahsan, M., et al [78]** for CO sensing. Nanostructured pure and Fe-doped WO_3 thin films of (300 nm) and grain size of 10–15 nm were synthesized by thermal evaporation method. The as-deposited films were highly amorphous and annealing at 400ºC significantly improved the crystallinity without altering much the grain size. Analysis showed that Fe was incorporated in WO_3 film as a substitutional impurity in the WO_3 matrix, rather than as a catalyst on the film surface. Fe incorporation resulted in shortening of lattice cell parameters and O-W-O bonds. The film also contained mixed tungsten states. This created a number of defects and ultimately high number of oxygen vacancies in the film. By doping with Fe and annealing at 400ºC, they achieved a response to CO at a temperature of 150ºC.

Xiaofang, C., et al. [79] prepared WO_3 and Fe-doped WO_3 thin films on Indium-Tin Oxide (ITO) glass substrates by a dip-coating. SEM micrographs for the WO_3 and Fe-WO_3 electrodes showed that both the films were uniform. After doping, the size of the particles increased slightly and the roughness of the surface also appeared to increase. EDX spectra showed that Fe element was detected on the surface of doped WO_3. The XRD patterns of WO_3 films and Fe-doped WO_3 films performed that the XRD patterns of the Fe-doped WO_3 samples exhibited similar phase to pure WO_3, which demonstrated that the crystal form of the WO_3 films did not change upon doping. The optical absorbance spectra of the film electrodes showed that the light absorption increased in the region of

280-600 nm when the doping concentration of Fe increased to 2%. A red-shift was caused by a narrowing of band gap of the films.

Tesfamichael, T., et al. [80] fabricated Fe-doped tungsten oxide thin films with different concentrations (0–2.6 at %). Thickness of the films lied between 155 and186 nm and grain size between 43 and 57 nm. Higher amount of defects were observed in the films. The visible transmittance of all the films remained similar (>70%) but their optical band gap decreased with increasing Fe concentration from 3.30 to3.15 eV. Enhanced NO_2 gas sensing at lower operating temperature was achieved from tungsten oxide film doped with 2.6 at% Fe and this was concluded due to the decreased in the optical band gap and an increased in the number of defects.

Barreca, D., et al. [81] reported nanostructured Fe_2O_3-WO_3 composite materials. High dispersion and reduced particle size was recorded by XRD pattern. FESEM analyzed evidenced the uniform growth of a globular Fe_2O_3 deposit, as well as a homogeneous distribution of WO_3 species over the iron (III) oxide matrix. The thickness, was estimated to be 250 nm.

Porous and photo electrochemically active Fe-doped WO_3 nanostructured thin films were studied by **Khare, C., et al. [82].** The measurement region with WO_3 nanostructures containing 1.7 at % Fe demonstrated maximum photocurrent density of ~72 μA cm^{-2}. The Fe-doping in WO_3 reflected in a decreasing band gap value from ~2.7 eV at 600 mV to ~2.48 eV at 1600 mV. High porosity and corresponding microstructure considerably affected the PEC performance of dealloyed thin films. The Eg shifted at higher potential might be a result of a phase becoming photo electrochemically 'visible' due to its higher photocurrent on-set potential.

Copper-doped WO_3 films were studied by **Gopalan, C., et al. [83]** for metallization cell memory devices. The highlights of this study were the intercalation products forming on the interface between the WO_3 and Cu during thermal evaporation and also after thermal or photo thermal diffusion of Cu into WO_3 films. Surface of WO_3 was where the measurement began and the point at which the Cu concentration saturated was treated as the boundary between the WO_3 and Cu. XRD patterns of the initial film, the photo-thermally diffused film and the thermally diffused film showed characteristic peaks around 2θ 23–28° in which the most intense peaks of WO_3 and WO_2 were situated.

Among the diffusion yield they identified Cu, CuO, Cu_2WO_4, $CuWO_4$, and Cu_3WO_6. There was a large dispersion in size distribution, ranging from 5 nm to 90 nm with an average size of 20 nm. The reduction-oxidation process on Cu insertion was even more profound when Cu was introduced in the WO_3 matrix as a result of thermal diffusion.

Shenmin Z., et al. [84] synthesized Cu-doped WO_3 materials with photonic structures for high performance sensors. From wide-angle XRD spectra they found monoclinic WO_3 phase. The positions of all the peaks were exactly the same as the pure WO_3 thus it seemed that the doped copper did not distort the matrix lattice. The peaks were relatively broad, indicating that the oxide cell walls were nanocrystalline. Optical properties were studied in terms of reflection measurements which were performed in the visible and near infrared wavelength regions. Pure WO_3 exhibited the highest reflection at 323 nm. The Cu doped WO_3 had strong reflection peaks at around 400, 500 and 680 nm. The refractive index of WO_3 was 1.57 and Cu doped WO_3 was 1.37 indicating photonic properties of Cu-doped WO_3. The Cu-doped WO_3 sensors have showed much higher sensitivity to $(CH_3)_3N$ gas than the pure WO_3 sensor due to the catalytic effect of lattice Cu on the interactions between the oxide surface and the gas. The photonic crystal (PC) Cu-doped WO_3 sensor had a much higher response sensitivity as well as a higher selectivity compared to the non-PC Cu-doped WO_3 sensor.

Yanyan, Y., et al. [85] prepared Cu/WO_3 composite sample by the addition of Cu concentrations at 0, 3 wt%, 8 wt%, and 12 wt%. Many small spherical aggregates particles were indicated by SEM micrograph. Although some ultrafine particle aggregations were found to be embedded the surface roughness of the coating was still maintained. 8 wt% Cu/WO_3 showed more roughness. They also studied antimicrobial and photo catalytic degradation performance and observed the decrease in viable E. coli cells on the 8 wt% Cu/WO_3.

Nanostructured copper doped WO_3 was fabricated using a hydrothermal method by **Hao, Z., et al [86].** XRD pattern of the 3wt% Cu-WO_3 sample calcined at 300ºC showed the monoclinic $W_{18}O_{49}$ structure. Two dominant peaks correspond to (010) and (020) lattice planes were observed. The monoclinic $W_{18}O_{49}$ structure was transferred to a monoclinic WO_3 structure during heating at 600ºC annealing temperature. The SEM images indicated that the Cu-WO_3 sample sintered at 300ºC was approximately 1 μm in size and consisted of an urchin-like structure. After calcination at 600ºC, this structure was converted to a

flower-like structure that was 1~2 μm in size and composed of many interconnected nanosheets. A coarse surface and a flower-like structure that was assembled from many approximately 100 nm thick nanosheets or nano squares were also observed.

Simple chemical co-precipitation method was employed to synthesize two dimensional copper (Cu) doped tungsten oxide (WO_3) nanoplates by **Mehmood, F., et al [87]**. The XRD results confirmed the monoclinic crystal structure of WO_3 nanoplates, and also successful doping of Cu ions into the WO_3 crystal lattice. The presence of functional groups and chemical bonding were verified through FTIR spectra. The SEM images demonstrated that both undoped and Cu doped WO_3 samples had square plate like morphology. The EDX spectra confirmed the presence of Cu, W and O ions. Diffuse reflectance spectroscopy (DRS) analysis revealed a substantial red-shift in the absorption edge and a decrease in the band gap energy of nanoplates with Cu doping. Furthermore, the differential cytotoxic properties of Cu doped WO_3 samples were evaluated against human breast (MCF-7) and liver (Hep-2) cancer cells with ectocervical epithelial (HECE) healthy cells. The present findings confirmed that the Cu doped WO_3 nanoplates can be used as an efficient biocompatible anti-cancer agent.

Nanocrystalline pure and Cu doped WO_3 nanoplates with nano rods were studied by **Deepa, B., et al [88]**. The XRD analyses were indexed to monoclinic structure with space group P21/n. The SEM revealed the nano-plate and nanorod shaped morphology and the diameter of the rod is ~ (80-100) nm and ~ (30-80) nm and their lengths are 0.1 μm and 0.2–0.5 μm range for pure and Cu doped WO_3 nanoparticles respectively. The optical absorbance edge observed in the region 350-500 nm and the value of band gap energy was 3.12 and 3.36 eV for pure and Cu doped WO_3 using Kubelka–Munk relation. From the resultant value, it is concluded that the divalent dopant enlarged band gap energy compared to pure WO_3. They also showed that Cu doped WO_3 nanoparticles improved the electrochemical behavior than the pure WO_3 nanoparticles.

Good crystalline Cu doped WO_3 thin films were prepared over quartz substrate using Radio Frequency (RF) magnetron sputtering by **V.S. Kavitha, V. S., et al [89].** Intense sharp peaks in the XRD patterns of all the films showed their good crystalline quality. All films were preferentially oriented along (200) crystal plane. Among the deposited thin films 3 wt% Cu doped WO_3 film showed improved crystalline quality compared to others. Morphology analysis showed a smooth surface morphology for undoped film and the film

with 1 wt% Cu doping concentration but at higher doping concentrations formation of bigger clusters were seen. EDX spectra confirmed the incorporation of Cu ions in WO_3 lattice and showed that Cu nanoparticles acted as growth centers for bigger structure formation in WO_3: Cu films. The dip observed in the transmittance spectra around 620 nm region and a corresponding enhancement in absorbance around this region for 5 and 7 wt% Cu doped WO_3 films were also reported.

2.4 Literature Review on Fe and Cu Doped CeO_2 Thin Films

Qi-Ye, W., et al. [90] synthesized Fe-doped CeO_2 by ceramic method and the effects of Fe doping on the structure and properties were characterized by ordinary methods. They showed that pure CeO_2 only had a small dielectric constant ε of 4, while a small amount of Fe (0.9 at. %) doping into CeO_2 promoted densification and induced a large ε of 23. The absorption coefficient of Fe-doped CeO_2 at frequency ranging from 0.2 to 1.8 THz was less than 0.35 cm^{-1}, implying that Fe-doped CeO_2 was a potential terahertz (THz) optical material.

Fe-doped CeO_2 thin films were prepared using pulsed laser deposition method by **Sharma, S. K., et al.[91].** They observed that all films showed peaks corresponding to the CeO_2 phase. The bulk CeO_2 sample exhibited the polycrystalline nature of the fluorite structure with maximum intensity for the (111) peak. It was seen that with doping, films still exhibited a single-phase fluorite polycrystalline structure, but the intensity of the peak (111) decreased as a function of doping concentration in comparison to the bulk target. On the other hand, a strong crystallographic texture appeared as indicated by high relative intensity ratios of the (200) peak and the (111) peak. it was noted that with the further increase of Fe concentration (x=0.03), the corresponding intensity ratio I (200)/I(111) started to decrease and attained a value of ~7% as compared to bulk CeO_2. **Wang, Z., et al. [92]** reported on Fe-doped CeO_2 nanorods via a simple co-precipitation method. The formation of the nanorod morphology strongly depended on Fe contents. Beyond the solid solution limit, only nanoparticles were observed. The morphology was also affected by precipitation agents, temperatures and aging times. The formation of the nanorods originated from the intrinsic anisotropy of Ce hydroxide. The recrystallization mechanism was thus proposed, in which the coexistent ammonia and/or Fe acted as the capping agents for the formation of nanorods. Simultaneously, the enrichment of Fe on the surface resulted in the nanorods with round shape and sharp tips.

Fe-doped CeO_2 nanoparticles were studied by **Wang, C. C., et al. [93].** Powder X-ray diffraction patterns of Fe-doped CeO_2 NPs with various Fe doping concentrations (from 1% to 11%) and undoped CeO_2 NPs showed the cubic fluorite structure. No diffraction peak from any impurity, such as pure Ce and Fe, or any other cerium oxide or iron oxide, was obtained within the detection limit. The peaks broadened as the Fe doping level increased.

Phokha, S., et al [94] reported undoped CeO_2 and Fe-doped CeO_2 ($Ce_{1-x}Fe_xO_2$, $0.01 \leq x \leq 0.07$) nanospheres with diameters of $100 \sim 200$ nm prepared by hydrothermal method. The XRD results showed that Fe-doped CeO_2 was single-phased with a cubic structure, and with Fe^{3+} successfully substituting in Ce^{4+} sites. It is observed that CeO_2 and Fe-doped CeO_2 nanoparticles experience considerable lattice distortion. Fe^{3+} doping caused redshift of the samples.

Channei, D., et al. [95] studied on nanoparticles of undoped CeO_2 and 0.50–5.00 mol% Fe-doped CeO_2 thin films for photo catalytic application. XRD patterns indexed as CeO_2, with a cubic fluorite structure. No other peaks from either metallic iron were found in the XRD analysis. Samples with higher doping revealed a shift in the peak associated with the (111) direction which shifted towards higher values. The superior photo catalytic performances of the Fe-doped CeO_2 films, compared with undoped CeO_2 films, was ascribed mainly to a decrease in band gap energy and an increase in specific surface area of the material. The 1.50 mol% Fe-doped CeO_2 film was found to be the optimal iron doping concentration for Methyl orange (MO) degradation.

Yang, W., et al. [96] synthesized CeO_2 with Cu leading. of 1%, 5%, 10% and 15%. XRD patterns of CuO/CeO_2 samples with copper loading showed that typical diffraction peaks of CeO2 were observed in all the samples, while CuO phases were not detected for CuO/CeO_2-1% sample. When the Cu loading increased up to 5%, typical peaks of CuO appeared and the intensities increased apparently with the increase of Cu loading. SEM micrograph showed regular spherical morphology and smooth surface.

Cu-doped CeO_2 ($Ce_{1-x}Cu_xO_2$) films with x=0.03 and 0.15 were deposited using a pulsed laser deposition technique by **Slusser, P., et al. [97].** XRD patterns of the $Ce_{1-x}Cu_xO_2$ films showed that in all the films, only the major diffraction peaks belonging to the (001) family of cubic cerium oxide were observed indicating the highly oriented nature of the

films. Comparison of (001) peak of $Ce_{1-x}Cu_xO_2$ with the corresponding peak of pure CeO_2 suggested a decrease in the lattice parameter. UV-vis optical absorption spectroscopy experiments showed that the absorption edge of $Ce_{1-x}Cu_xO_2$ films decreased in energy with increase in Cu concentration. The band gap of the samples was found to be direct in nature and was estimated to be 3.45, 3.43, and 3.39 eV for the x=0, x=0.03, and x=0.15 films, respectively.

Zhang, D., et al [98] synthesized Cu-doped CeO_2 spheres by a simple hydrothermal method. SEM images confirmed the hollow spheres with a rough surface consist of many tiny particles. An average diameter of hollow spheres ~126 nm. The hollow spheres were comprised of a large number of tiny particles with a mean size of 8–15 nm. They also analyzed from XRD that the peaks due to CuO or Cu_2O were not detected in the Cu-doped CeO_2 hollow spheres even when the amount of Cu reached 20%, which indicated homogeneous dispersion of copper species. The Cu-doped CeO_2 spheres exhibited high catalytic activity for the conversion of CO compared to pure CeO_2 and also possessed a desirable stability.

Knauth, P., et al [99] Cu-doped CeO_2 (8 mol% Cu) nanoparticles. XRD pattern show that no crystalline copper oxides, copper metal or new phases were detected. The FWHM was significantly reduced, showing that some crystallite growth took place; the average crystallite size remained low, however, at (10±6) nm. The electrical resistance of the as-received Cu-doped CeO_2 increased below 200ºC. The conductance in the temperature range 50-100°C follows an Arrhenius-type dependence (open dots) with an activation energy of about 1 eV. Undoped and Cu-doped CeO_2 (2.5, 5, 7.5 mol%) thin films were prepared **Sani, Z. K., et al [100]** on glass substrates using dip coating technique. X-ray diffraction investigations of the films revealed that the ceria thin film had a cubic structure and Cu doping inhibited the crystal growth. SEM micrographs showed that all films composed of fine nano-grain without any cracks that distributed homogenously on surface. The optical transmittance was enhanced and the absorption edge was shifted to lower wavelength by Cu doping. The refractive indices and extinction coefficients which were determined using theoretical approach were decreased by Cu doping. The electrochemical behavior of the films was examined in 1M propylene carbonate electrolyte. The total charge density of ceria thin film increased by Cu doping and 5 mol% Cu-doped CeO_2 film shad the highest ion storage capacitance.

$Cu_xCe_{1-x}O_2$ (x = 0.01, 0.03 and 0.05) nanostructures were produced by **Alla, S. K., et al [101].** X-ray diffraction patterns for nanocrystalline $Cu_xCe_{1-x}O_2$ (x = 0.01, 0.03 and 0.05) samples indicated that all the samples had face centered cubic type structure of CeO_2. Within the detection limit of XRD, other impurity phases were not observed in the samples. The optical absorbance for Cu substituted CeO_2 samples showed blue-shift of absorbance with increased Cu concentration. The optical band gap values progressively increased with increased Cu content.

The effect of Cu dopant ions on the structural and optical properties of $Ce_{1-x}Cu_xO_2$; (0.00 < x < 0.20) nanocrystals (NCs) synthesized via co-precipitation technique were reported by **Kumari, K., et al. [102].** XRD results confirmed the successful incorporation of Cu ions into CeO_2 single-phase cubic system. The decrease in the crystallite sizes (13 - 4 nm) as the Cu content increased indicated towards the decrease in the crystal quality and introduction of additional lattice defects. The spherical shape morphology was shown in the images of undoped CeO_2. However, the particles showed little agglomeration with increasing doping concentration. The analysis of UV absorption spectra for $Ce_{1-x}Cu_xO_2$; (0.00 < x < 0.20) nanoparticles showed sharp absorption edges and a little red shift. Average absorption observed was below 374 nm.

CHAPTER 3

EXPERIMENTAL DETAILS

3.1   Deposition Techniques

3.2   Synthesis of Thin Films by Spray Pyrolysis Technique

3.3   Characterization Methods

CHAPTER 3 EXPERIMENTAL DETAILS

This chapter deals with various thin film deposition techniques and mechanism of thin film formation, materials synthesis and characterization methods in details.

3.1 Deposition Techniques

Modern thin film technology has evolved into a sophisticated set of techniques used to fabricate many products. Thin film technology is the basic of outstanding development in solid state electronics. Generally thin films are prepared by depositing the film material, atom by atom on to a substrate. Modern technology requires thin films for different applications. Metal oxides thin films synthesis for various sensors and devices applications can be accomplished by various deposition techniques. The method of forming a thin film on a surface is known as thin-film deposition. The technique by which a thin layer of material is deposited onto a substrate or onto predeposited layer is known as thin-film deposition technique. "Thin" is a relative term, but most deposition techniques allow layer thickness to be controlled within the range of nanometers.

3.1.1 Classification of thin film deposition techniques

There are several ways of preparing transition and rare earth metal oxides thin films. Preparation techniques and method of producing these films range from very simple and cheap to complex and very expensive ones depending on the substrate coating materials and on the required performance of the films. Thin film deposition has led to many different approaches to the required goal. The methods for depositing thin films may be broadly classified under two headings: physical and chemical deposition techniques. Each methodology has associated pros and cons and careful consideration of the resulting film properties such as crystallinity, microstructure and adhesion must be taken into account.

Some common techniques leading to physical and chemical are shown in **Fig.** 3.1 by flow chart. Chemical techniques are simple, cost effective and offer large area of uniform and controlled deposition for the preparation of metal oxides thin films. The growth technique is the simplest and the cheapest chemical technique. This chapter will carry on the brief description of preparing transition and rare earth metal oxides thin films with emphasis on the solution growth technique employed in the present research work.
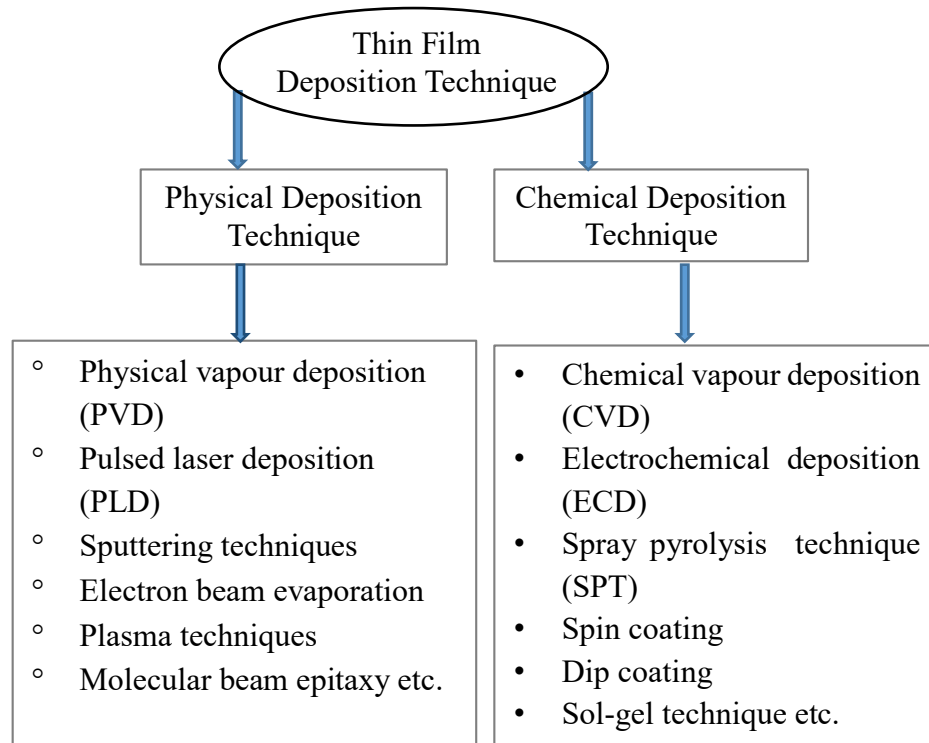
Fig. 3.1 Thin film deposition technique.

3.1.2 Chemical bath deposition (CBD) technique

The Chemical Bath Deposition method is the simplest, reliable and inexpensive method to deposit thin films of nanomaterials. In 1933, Bruckman first deposited Lead Sulfide (PbS) thin films by using chemical bath method [103]. Today also, this method is widely used in the laboratory and industry for the deposition of thin films and nanostructured semiconductors for many scientific and industrial application. We can deposit nanomaterials on any kind of substrate like conducting, non-conducting and flexible. This method is also known as 'solution growth', 'controlled precipitation', and 'electrode less deposition'. This technique operates at the molecular level hence the desired film structure is formed. The chemical bath deposition method involves three major steps, nucleation, particle growth and sintering of harvested films. In the CBD [104], the substrate is immersed into the aqueous chemical bath containing the precursor solution. Nucleation process starts on the substrate surface and thin layer of particles is formed. Prepared thin films are then annealed which attach particles strongly to the substrate. Schematic arrangement of the chemical bath deposition method is as shown in **Fig.** 3.2.
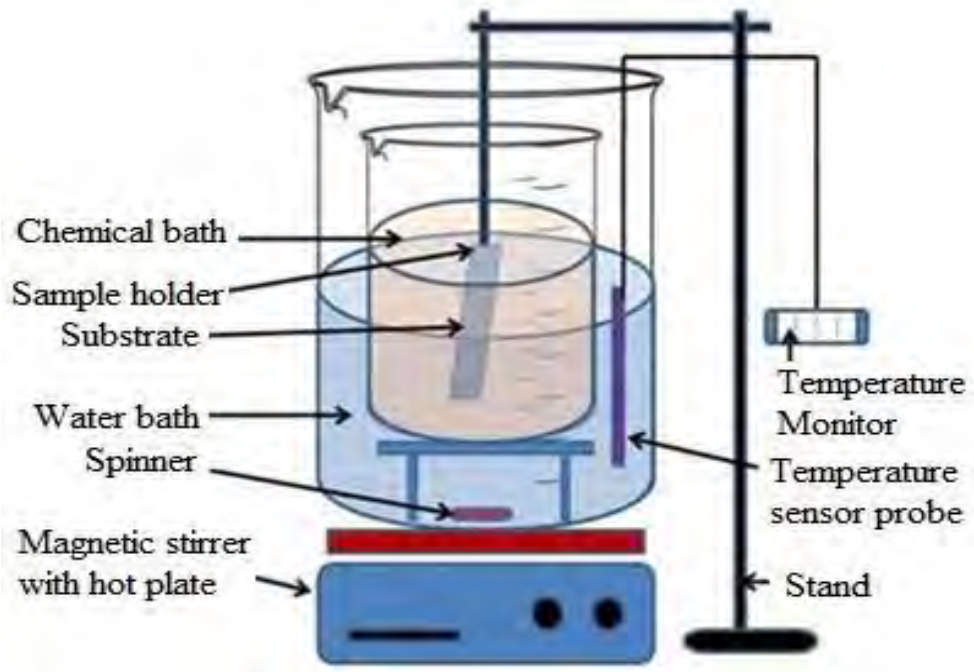
Fig. 3.2 Schematic diagram of a CBD system.

A reaction vessel is of 250 ml capacity Borosil glass beaker is placed inside the water bath. Chemical bath contains water solution with chemical precursors containing the desired components. A reaction mixture was maintained at 60°C temperature in the water bath with the help of hot plate. Temperature of the solution was measured by thermometer. The substrate like glass or stainless steel plates were mounted on specially designed substrate holder. The substrate holder is having fewer diameters than the beaker so that the substrate attached to the substrate holder can easily move in the chemical bath. The height of the substrate holder is adjusted in such a way that about 70 – 80 % of the portion of the substrates dip into the solution. Thin and uniform films are obtained having better orientation of the crystallites.

3.1.3 Spin coating technique

Spin coating has been used for several decades for the application of thin films. A typical process involves depositing a small puddle of a fluid resin onto the center of a substrate and then spinning the substrate at high speed (typically around 3000 rpm) [105-106]. Centripetal acceleration will cause the resin to spread to, and eventually off, the edge of the substrate leaving a thin film of resin on the surface. Final film thickness and other

properties will depend on the nature of the resin (viscosity, drying rate, percent solids, surface tension, etc.) and the parameters chosen for the spin process. Factors such as final rotational speed, acceleration, and fume exhaust contribute to how the properties of coated film are defined. One of the most important factors in spin coating is repeatability. Subtle variations in the parameters that define the spin process can result in drastic variations in the coated film. **Fig.** 3.3 shows the schematic diagram of the spin coating process.

Phase 1   Phase 2   Phase 3   Phase 4
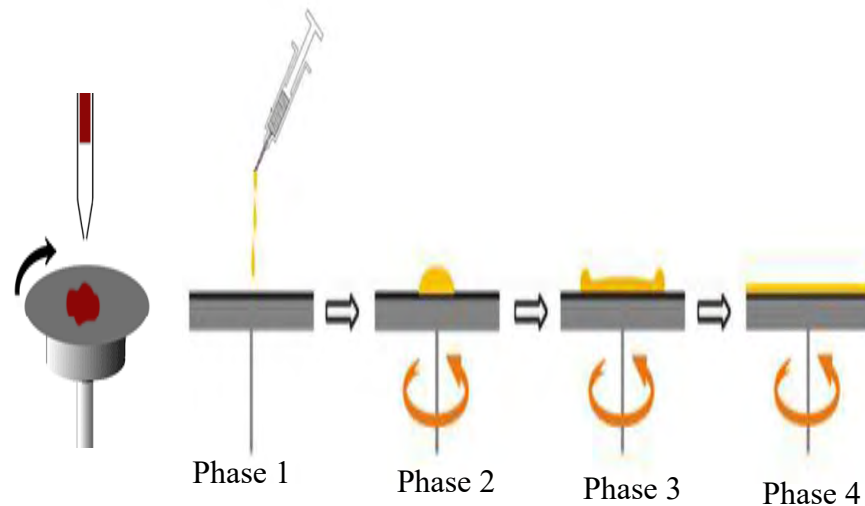
Fig. 3.3 Schematic diagram of the spin coating process.

For this technique, the material to be deposited is dissolved or dispersed into a solvent, and this coating solution is then deposited onto the substrate surface and spun off to leave a uniform layer of thin film on the substrate. As shown in **Fig.** 3.3, the four key phases in the spin-coating process are:

1. Deposition of solution onto the substrate.

2. Spreading of solution from center of substrate to the sides (spin-up).

3. Gradual thinning of solution (spin-off).

4. Gelation due to solvent evaporation

3.1.4 Sol-gel technique

As sol gel method is a wet chemical technique which usually depends on conditions of solution. To fabricate high quality metal oxides thin films it is necessary to study the various parameters like precursors, solvents, sol concentration, sol ageing time, sol pH

value, preheating temperature, preheating time, annealing temperature, annealing time, dopant concentration and so on. During sol-gel thin film formation via dipping, polymeric or particulate inorganic precursors are concentrated on the substrate surface by a complex process involving gravitational draining with concurrent drying and continued condensation reactions. The structure of films deposited from polymeric precursors depends on such factors as size and structure of the precursors, relative rates of condensation and evaporation, capillary pressure, and substrate withdrawal speed. **Fig. 3.4** shows the generalized scheme of sol-gel technique. Sol-gel method is also a solution growth chemical route for the synthesis of colloidal dispersions of oxides which can be altered to powders, fibers, thin films and monoliths [107-108]. In general, sol-gel method consists of hydrolysis and condensation reactions. Sol-gel coating is a process of preparation of single or multicomponent oxide coating which may be glass, glass ceramic or crystalline ceramic depending on the process. Also, the nanomaterial used in modern ceramic and device technology require high purity and facilitate to control over composition and structure.
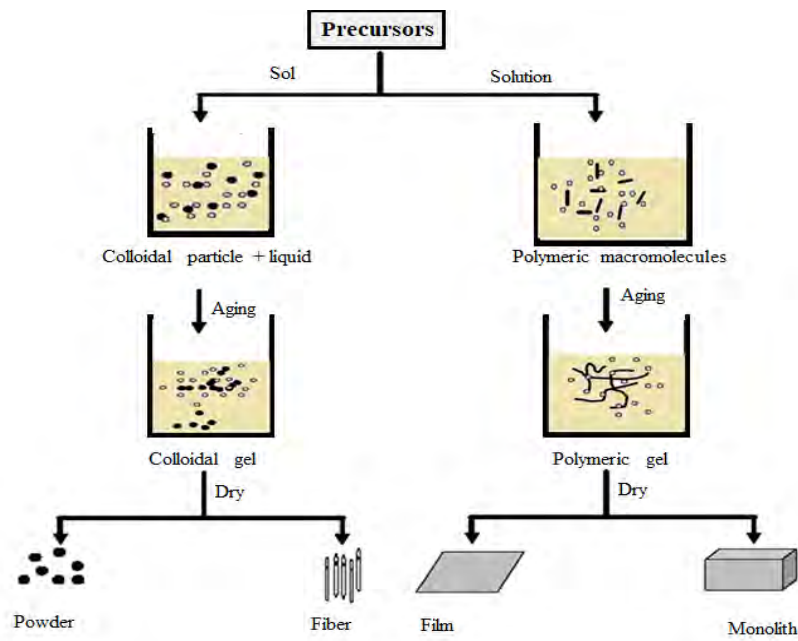
Fig. 3.4 Generalized scheme of sol-gel synthesis.

3.1.5 Dip-coating technique

Dip coating is one kind of wet chemical solution growth technique. A wet liquid film is formed after dipping a substrate into a solution. For this technique, the substrate to be

coated is immersed in the solution and then withdrawn at a well-defined speed under controlled temperature and atmospheric conditions. In order to have a uniform film thickness, vibration-free mountings and smooth movement of the substrate are essential. Compared to spin-coating, dip-coating requires more sophisticated equipment. **Fig.** 3.5 shows a schematic of dip-coating deposition technique. The three steps of this technique are substrate dipping, wet layer formation and solvent evaporation respectively [109-110].
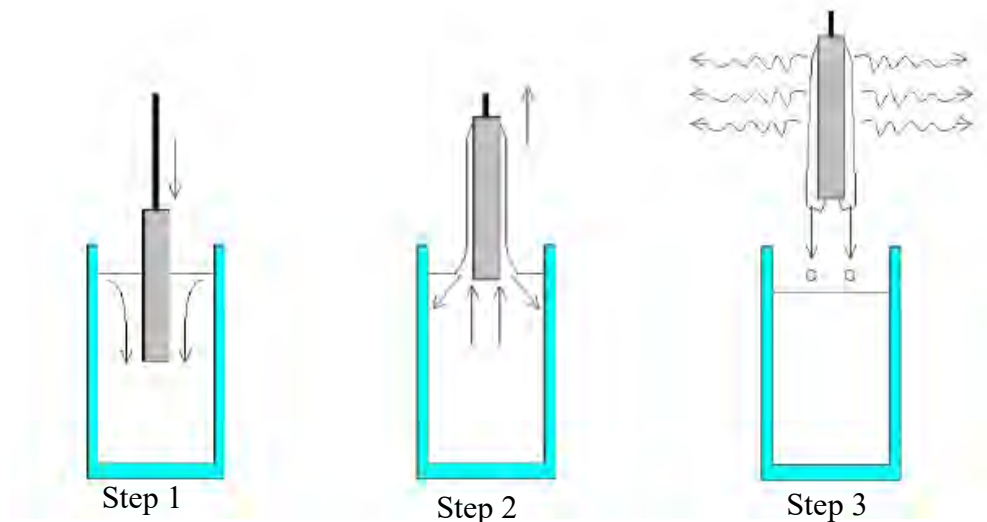
Fig. 3.5 Schematic of dip-coating deposition technique.

3.1.6 Spray pyrolysis technique

3.1.6.1 Spray pyrolysis system

Spray pyrolysis deposition technique involves spraying of an ionic solution, usually aqueous, containing soluble salts of the constituent atoms of the desired compound onto heated substrates. Hydrolysis and pyrolysis are the main chemical reactions involved in the process. In this technique, the chemicals vaporized and react on the substrate surface after reaching on it. In principle spray pyrolysis technique is very simple and is suitable for industrial and sensing applications and has been used for about 30 years for the manufacture of conductive glass. In 1966, Chamberlin and Skarman for the first time used spray pyrolysis method for the deposition of CdS thin films for solar cell applications [111]. This method is increasingly being used for some commercial processes due to its low cost. This method is used to deposit thin film of material on glass substrate. The main advantage of this method over other similar method is its uniform and high quality film

growing. **Fig.** 3.6 shows the schematic of spray pyrolysis deposition technique. The main advantages of spray pyrolysis over other similar techniques are given below:

- Low cost experimental set up
- Easy to fabricate the deposition parameters
- Suitable to prepare thin film of both porous and crystalline surface
- Capable of forming nanocrystalline thin film
- Capable seamless incorporation in a standard process.
- No high temperatures are required during processing.
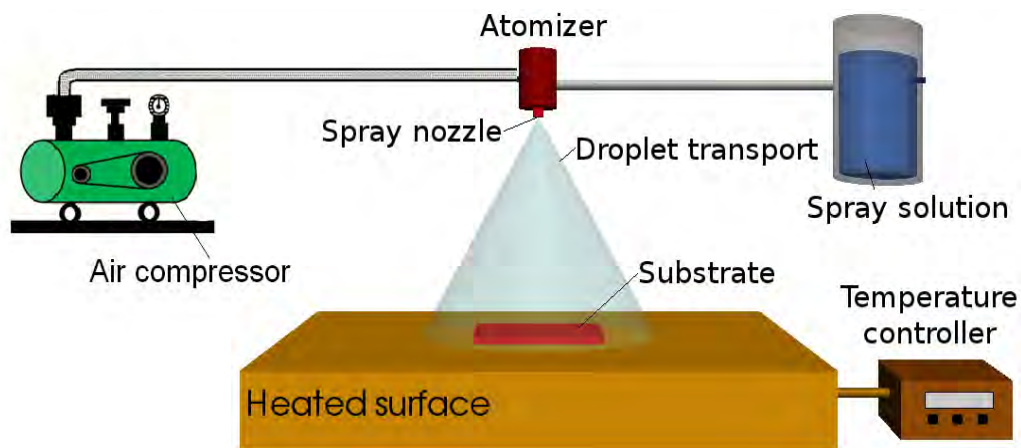
Fig. 3.6 General schematic of spray pyrolysis deposition technique.

A precursor solution which contains constituent reactant compounds is atomized in a nozzle to tiny droplets which are then sprayed onto a preheated substrate. The surface of the substrate must be sufficiently hot to initiate chemical reaction between the precursors in the droplet solution. Specifically, the droplet must still contain enough reactants in solution after reaching the substrate [112]. A film of stable compounds subsequently forms that adheres to the substrate due to chemical reaction and thermal decomposition of the solution. A pressure, or air blast, atomizer uses high speed air in order to generate an aerosol from a precursor solution. Increasing the air pressure causes a direct decrease in the generated mean droplet diameter. Inversely, increasing the liquid pressure causes a direct increase in the mean droplet diameter. All droplets sprayed from an air blast atomizer are contained within a 70° spray cone angle, while half are within a narrower 12° angle [113-114]. It was also determined that the flow rate has a very small influence on the spray characteristics, which can be mostly ignored for modeling.

3.1.6.2 Reaction mechanism of spray pyrolysis system

Fig. 3.7 shows the pyrolysis system in reaction chamber. Spray pyrolysis reactions proceed through droplet formation, transport of the droplets into a high-temperature environment, evaporation of the solvent, thermal decomposition to form products. These steps involve a wide range of physical and chemical processes. Phase segregation and morphology control are major challenges for SPT. Morphology control primarily consists of the ability to influence the interior hollowness of the product powder during particle formation [115-117]. During the initial formation of the particles the precursor droplets may undergo rapid drying, which can lead to surface precipitation instead of volume precipitation, resulting in a hollow interior [118-119]. Similarly, due to rapid gas evolution following the decomposition of the precipitated salts an impermeable melt may form, and thus the particles can be "inflated", which can also lead to a hollow interior. High temperature densification can be used to reduce the hollowness of the product powders to some extent, although this will lead to increased sintering of the primary particles.
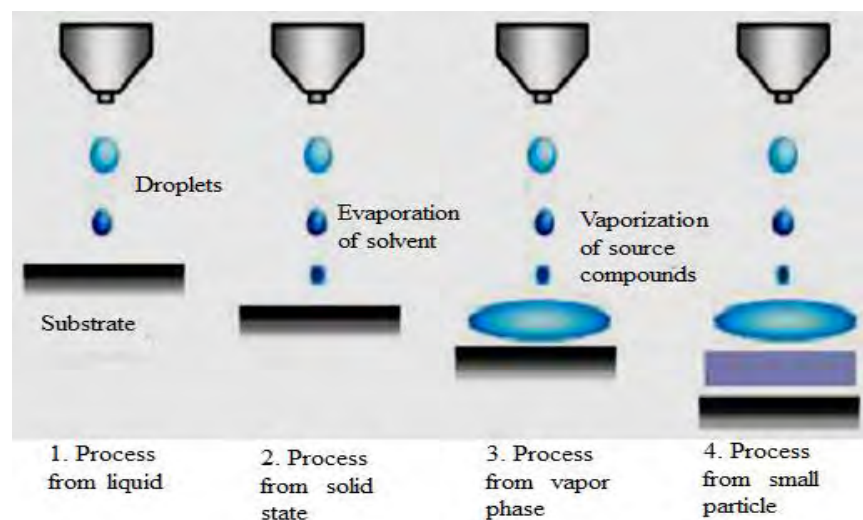
Fig. 3.7 Spray pyrolysis system in reaction chamber.

3.1.6.3 Substrate temperature dependence reaction mechanism

Generally spray pyrolysis technique carries on porous and amorphous thin films obtained below 300°C (process I). At high substrate temperatures (above 450°C) powdery films produced due to the vaporization and decomposition of the precursor before reaching the substrate (process III). At intermediate temperatures (300-450°C), both processes may

occur. At the optimum temperature the solvent evaporates close to the substrate, and the precursor is volatilized near the vicinity of the substrate and adsorbed onto the surface, followed by decomposition to yield a dense film with good adhesion (process II) [120]. This would correspond again to a heterogeneous CVD reaction where the optimum temperature lies between 400°C and 450°C. **Fig.** 3.8 shows temperature dependence reaction mechanism of spray pyrolysis system [121-122]. **Fig.** 3.8 deals with the following processes that occur with increasing substrate temperature:
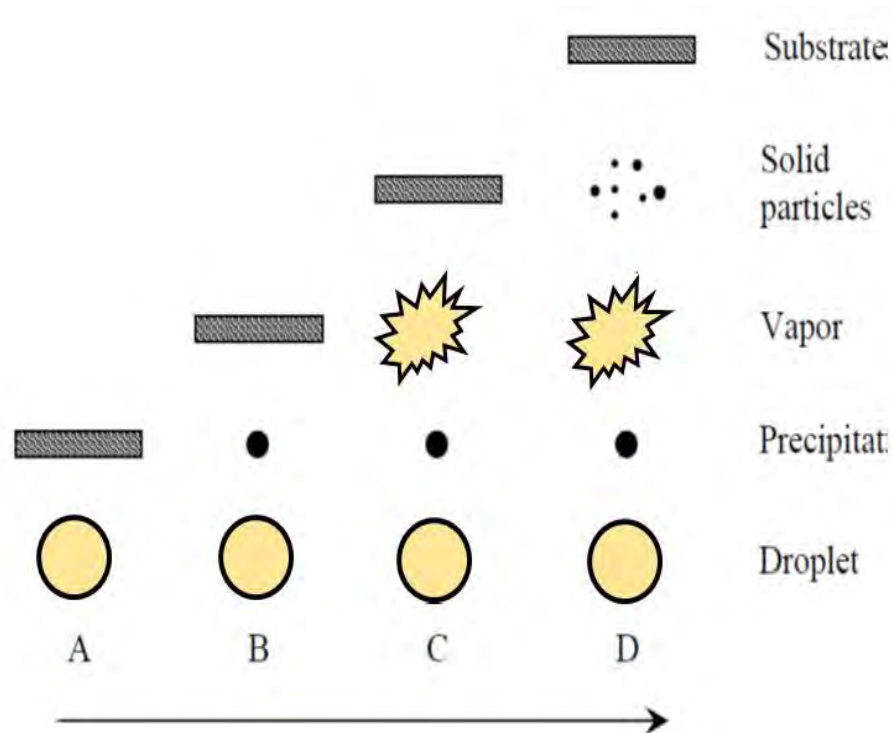
Fig. 3.8 Temperature dependence reaction mechanism of spray pyrolysis system.

In the lowest temperature regime (process A) the droplet splashes onto the substrate and decomposes. At higher temperatures (process B) the solvent evaporates completely during the flight of the droplet and dry precipitate hits the substrate, where decomposition occurs. At even higher temperatures (process C) the solvent also evaporates before the droplet reaches the substrate. At the highest temperatures (process D) the precursor vaporizes before it reaches the substrate, and consequently the solid particles are formed after the chemical reaction in the vapour phase. It was speculated that the processes A and D lead to rough or non-adherent films

3.1.6.4 Steps of process during deposition by SPT

There are mainly three processing steps for spray pyrolysis deposition; automation, aerosol transport of the droplet, droplet evaporation and film formation.

i. Automation

The automation process is the first step in which there is formation of droplets from a spray solution and is sent it with some velocity towards the substrate surface. The optimizers differ in 2formation of droplet size, rate of automization and velocity of droplets. The mass of a droplet, assuming a spherical shape depends on its density, $m = \frac{4\pi}{3} (\rho q r^3)$; where r is the droplet radius and ρq is the droplet density. The initial leaving velocity of the droplet is an important parameter as it determines the rate at which the droplets reach the substrate surface, the heating rate of the droplet, and the amount of time the droplet remains in transport.

ii. Aerosol transport of the precursor droplet

In this process, precursor solution is atomized through nozzle. The nozzle convert the solution into small droplets called aerosols. After the droplet leaves the atomizer, it travels through the ambient with an initial velocity determined by the atomizer. The aerosol droplets are transported with the aim of as many droplets as possible reaching the surface and send it towards preheated substrates. We can get thin films with desired properties only at optimum substrate temperature. The aerosol droplets evaporate during the transport to the substrate leads to a size reduction of the droplet, which increases the concentration within the droplet. When concentration exceeds the solubility limit, precursor precipitates on the surface of the droplet. As the droplets move through the ambient, they experience physical and chemical changes [123] depicted in **Fig.**3.9. **Fig.** 3.9 shows that spray pyrolysis droplets are modifying as they are transported from the atomizing nozzle to the substrate. Since the droplet traverses the ambient, there are four forces simultaneously acting on it, describing its path (A-D) moving towards the substrate. Those forces are gravitational, electrical, thermophoretic, and the Stokes force.
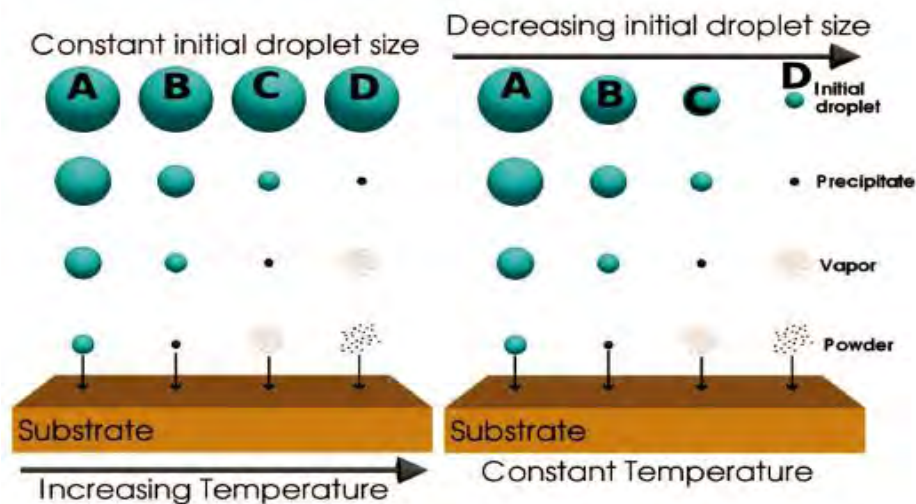
Fig. 3.9. Transportation of the precursor droplet.

Gravitational force: The gravitational force is the force pulling the droplet downward. This force depends on the mass of the traveling droplet. For small droplets the force of gravity is too small to allow it to arrive at the surface before it is fully evaporated. For larger particles, the force of gravity is the driving force behind the droplet transport.

Electrical force: The electrical force is applicable to spray pyrolysis systems which include an additional electrical source governing the droplet's trajectory. The electrical force acts on a droplet is usually several orders of magnitude abiding by $F_e = q_d.E$; where E is the generated electric field strength which acts at the liquid-gas interface to generate charged droplets and q_d is the droplet charge. This force acts between the ions into the droplets.

Stokes force: The Stokes force is the drag experienced by the droplet due to the air resistance in the ambient. The force is caused by the friction between the droplet and air molecules. The Stokes force is a factor of the particle's velocity and size.

Thermophoretic force: The thermophoretic force is a retarding force, causing droplets to significantly decrease their velocity as they approach the heated substrate. The thermophoretic force depends on the thermal gradient in the transport environment. it will have no effect on the droplet movement, when it is more than several (~5-7) mm away from the substrate. In high thermal gradient region, the thermophoretic force begins to dominate. This force only valid for droplets whose radius is much larger than the mean free path of the air molecules.

3.1.6.5 Film formation

Pyrolysis of the precipitate occurs before the precipitate reaches on the substrate. When it reaches on the substrate surface nucleation and the growth of thin films takes place. Finally, we get thin film layer of desired nanomaterial on substrate. Among different chemical methods, spray pyrolysis technique is the most popular technique of recent times, because of its applicability to deposit variety of conducting and semiconducting materials thin films [124-125]. Due to its capability to produce large area, high quality adherent films with uniform thickness are synthesized. **Fig.** 3.10 shows the film formation process by SPT.
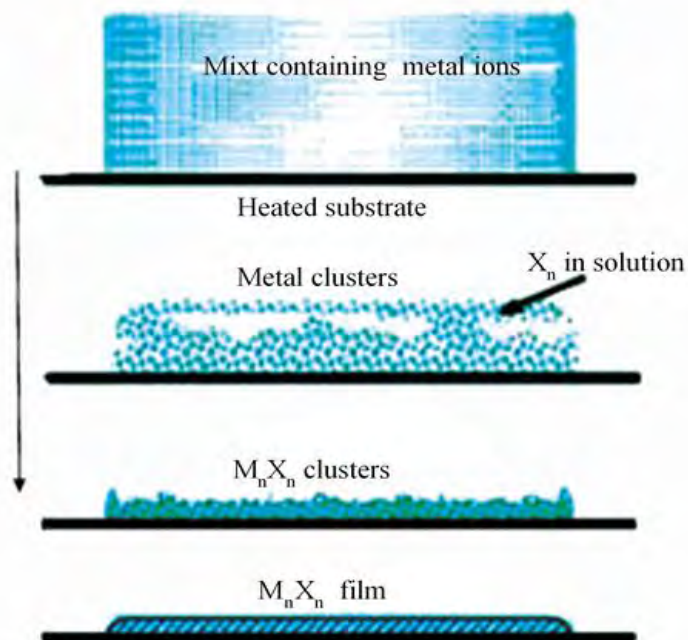
Fig. 3.10 Film formation process by SPT.

3.1.6.6 Nanocrystals formation by SPT

Recent studies have focused on the synthesis of the nanostructure materials. The nanostructures are particles, grains, functional structures and devices with dimensions in the 1–100 nanometer range. Spray pyrolysis method has advantages for the production of nano sized particles with narrow particle size distribution. This method is preferable to control particle size. In SPT system falling aerosol droplets onto large area surface is suitable for forming nanoparticles. Nanoparticle coating is produced on material surface in order to modify the surface properties. The degree of particle agglomeration is governed

by both physicochemical properties of the particle material and residence time in aerosol phase prior to deposition [126]. Nanocrystals formation by SPT is displayed in **Fig.** 3.11.
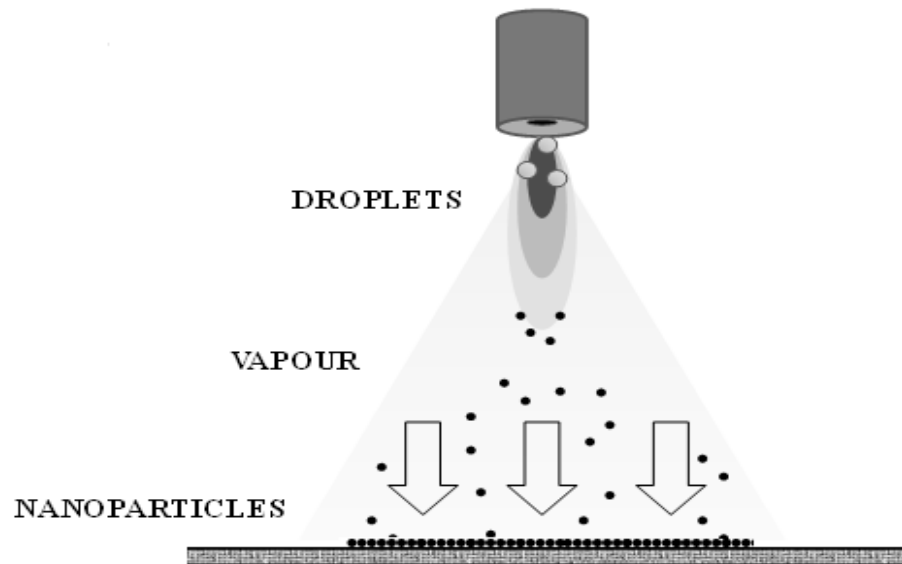
Fig. 3.11 Nanocrystals formation by SPT.

The formation of precursor aerosol droplets that are delivered by a carrier gas through a heating zone involved in **Fig**. 3.11 [127]. Precursor solutions of metal nitrates, metal chlorides, and metal acetates are atomized into fine droplets and sprayed into the thermal zone. Inside the heating zone, the solvent evaporates and reactions occur within each particle to form a product particle. Spherical, dense particles in the 100 to 1000 nm range can easily be formed in large volume by this method. The principal advantage of the spray pyrolysis method is the ability to form multicomponent nanoparticles as solutions of different metal salts can be mixed and aerosolized into the reaction zone

3.1.6.7 Thin film growth mechanism

There are three mechanisms for the growth of thin film which can be distinguished, depending on the strength of interaction between the atoms of the growing film and between the atoms of the film and substrate. These are:

- **Frank-Van-der Merwe mode:** The layer by layer growth mechanism.

- **Stranski-Krastanov model:** Absorption of a monolayer and subsequent nucleation on the top of this layer growth mechanism.
- **Volmer-Weber mode:** A three dimensional nucleation, forming, growth and coalescence of islands mechanism.

Fig. 3.12 shows the growth mechanism of thin film. In most cases, Volmer-Weber growth mechanism takes place and we shall focus our attention on this mechanism in brief.
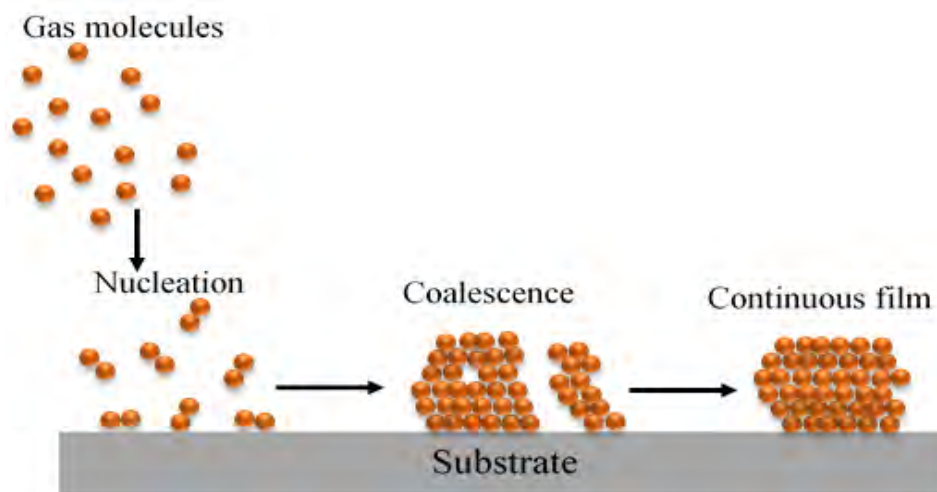
Fig. 3.12 Growth mechanism of thin film.

Condensation: Condensation simply means the transformation of a gas into a liquid or solid. The condensation of a vapor atom is determined by its interaction with the impinged surface in the following manner. The impinging atom is attracted to the surface by the instantaneous dipole and quadruple moments of the surface atoms. As a result, the atom loses its velocity component normal to the surface in a short time, provided the incident kinetic energy is not too high. The vapor atom is then physically absorbed (called "adatom"), but it may or may not be completely thermally equilibrated. It may move over the surface by jumping from one potential well to the other because of thermal activation from the surface and /or its own kinetic energy parallel to the surface. The adatom has a finite stay or residence time on the surface during which it may interact with other adatoms to form a stable cluster and be chemically absorbed with the release of the heat of condensation. If not absorbed, the adatom reevaporates or desorbs into the vapor phase. Therefore, condensation is the net result of equilibrium between the adsorption and desorption processes.

The probability that an impinging atom will be incorporated into the substrate (surface) is called the "condensation" or "sticking coefficient". It is measured by the ratio of the amount of material condensed on a surface to the total amount impinged. In fact, often the sticking coefficient is so small that observation is not observable by ordinary techniques. On the other hand, the sticking coefficient is found to be strongly dependent on the total time during which the substrate was subject to impingement, and also on the substrate temperature. A non unity sticking coefficient is usually explained in terms of monomers re-evaporation from the areas on the substrate which are outside the capture zones around each stable nucleus [128].Langmuir and Frenkel formulated condensation model (This model considers vapor$\rightarrow$ solid transformation. At high deposition temperatures, a vapor$\rightarrow$ liquid (amorphous)$\rightarrow$ solid condensation mode may occur. Semenoff suggested that heterogeneous nucleation always proceeds by formation of an amorphous film followed by nucleation of crystallites within the amorphous film in which the absorbed atoms move over the surface during their lifetimes to form pairs which, in turn, acts as condensation centers for other atoms.

Nucleation: Nucleation is the birth stage of film. Consideration is initiated by the formation of small cluster through the combination of several adsorbed atoms. These clusters are called nuclei and the process of cluster formation is called nucleation. There are two types of nucleation that occur during the formation of film: homogeneous and heterogeneous nucleation. A homogeneous nucleation theory which takes into account the total free energy of formation of a cluster of adatoms was postulated by Volmer, Weber, Becker and Doring. It was later extended to heterogeneous nucleation by Volmer and to the particular shapes of clusters in a thin film case by Pound et al. In this theory, clusters are formed by collisions of atoms on the substrate surface and in the vapor phase if super saturation is sufficiently high. They develop initially with an increase in free energy until a critical size is reached, above which growth continues with a decrease in free energy. In atomistic theory, at low substrate temperature or very high super saturations, the critical nucleus may be single atom, which will form a pair with another atom by random occurrence to become a stable cluster and grow spontaneously.

Growth: Growth is the final and completion stage of thin film formation. The process of enlargement of the nuclei to finally form a coherent is termed as growth. The growth sequence of a film was originally deduced by Andrade from the observed optical

transmission behavior of Ag films. This deduction is in remarkable agreement with the electron-microscopic observations first made by Uyeda and later in detailed by Levinstein. The clusters become larger and ultimately continuous film is produced. Pashley et al. distinguished four stages of the growth process based on the electron microscopic observations are:

I.   **The island stage**: When a substrate under impingement of condensate state monomers is observed in the electron microscope, the first evidence of condensation is a sudden burst of nuclei of fairly uniform size. The smallest nuclei detected have a size of 20 to 30 Å. Growth of nuclei is three-dimensional, but the growth parallel to the substrate is greater than that normal to it. This is probably because growth occurs largely by the surface diffusion of monomers on the substrate, rather than by direct impingement from the vapor phase. The tendency to form an island structure is increased by (1) at high substrate temperature, (2) at low boiling point film material, (3) at low deposition rate, (4) weak binding energy between film material and substrate, (5) a high surface energy of the film material and (6) a low surface energy of the substrate.

II. **The coalescence stage**: As islands increases their size by further deposition and come closer to each-other, the larger ones appear to grow by coalescence of the smaller ones. The coalescence occurs in less than 0.1s for the small nuclei and is characterized by a decrease in total projected area of the nuclei on the substrate (an increase in their height). In addition, nuclei having well-defined crystallographic shapes before coalescence become rounded during the event [129]. The composite island takes on a crystallographic shape again if left for a sufficiently long time before interacting with its neighbors. The triangular profile of the crystallites is characteristic of the nucleation stage. After coalescence has taken place, the islands assume a more hexagonal profile and are often faulted. The liquid like character of the coalescence leads to enlargements of the uncovered areas of the substrate, with the result that secondary nuclei form between the islands. This effect becomes noticeable when the primary islands have grown to about 1000 Å and continues until the final hole-free film is formed. The small nuclei surrounding island B are examples of those secondary nuclei. A secondary nucleus grows until it touches a neighbor and if this happens to be a much larger

island, the secondary nucleus coalesces very rapidly and becomes completely incorporated in the large island.

III. **The channel stage:** As the islands grow, there is a decreasing tendency for them to become completely rounded after coalescence. Large shape changes still occur, but these confined mainly to the regions in the immediate vicinity of the junction of the islands. Consequently, the islands become elongated and join to form a continuous network structure in which the deposit material is separated by long, irregular, and narrow channels of width 50 to 200 Å. As deposition continues, secondary nucleation occurs in these channels, and the nuclei are incorporated into the film as they grow and touch the sides of the channel. At the same time, channels are bridged at some points and fill in rapidly in a liquid like manner. Eventually, most of the channels are eliminated and the film contains many small irregular holes. Secondary nucleation takes place on the substrate within these holes and the growing nuclei are incorporated (in a liquid like manner) into the continuous regions of the deposit. The hole contains many secondary nuclei which coalescence with each other to form secondary islands, which then touch the edge of the hole and coalesce with the main film to leave a clean hole. Further, secondary nuclei then form and the process is repeated until the hole finally fills in.

IV. **The continuous film stage**: The final stage of film growth is a slow process of filling the empty channels, which requires a considerable amount of deposits. In channel stage large areas are vacated by coalescence. These empty channels are filled by secondary nucleation, growth and coalescence and in this way a continuous film is formed.

3.2 Synthesis of Thin Films by Spray Pyrolysis Technique

Preparation of thin films by solution based technique are generally divided into two steps; preparation of precursor solution and deposition of the solution via suitable reaction. In the present research work spray pyrolysis is used to prepare thin films. Hydrolysis and pyrolysis are the main chemical reactions involved in this process. In this technique, the chemicals vaporized and react on the substrate surface after reaching on it. Here the required experimental equipment and preparation of (Fe, Cu) doped transition and rare

earth metal oxides (Co_3O_4, MnO_2, WO_3 and CeO_2) thin films by spray pyrolysis technique are described.

3.2.1 Required equipment

3.2.1.1 Preparation of masks

The direct deposition of thin film pattern requires a suitably shaped aperture, commonly referred to as a mask. For the purpose of various experimental studies, film of specific size and shape are required. Mask was made from stainless steel plate with the desired pattern cut into it shown in **Fig.** 3.13. The aperture was made in a bath machine. The mask is placed in proximity to the substrate, thereby allowing condensation of the evaporate only in the exposed substrate areas. The mask was prepared in such a way that the edge of the mask is smooth so that it is helpful for determining the film thickness accurately.

3.2.1.3 The design of the reactor

It is a vertical batch type reactor composed of a galvanized iron enclosure heater and heat susceptor. For the rapid expulsion of the by-product gases there are opening at the side and at the top of the reactor. It helps focusing the incoming sprayed solution towards the substrate and also provides a chimney action to the exhaust gas upwards.

3.2.1.4 The fume chamber

It is a large type chamber with a slanting top and is provided with a chimney. There is an exhaust fan fitted at the mouth of the chimney to remove the unused gases from the chamber. The slanting top and the sidewalls are made of glass and wood. There are airtight doors in the front side shown in **Fig.** 3.14 . The chamber has purging facilities. The whole spray system and the reactor are kept inside this fume chamber at the time of film deposition because of the safety grounds and to check air current disturbances at the deposition site. These two points just stated are very important for the spray process when deposition is carried out in open- air atmosphere.

3.2.1.5 Air compressor

It is reservoir type electrical air compressor. A rotary pump in this section mode draws atmospheric air and keeps it reserved in a large capacity air tank. At the outlet of the tank a pressure gauge is attached which records the pressure of the air at the time of supplying

it from the tank. There is a by-pass control valve which can keep the output pressure constant.
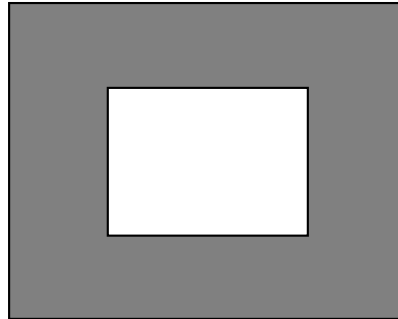
Fig. 3.13 Mask for the sample.

3.2.1.6 Spray nozzle

The single spray nozzle consists of capillary tubes (stainless steels) fitted perpendicular to the other tube. When compressed air is passed rapidly through the tube' in direction tangential to the mouth of the, a partial vacuum is created at the front part of the tube whose other end is kept immersed in the spray liquid. Due to this partial vacuum the liquid rises up through the tube and the compressed air drives it away in the form of fine spray particles. The thinner spray nozzle would give the finer spray particles [130]. A very fine needle shaped capillary tube was used for the spray nozzle and it may vary from nozzle to nozzle.

3.2.1.7 Cleaning of substrate

The Choice and cleaning of substrate has a major influence on the properties of the thin film deposited onto them [131]. Thin films cannot support themselves; and thus some carriers must be provided. This carrier, or substrate, would ideally have no interaction with the thin film except for sufficient adhesion to provide support. Glass, quartz and ceramic substrates are commonly used for polycrystalline films. Single crystal substrates of alkali halides, mica, MgO, Si, Ge etc. are used for epitaxial growth. The commonly used glass substrate (5 cm × 2.5 cm) having thickness 1 mm were used in the present work. Surface contaminations manifest it in pinholes, which can cause open resistor or localized high resistance [132-133].

The following procedures were used for substrate cleaning. The gross contamination of each of the substrates were first removed by Luke warm aqueous solution of sodium

carbonate and then washed with distilled water. After washing in distilled water, the substrates were dipped at first into nitric acid for some time and again washed in distilled water. These were then dipped into chromic acid for some time. Taking them out of chromic acid bath one by one and then these were washed and thoroughly rinsed with deionized water for several times. Finally, these were dried in hot air and preserved for use. During the whole process the substrates were always held by slide holding forceps.

Fig. 3.14 Setup of spray pyrolysis technique (Department of Physics, BUET).

3.2.2 Film deposition parameters

In the chemical spray deposition technique the structure, composition and other characteristics of the deposited films depend on a number of deposition parameters. The variable quantities such as the substrate temperature, solution and gas flow rate, deposition time, quality of the substrate material, size of atomized particles, solution concentration, and substrate to spray outlet distance, etc. are affected on the film properties. It is obvious that the substrate temperature and dopant concentrations are the most important deposition parameters for the formation of nanostructured thin films and these are controlled with great care. In this research work, the effect of Fe and Cu dopant concentrations on structure and properties of nanostructured transition and rare earth metal oxides (Co_3O_4, MnO_2, WO_3 and CeO_2) thin films are discussed keeping other parameters constant.

3.2.2.1 Deposition rate

The rate of flow of the working solution can be controlled by a suitable nozzle and adjusting the airflow rate. Spray rate is a parameter that influence the properties of the films formed. The crystallinity, surface morphology, resistivity and even thickness are affected by the change of spray rate [134]. The film deposited using the lower flow rate may slightly denser than that deposited using a higher flow rate. This can be attributed to a larger number of droplets deposited when the solution is fed using a higher flow rate give results in faster formation of agglomerates. Therefore, films deposited with the low precursor flow rate contain less agglomerates and look denser than that deposited with the high flow rate. In the present work spray rate was controlled at 0.5mL/min and kept constant throughout the deposition process.

3.2.2.2 Deposition time

Phase segregation can occur at different deposition time during the formation of the particles of thin film. Different chemical nature of the components precipitate at different deposition time. During the solvent evaporation phase of particle formation the surface morphology is strongly influenced by the composition of the precursor solution and deposition time [135-137]. Thin film of very porous morphology with agglomerates of small particles may obtained at optimum deposition time. This change of morphology is explained by considering the effect of droplet spreading. Most of the droplets arriving at the substrate are nearly dry. Therefore, they spread slowly and consequently discrete particles are formed on the surface. This leads to an increase in surface roughness, which enhances preferential landing and agglomeration due to time expansion. In this work the optimum deposition time kept 20 minutes constant for all the prepared films.

3.2.2.3 Solution concentration

Changing the concentration of the precursor solution provides us with an additional method to control the primary particle size of the product without impacting phase purity. For the range of concentrations considered here, concentration has a minor effect on secondary particle size. The secondary particle size is essentially determined by the nebulizer used in the synthesis process. Significant reduction in the concentration would be necessary to provide accurate control over the particle size of the product, which would limit the practical application of spray pyrolysis. The concentration should not be too high

for the deposition of dense, smooth films. On the other hand, a high salt concentration is desired to achieve high deposition rates. However, it is not always favorable, because the surface roughness of the deposited film increases with increasing salt concentration in the precursor solution. In the present research work, precursor solution was kept 0.1 mole constant. Fe and Cu doped nanostructured transition and rare earth metal oxides (Co_3O_4, MnO_2, WO_3 and CeO_2) thin films were prepared varying 0 at % to 10 at % Fe and Cu dopant concentration in this work.

3.2.2.4 Substrate temperature

The substrate temperature is the most important spray parameter. Thin film deposition using the spray pyrolysis technique involves spraying a metal salt solution onto a heated substrate. Droplets impact on the substrate surface undergo thermal decomposition. The shape and size of the particles depends on the momentum and volume of the droplet, as well as the substrate temperature. Consequently, the film is usually composed of overlapping particles of metal salt being converted to oxide on the heated substrate. In thermal spray pyrolysis system at temperatures below 200°C the droplets deposited are still rich in solvent. Therefore, a thin, wet layer is present on top of the film during deposition. Too fast drying of this layer results in stresses and subsequent cracking. At too high temperatures (>500°C) the deposited spray droplets are almost dry. Therefore, discrete particles are formed on the surface due to slow spreading. This increases the surface roughness. In this case, a temperature from 300°C±50°C to 400°C±50°C results in dense and nanostructured thin films. It follows that better quality films can be deposited using the thermal spray pyrolysis setup within this temperature range. In the present work substrate temperature was maintained at 450°C throughout the film deposition process.

3.2.2.5 Nozzle to substrate distance

In the thermal spray pyrolysis technique the air temperature between the nozzle and the substrate surface increases steeply due to the forced convection cooling effect of the air flow close to the substrate. The temperature begins to increase significantly at a distance of just 5 mm to the substrate. In this case, the minimal nozzle to substrate distance is limited not by the substrate size, but by the cooling effect of the air flow. At small distances pronounced cooling of the substrate occurs. Simultaneously, more heat is required from the heating plate, because the droplet mass flow density increases with decreasing

distance. Consequently, at a critical distance of spray gun to substrate surface it will be impossible to reach the optimal deposition temperature. We have observed that all films were cracked up to the maximum attainable substrate temperature of 450°C, when the spray gun was at 20 cm distance from the substrate surface. After increasing the distance to 25 cm while keeping all other spray parameters constant, we have prepared crack free films. It follows that under these experimental conditions the lower distance limit is 25 cm. The upper limit is determined by the distance at which the spray pattern collapses. Generally, the maximum distance depends on spray gun parameters such as the geometry of atomizer and air pressure.

3.2.2.6 Thickness control

In the present spray deposition process, the deposition time is the main factor for the thickness control, provided the other parameters, remain constant. Thickness plays an important role in the properties of thin films [138-140]. Since the deposition is carried out in normal atmosphere a direct and in situ control of thickness is not so easy. To control the film thickness therefore calibration chart may be used. These charts are generally plots of deposition time vs. thickness, and can be prepared at different constant substrate temperatures prior to the preparation of particular experimental samples using the same solution and deposition variables.

3.2.2.7 Solvent and solubility

Physical properties of the solvent influence the droplet size distribution and, as a consequence, the structure of the deposited films. The solubility of the precursor in the solvent is a very important parameter, since it determines the maximum salt concentration in the solvent. In order to achieve a reasonable deposition rate, the precursor concentration should be as high as possible. On the other hand, it cannot be too close to the solubility limit, because the salt can precipitate in a droplet due to solvent evaporation during aerosol transport, resulting in nanoparticle formation. Usually ethanol is used to dissolve the precursors. However, ethanol has low boiling point (78°C) and evaporates rapidly. To slow down solvent evaporation, and thereby to hinder particle formation, we mixed ethanol with the solvent of precursor which has a high boiling point. Usually, the volume ratio of the solvents in the mixture are set at 1:1. By changing the solvent, physical properties of the solution such as boiling point, solubility of salts, spreading behavior of

droplets on the substrate will change. Therefore, the type of solvent influences not only the maximum salt concentration, but also the deposition temperature, the optimal solution flow rate, and as a consequence the deposition rate. It is necessary to use a solvent with a high boiling point in order to deposit a dense film [141]. It follows that the boiling point of the solvent influences the lowest possible deposition temperature of the dense, crack free films.

3.2.2.8 Precursor materials

The choice of a salt is the most important decision to be made before parameter optimization can be undertaken. The type of salt directly influences three spray parameters: temperature (should be sufficiently high to decompose the salt), salt concentration (limits the maximal concentration in the solution) and type of solvent (restricts the choice of salts due to their insolubility in some solvents). Therefore, the optimal spray parameters usually differ considerably for each type of salt. The extremely large choice of precursors is one of the advantages of the spray pyrolysis technique. The main requirements for the precursor salt are: a salt must be soluble in an alcoholic solvent or water, and it must decompose into an oxide at the deposition temperature. Generally we use chlorides, nitrates and metal-organic salts as precursors.

Chlorides: Chlorides have the following advantages: high solubility in ethanol (more than 0.5 mol/L) and low price. Unfortunately they are extremely chemically aggressive and cause corrosion of the experimental setup. Also, part of the chlorine ions can remain in the deposited film, causing changes in the material properties. The chlorine impurities also hinder the crystallization of the initially amorphous thin film.

Nitrates: The main drawback of the chloride precursor is its corrosive action. Nitrates appear to be possible substitutes for the chlorides. The solubility of nitrate precursor in ethanol is adequate. At the same ratio the maximum solubility of solvent mixture is much lower than in the case of chlorides, where solutions of 0.1 mol/L concentration can be prepared very easily. Surprisingly, at higher deposition temperature the films are crack-free. When the deposition temperature is too low, the film is cracked. It seems that droplets produced using the air blast atomizer are large enough to avoid the precipitation during aerosol transport. Droplets arriving at the substrate do not contain any precipitates.

Metal-organic salts: Metal-organic salts have higher solubility in organic solvents. The surfaces of the films deposited using metal organic salts always contain a large number of incorporated particles. These particles may be formed on the surface due to solute precipitation and the slow spreading of impacted droplets. It can be seen that there are hardly any particles on the film surface and morphology. This can be attributed to the optimal droplet size distribution. This leads to the conclusion that thin films of better quality can prepared using metal organic salts in the spray pyrolysis system.

In the present work Cobalt acetate tetrahydrate [Co $(CH_3COO)_2 \cdot 4H_2O$] powder (Merck, Germany, 99% purity), Manganese (II) acetate tetra-hydrate [$Mn(CH_3COO)_2.4H_2O$] powder (Merck, Germany, 99.5% purity), Tungstic acid (H_2WO_4) powder ((Merck, Germany, 98% extra pure), Ammonium ceric nitrate [$(NH_4)_2Ce (NO_3)_6$] salt (Merck, Germany, 99% purity), Ferric chloride ($FeCl_3$) powder (Merck, Germany, 99% purity), Copper (II) acetate monohydrate [$Cu(CH_3COO)_2 \cdot H_2O$], powder (Merck, Germany, 99% purity) are used as precursor materials as a source of Co, Mn, W, Ce, Fe and Cu respectively in the (Fe, Cu) doped (Co_3O_4, MnO_2, WO_3 and CeO_2) thin films deposition.

3.2.3 Preparation of thin films

3.2.3.1 Preparation of precursor solution

The working solution was prepared by dissolving precursor materials into 100 mL deionized distilled water at room temperature. Water was taken as solvent and the volume of the solution kept 100mL constant. The precursor solution was then stirred with a magnetic stirrer at room temperature for about 1 h to form a homogeneous solution. Fiew drops of ethanol (C_2H_5OH) and hydrochloric acid were added in the solution to maintain P^H value. P^H value varied from 6 to 10 through the process. In the case of WO_3, 10 mL ammonia (NH_3) solution was added into the precursor solution to acquire homogeneous solution. Finally the prepared solution was filtered in order to spray through the spraying system.

3.2.3.2 Film deposition

It has been stated earlier that spray pyrolysis method for preparing nanostructured metal oxides thin films is an economically attractive method [142-144], which consist basically of spraying solution on a heated glass substrate. The apparatus needed to carry out the chemical spray process consists of a device to atomize the spray solution and a substrate

heater. A considerable amount of (100 mL) solution was taken in the beaker fitted with the spray nozzle. The cleaned substrate with a suitable mask was put on the susceptor of the heater. The distance between the tip of the nozzle and the surface of the glass substrate was kept 25 cm. Compressed air kept 0.5 bar constant. Before supplying the compressed air the substrate temperature was to be kept at a level slightly higher than the required substrate temperature because at the onset of spraying a slight fall of temperature is likely. The temperature of a substrate was controlled by controlling the heater power using a variac. The substrate temperature was measured by pyrometer focusing on the substrate. **Fig.** 3.15 shows a schematic diagram of spray pyrolysis technique. When compressed air is passed through air compressor at constant pressure (0.5 bar), a fine thin film was produced and was automatically carried to the reactor zone where film was deposited on the heated substrate. The whole spray pyrolysis process are divided into two stages: before and after droplet impact onto the substrate. In the first stage, the processes occurring during the droplet transport will be taken into account. In the second stage, film formation on the substrate surface will be considered. In the first stage, the droplets are transported from the nozzle to the heated substrate. Solvent evaporation is the most important process at this stage. The large droplets evaporate much slower compared to the small ones. The largest droplets play a more important role than the small ones, because they contain most of the precursor salt. Therefore, deposition temperature should be optimized for the large droplets. In the case of large droplets, solute precipitation during the droplet transportation is improbable.

The solvent of smaller droplets evaporates completely before reaching the substrate surface. Therefore, they will increase surface roughness. The first stage ends when a droplet impacts onto the substrate. The five possible results of droplet impact are focused. A droplet hitting the surface may stick, rebound, spread or splash on the surface. The spreading of impacted droplets can lead to the formation of a dense film or to rings. The sequence after the droplet has hit the surface depends on its size, viscosity and velocity. If droplets are too small they will rebound due to the retarding thermophoretic forces which are strongest close to the substrate, where the temperature gradient is largest. If they are too viscous or dry, they will stick and if they are too fast, they will splash. If the droplets spread but the velocity is too high, rings are formed.
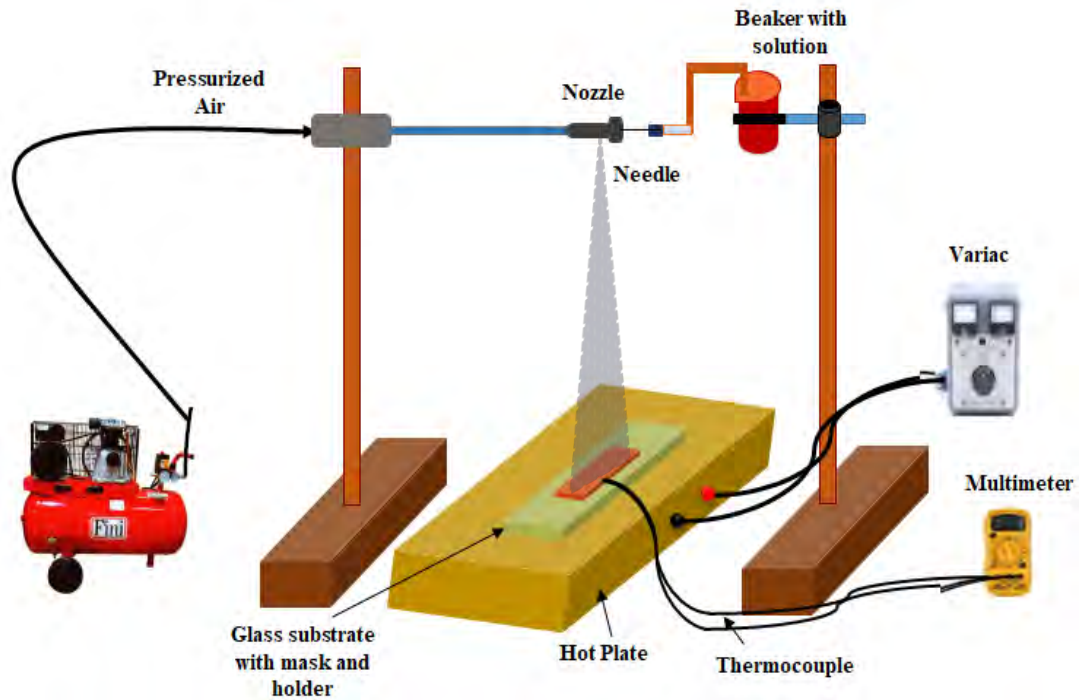
Fig. 3.15 A schematic diagram of spray pyrolysis technique.

3.3 Characterization Methods

Nanostructured metal oxide thin films are prepared, characterized and utilized for different purposes. The manipulation of atoms and molecules by using precise tools and new era of nano science and thin film technology, very sophisticated instruments are required from application point of view. For this purposes, Scanning electron microscope (SEM), Energy dispersive X-ray (EDX) spectroscopy, X-ray diffractometer (XRD), UV-VIS spectrophotometer etc. are used to assign the surface morphology, elemental composition, structural and optical properties of thin film respectively. These techniques are based on the various theoretical background. Here, the working principles and theories with formulas of various characterization techniques are discussed briefly.

3.3.1 Surface morphology by field emission scanning electron microscope (FESEM)

The technique is employed for morphological analysis of thin films. It may be classified under two groups, one dealing primarily with the "surface" structure and the other with "volume and surface" structure. A field emission scanning electron microscope (FESEM) is a powerful microscope that uses electrons rather than light to form an image of objects such as fractured metal components, foreign particles and residues, polymers, thin films electronic components, biological samples, and countless others. The shorter wavelength

of electrons permits image magnifications of up to 100,000X, as compared to about 2,000X for conventional light microscopy [145]. An FESEM also provides a greater depth of field than a light microscope, allowing complex, three-dimensional objects to remain sharp and in focus. This capability reveals details that cannot be resolved by light microscopy. Field emission scanning electron microscopy (FESEM) is a very versatile technique employed for the examination and analysis of the microstructure characteristics of solid objects. FESEM is capable of high resolution (values of the order of 10 nm), and its greater depth of focus allows more three-dimensional information to be gathered than optical microscopy. The technique uses a raftered electron beam (typically 2 to 30kV) to strike a solid sample and cause secondary electrons, back-scattered electrons, x-rays and Auger electrons to be emitted. The intensities of the emitted secondary electrons vary with topography and may be detected and displayed using a cathode ray tube screen, producing a detailed image of the surface. **Fig.** 3.16 depicts a field emission scanning electron microscope (FESEM) of model JEOL JSM-7600F.

Fig. 3.16 Field emission scanning electron microscope, model: JEOL JSM-7600F.

Basic principle: Electron Microscopes function exactly as their optical counterparts except that they use a focused beam of electrons instead of light to "image" the specimen and gain information as to its structure and composition. The basic steps involved in all Electron Microscopes are shown in **Fig.** 3.17 Electrons are harmonically emitted from a tungsten or lanthanum hex boride (LaB6) cathode and are accelerated towards an anode; alternatively, electrons can be emitted via field emission (FE). Tungsten is used because

it has the highest melting point and lowest vapour pressure of all metals, thereby allowing it to be heated for electron emission. The electron beam, which typically has an energy ranging from a few 100 eV to 100 keV, is focused by one or two condenser lenses into a beam with a very fine focal spot sized 0.4 nm to 5 nm. The beam passes through pairs of scanning coils or pairs of deflector plates in the electron optical column, typically in the objective lenses, which deflect the beam horizontally and vertically so that it scans in a raster fashion over a rectangular area of the sample surface. When the primary electron beam interacts with the sample, the electrons lose energy by repeated scattering and absorption within a teardrop-shaped volume of the specimen known as the interaction volume, which extends from less than 100 nm to around 5 μm into the surface. The size of the interaction volume depends on the electrons' landing energy, the atomic number of the specimen and the specimen's density.
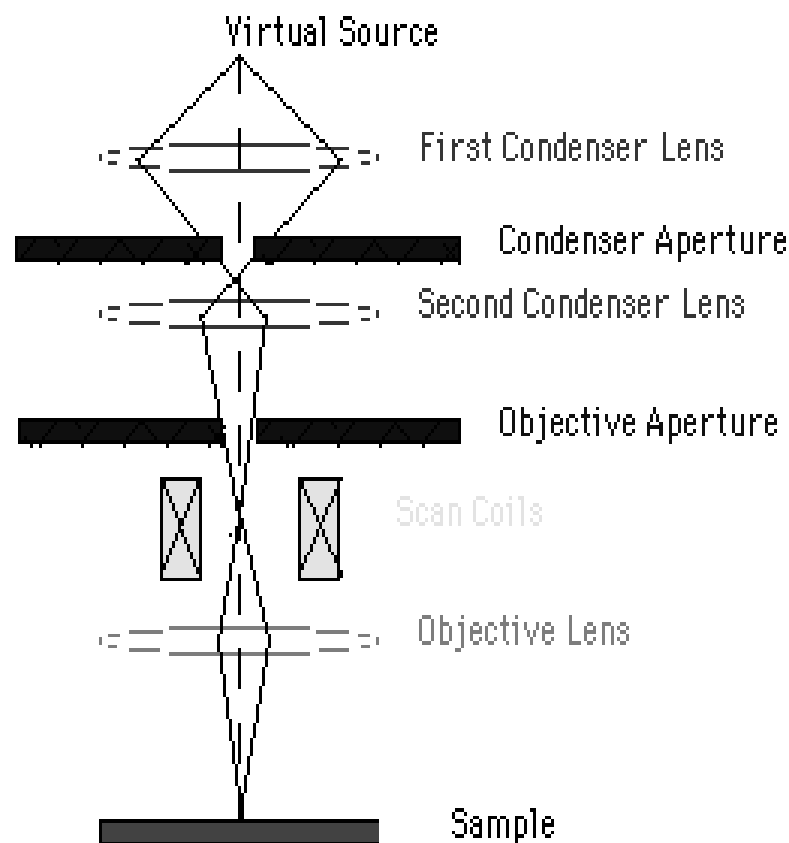
Fig. 3.17 Schematic diagram of a Scanning electron microscope.

The energy exchange between the electron beam and the sample results in the emission of electrons and electromagnetic radiation, which can be detected to produce an image. A stream of electrons is formed by the Electron Source and accelerated toward the Specimen

using a positive electrical potential This stream is confined and focused using metal apertures and magnetic lenses into a thin, focused, monochromatic beam. This beam is focused onto the sample using a magnetic lens Interactions occur inside the irradiated sample, affecting the electron beam. These interactions and effects are detected and transformed into an image [146-147].

3.3.2 Energy dispersive X-ray (EDX) spectroscopy analysis

EDX describes the compositional analysis of the thin films. This is done by the field emission scanning electron microscopy (FESEM) by focusing the X-ray beam on the full frame or a particular spot of the thin films. The analysis represents the individual weight (%) of the element that is present in the thin films. **Fig.** 3.18 represents the basic principle of EDX.

Basic principle: Its characterization capabilities are due in large part to the fundamental principle that each element has a unique atomic structure allowing X-rays that are characteristic of an element's atomic structure to be identified uniquely from one another. To stimulate the emission of characteristic X-rays from a specimen, a high-energy beam of charged particles such as electrons or protons or a beam of X-rays, is focused into the sample being studied.
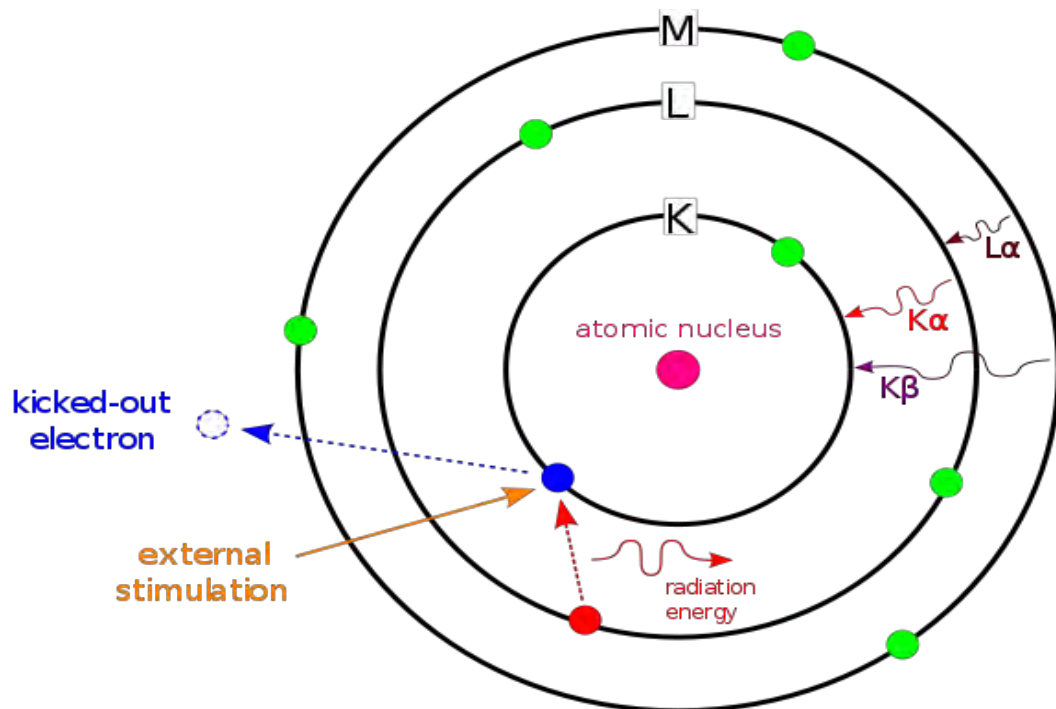
Fig. 3.18 Basic principle of Energy dispersive X-ray (EDX) spectroscopy analysis.

At rest, an atom within the sample contains ground state (or unexcited) electrons in discrete energy levels or electron shells bound to the nucleus. The incident beam may excite an electron in an inner shell, ejecting it from the shell while creating an electron hole where the electron was. An electron from an outer, higher-energy shell then fills the hole, and the difference in energy between the higher-energy shell and the lower energy shell may be released in the form of an X-ray. The number and energy of the X-rays emitted from a specimen can be measured by an energy-dispersive spectrometer [148].

3.3.3 Structural properties by X-ray diffraction (XRD)

The methods, which are commonly employed for the determination of the atomic arrangements and lattice parameters of different crystals, are based on diffraction of X-rays, electrons or neutrons. The most common method of structure determination is the technique of X-ray diffraction [149]. Structural properties analyzed by XRD are divided into two methods describes as follows:

3.3.3.1 The powder diffraction method

The Powder method derived by Debye and Scherrer and independently by Hull in 1919 is the most widely used method in the field of applied X-rays. When the crystalline material is not available in the form of discrete single crystals then X-ray diffraction patterns are obtained of aggregation of crystals usually of the form of fine powder using a powder camera or diffractometer [150]. Basically the method involves diffraction of monochromatic X-rays by a powdered or a fine-grained polycrystalline specimen and if properly employed can yield a great deal of structural information about the material under investigation. Each particle, a grain in the specimen, is tiny crystal oriented at random with respect to the incident beam. There is fair chance that a certain (hkl) plane will be correctly oriented to reflect the incident beam. Thus a variation of diffraction angle θ is obtained, not by rotating a single crystal about one of θ its axis but through the presence of many small crystals randomly oriented in space in the specimen. In powder diffractometer diffraction peaks appear at 2θ positions, which are recorded by a chart recorder. From the chart recorded diffraction pattern the Bragg angle as well as the heights (peak intensity) can be read out. The interplanar spacing'd' values corresponding to each peak can be calculated using the Bragg's relation. The interpretation of the powder diffraction pattern requires identification, i.e., determination of (hkl) values corresponding

to each diffraction peak. This is known as indexing which leads to the determination of the crystal structure. Below we describe the indexing of powder pattern by the reciprocal lattice concept.

3.3.3.2 Bragg's diffraction method

Bragg reflection is coherent elastic scattering in which the energy of the X-ray is not changed on reflection. If a beam of monochromatic radiation of wavelength λ is incident on a periodic crystal plane at an angle θ and is diffracted at the same angle as shown in **Fig.** 3.19 the Bragg diffraction condition for X-rays is given by

$$2d \; Sin\theta = n\lambda \tag{3.1}$$

where d is the distance between crystal planes and *n* is the positive integer which represents the order of reflection. [151]
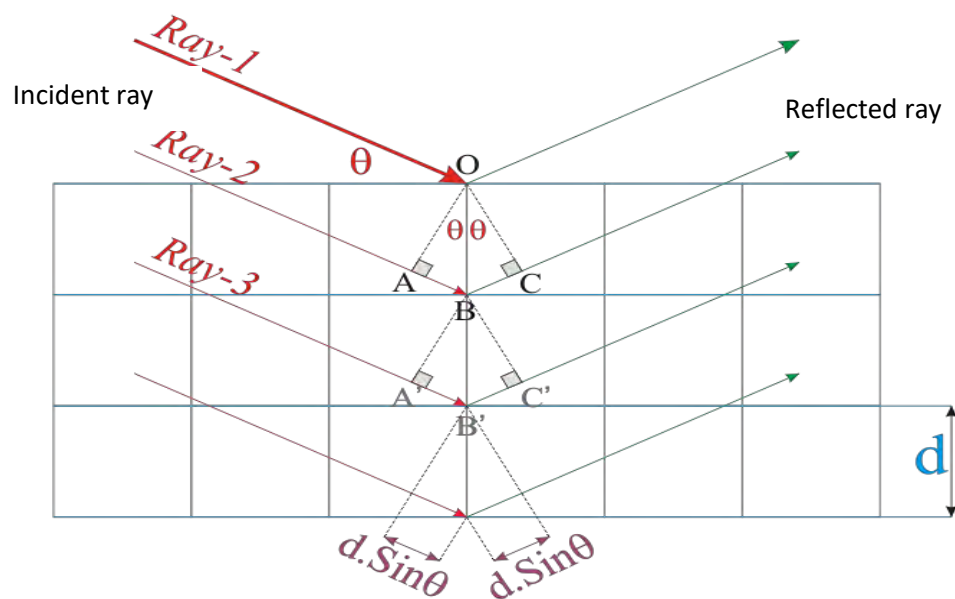
Fig. 3.19 Bragg law of diffraction.

Equation (3.1) is known as Bragg law. This Bragg law suggests that the diffraction is only possible when $\lambda \leq 2d$ [152]. For this reason we cannot use the visible light to determine the crystal structure of a material. The X-ray diffraction (XRD) provides substantial information on the crystal structure. The grain size D, of the samples is determined quantitatively using the formula.

$$D = \frac{k\,\lambda}{\beta \text{Cos}\theta} \qquad (3.2)$$

where, λ is the wavelength of the incident x-ray beam κ is a constant equal to 0.9 and θ is usual Bragg angle and β is Full width at half maxima of highest peak of XRD pattern. The interplanar spacing d_{hkl}, where h, k, and l represent miller indices are calculated using different formula for different crystal structure. Table 3.1 shows the various formula for relative crystal structure.

<p align="center">Table 3.1 Various formula for relative crystal structure</p>

Crystal structure	Formula
Cubic	$\dfrac{1}{d^2} = \dfrac{h^2 + k^2 + l^2}{a^2}$
Orthorhombic	$\dfrac{1}{d^2} = \dfrac{h^2}{a^2} + \dfrac{k^2}{b^2} + \dfrac{l^2}{c^2}$
Tetragonal	$\dfrac{1}{d^2} = \dfrac{h^2 + k^2}{a^2} + \dfrac{l^2}{c^2}$
Monoclinic	$\dfrac{1}{d^2} = \dfrac{1}{\text{Sin}^2\,\beta}\left(\dfrac{h^2}{a^2} + \dfrac{k^2\,\text{Sin}^2\beta}{b^2} + \dfrac{l^2}{c^2} - \dfrac{2hl\text{Cos}\beta}{ac} \right)$

The dimension of dislocation per unit volume associated with the density of defects in the sample demonstrated by dislocation density (δ) is calculated by the formula [153].

$$\delta = \frac{1}{D^2} \qquad (3.3)$$

X-ray peaks were analyzed to calculate the lattice strain and particle size using the simplest Williamson–Hall (W–H) method which differs between crystallite size and strain-induced peak broadening contemplated with the peak width as a function of $2\theta hkl$. The local distortion of the lattice generates strain and contributes to peak broadening considering responsive in all crystallographic directions, is written as [153]:

$$\varepsilon = \frac{\beta_{hkl}}{4\text{Cos}\theta_{hkl}} \qquad (3.4)$$

where ε is the strain in the crystal lattice. The XRD results were quantified by defining the texture coefficient randomly oriented crystallite. This factor was calculated for preferential growth orientation using the following equation [153-154]:

$$TC_{hkl} = \frac{I_m(hkl)/I_s(hkl)}{n^{-1}\sum_n I_{m(hkl)}/I_{s\,(hkl)}}$$ (3.5)

where TC $_{(hkl)}$ is the texture coefficient, Im (hkl) is the XRD intensity measured from a plane (hkl) of the films, Is(hkl) is typical intensity taken from the JCPDS data, and n is total peak numbers. An X-ray diffractometer (XRD); model: PANalytical Empyrean series 2, CuKα radiation, λ = 1.54056 Å is displayed in **Fig.** 3.20.

Fig. 3.20 X-ray diffractometer (XRD); model: PANalytical Empyrean series 2.

3.3.4 Thickness measurement by Fizeau fringes method

Optical interference method is one of the film thickness methods by which the thickness of the thin film can be determined accurately. In this method two reflecting surfaces are brought into close proximity to produce interference fringes. Weiner was the first to use interference fringes for the measurement of the film thickness. Later on using Fizeau fringes, Tolansky developed this method (interferometry method) to a remarkable degree and is now accepted as a standard method.[155-156] For the experimental setup a low power microscope, a monochromatic source of light, a glass plate and an interferometer

are required. To see the Fizeau fringes of equal thickness in a multiple beam interferometer a thin absorbing film on a glass substrate with an auxiliary reflecting coating on the film surface is required. For a transparent film with a very smooth surface no such auxiliary coating is necessary. [157].
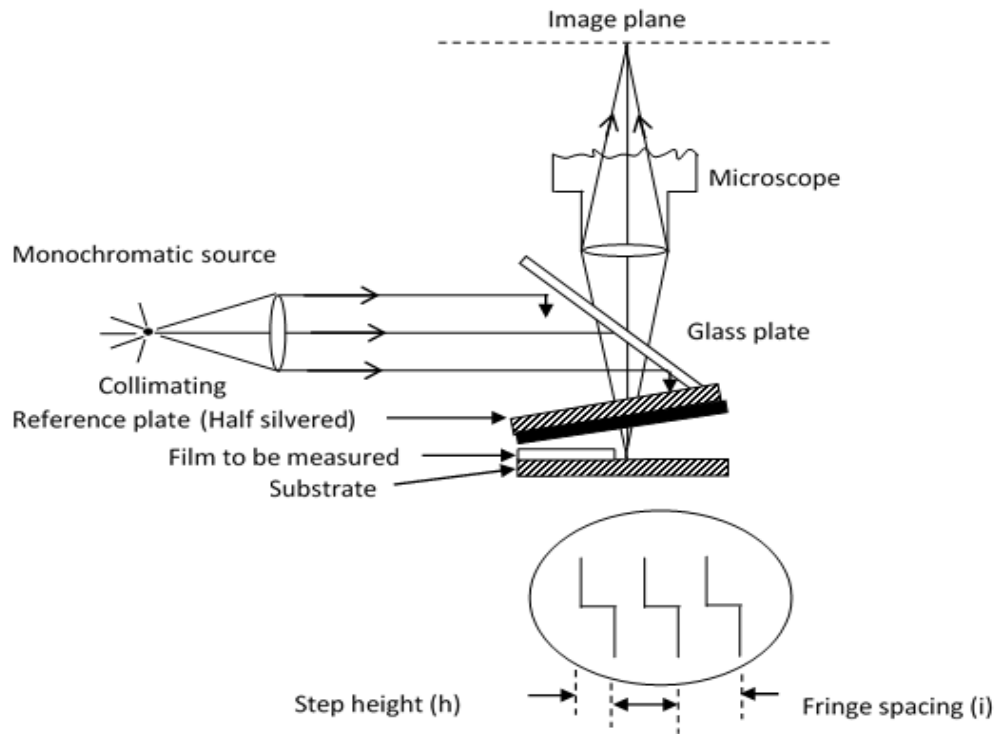
Fig. 3.21 Interferometer arrangement for producing reflection Fizeau fringes.

The film whose thickness is to be measured is required to form a step on a glass substrate and over it another plane glass plate (Fizeau plate) is placed. This type of interferometer is shown in **Fig.** 3.21. When the interferometer is illuminated with a parallel monochromatic beam of light (sodium light) at normal incidence, a fringe system is produced and is viewed with a low power microscope   Dark fringes are also observed against a white background. The displacement "h" of the fringe system across the film-substrate step is then measured to calculate the film thickness (t), using the relation

$$t = \frac{stepheight}{fringe-spacing} \times \frac{\lambda}{2} = \frac{h}{I} \times \frac{\lambda}{2}$$

(3.6) Where, λ is the wavelength of the monochromatic light (sodium light), I is the fringe-spacing. In this method, thickness from 3nm to 2000 nm can be measured with an accuracy of ± 5 nm.

3.3.5 Optical properties by UV-VIS spectrophotometer

Optical properties of thin films are analyzed by UV-VIS Spectrophotometer. In **Fig.** 3.22 an UV–Vis spectrophotometer; model: UV-2600, Pc: UV–Vis–NIR; Shimadzu is displayed. The optical components are coated with silica for durability. Halogen graphic gratings are used in each monochromatic for the ultraviolet/visible/near infrared (UV/VIS/NIR) range [158-159].The transmittance and absorbance are measured at normal incidence for the $200 \leq \lambda \leq 1100$ nm range. Using transmittance and absorbance different optical parameters are determined.

Fig. 3.22 UV–Vis spectrophotometer (Model: UV-2600,
Pc:UV–Vis–NIR; Shimadzu).

Basic principle: A diagram of the components of a typical spectrometer is shown in the following **Fig**. 3.23. The functioning of this instrument is relatively straightforward. A beam of light from a visible and/or UV light source (colored red) is separated into its component wavelengths by a prism or diffraction grating. Each monochromatic (single wavelength) beam in turn is split into two equal intensity beams by a half-mirrored device. One beam, the sample beam (colored magenta), passes through a small transparent container (cuvette) containing a solution of the compound being studied in a transparent solvent. The other beam, the reference (colored blue), passes through an identical cuvette containing only the solvent. The intensities of these light beams are then measured by

electronic detectors and compared. The intensity of the reference beam, which should have suffered little or no light absorption, is defined as I_0. The intensity of the sample beam is defined as I. Over a short period of time, the spectrometer automatically scans all the component wavelengths in the manner described. The ultraviolet region scanned is normally from 200 to 400 nm, and the visible portion is from 400 to 800 nm. If the sample compound does not absorb light of a given wavelength, $I = I_0$. However, if the sample compound absorbs light then I is less than I_0, and this difference may be plotted on a graph.
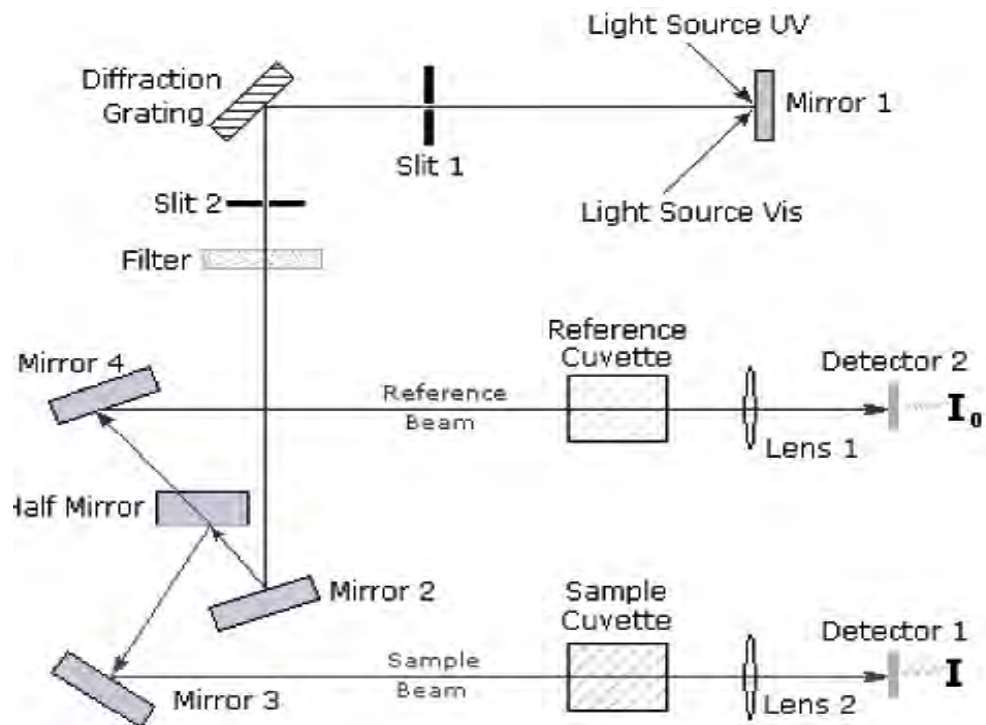
Fig. 3.23 Diagram of the components of a spectrophotometer.

Absorption may be presented as transmittance or absorbance. If no absorption has occurred, T = 1.0 and $A = 0$. Most of the sample compound does not absorb light of a given wavelength, $I = I_0$. Most spectrometers display absorbance on the vertical axis, and the commonly observed range is from 0 (100% transmittance) to 2 (1% transmittance). The wavelength of maximum absorbance is a characteristic value, designated as λ_{max}. Different compounds may have very different absorption maxima and absorbance. Intensely absorbing compounds must be examined in dilute solution, so that significant light energy is received by the detector, and this requires the use of completely transparent (non-

absorbing) solvents. The most commonly used solvents are water, ethanol, hexane and cyclohexane.

3.3.5.1 Optical parameters

(i) Transmittance: The transmittance (T) of a specimen is defined [160-162] as the ratio of the transmitted flux (I_t) to the incident flux (I_o) that is, $T = I_t/I_o$. Reflection at surfaces are usually taken into consideration, hence transmission is corrected for reflection and for scattering as well. With the corrections, the transmittance is called internal transmittance. If a specimen has a thickness d, an absorption coefficient, α and a reflectivity, R, the radiation reaching the first interface is $(1 - R)\,I_o$, the radiation reaching the second interface is $(1 - R)\,I_o \exp(-\alpha d)$ and only a fraction, $(1 - R)(1 - R)\,I_o \exp(-\alpha d)$ emerges. The portion internally reflected eventually comes out considerably attenuated. The end result is that overall transmission is given by as [160-162] :

$$T = I_t/I_o = (1-R)^2 \exp(-\alpha d)/(1-R^2)\exp(-2\alpha d) \tag{3.7}$$

Equation 2.2 accounts for the effect of multiple reflections in the film. When the product αd is large, the second term in the denominator becomes negligible and the transmittance is expressed as [162]

$$T = I_t/I_o = (1-R)^2 \exp(\alpha d) \tag{3.8}$$

If R and d are known, equation 2.3 is used to solve for α. The measurements of the transmittance of two samples having different thickness d1 and d2 can also be used to solve for α using equation 3.9,

$$T_1/T_2 = \exp[\alpha(d_2 - d_1)] \tag{4.9}$$

(ii) Absorbance: The absorbance (A) is the fraction of radiation absorbed from the radiation that strikes the surface of the material. Alternatively, A is the logarithm to base 10 of the transmittance, i.e, $A = \log_{10} I_t/I_o = \log_{10}T$. It follows from this equation that the transmittance and absorbance are related by $T = 10\,A$; it is used for calculating transmittance. Hence knowing one, the other can be calculated. The absorbance (A) is determined directly from absorbance spectra measurements and the instrument scales are often calibrated in this unit [162]. During the optical characterization of thin films, it is the spectral absorbance of the films that are obtained directly from the spectrophotometer.

The other properties are obtained from calculations based on the above quantities (transmittance and absorbance).

(iii) Reflectance: This is the fraction of the incident radiation of a given wavelength that is reflected when it strikes a surface. A relation between transmittance (T), spectral absorbance (A) and spectral reflectance (R), according to the law of conservation of energy is given by A + T + R = 1; this equation is used for calculating reflectance.

(iv) Absorption Coefficient : Absorption coefficient is the decrease in the intensity of a beam of photons or particles in its passage through a particular substance or medium. This is true when applied to electromagnetic radiation, atomic and subatomic particles. Absorption coefficient can be determined using the following two ways:

(a) In terms of absorbance

This method is based on the Beer-Lambert law [163] which is the linear relationship between absorbance and concentration of an absorbing species and usually written as:

 A = εbc;

where A is the measured absorbance, ε is the is the molar absorptivity with units of L mol^{-1}cm^{-1}, b is the path length of the sample, that is, the path length of the cuvette in which the sample is contained. The unit of b is centimeter. c is the concentration of the compound in solution, expressed in mol L^{-1}. The Beer-Lambert law can be derived from an approximation for the absorption coefficient for a molecule by approximating the molecule by an opaque disk whose cross-sectional area, σ, represents the effective area seen by a photon of frequency ν. If the frequency of the light is far from resonance, the area is approximately 0, and if ν is close to resonance the area is a maximum. Taking an infinitesimal slab, dz, of sample shown in **Fig.** 3.24 , I_o is the intensity entering the sample at z=0, I_z is the intensity entering the infinitesimal slab at z, dI is the intensity absorbed in the slab, and I is the intensity of light leaving the sample.Then, the total opaque area on the slab due to the absorbers is σNA dz. Then, the fraction of photons absorbed will be σNA dz / A so,

$$\frac{dI}{I_0} = -\sigma Ndz$$

Integrating this equation from z = 0 to z = b gives:

$\ln(I) - \ln(I_o) = -\sigma N b$

or, $-\ln(I / I_o) = -\sigma N b$.

Since N (molecules/cm^3) (1 mole / 6.023x10^{23} molecules) 1000 cm^3 / liter $= c$ (moles/liter) and $2.303 * \log(x) = \ln(x)$

then $-\log(I / I_o) = \sigma(6.023 \times 10^{20} / 2.303) cb$

or, $-\log(I / I_o) = A = \varepsilon bc$

where $\varepsilon = \sigma (6.023 \times 10^{20} / 2.303) = \sigma(2.61 \times 10^{20})$, and ε is called the molar absorptivity. Thus the intensity of the transmitted light can be expressed as $I = I_0 e^{-\alpha d}$ where d is the path length through the sample and α is the absorption coefficient. This equation can be written as, $\alpha = \dfrac{2.303A}{d}$
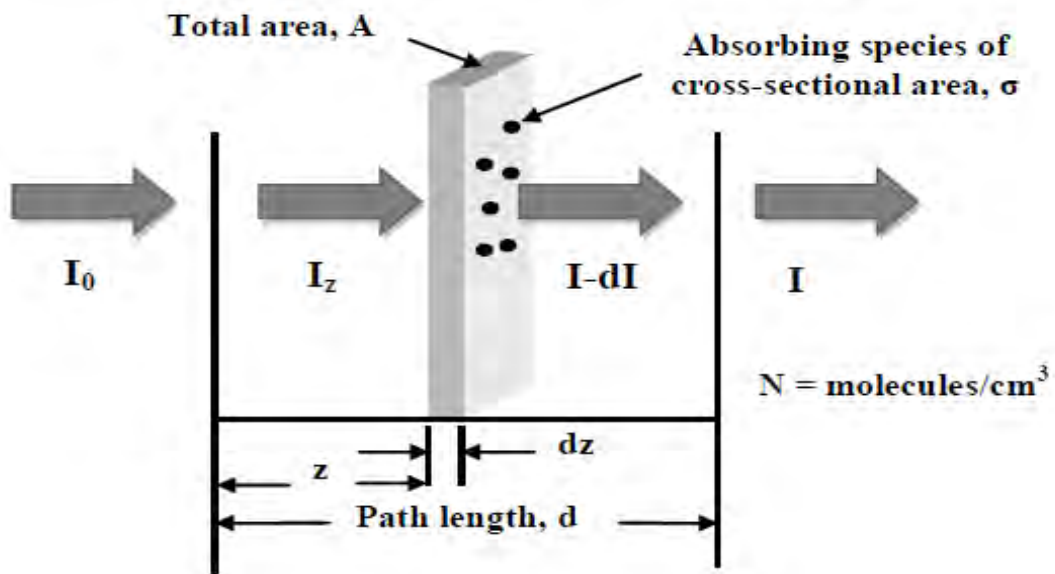
Fig. 3.24 Absorption of light by a sample.

(b) In terms of transmittance

When radiation of intensity I_o is incident on material of thickness d (μm) the transmitted intensity, I_t is given by [160,162] $I_t = I_o \exp(-\alpha d)$. For pure absorption, the constant (α) is the absorption coefficient. For scattering, obeying Bouguer-Beer''s law, α is the scattering coefficient. And for the total attenuation including both is the extinction

coefficient given by the sum of the absorption and scattering coefficient. $T = I_t/I_o = \exp(-\alpha d)$ and $\alpha = -[\ln T]/d$. For a unit distance trans versed, we have $\alpha = -[\ln T]/d \, (\mu m)^{-1}$. i.e. $\alpha = -[\ln T]/d \times 10^6 \, m^{-1}$ which is used to calculate the absorption coefficient in this work. For a selective transmitting surface, the selectivity merit is given as αT. This is the transmittance-absorptance product for the material.

3.3.5.2 Band gap

The band gap (E_g) is the energy needed to move a valence electron into conduction band. For a semiconductor it is the energy needed to free an electron from the nucleus of the parent atom. It is defined as $E_g = h\nu = 1.241/\lambda_o$ eV. When an electron undergoes transitions from an upper part of the valence band to the lower part of the conduction band, it causes dispersion near the fundamental absorption edge and gives the shape of the absorption spectrum. This could happen without phonon participation and without a change in the crystal in which case, it is called direct transition. But when this is a change in the crystal momentum and interaction with phonon, that changes electron energy, is called indirect transition. **Fig.** 3.25 shows the energy level diagram of direct and indirect band gap.
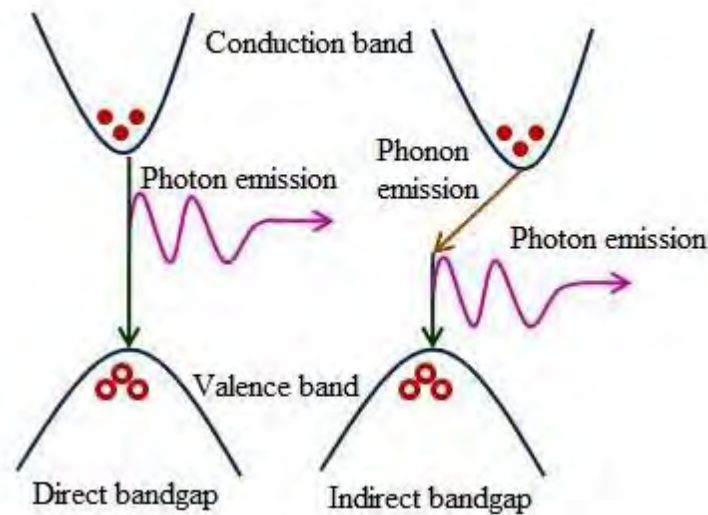
Fig. 3.25 Energy level diagram of direct and indirect band gap.

Both direct and indirect transitions give rise to different frequency dependency of the absorption coefficient near the fundamental absorption edge. The absorption coefficient for direct transition is given by [164-166]

$$\alpha = (h\nu - E_g)^n \tag{3.10}$$

where h is Planck's constant and n =1/2 If the transition between the upper part of the valence band to the lower part of the conduction band is allowed by the selection rules and n = 3/2, and if the transitions are forbidden, then $\alpha = (h\nu - E_g)^{1/2}$ for allowed transitions and $\alpha^2 = (h\nu - E_g)$ for forbidden transition, n = 2, Eg is the optical band gap. The indirect transitions give rise to

$$\alpha = (h\nu - E_g + E_p)^n \hspace{5cm} (3.11)$$

where Ep is the energy of a phonon with the required momentum. Both phonon emission and phonon absorption are possible, where n = 2 and 3 for allowed and forbidden transitions, respectively. The dependence of absorption coefficient on the energy of light quanta corresponding to direct allowed transition is given by $\alpha = (h\nu - E_g)^{1/2}$ i.e. $\alpha^2 = (h\nu - E_g)$. Thus a plot of α^2 against $h\nu$ will give a curve with straight line at certain portion. However, at the region of its absorption edge, the absorption values fall to such a low value that the path due to band-to–band transition becomes difficult to measure. Experimental equipment or loses in specimen or other incidental absorptions are attributed to such low values [164] at the region of absorption edge. The plot of α^2 against hf in this region deviates from being straight. Extrapolation of the straight portion of the graph to point of $\alpha^2 = 0$ gives the energy band gap, Eg. The plot obeys accurately an exponential dependence on photon energy [167].

$$\alpha = \alpha_o \exp [-\beta (E_o - h\nu)] \hspace{4cm} (3.12)$$

where α_o denotes the cofactors placed before the exponent. E_o is energy comparable to Eg and β is a constant (at room temperature) having values in the range of 10 to 20(eV)$^{-1}$. Some crystalline solids, notably alkali halides, show Urbach dependence given by $\beta = 0.8/K_\beta T$ where β is temperature dependent near 300K, where K_β is the Boltzmann constant, T is temperature. The minimum photon energy required to excite an electron from the valence to the conduction band is given by $h\nu = E_g - E_p$, where E_p is the energy of an absorbed phonon with the required momentum. For a transition involving phonon absorption, the absorption coefficient is given by

$$\alpha_a h\nu = B (h\nu - E_g + E_p)^2 / \exp (E_p / K_\beta T)^{-1} \hspace{3cm} (3.13)$$

and for a transition involving phonon emission

$$\alpha_e h\nu = B (h\nu - E_g - E_p)^2 /(1 - \exp (E_p / K_\beta T)^{-1} \hspace{3cm} (3.14)$$

Since both phonon emission and phonon absorption, are possible for hν > (E$_g$ –E$_p$), the absorption coefficient is then

$$\alpha h\nu = \alpha_a h\nu + \alpha_e h\nu \qquad (3.15)$$

For many amorphous semiconductors, the energy dependence of absorption is experimentally of the form [168-169]

$$(\alpha\, h\nu)^{1/2} = \alpha\,(h\nu - E_g) \qquad (3.16)$$

$$(\alpha\, h\nu) = B(h\nu - E_g)^2 \qquad (3.17)$$

where B is a constant which can be defined as $B = 4\lambda\sigma_o / ncE_e$; where c is the velocity of light, n is the refractive index, σ_o is the extrapolated conductivity at $1/T = 0$ and E_e is interpreted as the width of the tail of localized states in the band gap. **Fig.** 3.26 shows the intra-band gap transitions for metal oxides thin film which represents direct, indirect and forbidden transitions. An important conclusion is that one of the allowed indirect transitions is associated with an exciton transition according to the weakly bound electron–hole model [170].
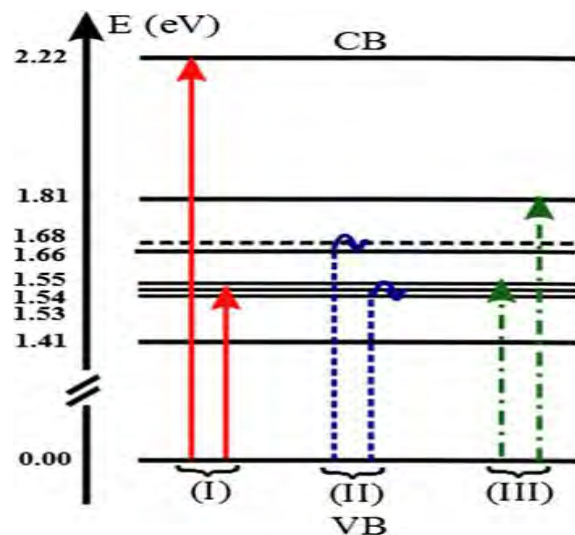
Fig. 3.26 Intra-band gap transitions for metal oxides thin film, where (I) represents direct, (II) indirect and (III) forbidden transitions.

3.3.6 Electrical measurements by four probe method

The resistivity of the semiconductor thin films are determined using several methods such as Direct method, Two-point method, linear four-probe method, Van der Pauw technique,

etc. Among these methods a four-point probe method is usually used for the determination of low resistivity of thin films. Four probe apparatus is one of the standard and most widely used apparatus for the measurement of resistivity of semiconductors. This method is employed when the sample is in the form of a thin wafer, such as a thin semiconductor material deposited on a substrate. The sample is millimeter in size and having a thickness. It consists of four probe arranged linearly in a straight line at equal distance S from each other. **Fig.** 3.27 shows the four point probe set up at the optical microscopy lab of department of Physics, BUET. An oven is provided with a heater at this set up to heat the sample so that behavior of the sample is studied with increase in temperature. A schematic diagram of four probe method is displayed in **Fig.** 3.28 which shows the arrangements of four probes that measure voltage (V) and supply current (A) to the surface of the crystal [171].

Fig. 3.27 Four point probe set up: Optical microscopy lab,
Department of Physics, BUET.

A constant current (I) is passed through the two probes and the potential drop V across the middle two probes is measured. The resistivity of a sample, relatively large compared to the probe spacing may be estimated from the following equation, $\rho = 2\pi S(V/I)$. The right hand side of the equation should be multiplied by correction factors of sheet resistance (C.F.1), film thickness (C.F.2) and temperature (C.F.3) [172]. Since, the thin films were square in shape and the ratio of the side of the square (D) and the probe distance (S) is <3, C.F.1 is not required here. The film thickness t is much less than S and t/S<0.4, thus C.F.2 is 1. Temperature correction for room temperature condition is ~1.0. So, equation (3.24) can directly be used for calculation of resistivity.
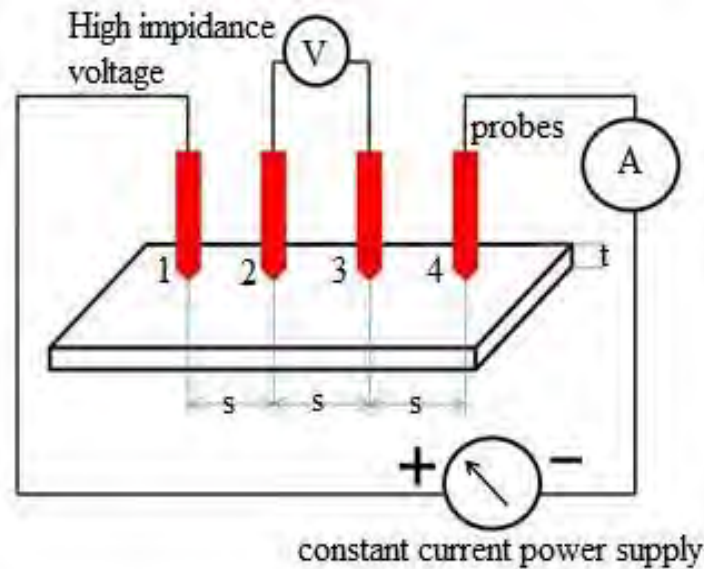
Fig. 3.28 Schematic diagram of four probe method.

3.3.7 Hall effect measurements

Hall effect gives information about the nature of the charge carriers in the semiconductor material, i.e. whether the sample is n-type or p-type. The conductivity measurements alone do not yield this information. To distinguish between the charges carriers (electrons or holes) a Hall effect study can be carried out. **Fig.** 3.29 shows the Hall effect measuring apparatus (ECOPIA HMS-5000, USA). Hall Effect measurements were performed at room temperature by this Hall Effect measuring apparatus under the magnetic field 0.54T and current 10 mA. The Hall effect occurs when a current is passed through a sample in the presence of a transverse magnetic field and a small potential difference, the Hall voltage, is developed between two opposite faces of the sample, in a direction perpendicular to both the current and applied magnetic field. The Hall effect also allows for the charge carrier density and mobility to be determined accurately. The Hall effect is observed due to the Lorentz force which is a combination of the electric and magnetic force. As the electron moves along the electric field, perpendicular to the applied magnetic field, it experiences a magnetic force normal to both directions. The direction of the force experienced can be predicted using the "right hand rule". As a constant current is injected into the sample in the presence of a magnetic field perpendicular to this, the electrons (charge carriers in n-type semiconductors) which are subjected to the Lorentz force drift away from the current direction, which results in excess negative surface electrical charge

and a potential drop across the two sides of the sample, known as the Hall voltage [173] as can be seen from schematic diagram for Hall effect measurements.

Fig. 3.29 Hall effect measuring apparatus (ECOPIA HMS-5000, USA).
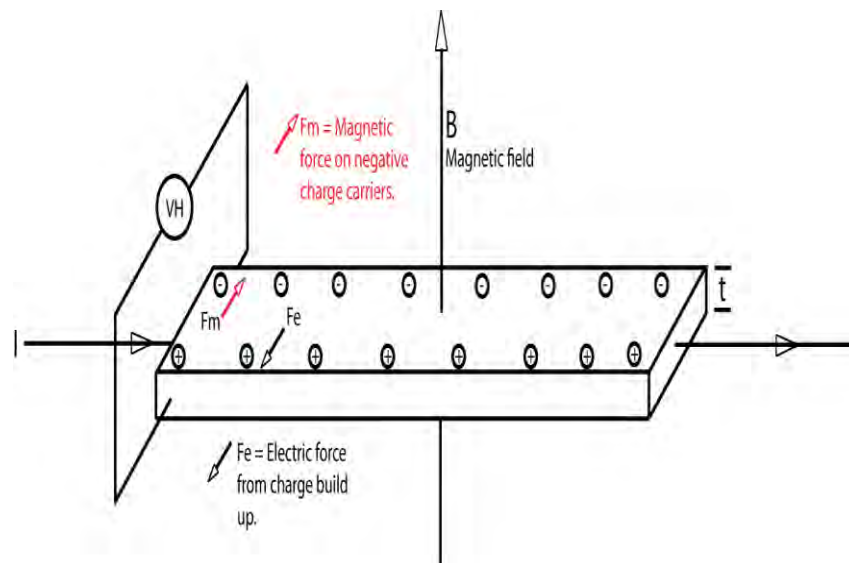
Fig. 3.30 Schematic diagram for Hall effect measurements.

Fig. 30 represented the schematic diagram of Hall effect measurements.. V_H is the Hall voltage, B is the applied magnetic field and I is the applied current through the sample. R_H is the Hall coefficient and is related to the carrier density by the following relationship:

$$V_H = R_H \, I \, (B/t) \tag{3.18}$$

$$R_H = (1/Ne) \tag{3.19}$$

3.3.8 Glucose sensing properties of thin films

3.3.8.1 Methods for sensing properties

Glucose sensing properties are measured basically into three ways depending on the measurement principles: i.e., potentiometric, impedimetric and ampherometric techniques.

(i) Potentiometric process: Potentiometric is commonly used to measure glucose concentrations greater than 10^{-5} M, which is in the physiological range in most cases. In potentiometric sensors, potential difference between a reference electrode and a working electrode is measured at zero applied current. The potential of the working electrode changes depending on the glucose concentration. It has been shown that these sensors can measure glucose concentrations of 10 μM or higher (the blood glucose level of a typical human is the range of 4–7mM) [174].The zero current potentials applied between those two electrodes are recorded as a function of the concentrations of target analytes in a logarithmic manner [175].

(ii) Impedimetric process: The impedimetric biosensor is less frequently used as compared to the potentiometric. Electrochemical impedance spectroscopy is a powerful analytical tool which allows us to effectively visualize the actual electrical double layer structure of a modified electrode [176] although recording of an impedance spectrum within a broad frequency range is time consuming. The glucose does not affect the dielectric spectrum in the MHz frequency region [177-178] and direct detection of the glucose is available. More improved sensitivity and wider linear response range could be available by tailoring the material properties, for example active surface area, three-dimensional structure, and electrical conductance of the film.

(iii) Amperometric process: Amperometry is a quite sensitive electrochemical technique in which the signal of interest is current that is linearly dependent on the target concentration by applying a constant bias potential. Glucose is oxidized at the working electrode composed of a noble metal oxides and the bio recognition species such as GOx for glucose sensing [179]. An Amperometric biosensor comprises two or three electrodes. The former consists of a reference and a working electrode. Application of the two-electrode system to biosensors is limited, because at high current flow the potential control becomes difficult. Instead, the third electrode is commonly introduced as an auxiliary

counter electrode having a large surface area to make most of current flows between the counter and the working electrodes, though voltage is still applied between the working and the reference electrodes. There are three modes of the glucose oxidation referred to as the first, the second and the third generation glucose sensors depending on the electron transfer mechanisms.

(a) First generation: In the first generation sensors a catalytic enzyme used to act as a catalyst for the reaction of glucose and oxygen, where free oxygen required to act as the reaction mediator which caused a serious problem for sensor operation. Here the another problem was the interference caused by electro active such as ascorbic acid, uric acid, and countless other drugs present in the blood [80].

(b) Second generation: In the second generation of glucose sensor technology, the use of a non-physiological and artificial mediator such as ferrocene derivatives and ferricyanide were proposed instead of the first generation mediator, oxygen to enhance electron transport. Thus, the second generation sensors were able to overcome some of the limitations of the first generation sensors. However, their performance and sensitivity were still dependent on the changes in the pH of the medium and changes in the temperature and humidity of the electrode surface.

(c) Third generation: In the third generation of glucose sensor technology, efforts were made to eliminate the need for a reaction mediator so as to transfer the electron directly from the enzyme to the electrode. Some nano- or micro porous materials have been chosen as the substrate for immobilization since the enhanced surface area of electrode surface can increase the electron transfer rate [181]. Though third generation sensors were expected to show some improvement over their first and second generation counterparts, they still suffered from the limitations arising from the dependency of enzyme's activity on the temperature, humidity, interference, etc.

(d) Fourth generation: The problems associated with these third generation, enzyme based glucose sensors have steered researchers to explore enzyme-free detection. This has led to the development of nonenzymatic glucose (NEG) sensors, which allow glucose to be oxidized directly on the electrode surface. NEG sensors constitute the fourth generation of glucose sensor technology. A tremendous amount of NEG sensor research is going on all around the world. The nanostructured metal-oxide based glucose sensor belong to the fourth generation. In the present work a method has been discussed that may be an

efficient for the fast and precise determination of sensing current and glucose concentration-response.

3.3.8.2 Glucose sensing properties measurements by four probe method

In the present work, the sensitivity was measured by determining current using the four point probe method. In this method, two electrodes are used: one is acted as reference (Zn-plate, positive electrode) and the other one is acted as counter (Cu-plate, negative electrode). Both the electrodes are placed into the prepared glucose solution; where an ammeter, voltage source and four point probes are connected and the deposited thin film was set as working electrode which is placed under four probe systems. The sensing element was not put into the glucose solution. In this study, 0.2 M $C_6H_{12}O_6$ (3.62gm) and 0.2 M NaOH (0.8gm) were dissolved into 200 ml distilled water. NaOH usually exists together with glucose. The precursors have been stirred about 1 hour with a magnetic stirrer to have a homogeneous glucose concentration. In the glucose solution NaOH was used to release the hydroxyl ions (OH⁻) and to accelerate ionic exchange mechanism. A constant supply voltage of +65V was applied for the sensitivity measurement. This method is supported by Adawiya J. H., et al. [182], where they characterized glucose sensing properties using four probe method of nanostructured SnO_2 thin films prepared by thermal evaporation method and Usman A., et al. [183], they explained glucose sensing properties of ZnO nanowires placing two electrodes into glucose solution.

3.3.8.3 Reaction mechanism

Glucose sensing depends on the oxidation of glucose molecules on the surface of the film layer and decomposition into gluconolactone ($C_6H_{10}O_6$) and hydrogen peroxide (H_2O_2). Also, NaOH was used in the $C_6H_{12}O_6$ solution for increasing current to reach a stable state as glucose and OH⁻ molecules are adsorbed in the film surface. The possible chemical reactions are given as [184-185]:

$$C_6H_{12}O_6 + H_2O + O_2 \rightarrow C_6H_{10}O_6 + H_2O_2$$

$$H_2O_2 \rightarrow O_2 + 2H^+ + 2e^-$$

$$NaOH \rightarrow Na^+ + OH^-$$

$$C_6H_{12}O_6 + H_2O + NaOH \rightarrow C_6H_{10}O_6 + O_2 + H^+ + 2e^-$$
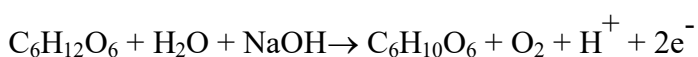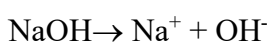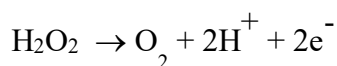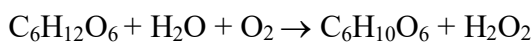
The electrons produced in those reactions are transferred through the film layer. The porous structure of the film gives the ability for the NaOH molecules adsorbing on the film surface. Although the mechanism of glucose oxidation at the electrode surface is still not fully understood, there are two main models which have been proposed to explain the above process.

First model: The first model, proposed by Pletcher [186], is known as the activated chemisorption model. It is believed that the oxidation process is initiated through the adsorption of the glucose molecule on the electrode surface. This allows the glucose molecule to form a bond with the electrode surface. At the same time, the hydrogen atom in the glucose molecule, which is attached to the hemiacetal carbon shown in **Fig.** 3.31, is extracted. Once extracted, this hydrogen atom bonds with the electrode surface at a site adjacent to the bound glucose [187]. A change in the oxidation state of the glucose molecule on the metal electrode results in a change in glucose-metal interaction, thereby lowering the glucose–metal bond strength, resulting in desorption of the glucose molecule. Because the electrode surface and the glucose molecules form and break their bonds in the catalytic process, a bond of intermediate strength is desired, as it is conducive for both the adsorption (bond forming) and desorption (bond breaking) processes.
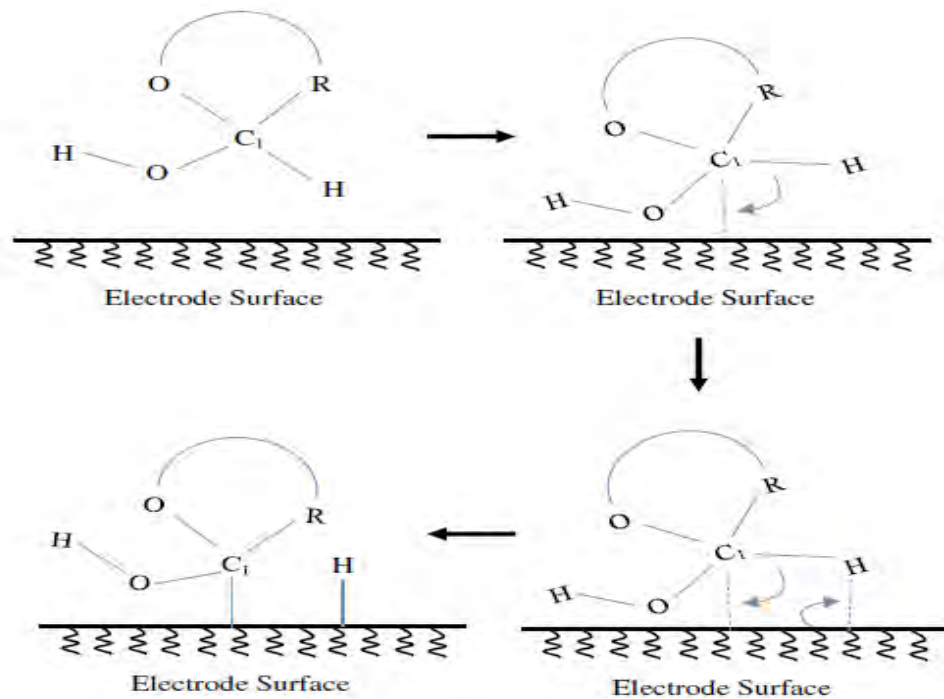
Fig. 3.31 An illustration of the concentric adsorption theory by Pletcher. [C_1: hemiacetalic carbon atom, R: the other parts of glucose molecule.].

Second model: The second model, known as the 'Incipient Hydrous Oxide Adatom Mediator' (IHOAM) model, was proposed by Burke [188]. Burke originally formulated this model based on the observation that there are active metal atoms on the electrode surface, which have low lattice stabilization and enhanced reactivity. These atoms undergo a premonolayer oxidation step, during which an incipient hydrous oxide, OH_{ads} , layer is formed which is believed to mediate the oxidation of glucose at the electrode surface. **Fig.** 3.32 shows a schematic illustration of the IHOAM model. Although both of these models are under scrutiny, they can still be used to explain the oxidation of glucose for different electrode materials.
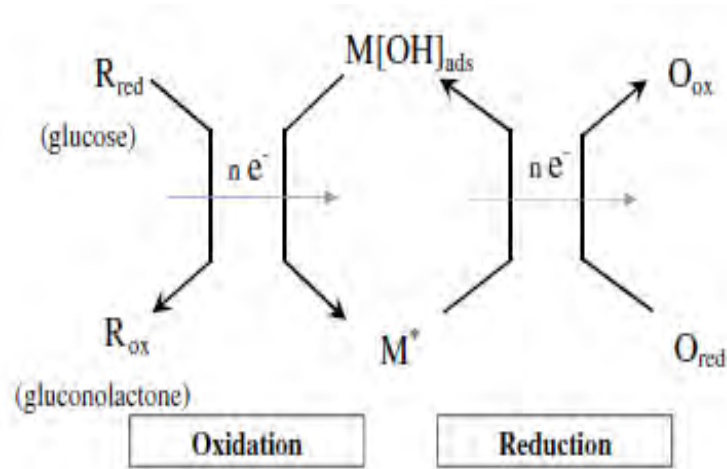
Fig. 3.32 Schematic illustration of the IHOAM model.

In the **Fig.** 3.32 M* is the reductive metal adsorption site, and M[OH]ads is the oxidative absorbed hydroxide radical. This figure illustrates how both oxidative and reductive processes are catalyzed at the metal electrode surface. The conductivity of a metal oxide film are dependent on the partial pressure of atmospheric oxygen. Thus, at elevated temperatures, the stoichiometry of semiconducting oxides changes as a function of the ambient oxygen. The change in stoichiometry affects the electrical conductivity of the materials. It is widely accepted that in an air environment, oxygen molecules adsorb onto the surface of the metal oxide layer to form O_2, O- and O^{2-} ions by extracting electrons from the conduction band depending on the temperature [189-190]. These negatively charged oxygen adsorbents play an important role in detecting glucose. In the case of n-type semiconducting oxides, the positively charged oxide surface and negatively charged adsorbed oxygen ions form a depletion region at the surface. Thus, the resistance of an n-type semiconducting oxide in air is high, due to the development of a potential barrier.

Since the charge carriers in p-type semiconducting oxides are positive holes, the resistance in air is low because of the formation of negatively charged oxygen adsorbents. The adsorption of oxidizing glucose molecule on p-type semiconducting oxides results in a increase in conductivity. A space charge layer is formed due to the electron depletion at the surface by chemisorption. grain structures, morphology or crystallinity are the dominant factors for controlling device sensitivity.

3.3.8.4 Working principle

According to the mechanism of charge transfer, the electrons from glucose solution transfer to the electrode surface, which can be changed by the electrode. The electron transfer between the glucose and the electrode is directly carried out without the electronic exchange between them. **Fig.** 3.33 shows the schematic representation of glucose sensing mechanism based on the nanostructured spherical metal oxides as an efficient electron mediators and by I-V measurement technique supported by Liu, X. W. et al. and Sang H. K., et al. [191-192] .

Oxidation of glucose molecules in the air (open air, oxygen) on the film surface is responsible for glucose sensing abilities which decompose into gluconolactone ($C_6H_{10}O_6$) and hydrogen peroxide (H_2O_2). Oxidation of glucose molecules results in hydrogen peroxide molecules are consequence by oxidation of glucose molecules that pass through the porous surface and adsorbed on the film surface. The surface area increases the speed of the reaction and the output current as a result of the oxidation of H_2O_2. In enhancing sensing ability of the prepared thin films concerning glucose ($C_6H_{12}O_6$) is a fast electron transfer between the films layer and the substrate to improve electron collection. The fast electron transfer provide probable interaction between the ions from glucose solution and the film surface. At the film surface oxygen ions may immediate interact and bonded with ions from glucose ($C_6H_{12}O_6$) molecules. This fast interaction provides a large number of charge carriers which causes sharp raise of sensing current as well sensing ability.
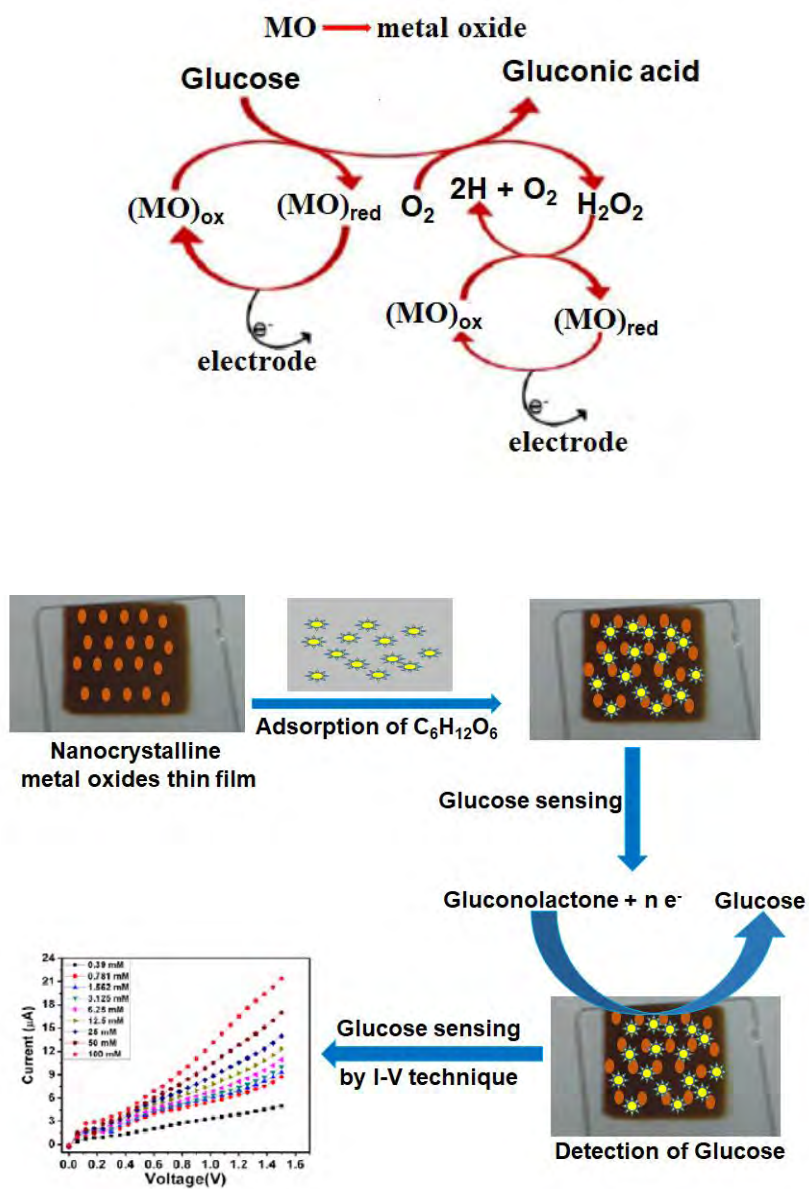
Fig. 3.33 Schematic representation of glucose sensing mechanism.

CHAPTER 4

RESULTS AND DISCUSSION

Part A: Results of Fe and Cu Doped Co_3O_4 Thin Films

Part B: Results of Fe and Cu Doped MnO_2 Thin Films

Part C: Results of Fe and Cu Doped WO_3 Thin Films

Part D: Results of Fe and Cu Doped CeO_2 Thin Films

Part E: Results of Glucose Sensing Properties of Thin Films

CHAPTER 4 RESULTS AND DISCUSSION

In this chapter the results and discussion of the various experimental studies viz. surface morphology structural, optical and electrical properties of (Fe, Cu) doped transition and rare earth metal oxides (Co_3O_4, MnO_2, WO_3 and CeO_2) thin films are presented and discussed part by part. The obtained results are compared with relative earlier reports.

Part A
Results of Fe and Cu Doped Co_3O_4 Thin Films

4.1 Results for the characterization of Fe and Cu Doped Co_3O_4 Thin Films

4.1.1 Results of Fe doped Co_3O_4 thin films

4.1.1.1 Photograph of Fe doped Co_3O_4 thin films

Photograph of composted Co_3O_4 thin film shows uniform deposition and surface consistency of the film slightly changed for Fe doping. **Fig.** 4.1 shows photograph of deposited undoped and Fe doped Co_3O_4 thin films varying with Fe concentration from 0-10 at %.
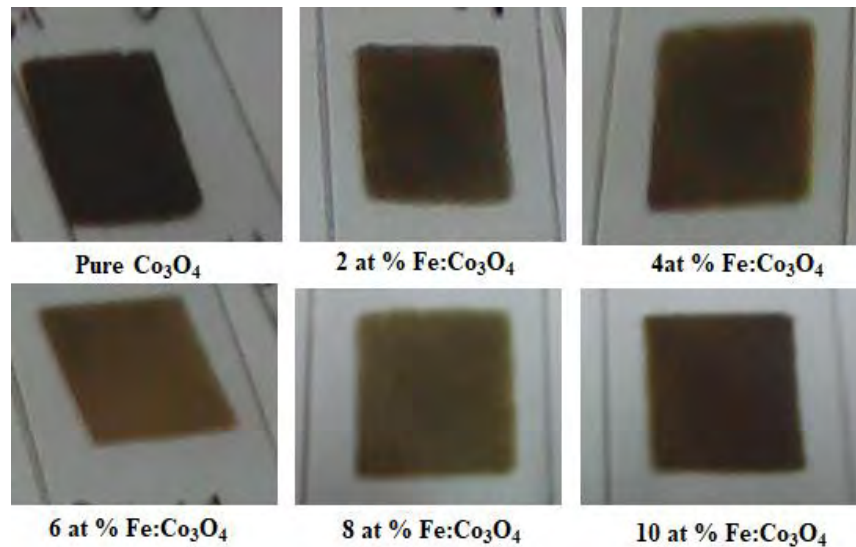
Fig. 4.1 Photograph of deposited undoped and Fe doped Co_3O_4 thin films.

All the films are densed and homogeneous. The colour of the films are very dark brown. A few variation of colour is observed for Fe doped Co_3O_4 thin films compare with pure

$Co_3O_4.$ This variations confirm the effect of Fe dopant concentration on Co_3O_4 properties. The thickness of undoped and Fe doped Co_3O_4 films were measured by the fizeau fringes method at Department of Physics, BUET, Dhaka. Thickness of the films varied with ±10 nm. The measured thicknesses were 257, 279, 295, 313, 321, and 330 nm for 0, 2, 4, 6, 8 and 10 at % Fe:Co_3O_4 thin films respectively.

4.1.1.2 Surface morphology analysis

FESEM images of 0, 2, 4, 6, 8 and 10 at% Fe doped Co_3O_4 thin films observed at 50,000 magnification are shown in **Fig.** 2.2 (a-f) respectively. All the images show that the substrates are uniformly covered with spherical nanoparticles. **Fig.** 2.2 (a) reveals the porous cobalt oxides layer which may due to the precursor materials contain organic phases with hydrophilic character and allows water molecules to spread across the surface than remain as droplets and make the surface with small pores [193-194]. After 2 at% Fe doping surface become compact and pores are larger shown in **Fig.** 4.2 (b), compared with pure Co_3O_4 because of incorporation of Fe^{2+} ions into Co_3O_4 lattice.
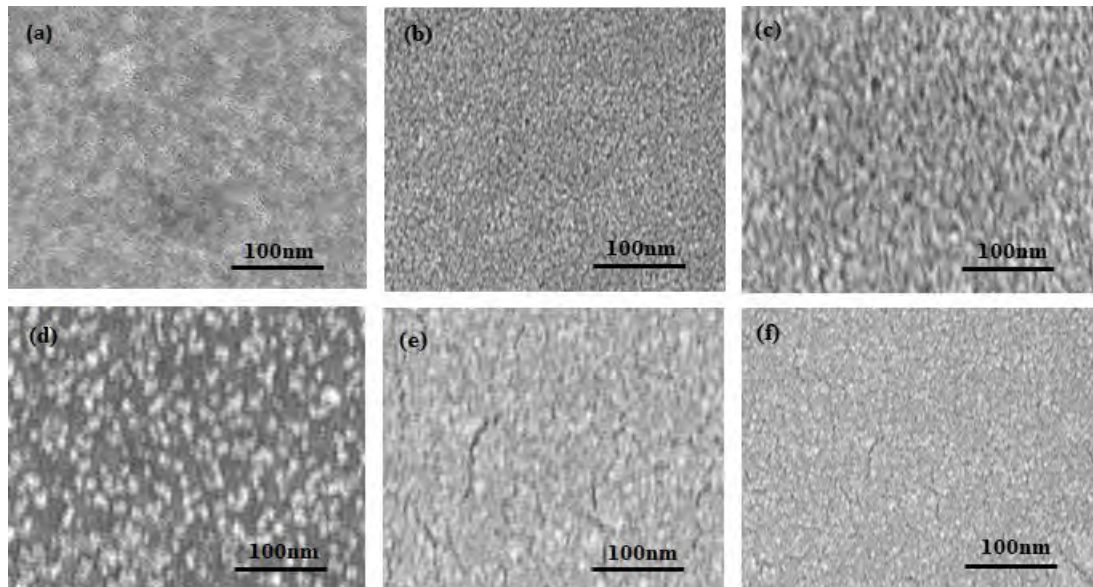
Fig. 4.2 (a-f) FESEM images of 0-10 at% Fe doped Co_3O_4 respectively.

Fig. 4.2 (c) shows that surface become highly porous for 4 at % Fe doping. This may due to the substitution of higher Co^{2+} (0.88Å) by lower Fe^{2+} (0.70Å) cations generating more oxygen vacancy. **Fig.** 4.2 (d) indicates that further increasing Fe contents at 6 at% the pores are disappeared due to higher combinational strength of Fe than Co. Some cracks are observed at 8 and 10 at % Fe content shown in **Fig.** 4.2 (e and f), because stress

generated higher Fe concentrations exceeds combinational strength. It is seen from the FESEM images that 4 at% Fe doped Co_3O_4 surface is more porous which may suitable for bio sensing applications. These results satisfy with the other earlier research works [195-196]

4.1.1.3 Elemental and compositional analysis

The quantitative analysis of the deposited films is carried out by EDX spectra. The composition of Fe doped Co_3O_4 thin films of 0-10 at% Fe concentrations have been confirmed by energy dispersive X-ray spectroscopy (EDX). **Fig.** 4.3 (a-c) show the elemental analysis from EDX spectra of the composition of deposited films at 0, 4 and 8 at % Fe doping. Different peaks corresponding to Co and O are found in the spectrum shown in **Fig.** 4.3(a) which confirms the Co_3O_4 thin film. For different concentrations of Fe in the solution, there are also Fe peak in the spectra shown in **Fig.** 4.3 (b-c) which confirm the composition of Co, Fe and O in the Fe doped Co_3O_4 thin films.
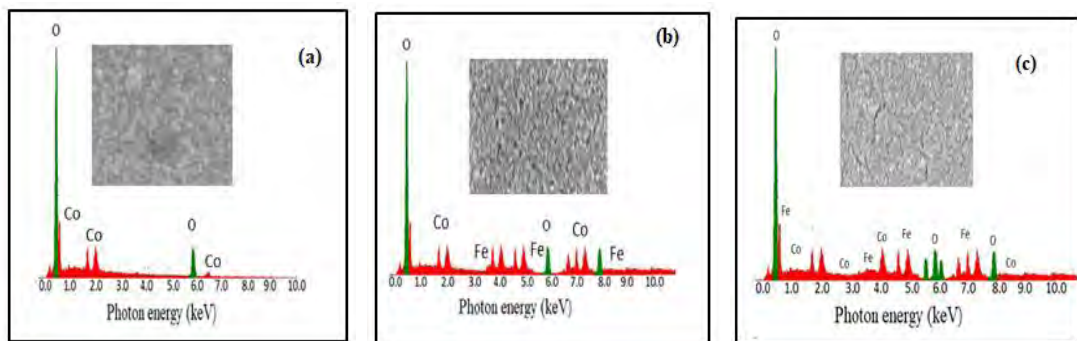
Fig. 4.3 (a-c) EDX spectra of 0, 4 and 8 at % Fe:Co_3O_4 respectively.

Fig. 4.4 shows the quantitative analysis of the composition of deposited films containing an average atomic percentage of Fe, Co and O. It is to mention that the deposited films are stoichiometric. It is cleared that the grains are typically comprised of both Fe and Co metals. There is a shift in the wavelength with respect to energy at which it occurs clearly signifying a crystal field effect. Hence from the EDX it is clear that the Fe ions act as dopants in the Co_3O_4 structure [197]. The at % of Co decrease gradually with the rise of at % of Fe which confirm the stoichiometry and homogeneity of the films.
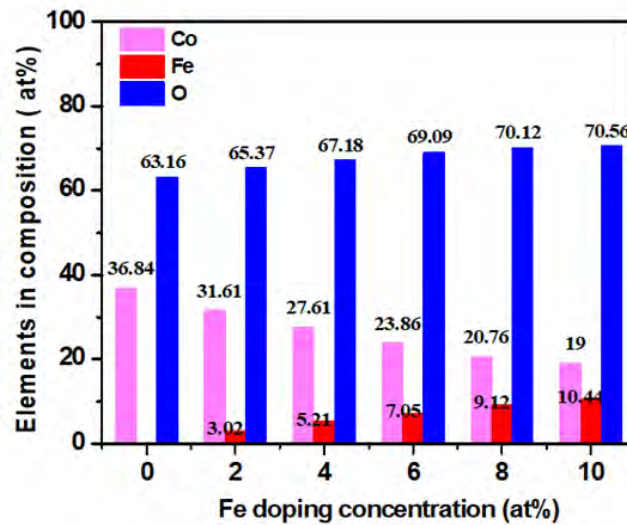
Fig. 4.4 Quantitative analysis of Fe doped Co_3O_4 thin films.

4.1.1.4 Structural properties

Fig. 4.5 shows the XRD pattern of Fe: Co_3O_4 films at different Fe concentrations of 0, 2, 6,8 and 10 at%, respectively. All of the diffraction peaks have been perfectly indexed corresponding to the (110), (220), (311), (511) and (440) reflection planes at $2\theta = 18.90°$, 31.30°, 36.81° 59.45° and 65.20° respectively and assigned to a spinel cubic phase of Co_3O_4 with *Fd3m* space group which are confirmed by JCPDS card no 42-1467 [198]. Incorporation of Fe atom strongly modifies the growth of the preferential orientation (311) plane. The crystallinity is increased with Fe concentration up to 4 at % due to the super-saturation of Fe atoms into the Co_3O_4 matrix. No other peak was observed without spinel Co_3O_4 up to 6 at % Fe doping which indicate a high purity and more stable of the samples.. At 8 and 10 at % Fe doping a new phase along (024) plane at 49.5° diffraction angle due to Fe_2O_3 which matches with JCPDS card no 24-0072 [199]. The crystalline phase of Fe doped Co_3O_4 is identical to the Co_3O_4 cubic spinel phase. When the Fe atoms introduced into the matrix it can either substitute or interstice in the lattice. Variations of structural parameters of Fe doped Co_3O_4 thin films are shown in Table 4.1. Lattice parameters have been calculated along preferential orientation plane (311) and found to decrease up to 4 at% Fe concentrations as shown in Table 4.1. These variations may due to increase of average crystallite size and shift of the peak towards higher angle. An increase of the cell parameter is observed with the increase of Fe concentration from 6 at % to 10 at%. This result can be related with the different ion sizes of cobalt and iron which leads to a lattice expansion. These results satisfy with other earlier research works [200-202].
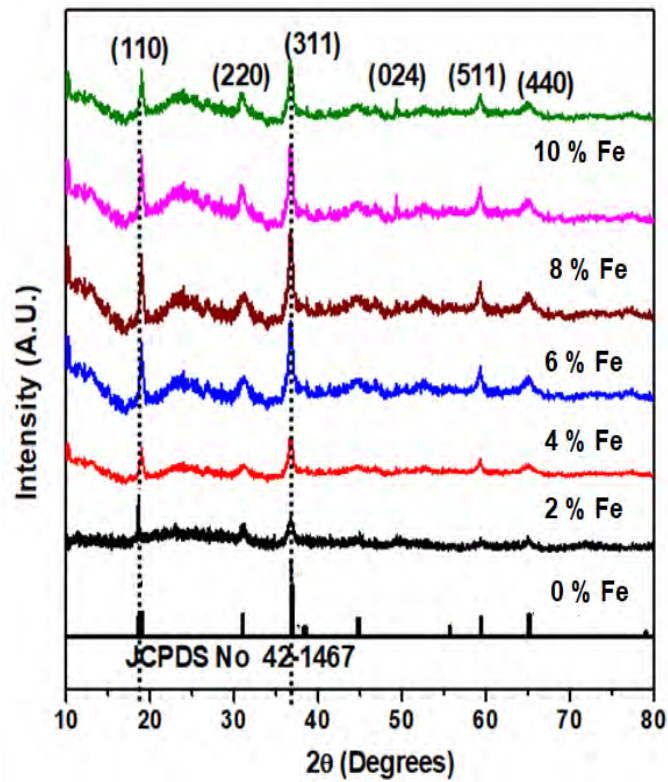
Fig. 4.5 XRD pattern of 0-10 at% Fe doped Co_3O_4 thin films.

Table 4.1 Structural parameters of Fe: Co_3O_4 thin films

Fe concentration (at%)	Average Grain size (nm) by image j software	Average crystallite size D (nm)	Lattice constants a=b=c (Å)	Dislocation density $\delta =1/D^2 \times 10^{15}$ (line/m^2)	Texture coefficient TC_{hkl}
0	33	29	8.076	1.189	0.953
2	36	31	8.051	1.041	0.995
4	38	35	8.043	0.816	1.002
6	34	32	8.059	0.977	1.113
8	31	30	8.065	1.111	1.158
10	32	27	8.069	1.372	1.167

Dislocation densities exhibit variation with increasing doping concentrations. From table (1) we notice that when D increase at 2 and 4 at % of Fe doping concentration, the

dislocation decrease and suggests that doping has induced lees defects in the system that leads to increase the crystallinity. But at 6-10 at% Fe doping D decrease and the dislocation increases because of decreasing crystallinity. Thus, in the present investigation, the variations of texture coefficient with Fe doping concentration showed randomly oriented crystallites for 4 at% Fe presenting $TC_{hkl} = 1.002$ (~ 1) [212].

4.1.1.5 Optical properties

Fig. 4.6 displays the optical transmission spectra of Fe-doped Co_3O_4 thin films at different Fe concentration from 0-10 at % varying with wavelength range from 400 nm to 1100 nm. It is noticed that the low percentage of transmittance is found about 10–43% near 400 nm which may for absorption of light of the excitation electrons from valence band (VB) to conduction band (CB). It is also observed that thin films exhibited a red shift into the absorption onset at 700 nm. In the vis-region, two sharp absorption edges are observed to lead the charge transfer event of ($O^{2-} \rightarrow Co^{2+}$) and ($O^{2-} \rightarrow Co^{3+}$) in Co_3O_4. In the IR region [203] high transmittance is obtained from 63% - 95% highlighted in **Fig**.4.6 which may for structural homogeneity. Maximum transmittance is observed about 95% for 4 at% Fe content. The increase of transmittance may refer to the effects of excess charge carrier for Fe doping that is attributed to the improvement in stoichiometry of the films.

Fig. 4.6 Transmittance spectra of Fe:Co_3O_4 at 0-10at% Fe concentration.
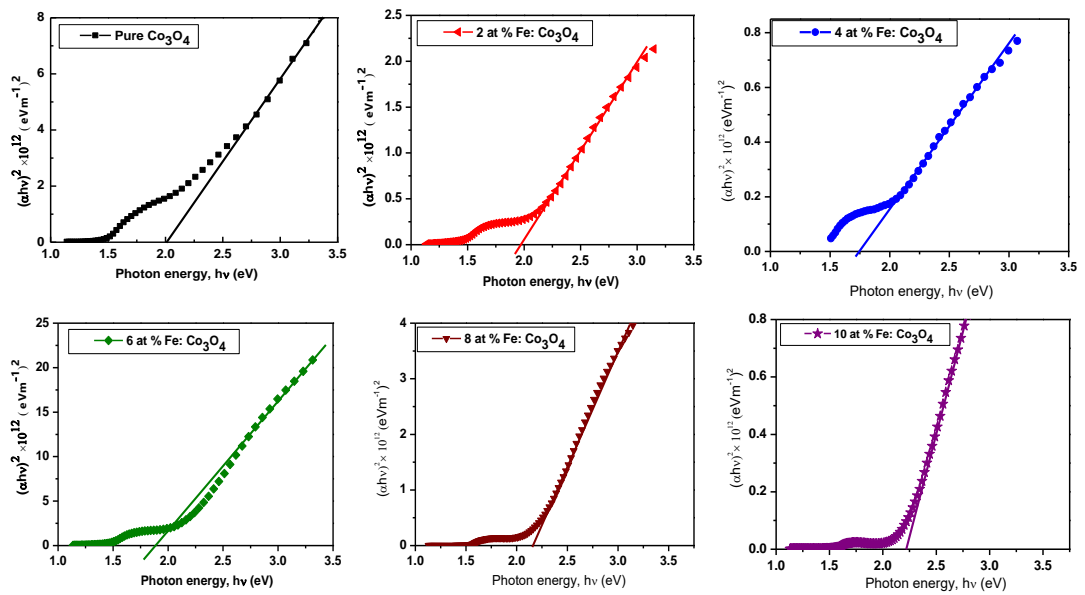
Fig. 4.7 Plot of $(\alpha h\nu)^2$ vs photon energy.

The band gap energy has been calculated using Tauc relation: $\alpha = A/h\nu\,(h\nu - E_g)^{1/2}$; where A is a constant, $h\nu$ is the photon energy and E_g is the optical band gap. In the Table 4.2 variation of optical band gap are shown which have been calculated in the NIR region (850-1100nm) and the band gaps decrease with increase of Fe concentration which may due to incorporation of Fe^{3+} ions into Co_3O_4 [204-206].

Table 4.2 Optical band gap of 0, 2, 4, 6,8 and 10 at% Fe doped Co_3O_4 thin films

Fe concentration (at %)	Thickness (nm)	Band gap E_g (eV)
0	257	2.02
2	279	1.96
4	295	1.73
6	313	1.89
8	321	2.15
10	330	2.21

4.1.1.6 Electrical properties

The variation of electrical resistivity with temperature ranging from 300-440 K for Co_3O_4 and 2, 4,6,8 and 10 at % Fe doped Co_3O_4 thin films are shown in **Fig** 4.8. It is noticed that the resistivity decreases with the rise in temperature. This type of variation indicates the semiconducting behavior of the films. The decrease in resistivity may be attributed to the increase of the acceptor states associated with the integration of Fe impurities into Co sites of the Co_3O_4 lattice. It is observed that at high temperature, the resistivity increase with the rise of Fe concentration up to 4 at% [207]. At 6- 10 at % Fe concentration resistivity decrease. The increase of resistivity may due to the creation of defect as a result of Fe^{3+} either substitution or incorporation into Co_3O_4 lattice. The decrease in resistivity may be attributed to the increase of the acceptor states associated with the integration of Fe impurities into Co sites of the Co_3O_4 lattice. Table 4.3 records the electrical properties of the Fe: Co_3O_4 thin films deposited at 0, 2, 4,6,8 and 10 at% Fe concentration. The carrier concentration increase with Fe concentration up to 4 at % which may due to the substitutional defects in the Co_3O_4 lattice. Carrier concentration decrease at 6-10 at% Fe doping concentrations that may as a result of crossing the solid solubility limit of Fe into $Co_3O_4.$ Hall mobility decrease in the range of 0-4 at% and increase at 6-10 at % Fe doping which are responsible for number of defects produced in Co_3O_4 by Fe^{3+} substitution or incorporation [208-210].
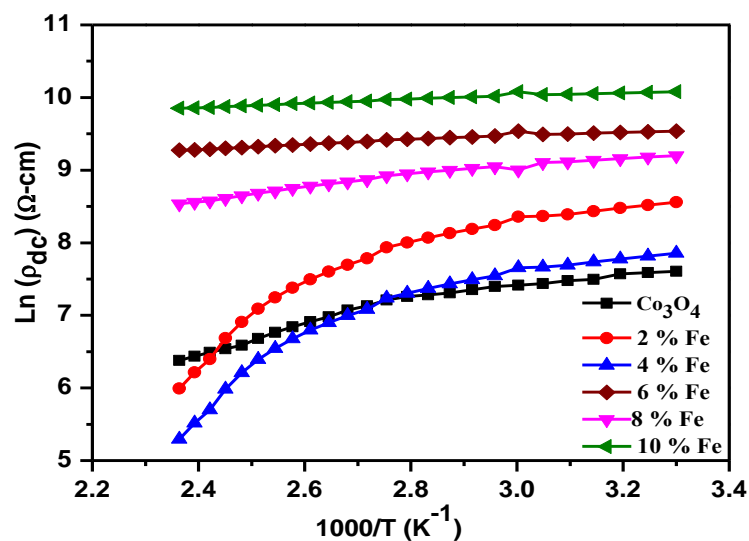
Fig. 4.8 Variation of resistivity with temperature of 0-10 at % Fe:$Co_3O_4.$

Table 4.3 Electrical parameters of Fe: Co_3O_4 thin films

Fe concentration (at%)	Resistivity, ρ ($\times 10^4$ Ω-cm)	Carrier concentration, n_c ($\times 10^{17}$ cm^{-3})	Hall mobility, μ ($cm^2 V^{-1} s^{-1}$)
0	0.23	2.39	1.81
2	0.19	3.97	1.23
4	0.12	5.78	0.87
6	0.59	4.56	1.23
8	1.67	4.29	1.72
10	1.98	3.18	1.97

4.1.2 Results for the characterization of Cu doped Co_3O_4 thin films

4.1.2.1 Photograph of Cu doped Co_3O_4 thin films

Photograph of composted Co_3O_4 thin film shows uniform deposition and surface consistency of the film slightly changed for Cu doping. **Fig** 4.9 shows photograph of deposited pure and Cu doped Co_3O_4 thin films varying with Cu concentration from 0-10 at %.
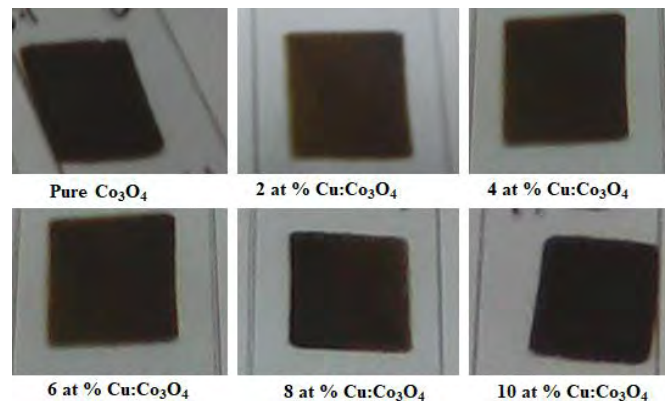
Fig. 4.9 Photograph of deposited pure and Cu doped Co_3O_4 thin films.

All the films are densed and homogeneous. The colour of the films are dark. There is no so variation of colour among the film. But the difference in film homogeneity and compactness are observed for pure and Cu doped Co_3O_4 films. This variations confirm the

effect of Cu dopant concentration on Co_3O_4 properties. The thickness of pure and Cu doped Co_3O_4 films were measured by the fizeau fringes method. Thickness of the films varied with ±10 nm. The measured thicknesses were 257, 272, 291, 306, 317, 326 nm for 0, 2, 4, 6, 8 and 10 at % Cu : Co_3O_4 thin films respectively.

4.1.2.2 Surface morphology

The FESEM images of undoped and 2 -10 at% Cu doped Co_3O_4 thin films are presented in **Fig.** 4.10 (a-d) respectively. All the images show that the substrates are uniformly covered with oxides. The surface morphology for pure Co_3O_4 is displayed in **Fig.** 1(a) reveals the porous cobalt oxides layer which may due to the evolution of O_2 during decomposition at high temperature (450ºC). After 2 at % Cu doping, the surface becomes smooth and compact because the macro defects are reduced due to the presence of low Cu doping level shown in **Fig.** 1 (b). **Fig.** 1 (c) shows relatively homogeneous particle sizes and distribution for 4 at % Cu concentration. Again, at 6 at% Cu concentration demonstrated in **Fig.** 1 (d), the surface becomes more porous and rough because of high amount of incorporated Cu, Cu^{2+} ions enter into the spinel Co_3O_4 lattice until stoichiometric [211].
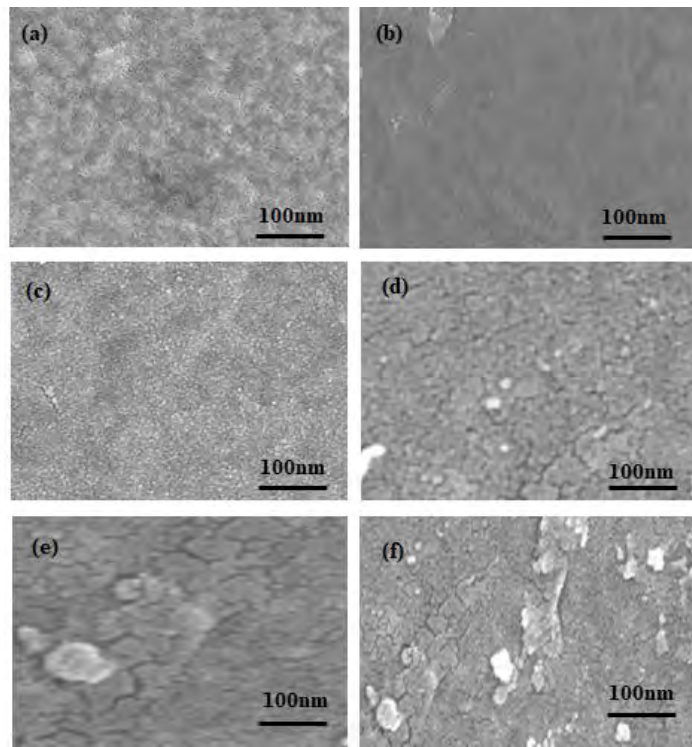
Fig. 4.10 (a-f) FESEM images of 0-10 at% Cu:Co_3O_4 respectively.

4. 1.2. 3 Compositional analysis

The elements of the composition of Cu doped Co_3O_4 thin films of 0-10 at% Cu concentrations were confirmed by energy dispersive X-ray spectroscopy (EDX).analysis carried out by EDX spectra. **Fig.** 4.11 (a-b) show EDX spectra of deposited films of 4 and 8 at % Cu doping. The presence of Co, Cu and O peak in the spectra shown in **Fig.** 4.11 (a-b) confirm the composition of Co, Cu and O in the Cu doped Co_3O_4 thin films. **Fig.** 4.12 shows the quantitative analysis of the composition of deposited films containing an average atomic percentage of Cu, Co and O. The variation of quantity of the elements indicate the significant stoichiometry and homogeneity of the films.
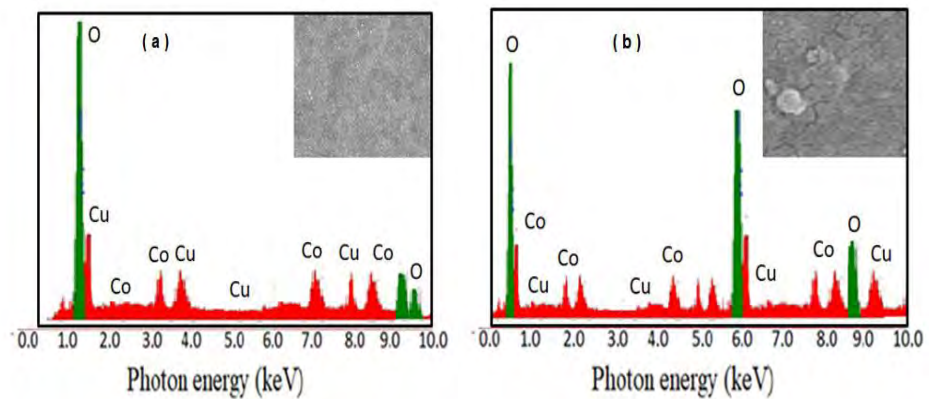
Fig. 4.11 (a-b) EDX spectra of 4 and 8 at % Cu doped Co_3O_4 thin films respectively.
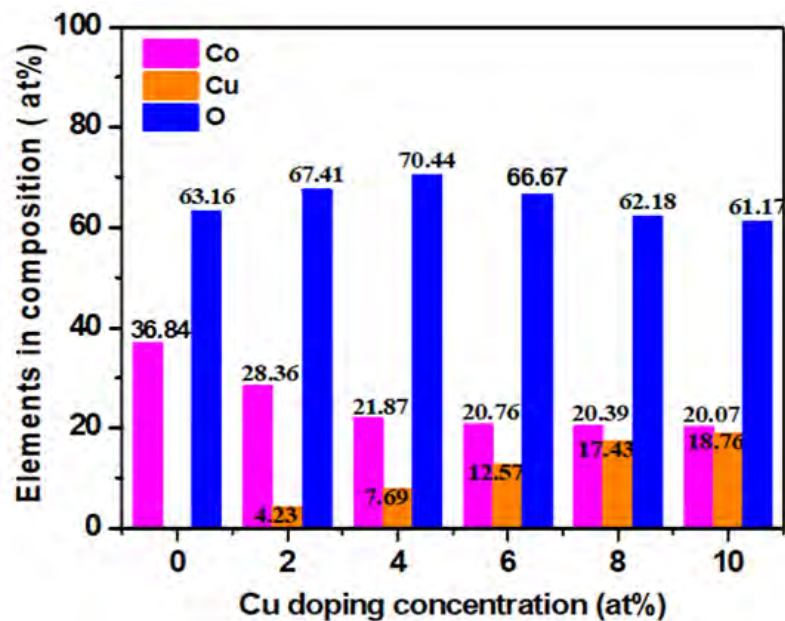
Fig. 4.12 Quantitative analysis of Cu doped Co_3O_4 thin films.

4.1.2.4 Structural properties

Fig. 4.13 exhibited the XRD pattern of Cu: Co_3O_4 films at different Cu concentrations of 0, 2,4 and 6 at%, respectively. All of the diffraction peaks were perfectly indexed corresponding to the (220), (311), and (440) reflection planes at $2\theta = 31.30°, 36.81°$ and 65.20° respectively and assigned to a pure spinel cubic phase of Co_3O_4 with a lattice constant of 8.0761 Å according to the (JCPDS file No 42-1467. Incorporation of Cu atom strongly modifies the growth of the preferential orientation (311) plane. At a higher doping level of 6 at %, the crystallinity is increased due to the super-saturation of Cu atoms into the Co_3O_4 matrix. The peaks become sharper at a higher Cu concentration, indicating larger grain size favorable for accumulation of large number of charges over the surface. The preferred orientation peak (311) was observed at 36.81. No other peaks associated with impurity phase were found with the increase of Cu concentrations which indicates that the phases are stable and Cu ions are uniformly incorporated within the Co_3O_4 lattice. The average crystallite size of Co_3O_4 thin film was estimated by using the classical Scherer's formula; $D = 0.89\lambda/\beta Cos\theta$ to the major peaks of diffraction spectrum where D is the crystallite size, β is full width at half maxima intensity of (311) plane, k = 0.89 is the spherical shape factor, λ is wavelength of X-ray used and θ is diffraction angle.
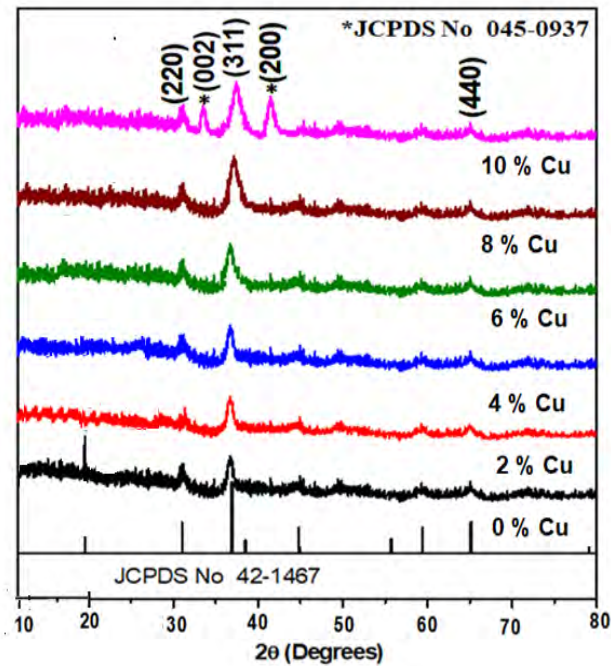
Fig. 4.13 XRD patterns of 0-10 at% Cu:Co_3O_4 respectively.

Table 4.4 Structural parameters of Cu: Co_3O_4 thin films

Cu concentration (at %)	Average Grain size (nm) by image j software	Average crystallite size D (nm)	Lattice constant a=b=c (Å)	Dislocation density $\delta = 1/D^2 \times 10^{15}$ (line/m²)	Texture coefficient TC_{hkl}
0	33	29	8.076	1.189	0.953
2	30	27	8.084	1.372	0.999
4	25	24	8.089	1.736	1.009
6	29	26	8.085	1.479	1.036
8	32	31	8.078	1.041	1.107
10	36	36	8.073	0.772	1.184

The XRD results were quantified by defining the texture coefficient TC_{hkl}. The value of the texture coefficient indicates a sample with randomly oriented crystallite.

This factor was calculated for preferential growth orientation using the following equation

$$TC_{hkl} = \frac{I_m(hkl)/I_s(hkl)}{n^{-1}\sum_n I_{m(hkl)}/I_{s(hkl)}};$$ where TC (hkl) is the texture coefficient, I_m (hkl) is the XRD

intensity measured from a plane (hkl) of the films, Is(hkl) is typical intensity taken from the JCPDS data, and n is total peak numbers. All the structural parameters are shown in Table 4.4. Dislocation densities exhibit variation with increasing doping concentrations. From table (1) we notice that when D decrease at 2 and 4 at % of Cu doping concentration, the dislocation increase and suggests that doping has induced defects in the system that leads to decrease the crystallinity due to the formation of stress, a contraction of lattice because of substitution of the cobalt by copper. But at 6 at% Cu D increase and the dislocation decreases because of improving of crystallinity. Thus, in the present investigation, the variations of texture coefficient with Cu doping concentration showed randomly oriented crystallites for 4 at% Cu presenting TC_{hkl} = 1.009 (~ 1) [212].

4.1.2.5 Optical properties

The optical parameters are the key factor in determining the quality of the prepared thin films and their suitability for the bio sensing applications. The optical absorbance of Co_3O_4 films is influenced by several factors e.g. surface roughness, porosity, photogenerated electron-hole carriers. **Fig.** 4.14 displays the optical transmission spectra of Cu-doped Co_3O_4 thin films. In the vis-region, two sharp absorption edges were observed to lead the charge transfer event of ($O^{2-} \rightarrow Co^{2+}$) and ($O^{2-} \rightarrow Co^{3+}$) in Co_3O_4 [213]. In the IR region, high transmittance was obtained from 60% - 75% highlighted in **Fig.** 4.14 which may for structural homogeneity. In the IR region (800 nm - 1100nm), we observe only a linear reflection line without other interference fringes, which indicates that the prepared films are smooth and uniform. In the present work the band gap energy has been calculated using Tauc relation: $\alpha = A/ h\nu (h\nu - E_g)^{1/2}$; where A is a constant, $h\nu$ is the photon energy and E_g is the optical band gap [214-215].

Fig. 4.14 Transmittance spectra of 0, 2, 4, 6,8,and 10 at % Cu:Co_3O_4.

In the UV region from 340 to 460 nm, Cu doped Co_3O_4 at different doping levels show slight variation in the band gap (E_g) compared to pure Co_3O_4. The maximum band gap for 4 at% Cu may be associated to the $O^{2-} \rightarrow Co^{2+}$ charge transfer (valence to conduction band excitation) and the minimum band gap for 6 at% Cu associated to the $O^{2-} \rightarrow Co^{3+}$ charge transfer (with the Co^{3+} level located below the conduction band). According to E_g analysis it is observed that band gaps increase with increasing Cu concentration up to 4

at% indicated a blue shift [216-217].The rise in optical band gap is attributed to the shift of conduction band towards higher energy and systematic increase in valence band to conduction band that leads to increase in Fermi level. At 6 at% Cu doping the band gap values decrease which may due to the creation of new recombination centers below the conduction band with lower emission energy out of more Cu ions in the Co_3O_4 matrix. The analyzed optical band gap values for pure Co_3O_4 and 2, 4, 6, 8 and 10 at% Cu doped Co_3O_4 thin films are given in Table 4.5.

Table 4.5 Optical band gap of 0, 2, 4, 6,8 and 10 at% Cu doped Co_3O_4 thin films

Cu concentrations (at %)	Thickness (nm)	Band gap E_g (eV)
0	257	2.02
2	272	2.11
4	291	2.18
6	306	2.09
8	317	2.03
10	326	1.97

4.1.2.6 Electrical properties

The variation of electrical resistivity with temperature ranging from 300-440 K for Co_3O_4 and 2, 4,6,8 and 10 at % Cu doped Co_3O_4 thin films are shown in **Fig** 4.15. It is noticed that the resistivity decreases with the rise in temperature. This type of variation indicates the semiconducting behavior of the films. The decrease in resistivity may be attributed to the increase of the acceptor states associated with the integration of Cu impurities into Co sites of the Co_3O_4 lattice. Cu is a popular acceptor dopant with good electrical conductivity which increases the hole concentration in the valence band at room temperatures [218]. In presence of Cu doping the inter-grain boundary area reduces and there is a decreasing tendency in the electron scattering. This results in the reduction of resistivity. Table 4.6 records the electrical properties of the Cu: Co_3O_4 thin films deposited at 0, 2, 4, 6, 8, and 10 at% Cu concentration. Therefore, based on the carrier concentration

values listed in Table 4.6, it can be concluded that, with increasing the Cu concentration, the number of Cu vacancies increases, resulting a higher hole carrier concentration. However, it can be seen an increase in the mobility and reduction in the carrier concentration might be due to the lower rate of Cu which can lead to a better crystallinity and reduce the number of defects in the lattice of the deposited film.
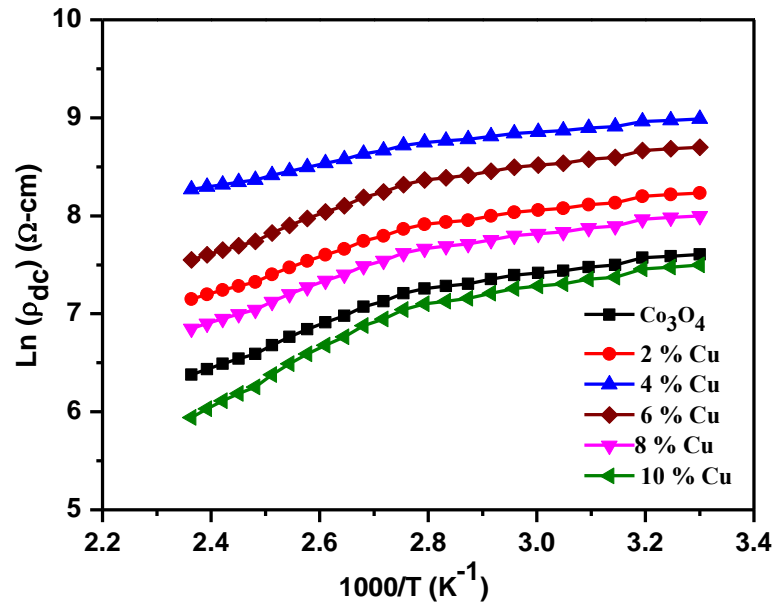
Fig. 4.15 Plot of resistivity vs temperature of 0, 2, 4, 6, 8,and 10 at % Cu:Co$_3$O$_4$..

Table 4.6 Electrical parameters of Cu: Co$_3$O$_4$ thin films

Cu concentration (at %)	Resistivity, ρ ($\times 10^4$ Ω-cm)	Carrier concentration, n_c ($\times 10^{17}$ cm^{-3})	Hall mobility, μ (cm^2 V^{-1} s^{-1})
0	0.23	2.39	1.81
2	0.27	2.67	2.15
4	0.45	3.13	1.97
6	0.39	3.82	2.39
8	0.25	4.18	2.83
10	0.17	4.39	3.26

4.2.3 Comparative study

It is observed that Fe doped Co_3O_4 thin films possess some differences in the characterizations in comparison with those of Cu doped Co_3O_4 thin films. The comparative properties among Fe and Cu doped Co_3O_4 thin films are highlighted in Table 4.7.

Table 4.7 Comparison among the characteristics of Fe and Cu doped Co_3O_4 thin films

Characterization techniques	Fe:Co_3O_4 thin films	Cu: Co_3O_4 thin films
Film images analysis	Film colour, homogeneity and density are influenced by Fe dopant	Film homogeneity and density are greatly influenced by Cu dopant but colour does not so affected due to Cu.
SEM analysis	Surfaces are comprised of spherical nanoparticles and agglomeration of the particles are influenced by Fe dopant	Surfaces are comprised of spherical nanoparticles and agglomeration of the particles increased with increase of Cu dopant
EDX analysis	Films are stoichiometric and Co ions decrease with increase of Fe content	Films are stoichiometric and Co ions decrease with increase of Cu content
XRD analysis	Spinel cubic cobalt oxide crystal structure was obtained .Additional peak for iron oxide observed for 8 ant 10 at% Fe dopants	Spinel cubic cobalt oxide crystal structure was obtained. Additional peak for Cu was observed at 10 at % Cu doping
UV-vis-NIR spectroscopy	Optical band gap decrease up to 4 at% Fe doping then increase	Optical band gap increase up to 4 at% Cu doping then decrease
Electrical measurements	Resistivity decrease up to 4 at% doping Fe then increase. Minimum resistivity was observed for 4 at% Fe.	Resistivity increase up to 4 at% Cu doping then decrease. Maximum resistivity was observed for 4 at% Cu.
Hall effect measurements	Carrier concentration increase with increasing Fe content up to 4 at % Fe	Carrier concentration gradually increase with increasing Cu content

PATR   B
RESULTS OF Fe AND Cu DOPED MnO₂ THIN FILMS

Part B
Results of Fe and Cu Doped MnO$_2$ Thin Films

4.2 Results on the Characterization of Fe and Cu Doped MnO$_2$ Thin Films

4.2.1 Results for Fe doped MnO$_2$ thin films

4. 2.1.1. Photograph of deposited Fe doped MnO$_2$ thin films

Photograph of composited MnO$_2$ thin film shows uniform deposition and surface consistency of the film slightly changed for Fe doping. **Fig.** 4.16 shows photograph of deposited pure and Cu doped Co$_3$O$_4$ thin films varying with Cu concentration from 0-10 at %.
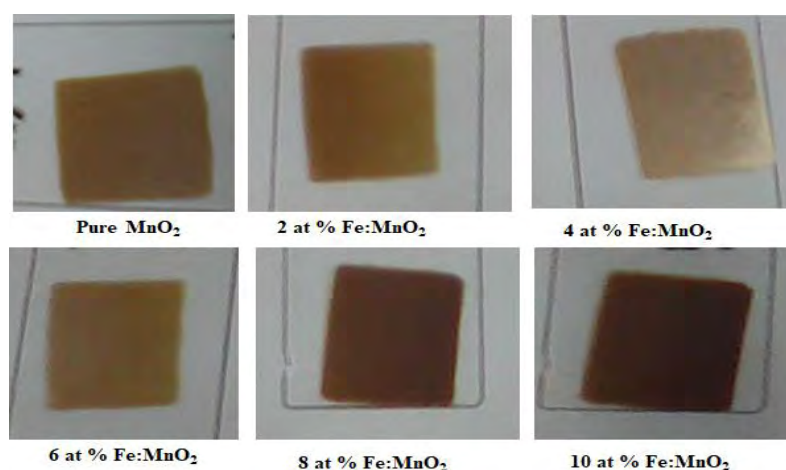
Fig. 4.16 Photograph of deposited pure and Fe doped MnO$_2$ thin films.

All the films are densed and homogeneous. The colour of the films are light brown. There is variation of colour among the films with Fe content. The differences in film homogeneity and compactness are also observed for pure and Fe doped MnO$_2$ films. This variations confirm the effect of Fe dopant concentration on MnO$_2$ properties. The thickness of pure and Fe doped MnO$_2$ films were measured by the fizeau fringes method. Thickness of the films varied with ± 10 nm. The measured thicknesses were 281, 293, 305, 315, 322, 331 nm for 0, 2, 4, 6, 8 and 10 at % Fe:MnO$_2$ thin films respectively.

4.2.1.2 Surface morphology analysis

The surface morphologies of pure and Fe-doped MnO_2 (Fe:MnO_2) thin films with different molar ratios have been investigated by FESEM. The important factors in the formation of surface morphology is nucleation and growth processes. The morphology of MnO_2 is altered with the change of the nucleation and growth stages of MnO_2.The effect of Fe on the morphology of MnO_2 thin films are supplementary in **Fig.** 4.17 (a–e).
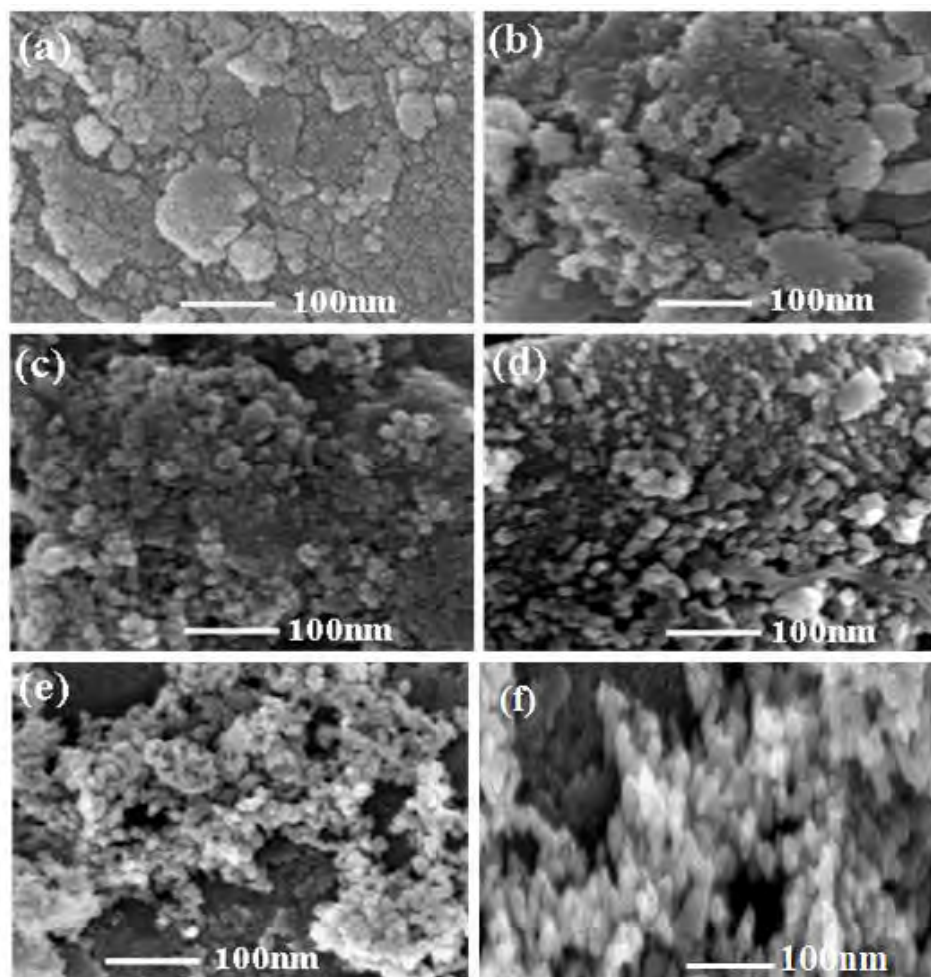
Fig. 4. 17 (a-f) FESEM images of 0-10 at% Fe:MnO_2 respectively.

Fig. 4.17 (a) demonstrates the surface morphology of the pure MnO_2 thin films made up of granular and zero-dimensional (0D) agglomerated nanoparticles [219]. The approximate size of this grain is about 15–30 nm. **Fig.** 4.17 (b) shows more compact agglomerated with 2 at % Fe nanoparticles. Some cracks are also found on the surface. **Fig.** 4.17 (c) indicates the highly porous surface. As the amount of Fe^{3+} continuously increased, the size and density of the nanoparticles severely degrade [220-221]. The

smaller particle size of the doped sample may associated with the iron oxide on the surface of the MnO_2 nanoparticles which prevents MnO_2 particle to be expanded further. The nucleation is responsible for nanoparticles formation during spraying system. At the time of primary stage of nucleation, some small and unstable particles with higher surface energies are produced. Subsequently, these small particles concentrate to the relatively larger particles to decrease the energy of the entire system. As the reaction progresses, the reactants in the reaction system are collapsing and their action transforms into a thermodynamically stable state. **Fig.** 4.17 (d) shows randomly oriented 0D and 3D mixed nanoparticles for 6 at% Fe. When the doping concentration is increased to 8at%, the morphology changes from crystalline to flower like shape outstanding at irregular agglomerated particles formation supplementary in **Fig.** 4.17(e). Similar phenomenon were reported by Dubal, D. P. et al. and Martinez et al [222-223]. Thus, the results showed that up to 4 at% Fe addition modifies the surface of the MnO_2 nanocrystalline thin films. This type of more compact and highly porous nanocrystalline structure is expected to be suitable for the developments of optoelectronics devices.

4.2.1.3 Compositional analysis

EDX analysis confirmed the elements of the compositions of pure MnO_2 and Fe doped MnO_2 thin films. EDX data have been collected at various points on the scan area. EDX data support the uniformity of the synthetic distribution of the prepared thin films. Amount of Mn reduces with the increment of Fe concentration in Fe doped MnO_2 thin films.
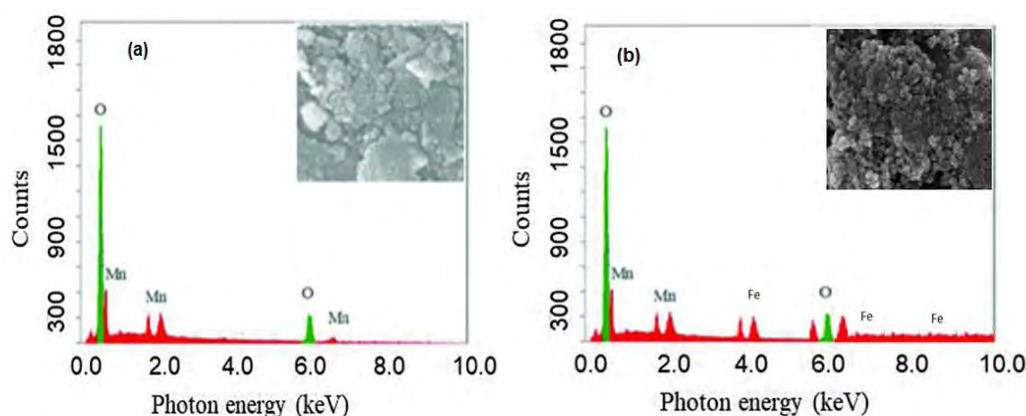
Fig. 4.18   EDX spectra of (a) Pure MnO_2 and (b) 4 at % Fe doped MnO_2 thin films.

The EDX data supported the logical substitution of Mn caused by Fe doping shown in **Fig.** 4.18 and shows the homogeneity of Fe:MnO$_2$ thin films. Amount of O increase with increasing Fe concentration. Water molecules and hydroxyl groups combined with Mn atoms resulted in a higher content of O.

4.2.1.4 Structural properties

The XRD spectra of pure MnO$_2$ and Fe: MnO$_2$ thin films are displayed in **Fig.** 4.19 The unit cell of the crystal system was found to be the tetragonal structure of α-phase with the presence of dominant peaks at (200), (310), (101), (211) and (521) planes. The XRD peaks were indexed and matched with the JCPDS card file no. 44-0141 of the tetragonal phase of α-MnO$_2$ [224-225]. No additional peaks are identified for iron oxide impurities in the MnO$_2$.
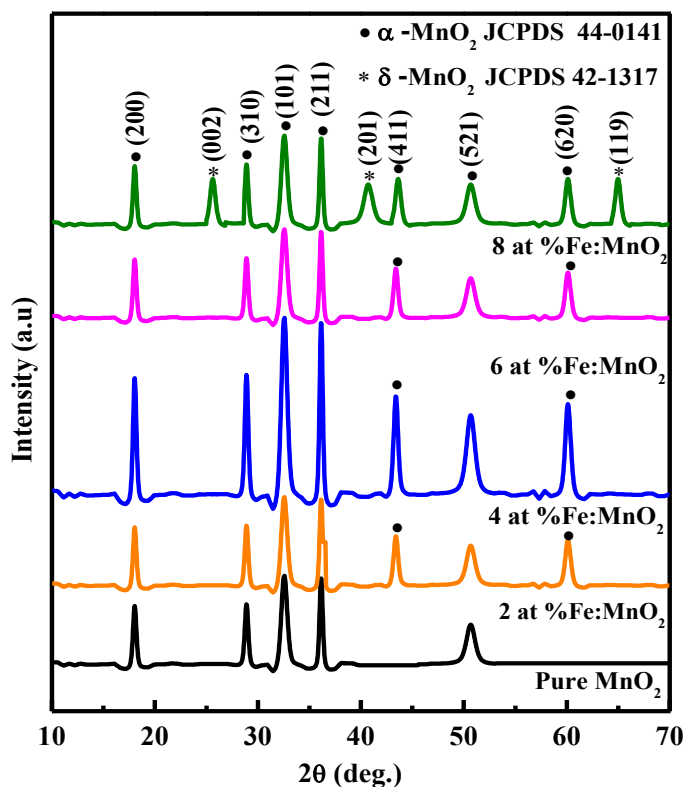
Fig. 4.19 XRD patterns of MnO$_2$ and 2, 4, 6 and 8at % Fe doped MnO$_2$

In comparing with the XRD pattern of α-MnO$_2$, the diffraction peaks slight shift to higher angles with the increase of Fe concentration suggesting a decrease in the lattice constant c.This result indicates that Fe doped α-MnO$_2$ slightly reduced the interlayer distances of the crystalline planes in the doped α-MnO$_2$. After incorporation of Fe^{3+} into MnO$_2$, the

peak intensity of α-MnO$_2$ becomes weak and the phase of δ-MnO$_2$ appears with prominent (002), (201), and (119) planes. The XRD data suggests that Fe: MnO$_2$ has a lower crystallization due to the disorders or defects of lattices resulting from the excessive Fe dopants. The reason is that Fe oxide has an amorphous nature and can influence the crystalline nature of α-MnO$_2$. With 2 at% Fe-doped MnO$_2$ thin films, the intensity of peaks is reduced and FWHM is increased in compared to undoped MnO$_2$ thin films revealing that the crystalline quality is weakened by introducing doping. However, The peak intensity is enhanced with decrease of FWHM at the rise of 4 at% Fe doping concentration. This suggests the crystalline quality of the MnO$_2$ thin film greatly improved by 4 at% Fe-doping. The crystalline quality is weakened again demonstrated by the reduction of peak intensity and rise in FWHM compared to lower doped ones at 6at% Fe doping concentration because the formation of new nucleation centers from the dopant atoms is favorable for the growth of MnO$_2$ crystals. However, the crystalline quality is degraded again when the Fe-doping concentration is 8at%. This may occur as the newer nucleation centers reach in saturation and due to the difference of ionic radius between Fe^{2+} (70 pm) or Fe^{3+} (60 pm) and Mn^{2+} (70 pm) and large number of Fe^{2+} or Fe^{3+} replace Mn^{2+} in lattice sites. A strain in MnO$_2$ lattice generated by incorporation of Fe^{2+} or Fe^{3+} with Mn^{2+} ions may lead to lattice distortion. When Fe ions exist in MnO$_2$ mostly in the form of Fe^{2+}, due to its larger ionic radius than that of Mn^{2+}, will point to compression strain in the films for a while shifting of XRD patterns towards the smaller angle turn up. On the contrary, Fe ions prevail in MnO$_2$ mainly on the point of Fe^{3+} will lead to tensile strain in the films for less ionic radius than that of Mn^{2+}, producing the peak altering towards higher angle. In Fe: MnO$_2$ alloys, Fe ions require to have a valence of +2 in order to properly substitute Mn^{2+} ionic sites while maintaining charge neutrality. When Fe^{3+} ions coexist with Fe^{2+} ions in Fe: MnO$_2$, the Fe^{3+} ions are likely to distort the lattice structure for holding charge neutrality. It is observed that increasing doping caused a reduction of interlayer spacing (d).The ionic radius of Fe^{3+} is smaller than that of Mn^{2+}, suggesting that Fe^{3+} replaces Mn^{2+} in the lattice and in a smaller interplanar spacing (d) value and lattice constants than that of undoped MnO$_2$ thin film. The Bragg's law is shown as; nλ =2d_{hkl} sin θ_{hkl}, where n stands for diffraction order, k is the X-ray wavelength, θ_{hkl} is for Bragg angle and d_{hkl} is the spacing between planes of Miller indices {hkl}. The interplanar spacing d_{hkl} associated with Miller indices and lattice constants a, c by

alliance [226] $\frac{1}{d_{hkl}{}^2} = \frac{h^2 + k^2}{a^2} + \frac{l^2}{c^2}$; The average particle size of pure MnO_2 and Fe: MnO_2 thin films for (200), (101) and (211) planes were calculated using Debye Scherer's formula [227], $D = \frac{\kappa\lambda}{\beta Cos\theta}$; where D represents crystallite size, k is for shape factor (0.94Å) and β mean full width at half maximum (FWHM). The peak shifting from 2θ may perform by means of some defects present in the films. The dimension of dislocation per unit volume associated with the density of defects in the sample demonstrated by dislocation density (δ) is calculated by the formula [227], $\delta = \frac{1}{D^2}$; X-ray peaks were analyzed to calculate the lattice strain and particle size using the simplest Williamson–Hall (W–H) method which clearly differ between crystallite size and strain-induced peak broadening contemplated with the peak width as a function of $2\theta_{hkl}$. The local distortion of the lattice generates strain and contributes in peak broadening considering responsive in all crystallographic directions, is written as [228]:$\varepsilon = \frac{\beta_{hkl}}{4tan\theta_{hkl}}$; where ε is the strain in the crystal lattice. The XRD results were quantified by defining the texture coefficient TC_{hkl}. The value of the texture coefficient indicates a sample with randomly oriented crystallite. This factor was calculated for preferential growth orientation using the following equation [229-230]:

$$TC_{hkl} = \frac{I_m(hkl)/I_s(hkl)}{n^{-1}\sum_n I_{m(hkl)}/I_{s(hkl)}}$$

where TC (hkl) is texture coefficient, I_m (hkl) is the XRD intensity measured from a plane (hkl) of the films, Is(hkl) is typical intensity taken from the JCPDS data, and n is total peak numbers. Thus, in the present investigation, the variations of texture coefficient with Fe doping concentration calculated for the three main diffraction peaks along (200), (101) and (211) planes showed better randomly oriented crystallites for 4 at% Fe.

4.2.1.5 Optical properties

Fig. 4.20 shows the optical transmittance spectra of pure MnO_2 and 2, 4, 6 and 8 at % Fe doped MnO_2 thin films varying with a spectral range from 200 nm to 1100 nm. It is observed that the transmittance of the prepared films decreases gradually with increasing Fe content from 4 at% in the visible - near-infrared region (400 nm -800 nm). Maximum transmittance varied between 48-76%. The increase of transmittance with increasing 2 at % Fe concentration may refer to less defect due to small amount of Fe. The decrease in

transmittance may for creating defect sites due to F^{3+} incorporated into MnO_2. Band gap of MnO_2 is obtained 3.81 eV and slightly increase (3.83eV) at 2 at % Fe doping compare to pure which may due to variation of ionic radius of Mn^{2+} and F^{3+}. At 4, 6 and 8 at % Fe band gap gradually decrease due to the effects of excess charge carrier for the sake of Fe doping that is attributed to the improvement in a stoichiometry of the films. These results satisfy with the earlier results by Michel C., et al. and Serin T.,et al. [231-232].

Fig. 4.20 Transmittance spectra of Fe:MnO_2 thin films.

4.2.1.6 Electrical and Hall effect measurements

Electrical properties were carried out on Fe: MnO_2 at room temperature. Table 4.8 shows all the electrical and Hall parameters. The electrical resistivity decrease at 2 and 4 at % Fe doping and increase at 6 and 8 at % Fe doping concentrations. Hall Effect measurements were carried out on Fe: MnO_2 at room temperature. Hall voltage (VH) developed from Fe: MnO_2 thin films over the entire composition range revealed that holes are majority current carriers in these films, irrespective of the composition of the films. Accordingly, the doping of Fe in MnO_2 always yields n-type donor carrier. The positive carriers contributing to the electrical conduction in Fe: MnO_2 films come apparently from the Mn vacancies as Mn may escape in the process of crystallization due to an increase in internal energy. The Hall mobility (μ) decrease with Fe concentration up to 4 at % which may agree with the shortening of the effective mean free path of conduction carriers by scattering from the surface of the film when Fe is doped into MnO_2. It is found that an increase of carrier concentration with an increase of Fe concentration is probably due to the creation of more acceptor levels within Mn ions as the Fe ions want to be half-filled

releasing an electron from its outer shell [233]. The Hall mobility increases with Fe doping concentration as well as thickness due to the lower effective mean free path of conduction carriers that occurred by scattering from the surface of the film. The increase of Hall mobility indicates that shallow acceptor levels exist in Fe: MnO_2 films due to stoichiometric defects. Also the increase of carrier concentration with increase of Fe doping and thickness for all compositions are attributed to lower defect density and less grain boundary scattering. The increase of carrier concentration with increase of Fe concentration is probably due to creation of more acceptor levels with addition of Fe indicated p-type carrier. The type of the semiconducting nature of the thin films was determined using the hot probe technique. The arrangement consists of a hot probe with which the film is touched and the direction of current implies whether the film is p-type or n-type as verified using a standard known sample. All the deposited films were tested by this technique and p-type conductivity is invariably observed for all the films.

Table 4.8 Electrical and Hall parameters of Fe:MnO_2

Fe concentration (at %)	Resistivity, ρ ($\times 10^4$ Ω-cm)	Carrier concentration, n_c ($\times 10^{12}$ cm^{-3})	Hall mobility, μ (cm^2 V^{-1} s^{-1})
0	3.56	4.24	2.88
2	2.17	8.62	2.32
4	1.95	11.89	1.87
6	3.88	5.62	1.99
8	4.49	4.17	2.17
10	5.13	3.89	2.68

4.2.2 Results for Cu doped MnO₂ thin films

4.2.2.1 Photograph of deposited Cu doped MnO₂ thin films

Photograph of composited MnO_2 thin film shows uniform deposition and surface consistency of the film slightly changed for Fe doping. **Fig.** 4.21 shows photograph of deposited pure and Cu doped MnO_2 thin films varying with Cu concentration from 0-10 at %.
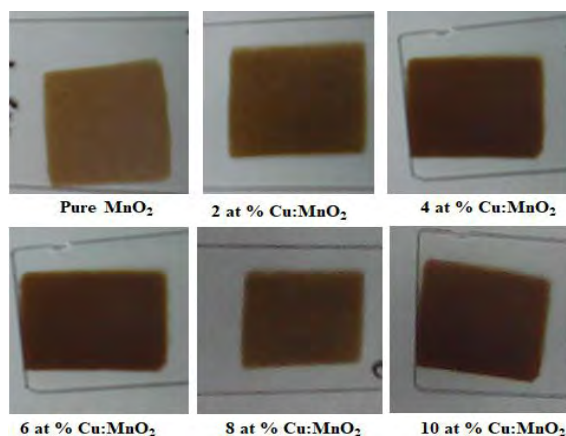
Fig. 4.21 Photograph of deposited pure and Cu doped MnO$_2$ thin films.

All the films are densed and homogeneous. The colour of the films are dark brown. There is no so variation of colour among the film. But the difference in film homogeneity and compactness are observed for pure and Cu doped MnO$_2$ films. This variations confirm the effect of Cu dopant concentration on MnO$_2$ properties. The thickness of pure and Cu doped MnO$_2$ varied with ±10 nm. The measured thicknesses were 281, 298, 303, 317, 324, 329 nm for 0, 2, 4, 6, 8 and 10 at % Cu:MnO$_2$ thin films respectively.

4.2.2.2 Surface morphology

The surface morphology of undoped and 2, 4, 6, 8, and 10 at% Cu-doped MnO$_2$ thin films are studied by taking FESEM images under 50,000 magnification. 100 nm scale bar length revealed in **Fig. 4.22** (a–d). **Fig.** 1 (a) reveals a granular surface of porous structures and order less distribution of grains with round shapes. Cu doped MnO$_2$ films display a different morphology compared with MnO$_2$. The incorporation of Cu ions (either + 2 or + 1) into the lattice of MnO$_2$ films greatly affects the morphological feature and porous nature. For 2 at% Cu doped MnO$_2$ film, the grains seem to be agglomerated and the surface is covered with dense and homogeneously distributed grains supplementary in **Fig.** 4.22 (b). In **Fig.** (c) and **Fig.** (d), as the Cu concentration is increased to 4 and 6 at%, the interior of the micro spherical MnO$_2$ films is collapsed and the grains are broken. The reason is that the presence of Cu^{2+} may have a tremendous effect on MnO$_2$ nanospheres, pointing to the formation of spherical structure. Hence Cu behaves as an interstitial dopant with high solubility in MnO$_2$. When Cu solubility limit is reached, nucleation occurs into the surface of MnO$_2$ Nanocrystals and yields phase shifts followed by the reduction of Cu^{1+} to Cu^{0+}. Cu impurities exhibited a high solubility limit in MnO$_2$ up to 4 at% nearly

saturating the nanocrystals. Additionally, the solubility limit is considerable affection for the possible side effects in nanocrystals. The size of MnO_2 is decreased for the increase of the Cu/Mn ratio. A low Cu/Mn ratio indicates that few Cu impurities are present in each MnO_2 nanocrystals [234-235].

4.2.2.3 Compositional analysis

EDX analysis confirmed the elements of the compositions of pure MnO_2 and Cu doped MnO2 thin films shown in **Fig.** 4.23 (a-b). The EDX reports were collected at various points on the scan area. EDX data support the uniformity of the synthetic distribution of the prepared thin films. Amount of Mn reduces with the increment of Cu concentration in Cu doped MnO_2 thin films. The EDX data supported the logical substitution of Mn caused by Cu doping.
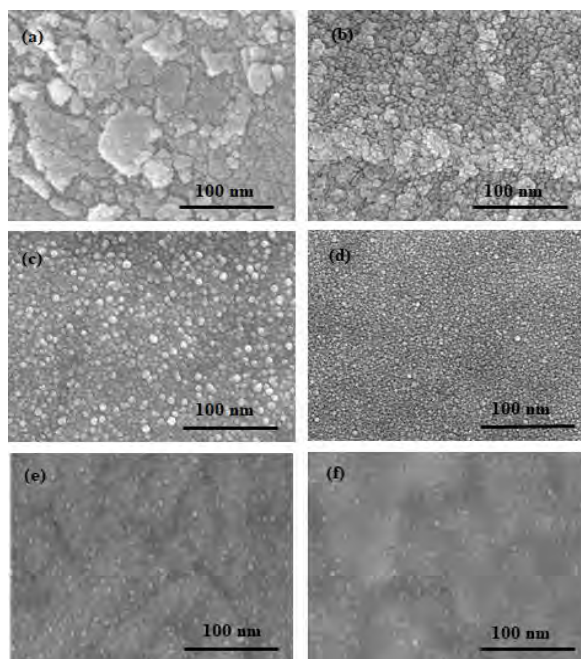
Fig. 4.22 (a-f) FESEM images of (0- 10 at%) Cu :MnO_2 respectively.
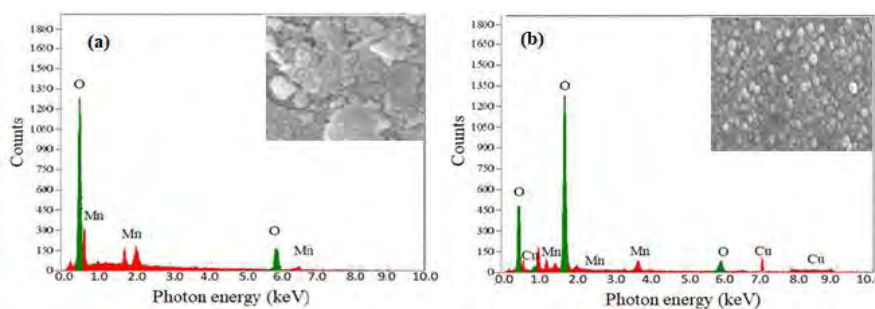
Fig. 4. 23 (a-b) EDX of MnO_2 and 4 at% Cu:MnO_2 thin films respectively.

4.2.2.4 Structural characterization

Fig. 4.25 (a-f) depicts the X-ray diffraction (XRD) patterns of undoped MnO_2 and 2, 4, 6,8 and 10 at % Cu doped MnO_2 thin films respectively. The incorporation of Cu into the MnO_2 lattice show a crucial aspect in the structure of the films. The diffraction peaks of pure and Cu doped MnO_2 corresponds to α-phase having tetragonal crystal structure up to 4 at % Cu doping. Some additional peaks are observed for the 6 at % Cu doped MnO_2 thin film, which may due to the partial reduction of Mn^{4+} and Cu^{2+} from surface sites in view of forming Mn^{3+} and Cu^+. All the patterns are polycrystalline with preferential orientation along (311), (211) and (301) plane at $2\theta = 32.5°$, $35.9°$ and $43.5°$, respectively (JCPDS no.44-0141). The additional peaks are due to δ-MnO_2 phase along (001), (111) and (213) plane at $2\theta° = 12.4°$, $40°$ and $74.6°$ (JCPDS no. 44-0142). Crystallite size reduces from 27 to 13 nm with the increase of Cu concentration from 2 to 10 at% in MnO_2 thin films. Micro strain and dislocation density rise with the increase of Cu concentration in MnO_2 films. It may be because of phase transformation and increase of defect states in the lattice MnO_2 caused by the increase of Cu doping. Crystallite size is an important parameter of a material to be useful in gas and bio sensing application. Smaller crystallite size shows better gas sensitivity [236]. It can be said that the doping of Cu into MnO_2 may improve the gas and bio sensing properties of MnO_2.

4.2.2.5 Optical properties

In order to study the effect of Cu concentrations onto MnO_2 over the optical properties, the transmission and reflectance spectra and band gap have been studied. **Fig.** 4.25 (a) shows the optical transmittance spectra of pure MnO_2 and 2, 4, 6,8, and 10 at % Cu doped MnO_2 thin films varying with spectral range from 200 nm to 1100 nm. It is observed that the transmittance of the prepared films increase gradually with increasing Cu content in the visible - near infrared region (400-800 nm) and the maximum transmittance is observed about 83% in 4 at% Cu doped MnO_2 thin film. The increase of transmittance with increasing Cu concentration may refer to the effects of excess charge carrier for the shake of Cu doping that is attributed to the improvement in stoichiometry of the films. Transmittance decreases at 6 at% Cu doping in the IR region (800-1100 nm) which may be due to the transformation of the crystalline phase of MnO_2 as revealed by XRD pattern shown in **Fig.** 4.24 . It can be noticed that the low percentage of transmittance is found

about 4–22% in the wavelength range 200–300 nm which may for absorption of light of the excitation electrons from valence band (VB) to conduction band (CB).
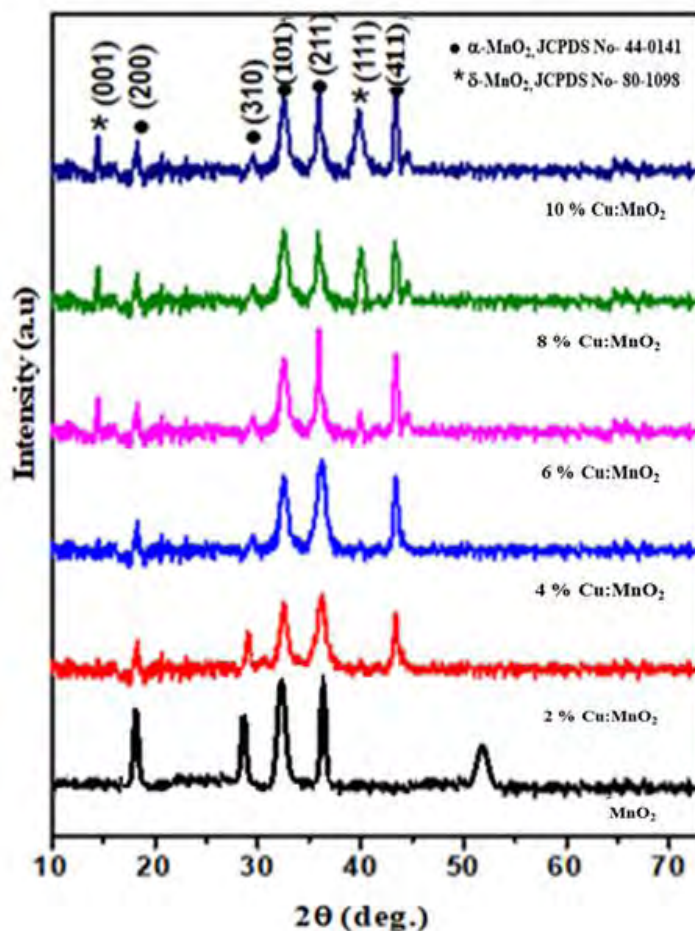
Fig. 4.24 XRD pattern of 0-10 at% Cu: MnO_2 respectively.

It is also observed that thin films exhibited a blue shift into the absorption onset at 400 nm. This absorption is associated to $O^{2-} \rightarrow Mn^{4+}$ charge transfer, related to electron agitation from the valence band to the conduction band. The blue shift in the absorption spectrum is mainly attributed to the confinement of charge carriers in the porous surface of the MnO_2 film. Band gaps were calculated by Tauc relation, $(\alpha h v)^2$ vs. photon energy (hv) for determination of optical band gap (Eg) related to the allowed direct transition of pure and 2, 4, 6, 8 and 10 at% Cu:MnO_2 thin films. The Eg of the films varies between 3.82 to 3.96 eV employing a gradual increment of Cu from 0 to 4 at%, which indicated that incorporation of a little amount of Cu affects the optical band transition and this may for the blue shift. A decrease in Eg with the increase of 6 at% Cu concentration is observed which is associated with the change in crystal structure from α to δ phase of MnO_2. Similar

variations of the Eg value of MnO_2 have been reported by some other workers [233, 237]. The reduction of Eg in higher Cu concentration may due to redshift which interpreted in terms of the sp-d exchange interaction among the band electrons and localized d electrons of the Mn^{4+} ions and Cu^+ ions give rise to a negative and a positive correction to conduction and valence band edges is obtained by s-p and p-d exchange interactions governing to the increase of Eg. [238].

Fig. 4.25 Transmittance spectra of 0, 2, 4, 6,8 and 10 at % $Cu:MnO_2$.

4.2.2. 6 Electrical resistivity and Hall effect measurements

The variation of electrical resistivity with temperature ranging from 300-440 K for MnO_2 and 2, 4,6,8 and 10 at % Cu doped MnO_2 thin films are show decreasing trend with the rise in temperature. This type of variation indicates the semiconducting behavior of the films. The resistivity devaluate with expand of Cu concentrations. oxygen adaption and desertion may occur into a polycrystalline oxide semiconductor at all temperatures when heat is treated in air. Oxygen decomposition process into the deposited films crop up the decrease in electrical resistivity. Hall mobility and carrier concentration increases with the rise of Cu concentrations in Cu doped MnO_2 thin films. The increase of carrier concentration with some contribution from the increase of mobility lead to relatively low resistivity.

4. 2.3 Comparative study

It is observed that Fe doped MnO_2 thin films possess some differences in the characterizations in comparison with those of Cu doped MnO_2 thin films. The comparative properties among Fe and Cu doped MnO_2 thin films are highlighted in Table 4.9.

Table .4.9: Comparison among the characteristics of Fe and Cu doped MnO_2 thin films

Characterization techniques	Fe: MnO_2 thin films	Cu: MnO_2 thin films
Film images analysis	Film colour, homogeneity and density are greatly influenced by Fe dopant	Film homogeneity and density are greatly influenced by Cu dopant but colour does not so affected due to Cu.
SEM analysis	Surfaces are comprised of spherical nanoparticles and agglomeration of the particles are influenced by Fe dopant	Surfaces are comprised of spherical nanoparticles and agglomeration of the particles increased with increase of Cu dopant
EDX analysis	Films are stoichiometric and Co ions decrease with increase of Fe content	Films are stoichiometric and Co ions decrease with increase of Cu content
XRD analysis	Tetragonal alpha MnO_2 oxide crystal structure was obtained and Fe does not change the structure of MnO_2 Additional peak for iron oxide observed for 8 ant 10 at% Fe dopants	Tetragonal alpha MnO_2 crystal structure was obtained and Cu does not change the structure of MnO_2 Additional peak observed from 6 at% Cu dopants
UV-vis-NIR spectroscopy	Optical band gap decrease from 4 at % Fe doping concentration	Optical band gap increase with increase up to 4 at % Cu doping concentration
Electrical measurements	Resistivity decrease with increasing Fe up to 4 at %	Resistivity increase with Cu up to 4 at% .
Hall effect measurements	Carrier con centration increase with increasing Fe content up to 4 at %	Carrier con centration increase with increasing Cu content up to 4 at %

PATR   C
RESULTS OF Fe AND Cu DOPED WO₃ THIN FILMS

Part C
Results of Fe and Cu Doped WO₃ Thin Films

4.3 Results on the Characterization of Fe and Cu Doped WO₃ Thin Films

4.3.1 Results for Fe doped WO₃ thin films

4.3.1.1. Photograph of deposited Fe doped WO₃ thin films

Photograph of composited WO_3 thin film shows uniform deposition and surface consistency of the film slightly changed for Fe doping. **Fig.** 4.26 (a-f) shows photograph of deposited pure and 2, 4, 6,8,10 at% Fe doped WO_3 thin films respectively. All the films are densed and homogeneous.
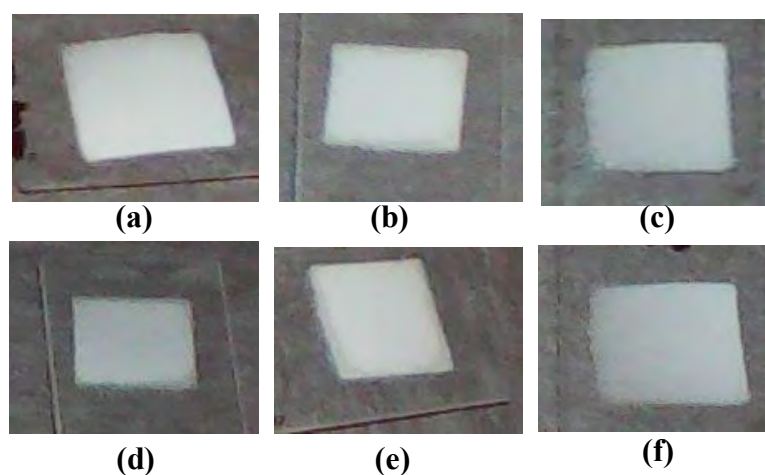
Fig 4.26 (a-f) Photograph of (0-10 at %) Fe doped WO_3 thin films respectively.

The colour of the films are white. There is variation of colour among the films with Fe content. The differences in film homogeneity and compactness are also observed for pure and Fe doped WO_3 films. This variations confirm the effect of Fe dopant concentration on WO_3properties. The thickness of pure and Fe doped MnO_2 films varied with ±10 nm.

4.3.1.2 Surface morphological analysis

The FESEM micrograph of undoped and 2, 4, 6, 8 and 10 at% Fe doped WO_3 thin films were 50,000 magnification shown in **Fig.** 4.27(a-f) respectively. All the images show that the substrates are uniformly covered with spherical nanoparticles. The regular distribution of grains is attributed all over the surface The particle size decrease with Fe concentration up to 4 at % and the agglomeration of the particles decreased which may be attributed to

both the oxidation of surface-adsorbed water molecules and the structural transformation of WO_3 that accompanies the loss of water molecules as vapor [239]. At 6-10 at% Fe concentration the particle increase. The surface remain homogeneous and smooth up to 4 at % Fe. At 8 at % and 10 at % Fe doping some crakes are observed over the surface which may due to oxidation of Fe^{+3} ions on the surface. The reason for the formation of crakes may be due to the evaporation of solvent (H_2O) from the film [240]. It is seen from the FESEM image that 4 at% Fe doped WO_3 surface is more porous which may suitable for bio sensing applications.
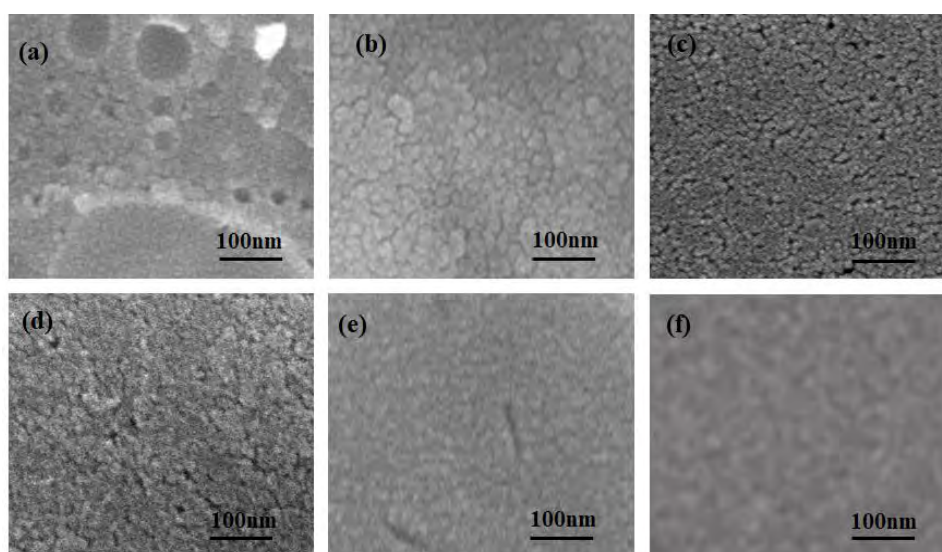
Fig. 4.27 (a-f) FESEM images of 0-10 at% Fe: WO_3 respectively.

4.3.1.3 Compositional analysis

EDX analysis confirmed the elements of the compositions of pure WO_3 and Fe doped WO_3 thin films. EDX data have been collected at various points on the scan area. EDX data support the uniformity of the synthetic distribution of the prepared thin films. Different peaks corresponding to W and O were found in the spectrum, which confirms the WO_3 thin film and peak for the composition of W, Fe and O indicate the Fe doped WO_3 thin films shown in **Fig.** 4.28. Amount of W reduces with the increment of Fe concentration in Fe doped WO_3 thin films. The EDX data supported the logical substitution of Mn caused by Fe doping.
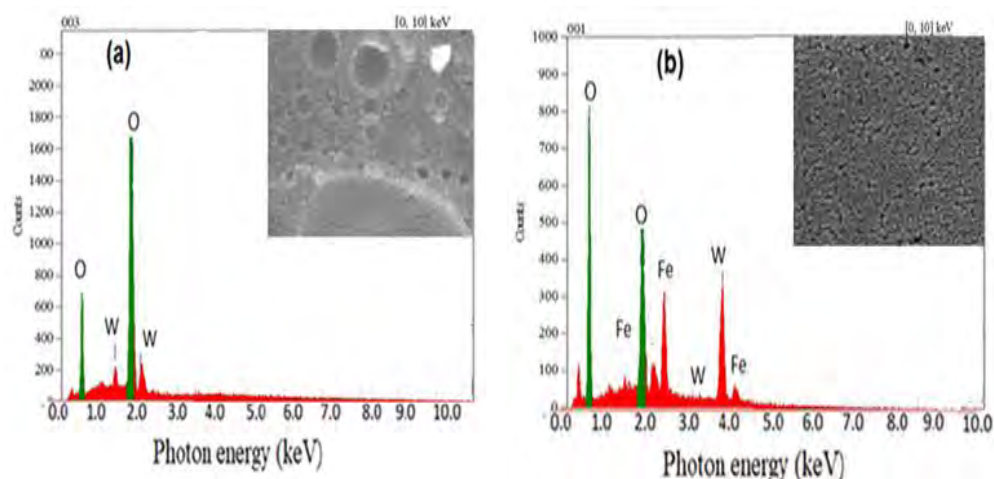
Fig. 4. 28 (a-b) EDX spectra of WO_3 and 4 at% Fe:WO_3 thin films respectively.

4.3.1.4 Structural properties

Fig. 4.29 shows the XRD pattern of Fe:WO_3 films at different Fe concentrations of 0, 2, 6,8 and 10 at%, respectively. The crystallographic structure of the prepared samples were characterized by XRD. The observed diffraction peaks are well matched with the monoclinic WO_3 crystal structure (JCPDS card No.043-1035 [241-242]. With Fe doping, no apparent peaks related to iron oxide or any other impurities has been found suggesting that the Fe ions are successfully incorporated in the crystal structure of WO_3. This may be attributed to the lower concentration of Fe ions and small difference between the ionic radii of host W^{6+} (0.62 Å) and dopant Fe3+ (0.64 Å) ions. Hence, Fe^{3+} ions may easily be substituted for W^{6+} ions in the host matrix and forming Fe-WO_3 finite solid solution. Moreover, the W^{6+} is octahedral coordinated with O^{2-}. In iron oxides, the crystal field stabilization energy of Fe^{3+} is higher for octahedral orientation than for tetrahedral orientation [243]. Therefore, Fe^{3+} can fulfil the same coordination as that of W^{6+}. Consequently, Fe-doped WO_3 film shows the same crystal structure as that of WO_3 film. Similar crystal structures were also observed by Han et al. [244]. The observed shift in peak positions of Fe-doped WO_3 film compared to WO_3 film, can be attributed to the small difference between the ionic radii of W^{6+} and Fe^{3+}. The ionic radius of Fe^{3+} is slightly greater than that of W^{6+} and this can cause slight distortion in the crystal lattice when WO_3 is doped with Fe, and consequently a shift in the diffraction peaks. Such distortions can also produce a number of defects in the film, making it a better candidate

for gas and bio sensing. Average crystallite size has been obtained 13nm with lattice constants a = 7.273 Å, b = 7.548 Å and c = 7.697 Å. Which match with JCPDS data. Crystallite sizes vary between 8-15nm with Fe doping concentration and minimum size is obtained at 4 at % Fe content.

Fig. 4.29 XRD pattern of Fe: WO_3 films.

4.3.1.5 Optical properties

The optical properties of the pure and Fe-doped tungsten oxide films were measured in the wavelength range 400-1100 nm. **Fig.** 4.30 shows the optical transmittance spectra of pure and Fe doped WO_3 the films. The absorption edge of undoped WO_3 and Fe-doped WO_3 films shifted to longer wavelengths indicating red shift. Maximum transmittance of

undoped WO_3 lies between 20% and 35%. This low transmissions may be the effects of non-specular light scattering caused by the highly crystalline, granular and porous WO3 thin films [245]. Fe-doped films showed lower transmittance compared to undoped films. The transmittance of films depends on the structural, morphological and compositional characteristics of the films. Sharp absorption edge of the films can be observed below 400 nm. It is hypothesized that Fe can be introduced in small quantities as a substitutional impurity due to a small difference of ionic radius and this can cause distortion in the WO_3 crystal structure. Such lattice mismatch combined with the properties of the film and the type of strain induced into the film can produce either blue or red shift in the optical absorption. Compressive strain can be expected in the films that would result a red shift in the optical absorption which would also influence the optical band gap energy of the films. The pure and Fe doped tungsten oxide films were found to be fairly transparent, having visible transmittance in excess of 95% for 4 at % Fe doping. it is well known that such transmission curves are associated with high concentrations of grain boundary defects that serve as electron-hole recombination sites [246]. Consequently, the concentration of surface defects (relative to the total volume), which provide surface-active sites remains nearly constant while the volume, which contains recombination sites at the grain boundaries, continues to increase as the film thickness increases.

Fig. 4.30 Optical transmittance spectra of pure and Fe :WO_3 the films.

The optical band gaps (Eg) of the various films were evaluated from the transmittance spectra by plotting $(\alpha h\nu)^2$ vs $h\nu$ that is appropriate for an direct band gap material and then using linear extrapolation to the energy axis ($(\alpha h\nu)^2 = 0$) [247]. There is a slight decrease in the optical band gap when Fe was incorporate into the tungsten oxide film. The red shift observed in the optical absorption caused a negative shift (reduction) in the band gap of the WO_3 film. The optical band gap of the Fe-doped tungsten oxide films obtained here are found to be within the ranges of optical band gap of the $Fe:WO_3$ films obtained by other earlier reported values [233]. The band gap energy for undoped WO_3 nanoparticles has been observed to be 2.72 eV which increased to 2.99 eV and 3.03 eV at 2 at % and 4 at% Fe doping and is decreased to 2.88eV, 2.79 eV and 2.74 eV with , 6 at%, 8 at% Fe and 10 at% Fe doping, respectively. This increase and decrease in the band energy of WO_3 nanoparticles can be understood the basis of hybridization between Fe 3d orbital and the O 2p orbital. As it is well known that in case of pristine WO_3, valance band is dominated by O 2p and conduction band is dominated by W 5d orbitals. But when Fe ions are introduced in the system, their 3d orbitals emerge around valance band and induce slight positive shift in it. Besides, Fe ions can also lead to downshift of conduction band. These corrections in the positions of valance and conduction bands lead to narrowing of the band gap which might help to harvest more visible light in it and generates more electron holes pairs.

4.3.1.6 Electrical properties

Temperature dependence of electrical resistivity of WO_3 thin films in the temperature range 300-440 K. The decrease in resistivity with temperature indicates the semiconductor behavior of the films. In fact, resistivity is the result of trade-off between two competing processes occurring simultaneously, namely, thermal excitation of electrons and adsorption of atmospheric oxygen on the film surface. The electronic transport of WO_3, in general, is believed to be controlled by the hopping conduction process, and the electrons are the major carriers via the oxygen vacancies [251]. The room temperature electrical resistivity of undoped WO_3 thin films has been found to be 3.46×10^4 Ω-cm which increases significantly up to 4 at % Fe doping then decrease. The effect of Fe concentrations on the electrical properties of nanostructured WO_3 thin films are summarized in Table 4.10.

Table 4.10 Effect of Fe concentration on electrical properties of WO$_3$ thin films

Fe concentration (at%)	Electrical resistivity, ρ ($\times 10^4$ Ω-cm)	n-type Carrier concentration, n_c ($\times 10^{11}$ cm^{-3})	Hall mobility, μ (cm^2 V^{-1} s^{-1})
0	3.46	7.63	9.72
2	4.59	7.95	7.89
4	5.16	8.35	7.43
6	4.87	8.76	8.19
8	4.31	9.46	8.97
10	3.83	10.59	8.46

4. 3. 2   Results of Cu Doped WO$_3$ thin films

4.3.2.2 Surface morphological analysis

The FESEM images of undoped and 2, 4, 6, 8 and 10 at% Cu doped WO$_3$ thin films were observed a 50,000 magnification shown in **Fig.** 4.31 (a-f) respectively. All the images show that the substrates are uniformly covered with spherical nanoparticles. The surface remain homogeneous and smooth up to 4 at % Cu. At 6- 10 at % Cu doping inhomogeneity and crakes are observed over the surface which may due to oxidation of Cu$^+$ ions on the surface [252]. It is seen from the FESEM image that 4 at% Cu doped Co$_3$O$_4$ surface is more porous which may suitable for bio sensing applications.

4.3.2.3 Compositional analysis

In **Fig.** 4.32 (a-b) EDX spectra of undoped and 4at% Cu doped WO$_3$ thin films are displayed respectively. EDX analysis confirmed the elements of the compositions of pure WO$_3$ and Cu doped WO$_3$ thin films. EDX data have been collected at various points on the scan area. EDX data support the uniformity of the synthetic distribution of the prepared thin films. Different peaks corresponding to W and O were found in the spectrum, which confirms the WO$_3$ thin film and peak for the composition of W, Cu and O indicate the Cu doped WO$_3$ thin films. Amount of W reduces with the increment of Cu concentration in Cu doped WO$_3$ thin films since the ionic size of Cu$_{2b}$ is somewhat higher than that of W$_{6b}$, there may arise some difficulty in incorporating Cu$_{2b}$ ions in W$_{6b}$ sites.
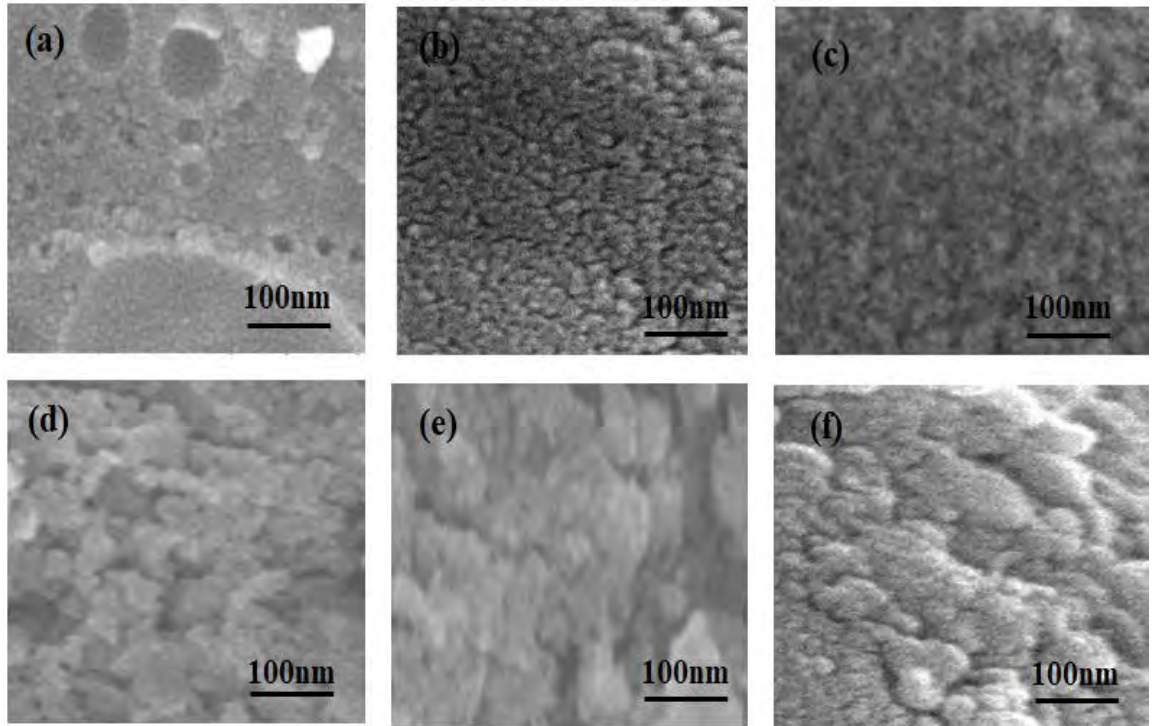
Fig. 4.31 (a-f) FESEM images of 0, 2,4,6,8 and 10 at% Cu: WO_3 respectively.
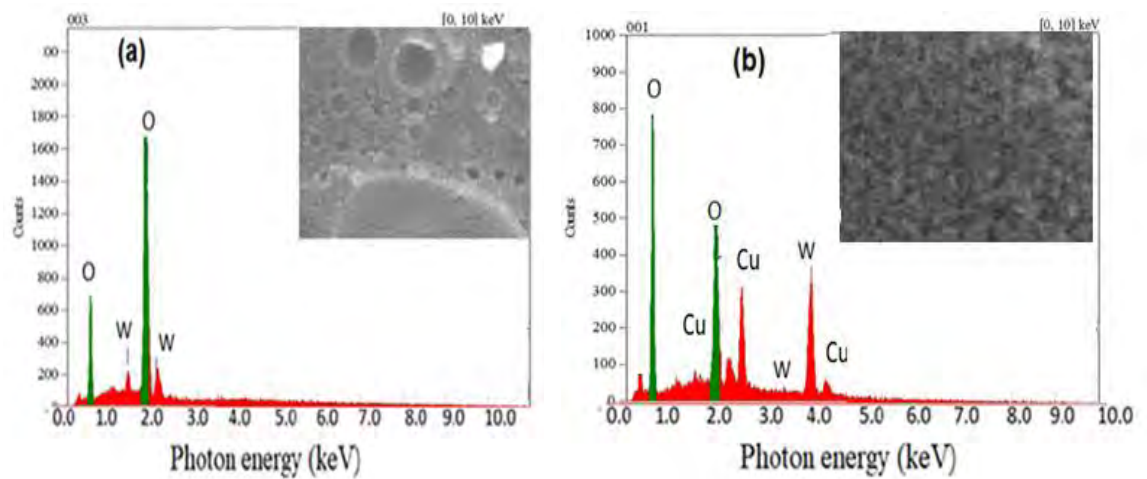
Fig 4.32 (a-b) EDX spectra of WO_3 and 4at% Cu: WO_3 thin films respectively.

4.3.2.4 Structural properties

The XRD patterns of undoped and Cu-WO$_3$ nanostructures are depicted in **Fig.** 4.33 and the peaks are indexed with the monoclinic structures with space group: P21/n match well with the JCPDS card No.043-1035. The sharp peaks indicate the formation of WO$_3$ crystallite particles without any impurities. The diffraction patterns of nanoparticles can be indexed to the spherical structure of WO$_3$. No other peaks corresponding to Cu related secondary or impurity phase was found in copper doped sample, which may be attributed to the incorporation of Cu ion into the W lattice site rather than interstitial ones. The obtained XRD pattern of Cu doped WO$_3$ nanoparticles show enhanced intensity compared to pure WO$_3$ nanoparticles. This indicates that doping is very effective for the growth of crystallites and hence in the formation of bonds between copper, tungsten and oxygen [254]. The effect of Cu doping on the structure is elucidated by an enlarged version of the three predominant peaks between 22∘ to 28∘ is shown in **Fig.** 4.34. 2% Cu-doped sample reveals sharpening of diffraction peaks which implies the degree of crystallinity is higher than the pure. The increase diffraction peak intensity is due to the Cu dopant in the WO$_3$ nanoparticles. The average crystallite size was found to 13 to 24 nm for pure and Cu doped WO$_3$ respectively. The lattice parameter value are varied and it was ascribed by the substitution of Cu^{2+} ion in W^{6+} sites, which has higher ionic radius than the W^{6+} ion . The ionic radii of W^{6+} and Cu^{2+} are 0.062 nm and 0.073 nm, the substitution of dopant ion intoW^{6+} lattice makes the deviation in d-spacing values due to the elevated growth of the nanoparticles in the Cu-doped materials. The unit cell volume of Cu dopedWO$_3$ sample decreased with optimum concentration (2%) of Cu^{2+}, that indicate the quantitative substitution of Cu ion in the lattice site The average crystallite size of 36 nm was obtained for the undoped sample, which reduces 22 nm for 8% Cu doped sample. As minor decrease in the lattice constants were also observed with Cu doping. These variations in crystallite size and lattice constant are probably linked with a slight difference in the ionic radii of Cu^{2+} and W^{6+} ions. This observation reveals that in the process of nanostructure formation, definite planes of the growth are affected by adding copper. Our results agree well with a previous report on the Cu doped WO$_3$ nanostructures [255-256].
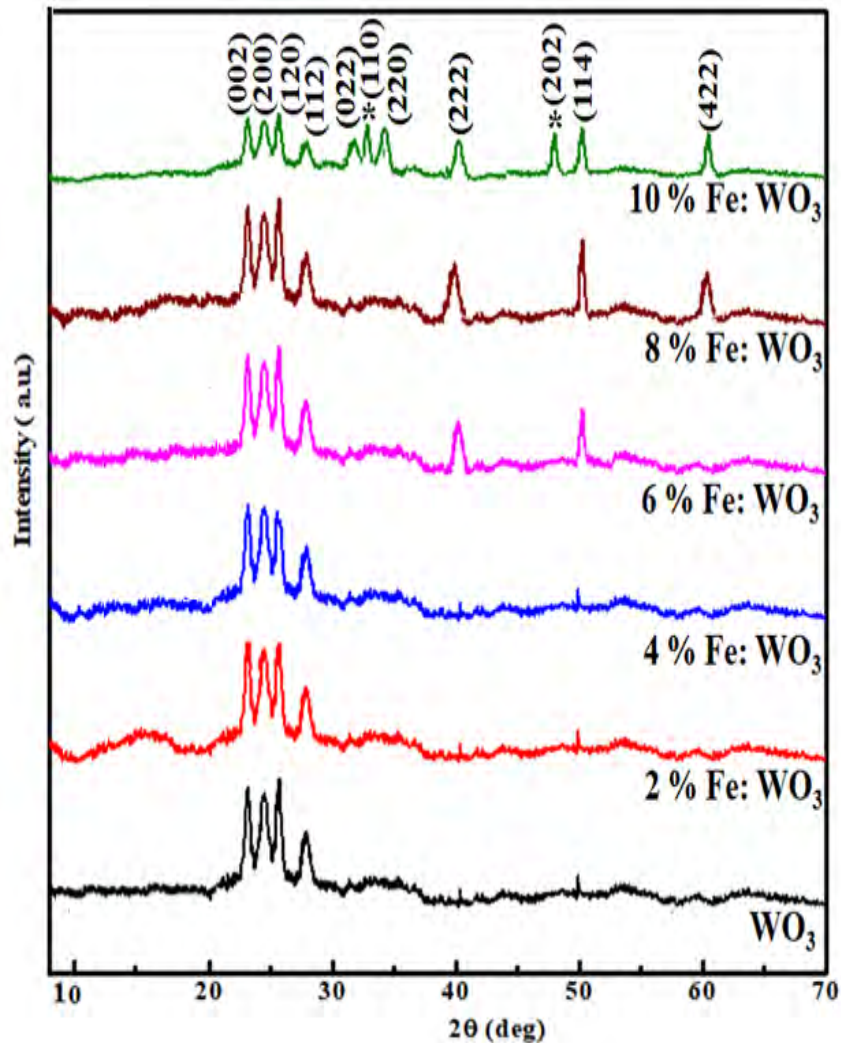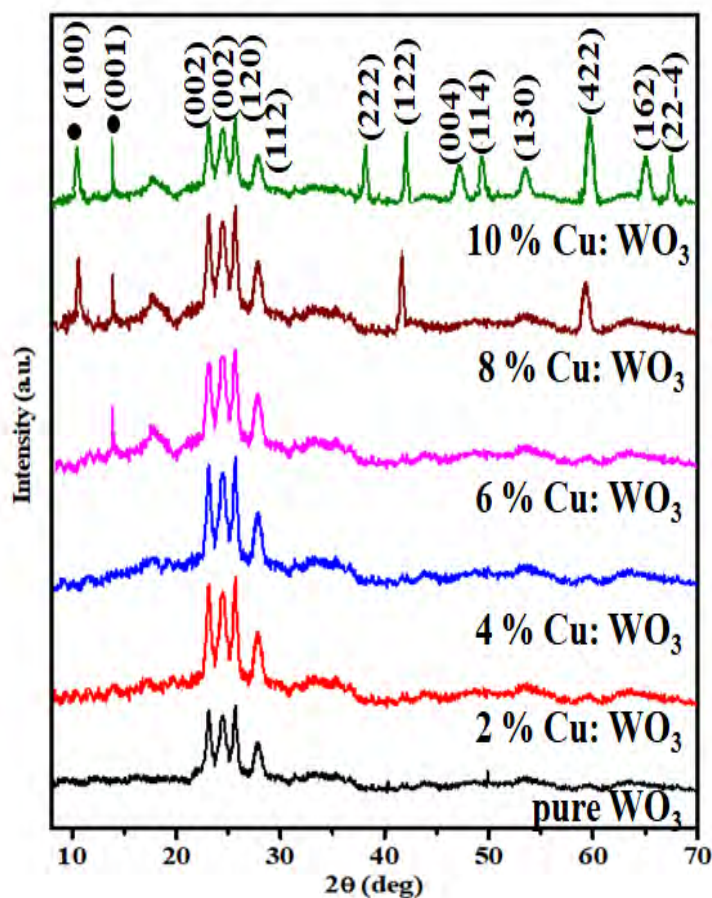
Fig. 4.33 XRD patterns of 0- 10 at% Cu:WO₃ films.

4.3.2.5 Optical properties

The optical properties of the pure and Cu-doped tungsten oxide films were measured in the wavelength range 400-1100 nm. **Fig.** 4.34 shows the optical transmittance spectra of pure and Cu doped WO₃ the films. The absorption edge of undoped WO₃ and Fe-doped WO₃ films shifted to longer wavelengths indicating red shift. Maximum transmittance of pure WO₃ lies between 20% and 35%. This low transmissions may be the effects of non-specular light scattering caused by the highly crystalline, granular and porous WO₃ thin films. Cu-doped films showed lower transmittance compared to undoped films. The transmittance of films depends on the structural, morphological and compositional characteristics of the films.

Fig. 4.34 Optical transmittance spectra of 0-10 at % Cu :WO$_3$ the films.

The optical band gaps (Eg) of the various films have been evaluated from the transmittance spectra by plotting $(\alpha h v)^2$vs hv that is appropriate for an direct band gap material and then using linear extrapolation to the energy axis $(\alpha h v)^2 = 0$. Band gap for WO$_3$ is 2.72 eV and there is a slight decrease in the optical band gap when Fe was incorporate into the tungsten oxide film up to 4 at % at 2.54 eV then started to increase. The red shift observed in the optical absorption caused a negative shift (reduction) in the band gap of the WO$_3$ film. The optical band gap of the Cu-doped tungsten oxide films obtained here are found to be within the ranges of optical band gap of the Cu-doped films obtained by other earlier reported values [223]. The variations in the band energy of WO$_3$ nanoparticles can be understood the basis of hybridization between Cu$_{3d}$ orbital and the O$_{2p}$ orbital. As it is well known that in case of pristine WO$_3$, valance band is dominated by O$_{2p}$ and conduction band is dominated by W$_{5d}$ orbitals. But when Cu ions are introduced in the system, their 3d orbitals emerge around valance band and induce slight positive shift in it. Besides, Cu ions can also lead to downshift of conduction band. These corrections in the positions of valance and conduction bands lead to narrowing of the band gap which might help to harvest more visible light in it and generates more electron holes pairs

4.3.2.6 Electrical properties

Temperature dependence of electrical resistivity of WO_3 thin films in the temperature range 300-440 K. The decrease in resistivity with temperature indicates the semiconductor behavior of the films. In fact, resistivity is the result of trade-off between two competing processes occurring simultaneously, namely, thermal excitation of electrons and adsorption of atmospheric oxygen on the film surface. Generally speaking, doping can change the conductivity of the materials by forming impurity defects when Cu elements are introduced in WO_3. When the amount of Cu is small (2 at %), W^{6+} is partially substituted by Cu^{2+} and the electron concentration in the semiconductor is decreased. Because WO_3 is an n-type semiconducting oxide and the electrons are acted as charge carriers, the resistance of the nanoparticles is increased. When the crystal structure of WO_3 is much disordered, which will hinder the electron movement and lead to the increase of the resistance. With the increasing of the Cu element content (≥ 4 at %), some Cu^{2+} partially substitute W^{6+} and the others permeate into the interstitial sites of WO_3 crystal lattice and donate electrons to WO_3 matrix, which increase the electron concentration in the semiconductor and decrease the resistance. So the resistance of Cu doping WO_3 is found to decrease little and then increase with further increasing of the Cu content [257-258] The effect of Cu concentrations on the properties of nanostructured WO_3 thin films are summarized in Table 4.11.

Table 4.11 Effect of Cu concentration on electrical properties of WO_3 thin films

Cu concentration (at %)	Electrical resistivity, $\rho \times 10^4$ (Ω-cm)	n-type Carrier concentration, $n_c \times 10^{11}$ (cm^{-3})	Hall mobility, μ ($cm^2 V^{-1} s^{-1}$)
0	3.46	7.63	9.72
2	3.17	8.78	8.62
4	2.61	10.46	7.12
6	2.93	8.39	7.69
8	3.46	7.89	8.75
10	3.95	7.54	8.89

4. 3.3 Comparative study

It is observed that Fe doped WO_3 thin films possess some differences in the characterizations in comparison with those of Cu doped WO_3 thin films. The comparative properties among Fe and Cu doped WO_3 thin films are highlighted in Table 4.12.

Table 4.12 Comparison among the characteristics of Fe and Cu doped WO_3 thin films

Characterization techniques	Fe: WO_3 thin films	Cu: WO_3 thin films
Film images analysis	Film colour are greatly influenced by Fe dopant	Film colour does not so affected due to Cu.
SEM analysis	Surfaces are comprised of spherical nanoparticles and agglomeration of the particles are not so influenced by Fe dopant	Surfaces are comprised of spherical nanoparticles and agglomeration of the particles increased with increase of Cu dopant
EDX analysis	Films are stoichiometric and Co ions decrease with increase of Fe content	Films are stoichiometric and Co ions decrease with increase of Cu content
XRD analysis	Monoclinic WO_3 oxide crystal structure was obtained and Fe does not change the structure of WO_3.	Monoclinic WO_3 crystal structure was obtained and Cu does not change the structure of WO_3.
UV-vis-NIR spectroscopy	Optical band gap increase with increase of Fe doping concentration up to 4 at %.	Optical band gap decrease with increase of Cu doping concentration up to 4 at %.
Electrical measurements	Resistivity increase with Fe concentration up to 4 at % then started to decrease	Resistivity decrease with increasing Cu up to 4 at %, then started to increase
Hall effect measurements	Carrier con centration increase with increasing Fe content up to 4 at %	Carrier con centration increase with increasing Cu content up to 4 at %

Part D
Results of Fe and Cu Doped CeO$_2$ Thin Films

4.4 Results on the Characterization of Fe and Cu Doped CeO$_2$ Thin Films

4.4.1 Results for Fe doped CeO$_2$ thin films

4.4.1.1 Photograph of deposited Fe doped CeO$_2$ thin films

Photograph of composited CeO$_2$ thin film shows uniform deposition and surface consistency of the film slightly changed for Fe doping. **Fig.** 4.35 shows photograph of deposited pure and 2, 4, 6,8,10 at% Fe doped CeO$_2$ thin films respectively. All the films are densed and homogeneous.
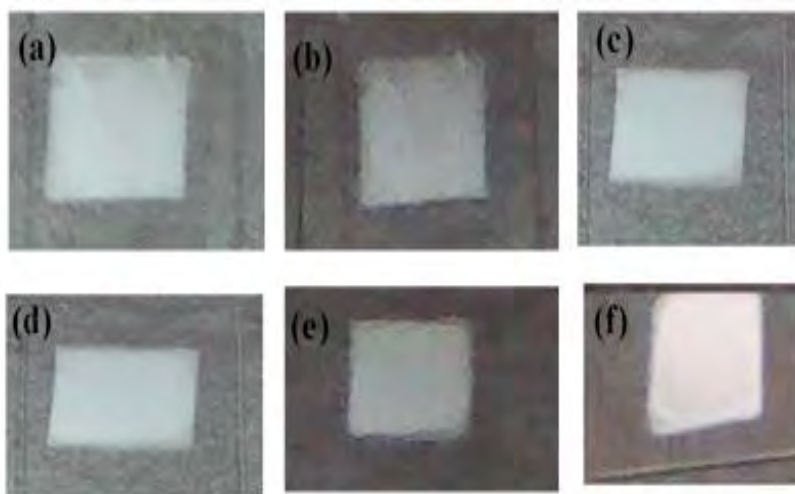
Fig 4.35 (a-f) Photograph of 0-10 at% Fe:CeO$_2$ thin films respectively.

The colour of the films are white. There is no variation of colour among the films with Fe content. The differences in film homogeneity and compactness are also observed for pure and Fe doped CeO$_2$ films. This variations confirm the effect of Fe dopant concentration on CeO$_2$ properties. The thickness of pure and Fe doped CeO$_2$ films varied with ±10 nm.

4.4.1.2 Surface morphological analysis

The FESEM images of undoped and 2, 4, 6, 8 and 10 at% Fe doped CeO$_2$ thin films have been observed at 50,000 magnification shown in **Fig.** 4.36 (a-f) respectively. All the images show that the substrates are uniformly covered with spherical nanoparticles. It can be seen that Fe-doped CeO$_2$ exhibits a dense and compact structure, while the pure

CeO_2 sample has a porous and looser structure. The particle size decrease with Fe concentration up to 6 at %. At 8 and 10 at% Fe concentration the particle increase. The surface remain homogeneous and smooth with agglomerated nanoparticles up to 6 at % Fe. At 8 and 10 at % Fe doping agglomeration decrease over the surface which may due to oxidation of Fe^{3+} ions on the surface. It is seen from the FESEM image that 6 at% Fe doped CeO_2 surface is more porous and compact which may suitable for bio sensing applications. These results are consistent with the previous work on Fe-doped CeO_2 reported by Zhang et al [254].
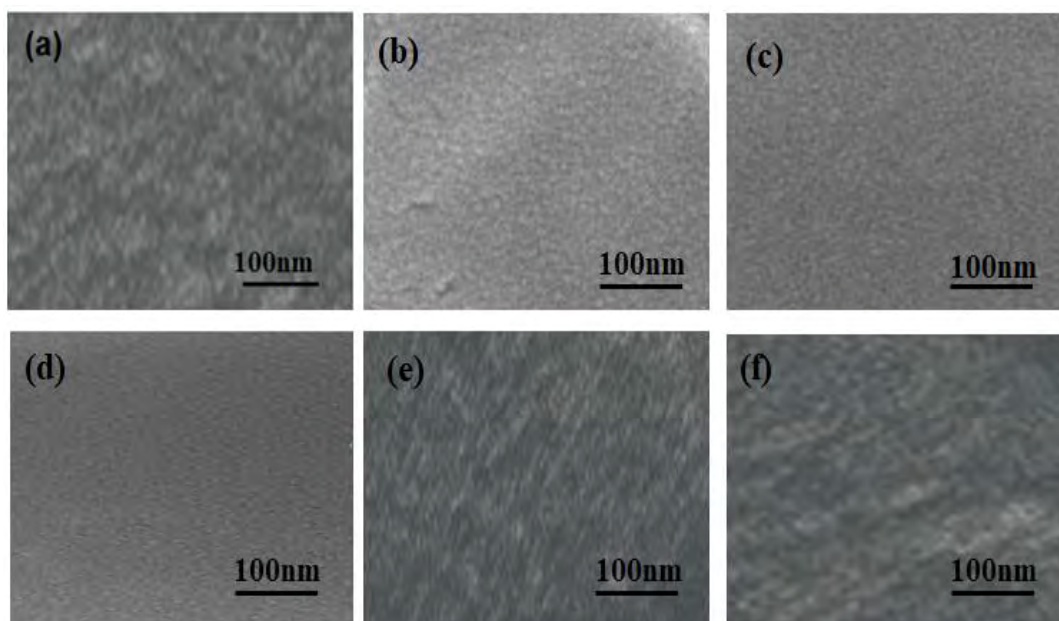
Fig. 4. 36 (a-f) FESEM images of 0- 10 at% Fe: CeO_2 respectively.

4.4.1.3 Compositional analysis

EDX analysis confirmed the elements of the compositions of pure CeO_2 and Fe doped CeO_2 thin films. EDX data have been collected at various points on the scan area. EDX data support the uniformity of the synthetic distribution of the prepared thin films. Different peaks corresponding to Ce and O were found in the spectrum, which confirms the CeO_2 thin film and peak for the composition of Ce, Fe and O indicate the Fe doped CeO_2 thin films shown in **Fig.** 4.37. From compositional analysis it is observed that amount of Ce reduces with the increment of Fe concentration in Fe doped CeO_2 thin films. The EDX data supported the logical substitution of Ce caused by Fe doping [259].
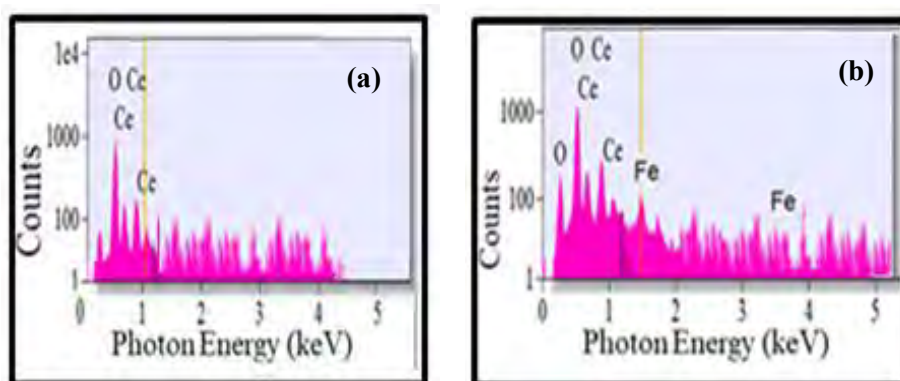
Fig. 4. 37 (a-b) EDX spectra of CeO_2 and 4at% Fe: CeO_2 thin films respectively.

4.4.1.4 Structural properties analysis

Fig. 4.38 shows the XRD patterns of the 0, 2, 4, 6, 8, and 10 at % Fe-doped CeO_2 thin films. All the samples exhibited peaks consistent with the face-centered cubic structure of CeO_2 matched with the standard data from JCPDS 34-0394 [260]. There are no secondary phases such as FeO, Fe_2O_3, or Fe_3O_4 in these samples. The average crystallite sizes of all samples were calculated from X-ray line broadening of the peaks at (111), (200), (220), and (311) planes using Scherer's equation. There was effect on the sizes of the crystallites with Fe doping. The average crystallite size and lattice constant along (220) plane haven obtained 15 nm and 0.5416 nm and changed with Fe concentration in comparison with undoped CeO_2. A decreasing trend of crystallite size is observed up to 6 at% Fe doping and at 8 and 10 at % crystallite size increase. This change is possibly due to the replacement of larger Ce^{4+} (0.92 ˚A) by smaller Fe^{3+} (0.65 ˚A) or Fe^{2+} (0.78 ˚A), introducing Ce^{3+} into the crystal lattice. Ce^{3+} have a higher ionic radius (1.034 ˚A) compared to Ce^{4+} and these ions introduce oxygen vacancy. It is observed that CeO_2 and Fe-doped CeO_2 nanoparticles experience considerable lattice distortion, which is in good agreement with earlier reports [261-263]. Those reports indicated that doping causes a change in the Ce-O bond length (lattice distortion) and the overall lattice parameter. The main reason behind the textured structure in the present case is a negligible lattice mismatch between the film and the substrate.
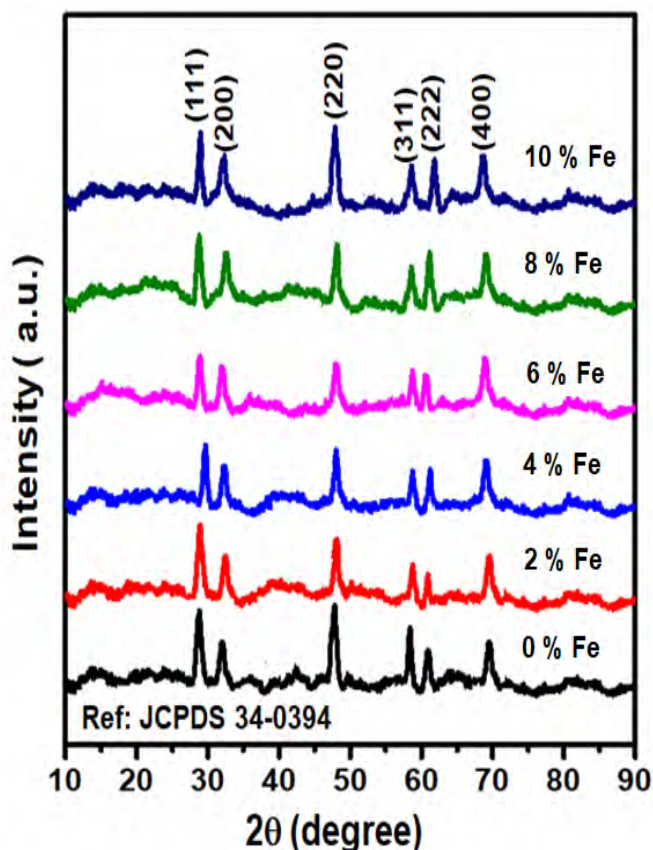
Fig. 4.38 XRD patterns of 0- 10 at % Fe:CeO$_2$ thin films respectively.

4.4.1.5 Optical properties analysis

The UV–Vis-NIR transmittance spectrum of pure and Fe doped CeO$_2$ nanoparticles are shown in **Fig. 4.39**. It exhibits a strong absorption band in the range 300–400 nm. The band gap energy corresponding to direct transition is calculated by extrapolating the linear portions of $(\alpha h\nu)^2$ as a function photon energy hν for the undoped and doped films. These values are higher than that of bulk value (3.19 eV) [264] which means a blue shift in the absorption due to quantum confinement effect. Confinement effect can affect both structural and electronic properties of nano semiconductor oxide. In the structural properties, the nanostructure may alter lattice symmetry and cell parameters. In the electronic properties, band gap and valence and conduction band are disturbed [265]. The absorption of 8 and 10 at% Fe doped ceria experiences a red shift. The redshift of an optical band gap of the ceria nanoparticles can be illustrated by two types of mechanism. The first one was due to the presence of defects caused by the charge transfer between Ce^{3+} and Ce^{4+}. This was the generally accepted mechanism for the redshift of CeO$_2$

nanoparticles. The second one was the size effect [266-267]. In the present study, the redshift of the band gap indirectly dictated the increase of crystallite size.

Fig. 4.39 Optical transmittance spectra of 0-10at % Fe: CeO_2 the films.

4.4.1.6 Electrical properties

Temperature dependence of electrical resistivity of CeO_2 thin films in the temperature range 300-440 K. The decrease in resistivity with temperature indicates the semiconductor behavior of the films. In fact, resistivity is the result of trade-off between two competing processes occurring simultaneously, namely, thermal excitation of electrons and adsorption of atmospheric oxygen on the film surface. Generally speaking, doping can change the conductivity of the materials by forming impurity defects when Fe elements are introduced in CeO_2. When the amount of Fe is small i.e. 2 at %, Ce^{4+} is partially substituted by Fe^{2+} and the electron concentration in the semiconductor is decreased. Because CeO_2 is an n-type semiconducting oxide and the electrons are acted as charge carriers, the resistance of the nanoparticles is increased. When the crystal structure of CeO_2 is much disordered, which will hinder the electron movement and lead to the increase of the resistance. With the increasing of the Fe element content (≥ 6 at %), some Fe^{2+} partially substitute Ce^{4+} and the others permeate into the interstitial sites of CeO_2 crystal lattice and donate electrons to CeO_2 matrix, which increase the electron concentration in the semiconductor and decrease the resistance. So the resistance of Fe doping CeO_2 is found to decrease little and then increase with further increasing of the Fe

content. The effect of Fe concentrations on the electrical properties of nanostructured CeO$_2$ thin films are summarized in Table 4.13. Decrease in resistivity with Cu dopant concentration may be attributed to incorporation of iron ions into CeO$_2$ lattice, resulting in increase in oxygen vacancy i.e. carrier concentration. Also, based on the size effects of electrical conductivity, when the crystallite size is below ~15 nm, the grain boundary scattering decreases significantly and therefore increases the conductivity [248]. This results satisfy the reported results by Lethy et al. and Whilst Patil et al. [249-250].

Table 4.13 Effect of Fe concentration on the electrical properties of CeO$_2$

Fe concentrations (at %)	Electrical resistivity, $\rho \times 10^{5}$ (Ω-cm)	Carrier concentration, n_c ($\times 10^{12}$ cm^{-3})	Hall mobility, μ (cm^2 V^{-1} s^{-1})
0	5.57	6.35	3.59
2	4.16	9.24	3.21
4	3.79	12.78	3.09
6	3.26	14.89	2.83
8	4.69	9.67	4.58
10	5.87	7.21	5.04

4.4.2 Results for Cu doped CeO$_2$ thin films

4.4.2.1 Surface morphology analysis

Fig. 4. 40 (a-f) shows the FESEM images of undoped and 2, 4, 6, 8 and 10 at% Cu doped CeO$_2$ thin films respectively. All the images show that the substrates are uniformly covered with spherical nanoparticles. It can be seen that Cu-doped CeO$_2$ exhibits a dense and compact structure of fine nano-grain without any cracks that distributed homogenously on surface while the pure CeO$_2$ sample has a porous and looser structure. The particle size decrease with Cu concentration up to 6 at %. At 8 at% and 10 at% Cu concentration the crystallite size increase. The surface remain homogeneous and smooth up to 6 at % Fe. At 8 and 10 at % Cu doping some crakes are observed over the surface which may due to oxidation of Cu^{2+} ions on the surface. It is seen from the FESEM image that 6 at% Cu doped CeO$_2$ surface is more porous which may suitable for bio sensing applications. [268].
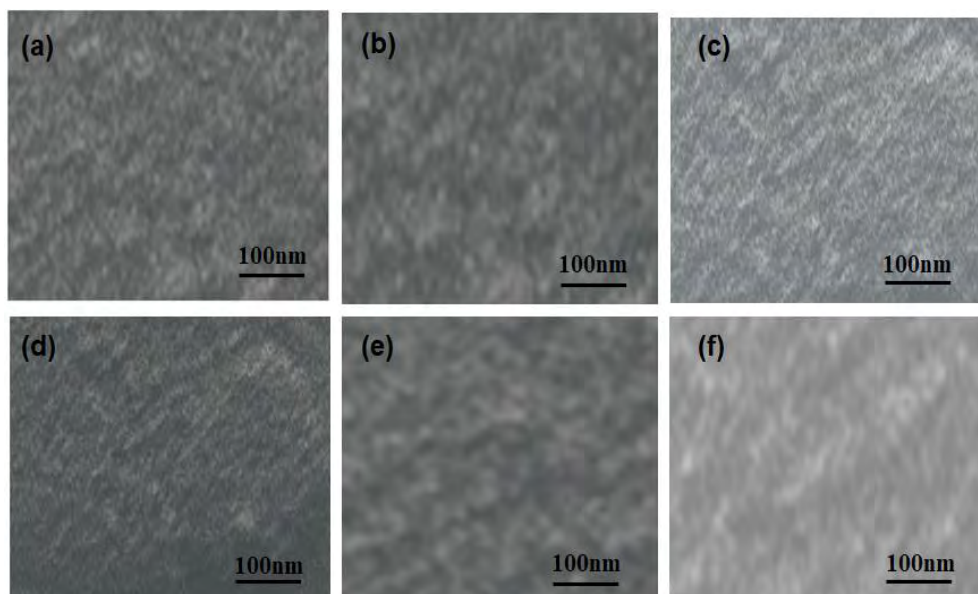
Fig. 4.40 (a-f) FESEM images of (0- 10 at%) Cu: CeO$_2$ respectively.

4.5.1. 3. Compositional analysis

In **Fig.** 4.41 spectra of undoped CeO$_2$ and 4at% Cu doped CeO$_2$ thin films are displayed. EDX analysis confirmed the elements of the compositions of pure CeO$_2$ and Cu doped CeO$_2$ thin films. EDX data have been collected at various points on the scan area. EDX data support the uniformity of the synthetic distribution of the prepared thin films.
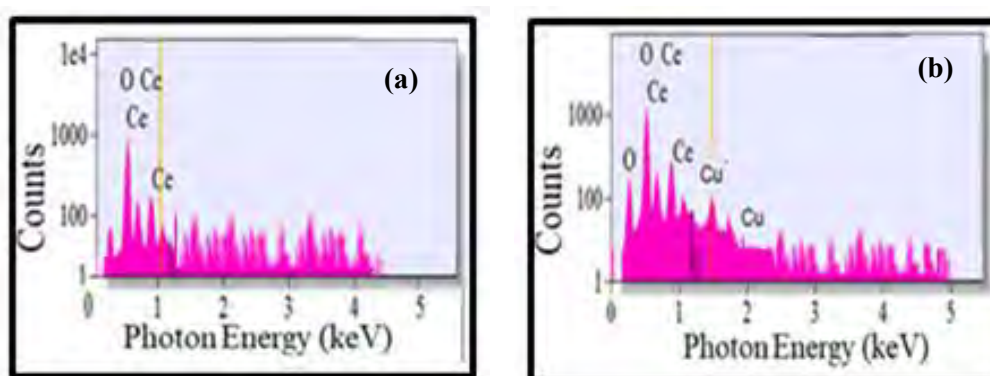
Fig. 6.41 (a-b) EDX spectra of CeO$_2$ and 4at% Cu:CeO$_2$ thin films respectively.

Different peaks corresponding to Ce and O were found in the spectrum, which confirms the CeO$_2$ thin film and peak for the composition of Ce, Cu and O indicate the Cu doped CeO$_2$ thin films. Amount of Ce reduces with the increment of Cu concentration in Cu

doped CeO$_2$ thin films which confirm the stoichiometry and homogeneity of the films [265]. The EDX data supported the logical substitution of Ce caused by Cu doping.

4.5.2.4 Structural properties analysis

Fig. 4.42 shows the XRD patterns of the undoped CeO$_2$ and Cu doped CeO$_2$. All the samples exhibited peaks consistent with the face-centered cubic structure of CeO$_2$ in the standard data from JCPDS 34-0394. The XRD patterns of the Cu-doped CeO$_2$ are the same as that of undoped CeO$_2$, indicating that Cu ions might have been substituted into the CeO$_2$ lattice, and there are no secondary phases for Cu in these samples. The average crystallite sizes of all samples were calculated from X-ray line broadening of the peaks at (111), (200), (220), and (311) planes using Scherer's equation.
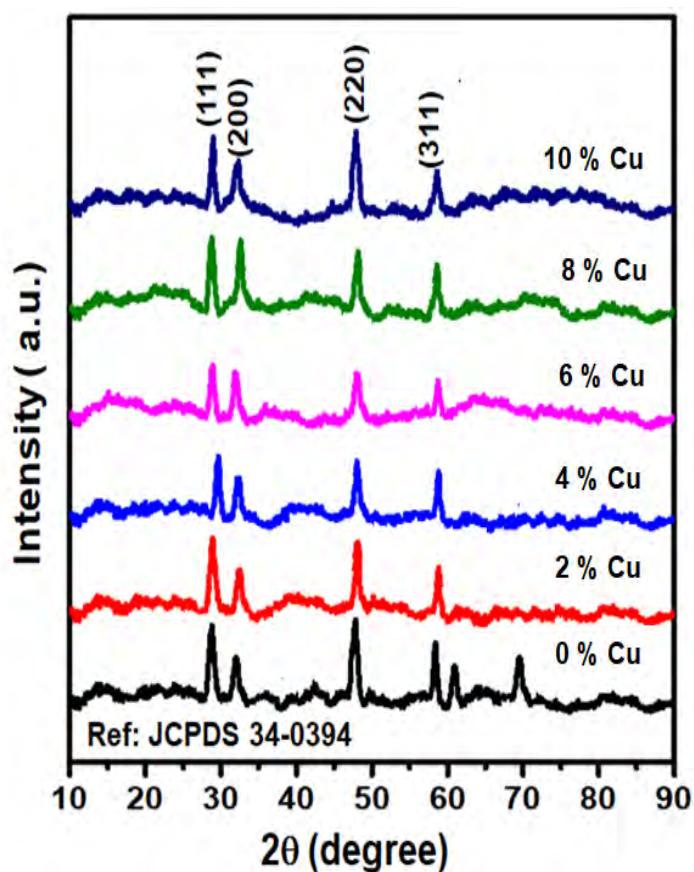
Fig. 4.42 XRD patterns of 0- 10 at % Cu:CeO$_2$ respectively.

There was effect on the sizes of the crystallites with Cu doping. The average crystallite size and lattice constant along (220) plane haven obtained 15 nm and 0.5416 nm and changed with Fe concentration in comparison with undoped CeO$_2$. A decreasing trend of crystallite size is observed up to 6 at% Fe doping and at 8 and 10 at % crystallite size

increase. This change is possibly due to the replacement of larger Ce^{4+} (0.92 ˚A) by smaller Cu^{2+} (0.74 ˚A) or Cu^+ (0.65 ˚A), introducing Ce^{3+} into the crystal lattice. Ce^{3+} have a higher ionic radius (1.034 ˚A) compared to Ce^{4+} and these ions introduce oxygen vacancy. It is observed that CeO_2 and Cu-doped CeO_2 nanoparticles experience considerable lattice distortion, which is in good agreement with earlier reports [269]. Those reports indicated that doping causes a change in the Ce-O bond length (lattice distortion) and the overall lattice parameter.

4.4.2.5 Optical properties analysis

The UV–Vis-NIR transmittance spectrum of pure and Cu doped CeO_2 nanoparticles are shown in **Fig.** 4.43. It exhibits a strong absorption band in the range 300–400 nm. The band gap energy corresponding to direct transition is calculated by extrapolating the linear portions of $(\alpha h\nu)^2$ as a function photon energy hν for the undoped and doped films. The obtained band gap for CeO_2 is 3.44 eV and this value is higher than that of bulk value (3.19 eV) which means a blue shift in the absorption. Band gap gradually increase with Cu concentration causing blue shift.
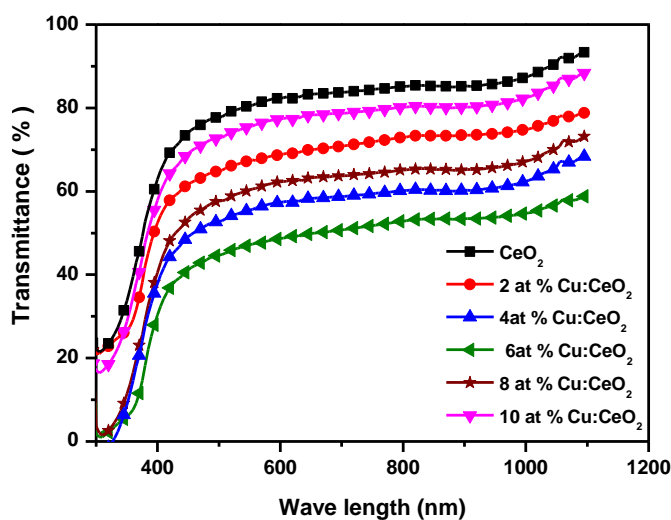
Fig. 4.43 Optical transmittance spectra of 0-10 at % Cu :CeO_2 the films.

The blue shift of an optical band gap of the ceria nanoparticles can be illustrated by two types of mechanism. The first one was due to the presence of defects caused by the charge transfer between Ce^{3+} and Ce^{4+} This was the generally accepted mechanism for the redshift of CeO_2 nanoparticles. The second one was the size effect. In the present study,

the redshift of the band gap indirectly dictated the increase of particle size. These results were satisfied as reported by some other groups of researchers [269-270].
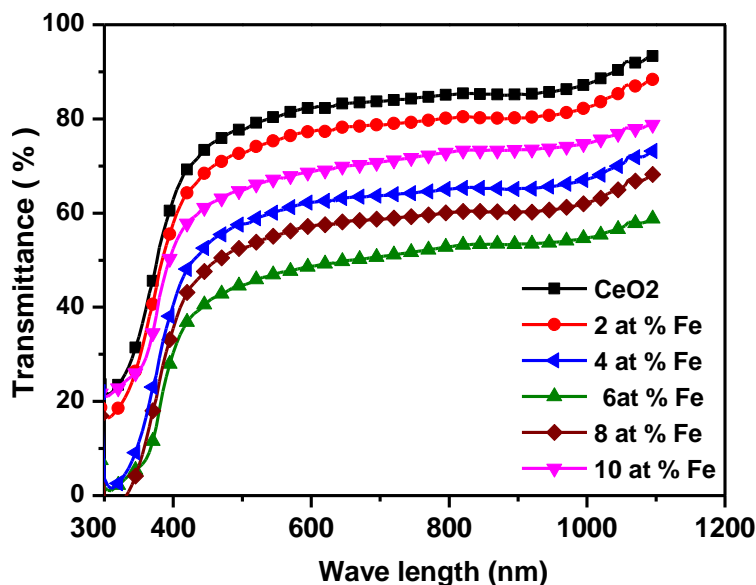
4.4.2.6 Electrical properties

Temperature dependence of electrical resistivity of CeO_2 thin films in the temperature range 300-440 K. The decrease in resistivity with temperature indicates the semiconductor behavior of the films. In fact, resistivity is the result of trade-off between two competing processes occurring simultaneously, namely, thermal excitation of electrons and adsorption of atmospheric oxygen on the film surface. Generally, doping can change the conductivity of the materials by forming impurity defects when Fe elements are introduced in CeO_2. When the amount of Cu is small i.e. 2 at %, Ce^{4+} is partially substituted by Cu^{2+} and the electron concentration in the semiconductor is decreased. Because CeO_2 is an n-type semiconducting oxide and the electrons are acted as charge carriers, the resistance of the nanoparticles is increased. When the crystal structure of CeO_2 is much disordered, which will hinder the electron movement and lead to the increase of the resistance. With the increasing of the Cu element content ($\geq$ 6 at %), some Cu2+ partially substitute Ce^{4+} and the others permeate into the interstitial sites of CeO_2 crystal lattice and donate electrons to CeO_2 matrix, which increase the electron concentration in the semiconductor and decrease the resistance. So the resistance of Cu doping CeO_2 is found to decrease little and then increase with further increasing of the Cu content. The effect of Cu concentrations on the properties of   nanostructured CeO_2 thin films are summarized in Table 4.14.

Table 4.14 Effect of Cu concentration on the electrical properties of CeO_2

Cu concentrations (at %)	Electrical resistivity $\rho \times 10^4$ (Ω-cm)	Carrier concentration, n_c ($\times 10^{12}$ cm^{-3})	Hall mobility, μ (cm^2 V^{-1} s^{-1})
0	5.57	6.35	3.59
2	5.38	7.29	3.41
4	5.09	10.54	3.13
6	5.36	12.63	2.87
8	5.79	9.77	3.06
10	6.11	7.69	3.21

4.4.3 Comparative study

It is observed that Fe doped CeO_2 thin films possess some differences in the characterizations in comparison with those of Cu doped CeO_2 thin films. The comparative properties among Fe and Cu doped WO_3 thin films are highlighted in Table 4.15.

Table 4.15 Comparison among the characteristics of Fe and Cu doped CeO_2 thin films

Characterization techniques	Fe: CeO_2 thin films	Cu: CeO_2 thin films
Film images analysis	Film homogeneity and density are greatly influenced by Fe dopant	Film homogeneity and density are greatly influenced by Cu dopant.
SEM analysis	Surfaces are comprised of spherical nanoparticles and agglomeration of the particles are influenced by Fe dopant	Surfaces are comprised of spherical nanoparticles and agglomeration of the particles increased with increase of Cu dopant
EDX analysis	Films are stoichiometric and Ce ions decrease with increase of Fe content	Films are stoichiometric and Ce ions decrease with increase of Cu content
XRD analysis	Cubic CeO_2 oxide crystal structure was obtained and Fe does not change the structure of CeO_2	Cubic CeO_2 oxide crystal structure was obtained and Cu does not change the structure of CeO_2.
UV-vis-NIR spectroscopy	Optical band gap is tuned Fe doping concentration...	Optical band gap increase with increase of Cu doping .
Electrical measurements	Resistivity decrease with increasing Fe concentration up to 6 at %	Resistivity decrease with increasing Cu concentration upto 6 at % .
Hall effect measurements	Carrier con centration increase with increasing Fe content up to 6 at % then decrease	Carrier con centration increase up to 6 at % with increasing Cu content up to 6 at %

PATR E
RESULTS OF GLUCOSE SENSING PROPERTIES OF
THIN FILMS

Part E

Results of Glucose Sensing Properties of Thin Films

4.5 Results of Glucose Sensing Properties

In this section glucose sensing performance on Fe doped MnO_2 thin films varying with Fe doping concentration and glucose concentration on nanostructured MnO_2 thin films are illustrated.

4.5.1 Measurement of the sensing current

The sensing current performance was measured at constant supply voltage varied with time for different Fe concentrations. **Fig.** 4.54 (a-d) shows the typical current-time response plot of pure and Fe: MnO_2 thin films in the prepared solution with successive stepwise changes of the Fe molar concentrations.
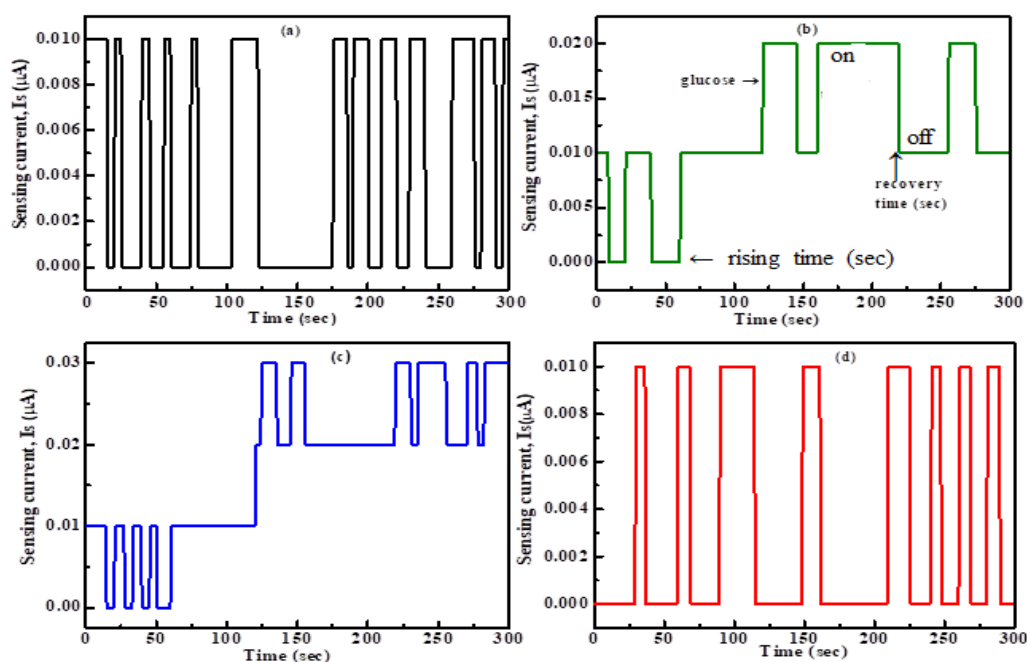
Fig. 4.54 (a-d) Current-time response plot of MnO_2, 4 at%, 6 at% and 8 at % Fe:MnO_2 thin films respectively.

It is noted that the sensing current is increased with the Fe concentration and the maximum current response is obtained at 4 at% Fe doping. It may due to the high textured film structure and high dense clusters' and provide more probable interaction between the additive solution and the film surface. The current is increased steeply with increasing

time reaching in a substantial phase. It is assumed that, since the adherence of the MnO_2 layer to the substrate was very strong, Fe-O-Mn bonds likely formed at the interface between the substrate and the MnO_2, which probably facilitated electron assignment beyond the interface, cause a high current response. The sensor (Fe: MnO_2 film) has a fast rise time which means that the oxygen ions at the film surface may immediately interact and bond with the glucose ($C_6H_{12}O_6$) molecules. A large number of charge carriers are responsible for this fast interaction and the sharp rise of the sensing current [271-272].

4.5.2 Sensitivity measurements

The following relation was used to calculate the glucose-sensing abilities of the prepared film:

$$S = \frac{I_x}{I_g} \times 100$$

Where I_x is the current in air and I_g is current with glucose. **Fig.** 4.45(a) shows the glucose response of pure and Fe doped MnO_2 thin films variation with Fe concentration and time. The response was dramatically increased with the increase of Fe concentration especially for 4 at% Fe higher than others shown in **Fig.** 4.51 (b).
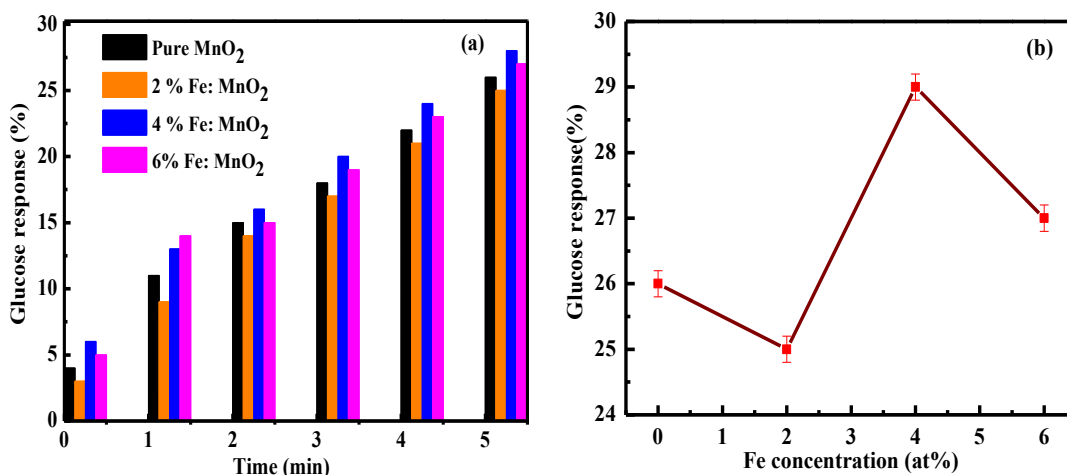
Fig. 4.45 (a-b) Glucose response of 0, 2, 4 and 6 at% Fe: MnO_2 thin films variation with time and variation with Fe concentration at 5 minutes respectively.

It is seen that the sensitivity of the present work is much higher than the other non-enzymatic glucose sensors such as flower like Ni doped MnO_2 nano composite prepared by electro deposition, $Cu:MnO_2$ synthesized by layer-by-layer assembly having sensitivity 1.04 mA mM^{-1} cm^{-2}, 26.96 μA mM^{-1} respectively [273-274]. These results manifested that the nanostructured Fe: MnO2 thin film is a pleasing material in the application of glucose biosensor.

4.5.3 Current response with different glucose concentration

The prepared MnO_2 and Fe doped MnO_2 thin films were examined for sensing the various concentration of the glucose solution. **Fig.** 4.46 (a, b) shows the resulted sensing current at (0.05, 0.1, 0.3, 0.5 and 1) mol/L glucose concentrations of pure MnO_2 and 4 at % $Fe:MnO_2$ respectively. The obtained curves supplementary in **Fig.** 4.52 (a, b) demonstrates the redox peak, indicating the redox reaction of ion and electron exchange with the conductive solution. It is observed that the sensing current is increased with the glucose concentration up to 0.5mol/L. The sensing current started to decrease above 0.5mol/L glucose concentration at high concentration, most of the active sites on the electrode are covered by glucose and so the current response is reduced. It is observed from **Fig.** 4.46 (b) that sensing current is higher for 4 at % Fe: MnO_2 than pure MnO_2 shown in **Fig. 4.46** (a) under the same glucose concentrations which indicates its superior catalytic activity [275-276]. **Fig. 4.47**(a-b) shows the response time of pure MnO_2 and 4 at% Fe doped MnO_2 thin films electrode as 1.13 sec and 1.02 sec respectively which have been measured current with glucose through film vs time plot.. This may for the incorporation of Fe into MnO_2, the Fe: MnO_2 may own more active sites for the detecting of glucose, displaying a shorter time.
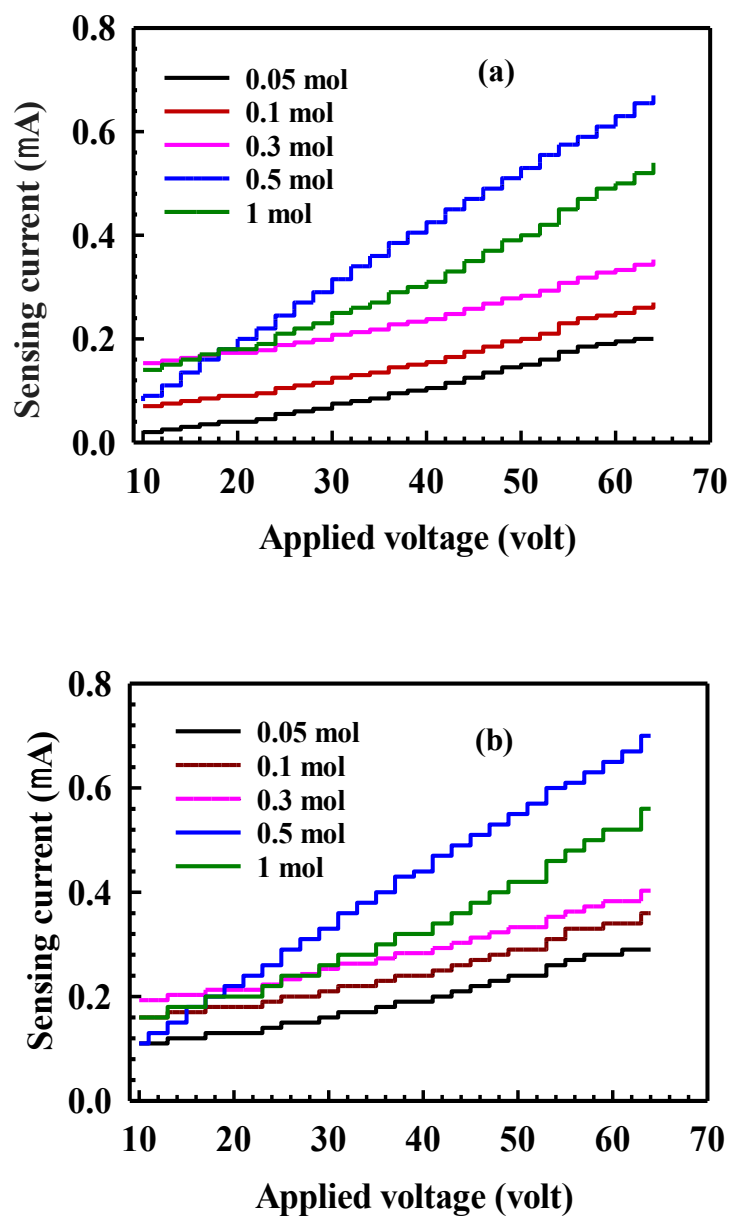
Fig. 4.46 (a-b) Sensing current at 0.05, 0.1, 0.3, 0.5 and 1 mol glucose concentrations of undoped MnO_2 and 4 at% Fe: MnO_2 respectively
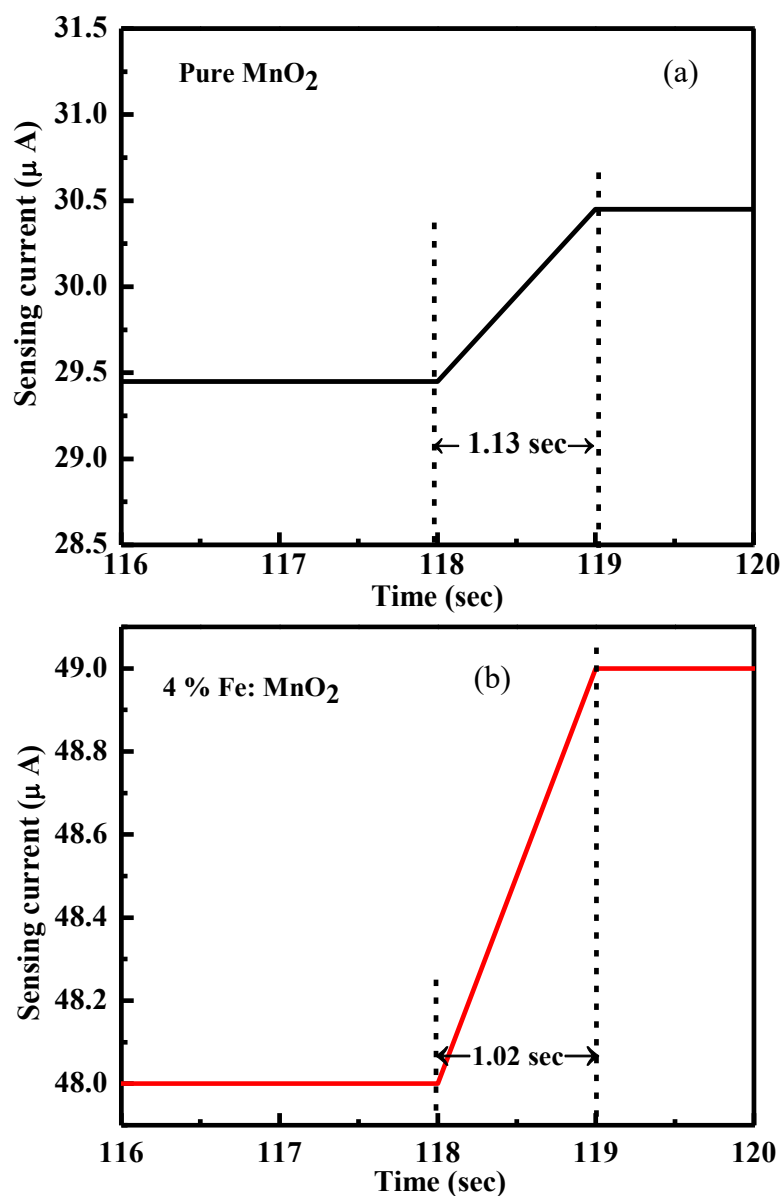
Fig. 4.47 (a-b) Plot current with glucose vs time to measure response time
of undoped MnO$_2$ and 4at% Fe:MnO$_2$ respectively

4.5.4 Sensitivity with different glucose concentration

Fig. 4.48 (a-e) shows the sensitivity of pure MnO$_2$ thin film with different glucose
concentrations 0.05, 0.1, 0.3, 0.5, and 1 mol/L respectively taken at 30 minutes..
Sensitivity increases with the increase of glucose concentration. Maximum sensitivity was
obtained at 0.5 mol/L glucose concentration and decreases at 1mol/L. This may be due to

the increase of oxidation of MnO_2 with enhancing glucose concentration. This indicates that MnO_2 acts as an electrode which has better catalytic properties for the oxidation of glucose.
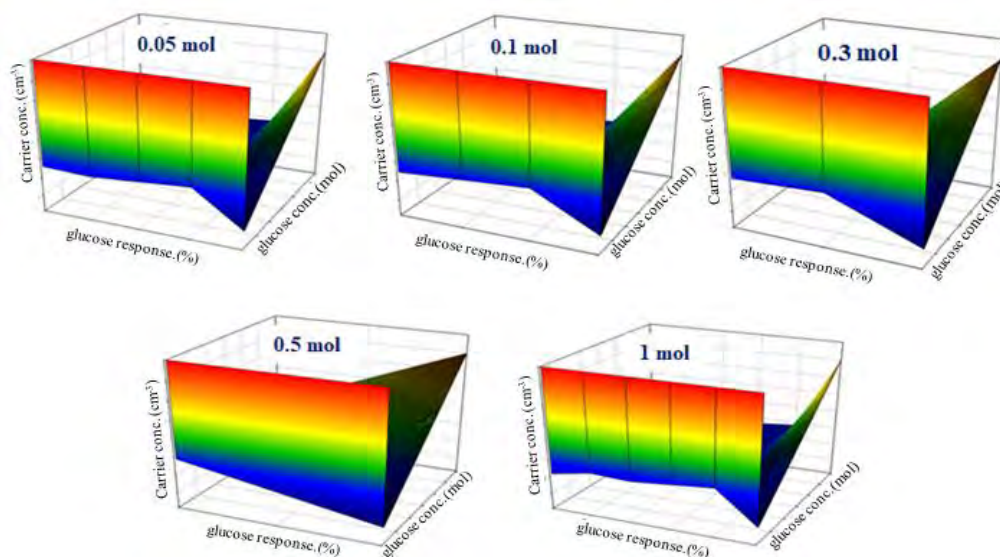
Fig. 4.48 (a-e) Sensitivity of Pure MnO_2 at different glucose concentrations of 0.05 mol, 0.1 mol, 0.3 mol, 0.5 mol and 1 mol respectively.

3D views are shown in **Fig.** 4.48 drawn by sigma plot-14 software has a descending trend of the cross-section up to 0.5 mol/L glucose concentration which indicates an increase in sensitivity of MnO_2 nanoparticles. In the 3D views, the blue color represents the direct recombination of conducting electrons, green color represents the recombination of surficial electron leading to visible emission. In the red and violet region, the oxidation-reduction reaction occurred. The cross-sectional images may due to the oxidation of glucose on the MnO_2. The oxidation is generated by deprotonating of glucose followed by adsorption onto the MnO_2 surface and oxidation by Mn^{2+} and Mn^{4+}. The Mn^{4+} ions are suggested for exploiting as an electron-transfer medium [277]. First Mn^{2+} would be oxidized to Mn^{+4}. Then the oxidative Mn^{4+} could catalyze glucose oxidation to generate gluconolactone, and then gluconolactone is further oxidized to glucose acid shown as bellow

$MnO_2 + OH \rightarrow MnOOH + 2e^-$

$MnOOH + 2e^- + glucose\ (C_6H_{12}O_6) \leftrightarrow MnO_2 + OH + gluconic\ acid$
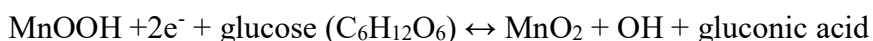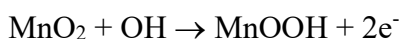
In **Fig.** 4.49 the dark red portion shows the sensitivity of 4 % Fe doped MnO_2 at different glucose concentrations, 92% for 0.05 mol/L, 97% for 0.1 mol/L, 102 % for 0.3 mol/L, 112% for 0.5 mol/L and 107% for 1 mol/L. It is observed that sensitivity of 4 at% Fe: MnO_2 is larger than pure MnO_2 under the same glucose concentration. Which may due to the oxidation mechanism for glucose.
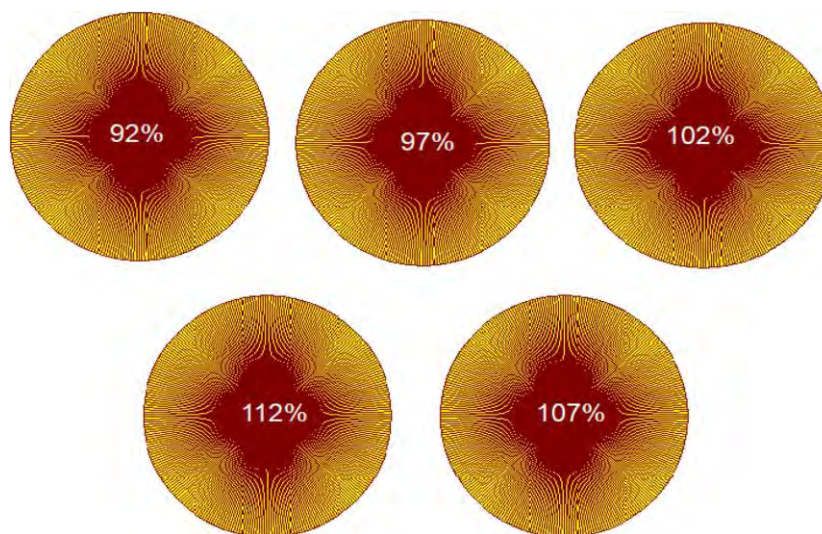
Fig. 4.49 (a-e) Sensitivity of 4 % Fe doped MnO_2 at different glucose concentrations, of 0.05 mol, 0.1 mol, 0.3 mol, 0.5 mol and 1 mol respectively.

In their oxidation process Fe^{2+} and Mn^{2+} present in the Fe: MnO_2 electrode is converted into Fe^{3+} and Mn^{4+} by oxidation reaction, and these oxidation products are glucose, which can be rapidly oxidized to glucose lactone as bellow:

$Fe^{3+} + C_6H_{12}O_6 \rightarrow Fe^{2+} + C_6H_{10}O_6,$

$Mn^{4+} + C_6H_{12}O_6 \rightarrow Mn^{2+} + C_6H_{10}O_6$
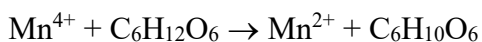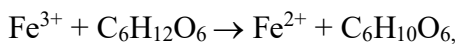
The high sensitivity of 4 at% Fe: MnO_2 indicates the superior catalytic activity than pure MnO_2.

Table 4.16 Summary of Findings on (Fe, Cu): (Co_3O_4, MnO_2, WO_3, CeO_2)

Sample	Surface	Structure	D (nm)	Eg (eV)	$\rho_{dc} \times 10^4$ (Ω-cm)	n_c (cm^{-3})	μ (cm^2 V^{-1} s^{-1})	Ref.
Co_3O_4	porous	spinel cubic	29	2.02	0.23	2.39×10^{17}	1.81	[194] [200] [207]
4at% Fe:Co_3O_4	more porous	spinel cubic	35	1.73	0.12	5.78×10^{17}	0.87	
4at % Cu:Co_3O_4	compact and more porous	spinel cubic	25	2.18	0.45	3.13×10^{17}	1.97	
MnO_2	agglomerated granular	body centered tetragonal	24	3.81	3.57	4.24×10^{12}	2.88	[231] [232] [233]
4at% Fe:MnO_2	more porous	boy centered tetragonal	20	3.07	1.95	11.89×10^{12}	1.87	
4at% Cu:MnO_2	more porous	body centered tetragonal	15	3.99	8.61	8.45×10^{12}	1.69	
WO_3	porous	monoclinic	13	2.72	3.46	7.63×10^{11}	9.72	[239] [244] [254]
4at% Fe:WO_3	more porous	monoclinic	8	3.03	5.16	8.35×10^{11}	7.43	
4at% Cu:WO_3	more porous	monoclinic	24	2.54	2.61	10.46×10^{11}	7.12	
CeO_2	porous	fcc	15	3.44	5.57	6.35×10^{12}	3.59	[265] [269] [270]
6 at% Fe:CeO_2	more porous	fcc	7	3.94	3.26	14.89×10^{12}	2.83	
6 at % Cu:CeO_2	more porous	fcc	8	3.72	5.06	12.63×10^{12}	2.87	

CHAPTER 5

SUMMARY AND CONCLUSIONS

5.1   Summary

5.2   Conclusions

5.3   Suggestions for Future Work

CHAPTER 5 SUMMARY AND CONCLUSIONS

The purpose of this chapter is to summarize the results obtained in the present research work. As demonstrated, the low-cost spray pyrolysis deposition (SPD) technique, described in this study, can be used to obtain uniform conductive layers of nanostructured pure and doped transition and rare earth metal oxides thin films. From this view point the summary and conclusions of the present work are given as follows:

5.1 Summary

The successful synthesis and characterization of nanostructured Fe and Cu doped transition and rare earth metal oxides (Co_3O_4, MnO_2, WO_3 and CeO_2) thin films are described in this research work. Different characterization processes were employed to show the effect of Fe and Cu dopant concentrations on the fabricated Co_3O_4, MnO_2, WO_3 and CeO_2 thin films suitability for sensing applications.

It is mentioned that spray pyrolysis is a suitable and novel technique for the synthesize of nanostructured Fe and Cu doped Co_3O_4, MnO_2, WO_3 and CeO_2 thin films. The substrate temperature is an important parameter that should be controlled during spraying. Before spraying, the temperature distribution contributes to the non-uniformity of deposition on the substrate. Fe and Cu doped Co_3O_4, MnO_2, WO_3 and CeO_2 thin films were prepared by spray pyrolysis method on glass substrate keeping the substrate temperature at 450°C and deposition time at 20 min constant which were optimized throughout the process. Different physical properties such as surface morphology, structural, optical and electrical properties were analyzed depending on 2,4,6,8 and 10 at % Fe and Cu dopant concentrations. Deposited films were found to be good one in terms of their uniformity of thickness and color. From film photograph, it was revealed that Fe and Cu ions change the colour of (Fe, Cu): Co_3O_4 and (Fe, Cu):MnO_2 thin films slightly. But the color of (Fe, Cu):WO_3 and (Fe, Cu):CeO_2 thin films did not changed due to the effect of Fe and Cu ions.

Effect of Fe and Cu doping concentration on morphological, elemental, structural, optical and electrical properties of nanostructured spinel cubic Co_3O_4 were studied. The surface homogeneity of the deposited films increases with Fe and Cu content due to the effect of friction among the charge carriers. XRD patterns indicated that the Fe and Cu ions replaced Co ions without changing the structure. Most prominent peak along (311) plane

are observed in both Fe and Cu doped Co_3O_4 thin films. Optical band gap increase with increase of Fe doping concentration where Optical band gap decrease with increase of Cu doping concentration. Electrical resistivity and carrier con centration increase with increasing Fe and Cu content up to 6 at %. Small crystallite size, regularity of surface morphology, high transmittance, and tunable band gap, high conductivity, of Fe and Cu doped Co_3O_4 thin films suggest the suitability of the material in optoelectronic devices and bio sensing applications.

The surface homogeneity of the deposited films increases with Fe and Cu content due to the effect of friction among the charge carriers. Films were stoichiometric and Mn ions decreased with increase of both Fe and Cu content. Tetragonal crystal structure of alpha phase MnO_2 was identified by XRD analysis. XRD patterns indicated that the Fe and Cu ions replaced Mn ions without changing the structure. Most prominent peak along (211) plane are observed in both Fe and Cu doped MnO_2 thin films. Resistivity gradually increase with increasing Fe concentration up to 6 at %. On the other hand Resistivity increase with increasing Cu concentration but minimum resistivity was observed for 4 at% Cu. Carrier con centration increase with increasing Fe and Cu contents. The obtained crystallite size, regularity of surface morphology, high transmittance, and tunable band gap, high conductivity of Fe and Cu doped MnO_2 thin films suggest the suitability of the material in optoelectronic devices and bio sensing applications.

Surfaces of both Fe and Cu doped WO_3 thin films were comprised of spherical nanoparticles and agglomerated. Agglomeration of the particles are not so influenced by Fe dopant but agglomeration of the particles increased with increase of Cu dopant. The surface homogeneity of the deposited films increased with Fe and Cu content due to the effect of friction among the charge carriers. Monoclinic WO_3 oxide crystal structure was obtained from XRD analysis. XRD patterns indicated that the Fe and Cu ions replaced W ions without changing the structure. Additional peak was not observed for Fe and Cu dopants. Optical band gap increase with increase of Fe and Cu doping concentration up to 6 at %. Resistivity and carrier con centration varied with increasing Fe and Cu content. crystallite size, regularity of surface morphology, high transmittance, and tunable band gap, high conductivity, of Fe and Cu doped WO_3 thin films obtained from these studied suggested the suitability of the material in optoelectronic devices and bio sensing applications.

Surfaces are comprised of spherical nanoparticles and agglomeration of the particles are influenced by Fe and Cu dopant. Films were stoichiometric and Ce ions decreased with increase of Fe and Cu content. Cubic CeO_2 oxide crystal structure was obtained and Fe and Cu does not change the structure of CeO_2. Optical band gap was tuned by Fe doping concentration and optical band gap increase with increase of Cu doping. Small crystallite size, regularity of surface morphology, high transmittance, and tunable band gap, high conductivity, of Fe and Cu doped CeO_2 thin films suggest the suitability of the material in optoelectronic devices and bio sensing applications.

Glucose sensing properties were successfully analyzed by measuring current using electrical four probe method. The highest glucose-sensing response was recorded at about 29% at 5 min for 4 at% Fe concentration into MnO_2. From XRD analysis, it was demonstrated that the maximum sensitivity was obtained for lowest crystallite size of 20 nm. It was evidently shown that and 3D views has a descending trend of the cross-section up to 0.5 mol/L glucose concentration which indicates an increase in sensitivity of MnO_2 nanoparticles. The sensitivity of 4% Fe doped MnO_2 at different glucose concentrations, indicating 92% for 0.05 mol/L, 97% for 0.1 mol/L, 102% for 0.3 mol/L, 112% for 0.5 mol/L and 107% for 1 mol/L respectively. It can be mentioned that sensitivity of 4 at% Fe: MnO_2 is higher than pure MnO_2 under the same glucose concentration. It is demonstrated that Fe: MnO_2 thin film could be a favorable nanostructured biomedical sensor for glucose ($C_6H_{12}O_6$) response. Good sensitivity and response for 4 at % Cu:MnO_2 were obtained. Spray deposited MnO_2 and Cu: MnO_2 thin films give the considerable distinct surface area of the film layer as well as its firm adhesion to the substrate, which in turn contributed to the superior sensitivity of the prepared films.

5.2 Conclusions

In this research work, the surface morphology, structural, optical electrical and glucose sensing properties of Fe and Cu doped Co_3O_4, MnO_2, WO_3 and CeO_2 nanostructured thin films prepared by the spray pyrolysis technique are investigated varying with Fe and Cu doping concentration ranging from 0 to 10 at%. The surface homogeneity increases with Fe and Cu content due to the effect of friction among the charge carriers consisting of agglomerated nanoparticles. Spinel cubic, tetragonal, monoclinic and simple cubic structures were identified for Co_3O_4, MnO_2, WO_3 and CeO_2 thin films respectively by XRD analysis. The Crystallite size lies below 30 nm for all the samples varying with

dopant concentration from 0 to 10 at %. Optical band gaps calculated using Taue relation were 2.02 eV, 3.81eV, 2.72 eV and 3.44 eV for deposited pure Co_3O_4, MnO_2, WO_3 and CeO_2 thin films respectively. The ban gaps were tuned by doping Fe and Cu with different dopant concentration. Carrier concentration also increased with increasing Fe and Cu contents for all oxides. . The highest glucose-sensing response was recorded at about 29% at 5 min for 4 at% Fe concentration into MnO_2. From XRD analysis, it was demonstrated that the maximum sensitivity was obtained for lowest crystallite size of 20 nm. It was evidently shown that and 3D views has a descending trend of the cross-section up to 0.5 mol/L glucose concentration which indicates an increase in sensitivity of MnO_2 nanoparticles. The sensitivity of 4% Fe doped MnO_2 at different glucose concentrations, indicating 92% for 0.05 mol/L, 97% for 0.1 mol/L, 102% for 0.3 mol/L, 112% for 0.5 mol/L and 107% for 1 mol/L respectively. It can be mentioned that sensitivity of 4 at% Fe: MnO_2 is higher than pure MnO_2 under the same glucose concentration. It is demonstrated that Fe: MnO_2 thin film could be a favorable nanostructured biomedical sensor for glucose ($C_6H_{12}O_6$) response. Good sensitivity and response for 4 at % Cu:MnO_2 were obtained. Thus, the obtained crystallite size, regularity of surface morphology, high transmittance, and tunable band gap, high conductivity of 4 at % Fe and Cu doped Co_3O_4, MnO_2, WO_3 and CeO_2 thin films suggest the suitability of the material in optoelectronic devices and bio sensing applications.

5.3 Suggestions for Future Work

This is the first time that nanostructured metal oxides thin films have been prepared and characterized in our laboratory for bio sensing performance. In recent years nanostructured metal oxides specially transition and rare earth metal oxides thin films have a variety of applications for the development of biosensor devices technology. In this digital age, nanostructured Fe and Cu doped Co_3O_4, MnO_2, WO_3 and CeO_2 thin films have vast applications in glucose biosensor technology. To prepare high quality of these films and for their details characterization, more studies are necessary.

Hence to get better performance of these materials prepared by spray pyrolysis method, it is need to characterize magnetic properties characterization of M-H hysteresis curve to measure saturation magnetization (Ms), and magnetic coercivity (Hc) which attribute strong antiferromagnetic coupled interaction between dopants and pure metal ions and show the uniform crystal structure.

Study of transmission electron microscopy (TEM) for better understanding of nanostructures and study of X-ray photoelectron spectroscopy (XPS) for better understanding of composition

Study of glucose sensing properties of the rest films of this thesis work and then find the best suitable candidate for development of biosensor. Study of C_2H_5OH, CH_4, NH_3 etc. gas sensing properties of the films.

Novelty of Ph.D Thesis Work

Metal oxides thin films have wide applications in the field of electronics, optoelectronics, gas sensing and bio sensing devices from many years ago and although a large number of studies have been performed, nowadays nanostructured Co_3O_4, MnO_2 and WO_3 transition metal oxides and CeO_2 rare earth metal oxides thin films are widely applied in biosensor devices because of their cost-effectiveness, quick response, acceptable band gap (1.5-4.0 eV), crystallite size (below 50 nm) and high conducting behavior.

In the present work, we have synthesized nanostructured Co_3O_4, MnO_2, WO_3 and CeO_2 thin films by low cost spray pyrolysis technique and obtained significant properties as porous surface morphology, optical band gap (1.73 eV -3.99 eV), crystallite size (below 40 nm), maximum transmittance (76% -96%) and resistivity of 10^4 Ω-cm in order. We have also observed highest glucose sensing response of MnO_2 thin films. Because of these properties, Co_3O_4, MnO_2, WO_3 and CeO_2 thin films could be suitable candidate for biosensor developments.

REFERENCES

References

[1].   Kaushik, A., Arya, S. K.,   Vasudev, A., and Bhansali, S., " Nanocomposites based on chitosan - metal/metal oxides hybrids for biosensors applications," *J. Nano Scie. Lett.,* Vol. 3, pp 32, 2013.

[2].   Huang, Y. W., Wu, C., and Aronstam, R. S., "Toxicity of transition metal oxide nanoparticles: recent insights from in vitro Studies," *J. of Materials, Scie.* Vol. 3, pp 4842-4859, 2010.

[3].   Bhargava, R., "Properties of wide band gap semiconductors", London, United, Kingdom INSPEC, the Institution of   Electrical Engineers, *J. Chin. Phys. B,* Vol. *22* pp 238, 1997.

[4].   Jyoti Borah, P., Barman, J., and Sarma, K. C., "Structural and optical properties of metal oxides nanoparticles", *J. Appl. Phys Lett,* Vol. 5, No. 9, pp 201- 208, 2008.

[5].   Nithya prakasha, D., Rama murthya, M.,Thiruna vukarasub, P., Balasu pramaniamc,. T.,Chandrasekarana J., and   Maadeswaran, P., "Effect of substrate temperature on structural, optical and thermal properties of chemically sprayed metal oxides thin films", *J. Matt. Research*, Vol. 1, No.1,pp. 42-51, 2009.

[6].   Vinotha   Boorana   Lakshmi, P.,   Sakthi   Raj, K., and   Ramachandran,   K., "Synthesis and   Characterization of nano ZnS doped with Mn", *J. Solid State Electrochem,*   Vol. 44, No. 2, pp 153 – 158, 2009.

[7].   Dinsmore, A. D., Hsu, S. B., Quadri, J.O., Kennedy, T. A., and Gray, H. F., "Structure and luminescence of annealed nanoparticles of ZnS : Mn", *J. Power Source,*   Vol. 88, pp 9, 2000.

[8].   Bhattacharjee, B., Ganguli, D., and Chaudhuri, S., "Synhesis and characterization of sol- gel derived ZnS : Mn^{2+} nanocrystallites embedded in a silica matrix," *J. Adv. Matter*, Vol. 25, No. 3, pp 175-180, 2002.

[9].   Biswas, S., Kar, S., and Chaudhuri, S., "Optical and Magnetic   properties of Manganese-incorporated into oxides nanorods by a solvothermal process", *J. Appl. Mater Interface*, Vol. 109, pp 17526-17530, 2005.

[10].   Uble, A. U., Sangawar, V.S. and Kulkharni, D. K. " Size dependent optical character- ristics of chemically deposited nanostructured ZnS thin films", *J. Mater Res Bull,* Vol. 30, No. 2, pp.147-151, 2007.

[11].   Xu, Y., and Martin A. A. S., "The absolute energy positions of conduction and valence bands of selected semiconducting minerals," *J. of American Mineralogist*, Vol. 85, pp 543, 2000.

[12].   Nasser, A. M. B., Myung, S. K., Faheem, A., S.,| and Hak, Y. K., "Synthesis and optical properties of two Cobalt oxides (CoO and Co_3O_4) nanofibers produced by electro spinning process" *J. Phys. Chem. C,* Vol. 112, pp 12225, 2008

[13].   Jia, C., Xifan, W., Annabella, S., "Electronic structure and bonding properties of cobalt oxide in the spinel structure," *J. of Phys. Rev. B,* Vol. 83, pp 245204, 2011.

[14]. Sahay, P. P., and Kushwaha, A. K., "Electrochemical super capacitive performance of potentiostatically cathodic electrodeposited nanostructured MnO_2 films," *J. Solid State Electrochem,* Vol. 21, pp 2393-2405, 2017.

[15]. Duan, Y., Liu, Z., Zhang, Y., Wen, M., "A theoretical study of the dielectric and magnetic responses of Fe-doped α-MnO_2 based on quantum mechanical calculations," *J. Mate. Chem. C1,* pp 1990–1994, 2013.

[16]. Tian, K., Prestgard, M., and Tiwari, A., "A review of recent advances in nonenzymatic glucose sensors," *Mate. Sci. and Engine. C,* Vol. 41, pp 100-118, 2014.

[17]. Marie, M., Mandal, S., and Manasreh, O., "An Electrochemical Glucose Sensor Based on Zinc Oxide Nanorods," *Sensors,* Vol. 15, pp 18714-18723, 2015.

[18]. Santato, C., Odziemkopwski, M., Ulmann, M., and Augustynski, J., "Crystallographically oriented mesoporous WO3 films: synthesis, characterization, and applications", *J. of Am. Chem. Soc,* Vol. 123, pp 10639-10649, 2001.

[19]. Guo, D. Z., Yu-Zhang, K., Glote, A., Zhang, G. M., and Xue, Z. Q., "Synthesis and characterization of Tungsten oxide nanorods," *J. Mater. Res,* Vol. 19, pp 3665-3670, 2004.

[20]. Granqvist, C. G., "Sol. Energy," *J. Mater. Sol. Cells*, Vol. 60, pp 201, 2000.

[21]. Bamwenda, R. G., Sayama, K., and Arakawa, H., *J. Photochem. Photobiol* A, Vol. 122, pp 175, 1999.

[22]. O-Rueda de Leon, J. M., Acosta, D. R., Pal, U., and Castaneda, L., " Improving electrochromic behavior of spray pyrolised WO_3 thin solid films by Mo doping," *Electrochem. Acta,* Vol. 56, pp 2599–2605, 2011.

[23]. Z Hu, S Haneklaus, G Sparovek and E Schnug Commun. Soil. Sci. Plant. Anal. Vol. 37, pp 1381, 2006.

[24]. A Medalia and B Byrne Anal. Chim, Vol.. 23, pp 453, 1951.

[25]. Sun, C., Li, H., Zhang, H., Wang, Z., Chen, L., "Controlled synthesis of CeO_2 nanorods by a solvothermal method," J. of *Nanotech.,* Vol. 16, pp 1454–1463, 2005.

[26]. Ho, C., Yu, J.C., Kwong, T., Mak, A. C., Lai, S., "Morphology-controllable synthesis of mesoporous CeO_2 nano-and microstructures," *J. of Chem. Mate.,* Vol. 17, 4514–4522, 2005.

[27]. Tang, B., Zhuo, L., Ge, J., Wang, G., Shi, Z., Niu, J., "A surfactant-free route to single-crystalline CeO_2 nanowires," *J. of Chem. Cmmun,* Vol. 28, pp 3565–3567, 2005.

[28]. Jiang, Y. Z., and Bahlawane, N., "Changes in the structural and optical properties of CeO_2 nanocrystalline films: effect of film thickness," *J. Alloys Comp*, Vol. 485, pp L52–L55, 2009.

[29]. Bhosale, A. K., Tarwal, N. L., Shinde, P. S., Kadam, P. M., Patil, R. S., Barman, S. R., and Patil, P. S., "Effective utilization of spray pyrolysed CeO_2 as optically passive counter electrode for enhancing optical modulation of WO_3," *J. of Solid State Ionics,* Vol. 180, pp 1324–1331, 2009.

[30]. Listorti, A., Oregan, B., Durrant, R., "Electron transfer dynamics in dye-sensitized solar cells," *J. of Chem Mater,* Vol. 23, pp 3381–3399, 2011.

[31]. Qu, Q., Wang, B., Chen, Y., Tian, S., Wu, Y., Holze, R., "Electrochemical performance of MnO_2 nanorods in neutral aqueous electrolytes as a cathode for asymmetric supercapacitor," *J. of Phys Chem C,* Vol. 113, pp 14020-14027, 2009.

[32]. Li, Q., Sun, X., Lozano, K., Mao, Y., "Asymmetric super capacitors with dominant pseudo capacitance based on manganese oxide nano flowers in a neutral aqueous electrolyte," *J. of RSC Adv,* Vol. 3, pp 24886–24890, 2013.

[33]. Hyun-Jeong, N., Takeshi, S., Naoto K., "Optical CO gas sensor using a cobalt oxide thin film prepared by Pulsed Laser deposition under various Argon pressures.," *J. of Phys. Chem. B,* Vol. 110, pp 23081-23084, 2006.

[34]. Ajeet, K., Sunil, K., Arya, A. V., Shekhar, B., "Nano composites based on chitosan-metal/metal oxides hybrids for biosensors applications", *J. Nano. Sci. Let.* Vol. 3, pp. 32, 2013.

[35]. Gavin, J. R., "The importance of monitoring blood glucose in US endocrine disease ,Touch Briefings," *Atlanta, GA, USA,* pp. 1–3, 2007.

[36]. Hartono, A., Sanjaya, E., Ramli, R., "Glucose sensing using capacitive biosensor based on Polyvinylidene fluoride thin film," *J. of Biosensors,* Vol. 8, pp 12, 2018.

[37]. Marie, M., Mandal, S., Manasreh, O., "An electrochemical glucose sensor based on cobalt oxide nanofiber," *J. of Sensors,* Vol. 15, pp 18714-18723, 2015.

[38]. Clark, L. C., and Lyons, C., "Electrode systems for continuous monitoring in cardiovascular surgery," *J. of Ann. N. Y. Acad. Sci,* Vol. *102,* pp 29–45, 2006.

[39]. Updike, S. J., and Hicks, G. P., "The Enzyme Electrode," *Nature,* Vol. 214, pp 986–988, 1967.

[40]. Shervedani, R. K., Mehrjardi, A. H., and Zamiri, N., " A novel method for glucose determination based on electrochemical impedance spectroscopy using glucose oxidase self-assembled biosensor," *J. of Bio electro chem,* Vol. 69, pp 201–208, 2006.

[41]. Tang, H., Chen, J. H., Yao, S. Z., Nie, L. H., Deng, G. H., and Kuang, Y. F., "Ampherometric glucose biosensor based on adsorption of glucose oxidase at platinum nanoparticle-modified carbon nanotube electrode," *J. of Anal. Biochem,* Vol. 331, pp 89–97, 2004.

[42]. Heller, A., and Feldman, B., "Electrochemical glucose sensors and their applications in diabetes management," *J. of Chem. Rev,* Vol. 108, pp 2482–2505, 2008.

[43]. Liu, A., "Towards development of chemosensors and biosensors with metal-oxide-based nanowires or nanotubes," *J. of Biosens. Bioelectron,* Vol. 24, pp 167–177, 2008.

[44]. Zhai, T., Fang, X., Liao, M., Xu, X.; Zeng, H., Yoshio, B., and Golberg, D., " A comprehensive review of one-dimensional metal-oxide nanostructure photo detectors," *Sensors,* Vol. 9, pp 6504–6529, 2009.

[45]. Huang, J., and Wan, Q., "Gas sensors based on semiconducting metal oxide one-dimensional nanostructures," *Sensors,* Vol. 9, pp 9903–9924, 2009.

[46]. Wang, Z. L., "Nanobelts, nanowires, and nano diskettes of semiconducting oxides-from materials to nanodevices," *J. of Adv. Mater,* Vol. 15, No. 5, pp 432–436, 2003.

[47]. Shaban, M., Abdelkarem, K., and Sayed, A. M. E., "Structural, optical and gas sensing properties of Cu_2O/ CuO mixed phase: effect of the number of coated layers and (Cr + S) co-doping," *J. of Phase Transit,* Vol. 92, pp 347–359, 2019.

[48]. Liu, Y, Wang, N., Yao, M., Yang, C., Hu, W., and Komarneni, S., " Porous Ag-doped MnO_2 thin films for supercapacitor electrodes," *J. of Porous Mater,* Vol. 24, pp 1717–1723, 2017.

[49]. Tian, Q., Wang, X., Huang, G., and Guo, X., "Nanostructured (Co, Mn)3O4 for high capacitive supercapacitor applications," *J. of Nanoscale Res Lett,* Vol. 12, pp 214–220, 2017.

[50]. Shaban, M., and Sayed, A. M. E., "Structural, optical and photo catalytic properties of Fe and (Co, Fe) co-doped copper oxide spin coated films" *Spectrochim Acta A Mol Biome Spectrosc,* Vol. 149, pp 638–646, 2015.

[51]. Newman, J., and Turner, A. P. F., "Home blood glucose biosensors: A commerical perspective," *Biosens. Bio electron.* **2005**, Vol. 20, pp 2435–2453, 2005.

[52]. Boiroux, D., Batora, V., Hagdrup, M., Tarnik, M., Murgas, J., Schmidt, S., Norgaard, K., Poulsen, N. K., Madsen, H., and Jorgensen, J. B., "Comparison of prediction models for a dual-hormone artifical pancreas," *IFAC-Papers Online* Vol. 48, pp 7–12, 2015.

[53]. Laouinia, E., Hamdani, M., Pereira, M. I. S., Doucha, J., Mendonc, M. H., Y. Berghoutea, Y., and Singh, R. N., " Preparation and electrochemical characterization of spinel type Fe - Co_3O_4 thin film electrodes in alkaline medium," *J. of hydrogen energy*, Vol. 33, pp 4936-4944, 2008.

[54]. Bahlawane, N., Herve, P., Ngamou,T., Vannier,V., Kottke,T., Heberle, J., and Kohse-Hoinghaus, K., "Tailoring the properties and the reactivity of the spinel cobalt oxide," *J. of Phys. Chem*, Vol. 11, pp 9224–9232, 2009

[55]. Garcia, H. A., Melo J. R. P., Azevedo, A., and Araujo, C. B., "Optical and structural characterization of iron oxide and cobalt oxide thin films at 800 nm," *J. of Appl. Phys. B,* Vol. 111, pp 313-321, 2013.

[56]. Grewe, T., Deng, X., and Tuysuz, H., "Influence of Fe doping on structure and water oxidation activity of nano cast Co_3O_4," *J. of Chem. Mater*, Vol. 26, pp 3162-3168, 2014.

[57]. Manickam, M., Ponnuswamy, V., Sankar, C., Suresh, R., Mariappan, R., A. Chandrabose, A., and Chandrasekaran, J., "Structural, optical, electrical and electrochemical properties of Fe:Co_3O_4 thin films for supercapacitor applications," *J. of Mater Sci: Mater Electron,* DOI. 10.1007/s10854-017-7849-7

[58]. Toro, L. R. A., Berenguer, R., Quijada, C., Montilla, F., Morallon, E., and Vazquez, J. L., "Preparation and characterization of copper-doped cobalt oxide electrodes", *J. of Phys. Chem. B,* Vol. 110, pp 24021-24029, 2006.

[59]. Yamada, Y., Yano, K., Xu, Q., and Fukuzumi, S., "Cu/Co$_3$O$_4$ nanoparticles as catalysts for Hydrogen evolution from Ammonia Borane by hydrolysis", *J. of Phys. Chem. C*, Vol. 114, pp 16456-16462, 2010.

[60]. Mehrabadi, Z. S., Ahmadpour, A., Shahtahmasebi N., and Mohagheghi, M. M. B., "Synthesis and characterization of Cu doped cobalt oxide nanocrystals as methane gas sensors," *J. of Phys. Scr*, Vol. 84, pp 015801, 2011.

[61]. Amri, A., Jiang, Z. T., Bahri, P. A., Yin, C. Y., Zhao, X., and Xie, Z., "Surface electronic structure and mechanical characteristics of copper-cobalt oxide thin film coatings: soft X-ray synchrotron radiation spectroscopic analyses and modeling," *J. of Phys. Chem. C*, Vol.117, pp 16457−16467, 2013.

[62]. Hassan, A. I., "Preparation and characterization of Cu:Co$_3$O$_4$/Si heterojunction prepared by spray pyrolysis," Energy Procedia, Vol. 119, pp 961-971 967, 2017.

[63]. Harry, M., Chowdhury, M., and Cummings, F., "Elemental Cu doped Co$_3$O$_4$ thin film for highly sensitive non-enzymatic glucose detection," *Sensing and Bio-Sensing Research*, https://doi.org/10.1016/j.sbsr.2019.100262, 2019.

[64]. Shen, X., Morey, A. M., Liu, J., Ding, Y., Cai, J., Durand, J., and Wang, Q., "Characterization of the Fe-Doped mixed-valent tunnel structure manganese oxide KOMS-2," *J. Phys. Chem. C*, Vol. 115, pp 21610-21619, 2011.

[65]. Dubal, D. P., Kim, W. B., Lokhande, C. D., "Galvanostatically deposited Fe:MnO$_2$ electrodes for supercapacitor application," *J. of Phys and Chem of Solids*, Vol. 73, pp 18-24, 2012.

[66]. Ma, Y., Fang, C., Ding, B., Ji, G., and Lee, J. Y., "Fe doped Mn$_x$O$_y$ with hierarchical porosity as a high-performance Lithium-ion battery anode," *J. of Adv. Mater*, Vol. 25, pp 4646-4652, 2013.

[67]. Yang, P., Ding, Y., Lin, Z., Chen, Z., Li, Y., Qiang, P., "Low cost high-performance solid-state asymmetric supercapacitor based on MnO$_2$ nanowires and Fe$_2$O$_3$ nanotubes," *J. of Nano Lett*, http://pubs.acs.org, 2014.

[68]. Huang, R., Liu, Y., Chen, Z., Pan, D., Li, Z., Wu, M., and Shek, C. H., "Fe species loaded mesoporous MnO$_2$ super structural requirements for enhanced catalysis," *ACS Appl. Mater. Interfaces*, http://pubs.acs.org, 2015.

[69]. Chodankar, N. R., Dubal, D. P., Lokhande, A. C., Patil, A. M., Kim, J. H., and Lokhande, C. D., "An innovative concept of use of redox-active electrolyte in asymmetric capacitor based on MWCNTs/MnO$_2$ and Fe$_2$O$_3$ thin Films," *Scientific Reports*, DOI: 10.1038/srep39205, Vol. 6, pp 39205, 2016.

[70]. Hiraga, H., Fukumura, T., Ohtomo, A., T. Makino, T., Ohkubo, A., Kimura, H., and Kawasaki, M., " Optical and magnetic properties of CuMnO$_2$ epitaxial thin films with a delafossite-derivative structure," *J. of Appl. Phys. Lett*, Vol. 95, pp 032109, 2009.

[71]. Caia, L. N., Guoa, Y., Lua, A. H., Branton, P., and Li, W. C., "The choice of precipitant and precursor in the co-precipitation synthesis of copper manganese oxide for maximizing carbon monoxide oxidation," *J. of Molecular Catalysis A: Chemical* Vol. 360, pp 35-4, 2012.

[72]. Falahatgar, S. S., Ghodsi, F. E., Tepehan, F. Z., Tepehan, G. G., and Turhan, I., Electrochromic performance, wettability and optical study of copper manganese oxide thin films: Effect of annealing temperature," *J. of App. Surf Sci*, Vol. 289, pp 289-299, 2014.

[73]. Poonguzhali, R. S., Gobi, R., Shanmugam, N., Animalia Senthil Kumar Govintha, K. A. S., Kannadasan, V. N., "Enhancement in electrochemical behavior of copper doped MnO$_2$ electrode," *J.   of   Mater   Lett*,   2015, http://dx.doi.org/10.1016/j.matlet.2015.05.086.

[74]. Falahatgar, S. S., and Ghodsi, F. E., "Annealing Temperature Effects on the Optical properties of MnO$_2$:Cu nanostructured thin films," *J. of Nano sci. Nanotech,* Vol. 12, No. 1, pp 7-18, 2016.

[75]. Xu, S., Lu, L., Liu, L., Luo, Z., Wang, S., Guohu, L., and Feng, C., Hydrothermal synthesis of Cu doped MnO$_2$ nanorods as cathode material for Lithium ion battery applications," *J. of Nano sci. Nanotech*, Vol. 17, pp 3, 2017.

[76]. Comini, E., Pandolfi, L., Kaciulis, S., Faglia, G., and Sberveglieri, G., "Correlation between atomic composition and gas sensing properties in tungsten-iron oxide thin films," *Sens. and Actus B*, Vol. 127, pp 22-28, 2007.

[77]. Dongqin, B., and Yiming, X., " Improved photo catalytic activity of WO$_3$ through clustered Fe$_2$O$_3$ for organic degradation in the presence of H$_2$O$_2$," *Langmuir,* Vol. 27, pp 9359-9366, 2011.

[78]. Ahsan, M., Tesfamichael, T., Ionescu, M., Bell, J., Motta, N., "Low temperature CO sensitive nanostructured WO$_3$ thin films doped with Fe," *Sens and Actus B*, Vol. 162, pp 14-21, 2012.

[79]. Xiaofang, C., Hongwu, F., and Yanqin, W., "Enhanced photo electro chemical performance of Fe doped WO$_3$ film electrode under visible light," *Key Engineering Materials*, Vols. 531-532, pp 230-233, 2013.

[80]. Tesfamichael, C., Pilotou, M., and Arita, J. B., " Fabrication of Fe-doped WO$_3$ films for NO$_2$ sensing at lower operating temperature T," *Sens and Actus B,* Vol. 221, pp 393-400, 2015.

[81]. Carraro, D. B. G., Gasparotto, A., and Maccato, C., "Fe$_2$O$_3$-WO$_3$ nano systems synthesized by a hybrid CVD/sputtering route, and analyzed by X-ray photoelectron spectroscopy," *J. of Surf. Sci. Spectra*, Vol. 23, pp 93, 2016, doi: 10.1116/1.4964351.

[82]. Khare, C., Sliozberg, K., Stepanovich, A., Schuhmann, W., and Ludwig, A., "Combinatorial synthesis and high through put characterization of structural and photo electrochemical properties of Fe:WO$_3$ nanostructured libraries," *J. of Nanotech*, Vol. 28,   pp 185604, 2017

[83]. Gopalan, C., Kozicki, M. N., Bhagat, S., Thermadam, S. C. P., Alford, T. L., and Mitkov, M., " Structure of copper-doped tungsten oxide films for solid-state memory," *J. of Non-Crystalline Solids,* Vol. 353, pp 1844-1848, 2007.

[84]. Zhu, S., Liu, X., Chen, Z., Liu, C., Feng, C., Gu, J., Liu, Q., and Zhang, D., "Synthesis of Cu-doped WO$_3$ materials with photonic structures for high performance sensors," *J. of Mater. Chem,* Vol. 20, pp 9126-9132, 2010.

[85]. Yao, Y., Yamauch, K., Yamauch, G., Ochia, T., Murakam, T., and Kubot, Y., "Synergistic antibacterial performance of a Cu/WO₃-added PTFE particulate super hydrophobic composite under visible-light exposure," *J. of Biomats and Nano biotech,* Vol. 3, pp 421-430, 2012.

[86]. Zhou, H., Xu, D. Y., Zuo, H. Q., Liu, W., and Lin, S., " Preparation of flower-like Cu-WO₃ nanostructures and their acetone gas sensing performance," *J. of Chem ,* Vol. 10, pp 1155, 2015, http://dx.doi.org/10.1155/2015/382087.

[87]. Mehmood, F., Iqbal, J., Ahmed, W., and Ismail, M., "Facile synthesis of Cu doped 2-D WO₃ nanoplates with structural, optical and differential anti cancer characteristics," *Physica E: Low-dimensional Systems and Nanostructures*, 2016, http://dx.doi.org/10.1016/j.physe.2016.12.008.

[88]. Deepa, B., and Rajendran, V., "Pure and Cu metal doped WO₃ prepared via co-precipitation method and studies on their structural, morphological, electrochemical and optical properties," *Nano-Structures & Nano-Objects,* Vol. 16, pp 185-192, 2018.

[89]. Kavitha, V. S., Chalana, S. R., Krishnan, R. R., Gopchandran, K. G., V.P. Pillai, V. P.M., "High quality, highly transparent Cu incorporated WO₃ thin films suitable for blue LED application," *J. of Vacuum,* Vol. 172, pp 1090442, 2020.

[90]. Yang, W., Li, D., Xu, D., and Wang, X., "Effect of CeO₂ preparation method and Cu loading on CuO/CeO₂ catalysts for methane combustion," *J. of Natural Gas Chemistry,* Vol. 18 No. 4, 2009.

[91]. Slusser, P., Kumar, D., and Ashutosh Tiwari, A., " Unexpected magnetic behavior of Cu-doped CeO₂" J. of Appl. Phys. Lett, Vol. 96, pp 142506, 2010.

[92]. Zhang, D., Qian, Y., Shi, L., Mai, H., Gao, R., Zhang, J., Yu, W., and Weiguo C., " Cu-doped CeO₂ spheres: synthesis, characterization, and catalytic activity," Catalysis Communications, Vol. 26, pp 164-168, 2012.

[93]. Knauth, P., Saltsburg, H., Engel, J., and Tuller, H. L., "In situ dilatometric and impedance spectroscopic study of core-shell like structures: insights into the exceptional catalytic activity of nanocrystalline Cu doped CeO₂," *J. Mater. Chem. A,* Vol. 3, No. 55, pp 41, 2015, DOI: 10.1039/c4ta07181f.

[94]. Sani, K. Z., Ghodsi, E. G., and Mazloom, J., " Surface morphology effects on Li ion diffusion toward CeO₂:Cu nanostructured thin films incorporated in PEG matrix," *J. of Sol-Gel Sci Technol*, Vol. 82, pp 643–653, 2017, DOI 10.1007/s10971-017-4364-5.

[95]. Alla, S. K., Kollu, P., Mandal, R. K., and Prasad N. K., " Magnetic properties of Cu doped CeO₂ nanostructures prepared by microwave refluxing technique," *Ceramics International*, 2018, https://doi.org/10.1016/j.ceramint.2018.01.171.

[96]. Kumara, K., Alafia, R. N., Chawla, A. K., Kumar, R., P.A. Alvi, P. A., Alshoaibi, A., Vij, A., Ahmed, F., Abu-samak, M., S. Kumar, S., " Engineering the optical properties of Cu doped CeO₂ NCs for application in white LED," *Ceramics International*, Vol. 11, pp 246, 2019.

[97]. Qi-Ye, W., Hua-Wu, Z., Qing-Hui, Y., Sheng, L., De-Gang, X., Jian-Quan, Y., "Fe-doped polycrystalline CeO_2 as terahertz optical material," *J. of Chin. Phys. Lett,* Vol. 26, No. 4, pp 047803, 2009.

[98]. Sharma, S. K., Thakur, P., Kumar, S., Shukla, D. K., Brookes, N. B., Lee, C. G., Pirota, K. R., Koo, B. H., Knobel, M., "Room temperature ferromagnetism in Fe-doped CeO_2 thin films grown on LaAlO3 (001)," *Thin Solid Films,* Vol. 519 pp 410-413, 2010.

[99]. Wanga, Z., Xina, Y., Zhanga, Z., Li, Q., Zhanga, Y., and Zhou, L., "Synthesis of Fe-doped CeO_2 nanorods by a widely applicable precipitation route," *J. of Chem Eng.,* Vol. 178, pp 436-442, 2011.

[100]. Wang, W. C., Chen, S, Y., Glans, P. A., Guo, J., Chen, R. J., and Fong, K. W., "Towards understanding the electronic structure of Fe-doped CeO_2 nanoparticles with X-ray spectroscopy," *J. of Phys. Chem. Chem. Phys.*, Vol. 15, pp 14701, 2013.

[101]. Phokha, S., Pinitsoontorn, S., and Maensiri, S., "Structure and magnetic properties of monodisperse Fe^{3+} doped CeO_2 Nanospheres," *J. of Nano-Micro Lett.*, Vol. 5, No. 4, pp 223-233, 2013.

[102]. Channei, D., Inceesungvor, B., Wetchakun, N., Ukritnukun, S., Nattestad, A., Chen, J., and Phanichphant, S., "Photocatalytic degradation of methyl orange by CeO_2 and Fe-doped CeO_2 films under visible light irradiation," *Scientific Reports*, Vol. 4, pp 5757, 2014, DOI: 10.1038/srep05757

[103]. http://en.wikipedia.org/wiki/Chemical bath deposition.

[104]. Lincot, D., and Hodes, G., "Chemical solution deposition of semiconducting and non-metallic films," *Proc. Int. Symp. Electrochem. Soc.*, pp 2003-2032, 2006.

[105]. "Spin Coaters, Information." http://www.globalspec.com/learnmore/ manufacturing process equipment/surface coating protection/spin coaters. Accessed: 2015.

[106]. Scriven, L. E., "Physics and applications of dip coating and spin coating", *J. of Mater. Res. Soc. Symp. Proc.,* Vol. 121, pp 717-729, 1988.

[107]. Brinker, C. J., Hurd, A. J., Frye, G. C., Ward, K. J., and Ashley, C, S., "Sol-gel thin film formation", *J. of Non-Crystalline Solids,* vol. 121 No. 1-3, pp 294-302, 1990.

[108]. Hench, L. L., West, J.K., "The Sol-Gel Process", *J. of Chem. Rev.*, Vol. 90, No. 1, pp 33-72, 1990.

[109]. "Wet coating technologies for glass." http://www.solgel.com/articles/Nov00/ mennig.htm. Accessed: 18 May 2015.

[110]. Brinker, C. J., Frye, G. C., Hurd, A. J., and Ashley, C. S., "Fundamentals of sol-gel dip coating", *Thin Solid Films*, Vol. 201, No. 1, pp 97-108, 1991.

[111]. Nithyaprakash, D., Ramamurthy, M., Thirunavukarasu, P., Balasubramaniam, T., Chandrasekaran, J., and Maadeswaran, P., "Effect of substrate temperature on structural, optical and thermal properties of chemically sprayed ZnS thin films," *J. of Optoelectronic and Biomedical Materials*, Vol. 1, No. 1, pp 42-51, 2009.

[112]. Khatami, S. M. N., and Ilegbusi, O. J., "Droplet evaporation and chemical reaction in a single multi-component droplet to synthesis mixed-oxide film using spray pyrolysis

method." *International Mechanical Engineering Congress and Exposition, Houston,* https://doi.org/10.1115/IMECE2012-86382, pp 633-638. 9-15 November 2012.

[113].   Mooney, J. B., and Radding, S. B., "Spray Pyrolysis Processing", Annual Review of Materials Science, Vol. 12, pp 81-101, 1982.

[114].   Patil, P. S., "Versatility of chemical spray pyrolysis technique", *J. of Mate Chem and Phys,* Vol. 59, No. 3, pp 185-198, 1999.

[115].   Messing, G. L., Zhang, S. C, Jayanthi, G. V., " Ceramic powder synthesis by spray-pyrolysis," *J. of Am Ceram Soc,* Vol. 76, pp 2707-2726, 1993.

[116].   Jain, S., Skamser, D. J., and Kodas, T. T., "Morphology of single-component particles produced by spray pyrolysis," *J. of Aerosol Sci Technol*, Vol. 27, No. 5, pp 575-590, 1997.

[117].   Kodas, T. T., Hampden-Smith, M., J., "Aerosol processing of materials," Wiley-VCH publication, 1999.

[118].   Gurav, A., Kodas, T., Pluym, T., Xiong, Y., "Aerosol processing of materials," *J. of Aerosol Sci Technol*, Vol. 19, pp 411, 1993.

[119].   Xiong, Y., Kodas, T., "Droplet evaporation and solute precipitation during spray pyrolysis," *J. of Aerosol Sci*, Vol. 24, No. 7, pp 893-908, 1993.

[120].   Choy, K. L., and Su, B., "Growth behavior and microstructure of CdS thin films deposited by an electrostatic spray assisted vapor deposition (ESAVD) process", *Thin Solid Films,* Vol. 388, No. 1-2, pp 9-14, 2001.

[121].   Viguie, J. C., and Spitz, J., "Chemical vapor deposition at low temperatures", *J. of the Electrochemical Society,* Vol. 122, No. 4, pp 585-588, 1975.

[122].   Afify, H. H., Nasser, S. A., and Demian, S. E., "Influence of substrate temperature on the structural, optical and electrical properties of ZnO thin films prepared by spray pyrolysis," *J. of Mate Scie: Mate in Elect*, Vol. 2, No. 3, pp 152-156, 1991

[123].   Siefert, W., "Properties of thin In_2O_3 and SnO_2 films prepared by corona spray pyrolysis, and a discussion of the spray pyrolysis process," *Thin Solid Films*, vol. 120, No. 4, pp 275–282, 1984.

[124].   Chamberlin, R. R., and Skarman, J. S., "Chemical spray deposition process for inorganic films," *J. of Electrochemical Society*, Vol. 113, No. 1, pp 86-89, 1966.

[125].   Chen, C. C., Nasrallah, M. M., and Anderson, H. U., "Synthesis and characterization of $(CeO_2)_{o.8}(SmO_{1.5})_{0.2}$ thin films from polymeric precursors," *J. of the Electrochemical Society*, Vol. 140, No. 12, pp 3555-3560, 1993.

[126].   Stepien et al. "Nanoparticle formation" *Nanoscale Research Letters,* Vol. 8 (1) , pp. 1-6, 2013.

[127].   G. Messing, S. Zhang, and V. Jayanthi, J. Amer. Ceram. Soc., 76, 2707, 1993.

[128].   Chopra, K. L., "Nucleation, Growth and Structure of Films" Thin Film Phenomena, McGraw-Hill Book Company-New York, pp 110-137, 1969.

[129]. Pashley, D. W. and Stowell M. J., in S.S. Breese (Ed.), Proc.5th Intern. Cogner. Electron microscope, PGGI. Academic press Inc, New York, 1962.

[130]. Lampkin, Curt M., "Aerodynamics of nozzles used in spray pyrolysis". Prog. Crysal Growth Chract. Vol. 1, pp. 406-416, 1979.

[131]. Choudhury, C., Sehgal H. K., "Properties of spray deposited cobalt oxide selective coating on aluminum and galvanized iron substrate", Appl. Energy, 10, 313-324, 1982.

[132] Brown, R., Maissel, L. L., and Glang, R. (eds), "Hand Book of Thin Film Technology", Mc Graw Hill, New. York, pp. 10-12, 1970

[133]. Tareev, B., "Physics of Dielectric Materials", Mir Publisher, Moscow, pp 46, 1975.

[134]. Sebastain , T., Jayakrishnan, R,. Kartha, C. S., Vijayakumar, K. P., "Characterization of spray pyrolysed CuInS$_2$ thin films", *Open Surf Sci*, Vol. 1, No. 1, pp 1-6, 2009.

[135]. Messing, G. L., Zhang, S. C., Jayanthi, G. V., "Ceramic powder synthesis by spray-pyrolysis," *J. of Am Ceram Soc*, Vol. 76, pp 2707-2726, 1993.

[136]. Gurav, A., Kodas, T., Pluym, T., Y. Xiong, Y., " Aerosol processing of materials," *Aerosol Sci Technol*, Vol. 19, pp 411, 1993.

[137]. Lyons, S. W., Wang, L. M., Kodas, T. T., "Nanophase oxide formation by interparticle reaction," *Nanostructure Mater*, Vol. 1 pp 283-291, 1992.

[138]. Kadam, L. D. , Patil P. S., "Thickness- dependent properties of sprayed cobalt oxide thin films," *J. of Mater. Chem. Phys*, Vol. 68, pp 225-232, 2001

[139]. Islam, M. R., Podder J., "Optical properties of ZnO nanofiber thin films grown by spray pyrolysis of zinc acetate precursor", *Cryst. Res. Technol.*, Vol. 44, No. 3, pp 286- 292, 2009.

[140]. Affreen, S., Balamurugan D., Jeyaprakash B.G., "Thickness dependent physical property of spray deposited ZnFe2O4 thin film" *J. Appl. Sci.*, Vol. 12, pp 1636-1640, 2012.

[141]. Chen, C. H., Kelder, E. M., Puw, P.J.M. V., and Schoonman, J., "Morphology control of thin LiCoO$_2$ films fabricated using the electrostatic spray deposition (ESD) technique," *J. of Mate Chem*, Vol. 6, No. 5, pp 765-771, 1996.

[142]. Chamberlin, R. R., Skarman J. S., "Chemical spray deposition process for inorganic films", *J. Electrochem. Soc,* Vol. 113, No. 1, pp 86-89, 1966.

[143]. Altiokka, B., Aksay S., "Optical properties of CuInS2 films produced by spray pyrolysis method", *J. Arts and Sci. Sayi.*, Vol. 3, pp 27-34, 2005.

[144]. Riveros R., Romero E., Gordillo G., "Synthesis and characterization of highly transparent and conductive SnO2:F and In2O3:Sn thin films deposited by spray pyrolysis", *Braz. J. of Phys.*, Vol. 36, No. 3B, pp 1042-1045, 2006.

[145]. Lewis, B., and Champbell, D. S., "Nucleation and initial growth behavior of thin film deposits," *Vac. Sci. Technol.* Vol. 4, No. 5, pp 209, 1967.

[146]. Brown, R., Maissel, L. L., and Glang, R. (eds), "Hand Book of Thin Film Technology", Mc Graw Hill, New. York, pp 10-12, 1970.

[147]. Altiokka, B., and Aksay, S., "Optical properties of CuInS$_2$ films produced by spray pyrolys is method," *J. of Arts and Scie*, Vol. 31, pp 27-34, 2005.

[148]. Goldstein, J., Scanning Electron Microscopy and X-Ray Microanalysis, Springer, ISBN 978-0-306-47292-3. Retrieved 26 May 2012.

[149]. Syuhaimi, M., Rahman, A., Azie, N., Arif, A. M., and Shaari,S., "Effect of thermal treatment on the morphology of ZnS:Mn nanocrystals", *J. of World Appl Scie,* Vol. 12, No. 9, pp 1505-1511, 2011.

[150]. Yamamura, S., Momose, Y., "Quantitative analysis of crystalline Pharmaceuticals in powders and tablets by a pattern-fitting procedure using X-ray powder diffraction data", *Int. J. of Pharmaceutics*, Vol. 212, pp 203-212, 2001.

[151]. XRD picture. Available, http://tap.iop.org/atoms/xray/530/imgfull47305.gif

[152]. Kittel, C., "Introduction to Solid State Physics", 7th edition, Jhon wiley and Sons, Inc., New York, CIP. 14445, Vol. 95, 1996.

[153]. Cullity, B. D., S.R. Stock, S. R., "Elements of X-Ray Diffraction," third ed., Prentice-Hall, New Jersey, pp 664, 2001.

[154]. Barret, C. S., Massalski, T. B., "Structure of Metals: Crystallographic Methods, Principles, and Data," Pergamon Press, Oxford, UK, pp 204, 1980.

[155]. Wiener, O. Wied, Journal of Electronic materials, 31, p53, 1887.

[156]. Tolansky S., " Multiple Beam Interferometry of Surface and Films", Oxford University Press, 1948.

[157]. Gtting, J. G., and Nikol, W. S., "Double- Layer Interference in Air CdS Films", *J. of Opt. Soc. Am.,* Vol. 56, No. 9, pp 1227-1230, 1966.

[158]. Kittel, C., "Introduction to Solid State Physics", 7th edition,Jhon wiley and Sons, Inc., New York, Vol. 95, No. 14445, 1996.

[159]. Bardeen, R. "Chem. Vap. Deposition" , Vol. 56, pp 53, 1887.

[160]. Pankove, J. I., "Optical processes in semiconductors," Prentice-Hall, New York, 1971.

[161]. Fredrick, W., "Optical properties of solids," Academic Press. New York, 1972.

[162]. Lothian, G. F., "Absorption Spectrophotometry" 2nd edn, Hisher and Watts Ltd., London, Vol. 19, No. 20, 1958.

[163] Bouguer, P., "Essai optique surla gradation de la lumière", Claude Jombert, Paris, 1729.

[164]. Moss, T. S., 'Optical properties of semiconductors," Butterworth and Co Pub. Ltd., London, Vol. 2, 1961.

[165]. Harbeke, G., "Optical properties of semiconductors," North-Holland Pub. Co. Amsterdam, 1972.

[166]. Mahon, M. B., Kurtz, S., Emery, K., and Young, M., " Criteria for the design of GaIn P/Ga As/Ge triple junction cells to optimize their performance outdoors," *29th IEEE PVSC*, New Orleans, 2002.

[167]. Pentia, E., Draghici, V., Sarua, G., Mereu, B., Pintilie, L., Sava, F., and Popescu, M., "Structural electrical and photoelectrical properties of CdxPb1-xS thin film prepared by chemical bath deposition," *J. Electrochem. Soc.* Vol. 151 (11) 729-733, 2004.

[168]. Elliot, S.R.(1984), Physics of amorphous materials, Longman London.

[169]. Seraphin, B.O. and A.B.Meinel (1976), Optical properties of solids. New development, B.O Seraphin (ed), North-Holland Pub. Amsterdan 927.

[170]. Heavens, O.S.(1955), Optical properties of thin solid films, Butterworths, London.

[171]. Zor. M., Aksay, S., Kul, M., and Aybek, A. S., "DC and AC Properties of the Compound Semiconductors Prepared by Spray Pyrolysis", Balkan Phys. Lett., Vol. 5, pp. 1132-1135, 1997

[172]. Paulnack, C. L., Chaplin, N.J., "Minimal Maintenance Probe for Precise Resistivity Measurement of Semiconductors", Rev. Sci. Instrum. 33, 873-875, 1962.

[173]. Hamnett A. Solid State Chemistry. Cheetham A, Day P, editors. Oxford; 1988.

[174]. Rahman, M. M., Ahammad, A. J. S., Jin, J. H., Ahn, S. J., and Lee, J.J., "A comprehensive review of glucose biosensors based on nanostructured metal-oxides," *Sensors*, Vol. 10, pp 4855, 2010.

[175]. Wang, Y., Xu, H., Zhang, J., and Li, G., "Electrochemical sensors for clinic analysis," *Sensors,* Vol. 8, pp 2043-2081, 2008.

[176]. Guan, J. G., Miao, Y. Q., and Zhang, Q. J., "Impedimetric Biosensor," *J. Biosci. Bioeng.,* Vol. 97, pp 219-226, 2004

[177]. Fuchs, K., and Katz, U., "Molecular dynamics of carbohydrate aqueous solutions. dielectric relaxation as a function of glucose and fructose concentration," *J. Phys. Chem., Sect. B*, Vol. 105, pp 2036-2042, 2001.

[178]. Caduff, A., Hirt, E., Feldman, Y., Ali, Z., and Heinemann, L., " First human experiments with a novel non-invasive, non-optical continuous glucose monitoring system," *Biosens. Bioelectron*., Vol. 19, pp 209-217, 2003.

[179]. Wang, J., "Ampherometric biosensors for clinical and therapeutic drug monitoring: a review," *J. Pharm. Biomed. Anal*., Vol. 19, pp 47-53, 1999.

[180]. Zhu, Z., Gancedo, L. G., Flewitt, A. J., Xie, H., Moussy, F., and Milne, W. I., "A critical review of glucose biosensors based on carbon nanomaterials: carbon nanotubes and graphene," *Sensors,* Vol. 12, pp 5996, 2012.

[181]. Park, S., Boo,H., and Chung, T. D., " Electrochemical non-enzymatic glucose sensors," *Anal. Chim. Acta*. Vol. 556, pp 46-57, 2006.

[182]. Adawiya, J. H., Ali J. M., Suaad, S. S., Khaled, Z. Y., and Mohammed, J. H., "Sensing characteristics of nanostructured SnO2 thin films as glucose sensor," *Energy Procedia*, Vol. 119, pp 473-481, 2017.

[183]. Willander, M., Usman A. S. M., Nur, O., and Danielsson, B., " Glucose detection with a commercial MOSFET using a ZnO nanowires extended gate," *IEEE Ttrans. On Nanotech.*, Vol. 8, N0. 6, pp 678-783, 2009.

[184]. Kondo,T., et al., "Amperometric sensing of H2O2 and glucose using wet-chemically deposited MnO2 thin films," *J. Ceram. Soc. Jpn.,* Vol. 126, pp 260–262, 2018.

[185]. Zhang, M., et al., "Highly sensitive glucose sensors based on enzyme-modified whole-graphene solution-gated transistors," *Sci. Rep.* Vol. 5 (2015) pp 8311, 2015 https://doi.org/10.1038/srep083112.

[186]. Pletcher, D., "Electrocatalysis: present and future," *J. Appl. Electrochem.* Vol. 14, pp 403-415, 1984.

[187]. Deng, C., Wang, A., Fu, D., Chen, J., and Zhang, X., "Rapid analysis of essential oil from Fructus Amomi by pressurized hot water extraction followed by solid-phase micro extraction and gas chromatography–mass spectrometry," *J. Pharm. Biomed. Anal,* Vol. 38, pp 326-331, 2005.

[188]. Burke, L. D., "Premonolayer oxidation and its role in electro catalysis," *Electrochem. Acta*, Vol. 39, pp 1841, 1994.

[189]. Esser, P., and Gopel, W., "Physical adsorption on single crystal zinc oxide," *Surf. Sci.,* vol. 97, pp. 309-318, 1980.

[190]. Wilson, D. M., Hoyt, S., Janata, J., Booksh, K., and Obando, L., "Chemical sensors for portable, handheld field instruments," *J. IEEE Sensors,* vol. 1, no. 4, pp 256-274, 2001.

[191]. Liu, X.W., Hu, Q., Wu, Q., Zhang, W., Fang, Z., Xie, Q., "Aligned ZnO Nanorods: A useful Film to fabricate ampherometric glucose biosensor," *Colloid Surf. B-Bio interfaces,* Vol. 74, pp 154-158, 2009.

[192]. Sang, H. K., Umar, A., Hwang, S. W., "Rose-like CuO nanostructures for highly sensitive glucose chemical sensor application," Ceramics International, http://dx.doi.org/10.1016/j.ceramint.2015.04.003 , *j. Ceram Int.,* Vol. 4, pp 1-26, 2015.

[193]. Grewe, T., Deng, X., and Tuysuz, H., "Influence of Fe doping on structure and water oxidation activity of nanocast Co_3O_4," *J. Chem. Mater.* Vol. 26, pp 3162-3168, 2014

[194]. Yu J. C., Yu, J. G., Tang, H. Y., Zhang, L. Z., "Effect of surface microstructure on the photo induced hydrophobicity of porous TiO_2 thin films," *J. Mater Chem*, Vol. 12, pp 81-85, 2002.

[195]. Manickam, M., Ponnuswamy, V., Sankar, C., Suresh, R., Mariappan, R., Bose, A. C., Chandrasekaran, J., "Structural, optical, electrical and electrochemical properties of Fe:Co_3O_4 thin films for supercapacitor applications," DOI 10.1007/s10854-017-7849-7 , *J. Mater Sci: Mater Electron*, pp 1-15, 2017..

[196]. Nagato, K., Furubayashi, M., Hamaguchi, T., Nakao, M., "Direct synthesis of vertical α-Fe_2O_3 nanowires from sputtered Fe thin film," *J. Vac. Sci. Technol. B, Vol.* 28, pp C6P11, 2010.

[197]. Mariappan, R., Ponnuswamy, V., Suresh, P., Suresh, R., Ragavendar, M., "Nanostructured $Gd_xZn_{1-x}O$ thin films by nebulizer spray pyrolysis technique: role of doping concentration on the structural and optical properties," *Super lattices and Microstructures*, Vol. 59, pp 47–59, 2013.

[198]. Cullity B. D., and Stock, S. R., "Elementary of X-Ray Diffraction", Third Edition, Prentice Hall in the United States of America, 2001.

[199]. Blake, R. L., Hessevick, R. E., Zoltai, T., and Finger, L. W., "Refinement of the Hematite Structure," *Am.Mineral.*, vol. 51, pp 123-129, 1966.

[200]. Jogade, S. M., Sutrave, D. S., Patil, V. B., "Structural and morphological properties of Mn-doped Co_3O_4 thin film deposited by spin coat method," *J. Eng. Research Appl,* Vol. 6, pp 41-46, 2016.

[201]. Bahlawane, N., Ngamou, P. H. T., Vannier, V., Kottke, T., Heberle, J., and Kohse-Hoinghaus, K., "Tailoring the properties and the reactivity of the spinel cobalt oxide," *J. Phys. Chem. Chem. Phys,* Vol.11, pp 9224–9232, 2009.

[202]. Laouini, E., Hamdani, M., Pereira, M. I. S., Douch, J., Mendonça, M. H., and Singh, R. N., "Preparation and electrochemical characterization of spinel type Fe-Co_3O_4 thin film electrodes in alkaline medium," *Int. J. Hydrogen Energy,* Vol. 33, pp 4936-4944, 2008.

[203]. Louardi, A., Rmili, A., Ouachtari, F., Bouaoud,A., Elidrissi, B., and Erguig, H., *J. Alloys Compd.* Vol. 509, pp 9183-9189, 2011.

[204]. Kadam, L. D., and Patil, p. S., *J. Mater. Chem. Phys*. Vol. 68, pp 225-232, 2001.

[205]. Pal, J., Chauhan,P., *J. Mater. Charact*. Vol.61, pp 575-579 , 2010.

[206]. Manogowri, R., Mathelane, R. M., Valanarasu, S., Kulandaisamy, I., A. B., Fathima, and Kathalingam, A., *J. Mater. Sci*. Vol. 27, pp 3860-3866, 2015.

[207]. Manickam, M., Ponnuswamy, V., Sankar, C., and Suresh, R., *Optik,* Vol. 127, pp 5278-5284, 2016.

[208]. Windisch, C. F., Exarhos, G. J., Ferris, K. F., Engelhard, M. H., and Stewart, D. C., *J.Thin Solid Films*, Vol. 45, pp 398–399, 2001.

[209]. Svegl, F., Orel, B., Grabec-Svegl, I., and Kaucic, V., *J. Electrochim. Acta*, Vol. 45,pp 4359-4371, 2000.

[210] G. J. Exarhos, C. F. Windisch, K. F. Ferris and R. R. Owings, Appl. Phys. A: Mater. Sci. Process., 2007, 89, 9–18.

[211]. Amri, A., Duan, X., Yin, C. Y., Jiang, Z. T., Rahman, M. M., Pryor, T., "Solar absorptance of copper-cobalt oxide thin film coatings with nano-size, grain-like morphology: optimization and synchrotron radiation XPS studies," *Appl. Surf. Sci,* Vol. 275, pp 127-135, 2013.

[212]. Abu-Zied, B. M., Bawaked, S. M., Kosa, S. A., and Schwieger, W., "Effect of microwave power on the thermal genesis of Co_3O_4 nanoparticles from cobalt oxalate micro-rods," *Appl. Surf. Sci.,* Vol. 351, pp 600-609, 2015.

[213]. Qu, Q., Wang, B., Chen, Y., Tian, S., Wu, Y., and Holze, R., "Electrochemical performance of Co_3O_4 nanoparticle in neutral aqueous electrolytes as a cathode for asymmetric supercapacitorsors," *J. Phys. Chem. C*, Vol. 113, pp 14020-14027, 2009.

[214]. Pankove,J., "Optical Processes in Semiconductors," Englewood Cliffs: Prentice-Hall; 1971.

[215]. Ali, G., Fouad, O. A., and Makhlouf, S. A., "Structural, optical and electrical properties of sol-gel prepared mesoporous Co_3O_4/ SiO_2 nanocomposites," *J. Alloys and Comp,* Vol. 579, pp 606-611, 2013.

[216]. Das, C. R., Venkatesh, R., Sivakumar, R., A. M. E. Raj, A. M. E., and Sanjeeviraja, C., "Fast electrochromic response of porous-structured cobalt oxide (Co_3O_4) thin films by novel nebulizer spray pyrolysis technique," DOI 10.1007/s11581-016-1707-0, *J. Ionics*, 2016.

[217]. Kandalkar, S. G., Gunjakar, j. L., Lokhande, C. D., and Joo, O. S., "Synthesis of cobalt oxide interconnected flacks and nano-worms structures using low temperature chemical bath deposition," *J. Alloys Comp,* Vol. 478, pp 594-598, 2009.

[218]. Li, Q., Sun, X., Lozano, K., and Mao, Y., "Asymmetric supercapacitors with dominant pseudo capacitance based on cobalt oxide nanoflowers in a neutral aqueous electrolyte," *RSC Advances*, Vol. 3, pp 24886-24890, 2013.

[219]. Dubal, D. P., and Lokhande, C. D., "Significant improvement in the electrochemical performances of nano-nest like amorphous MnO_2 electrodes due to Fe doping," *J. Ceramic. Int.* Vol. 39, pp 415-423, 2013.

[220]. Duan, Y., Liu, Z., Zhang, Y., and Wen, M., "A theoretical study of the dielectric and magnetic responses of Fe-doped α-MnO_2 based on quantum mechanical calculations," *J. Mate. Chem. C,* Vol. 1, pp 1990-1994, 2013.

[221]. Yuping, D., Jia, Z., Hui, J., and Shunhua, L., "Morphology controlled synthesis and novel microwave electromagnetic properties of hollow urchin-like chain Fe-doped MnO_2 under 10T high magnetic field," *J. Solid State Chem.* Vol.184, pp 1165–1171, 2011.

[222]. Dubal, D. P., Kim, W. B., and Lokhande, C. D., "Galvanostatically deposited Fe: MnO_2 electrodes for supercapacitor application," *J. Phys. Chem. Solids*, Vol. 73, pp 18-24, 2012.

[223]. Martinez, F., Calleja, G., Melero, J. A., and Molina, R., "Iron species incorporated over different silica supports for the heterogeneous photo-fenton oxidation of phenol," *J. Appl. Catal. B*, Vol. 70, pp 452-460, 2007.

[224]. Rossouw, M. H., Liles, D. C., and Thackeray, M. M., "Alpha manganese dioxide for lithium batteries: a structural and electrochemical study," *J. Mat. Res. Bull.* Vol. 27, pp 221-230, 1992.

[225]. H.Guan, et al., Facile synthesis of α-MnO_2 nanorods at low temperature and their microwave absorption properties, *J. Mate. Chem. Phy.* Vol. 143, pp 1061-1068, 2014.

[226]. Cullity, B. D., and Stock, S.R., "Elements of X-ray diffraction," 3rd eds. (New Jersey: Prentice-Hall), Vol. 664, 2001.

[227].   Barret, C. S. and Massalski, T. B. "Structure of metals: crystallographic methods, principles, and data," *Pergamon Press: Oxford, UK*, Vol. 204, 1980.

[228].   Michel C., Mejda A., Najoua K., Optik, 126 (2015) 708–714.

[229].   Serin T., Serin N., Karadeniz S., Sarı H., Tugluoglu N., Pakma O., J. Non-Cryst. Solids, 352 (2006) 209.

[230].   Dildar, I. L., et al., " Hall effect measurements on strained and unstrained thin films of $La_{0.7}Ca_{0.3}MnO_3$ and $La_{0.7}Sr_{0.3}MnO_3$," Phys. Rev. B, Vol. 85, pp 205103, 2012.

[231].   Forouhi, A. R., and Bloomer, I., "Optical Properties of Crystalline Semiconductors and Dielectrics," *J. Phys Rev B,* Vol.38, pp 1865-1874, 1988.

[232].   Pishdadian, S., and Ghaleno, A. M. S., "Influences of annealing temperature on the optical and structural properties of manganese oxide thin film by Zn doping from sol-gel technique," *j. Acta Physica Polonica A.,* Vol. 123, pp 9741-745, 2013

[233].   Iligan, S., Caglar, M., Caglar, Y., "The effect of deposition parameters on the physical properties of $Cd_xZn_{1-x}S$ films deposited by spray pyrolysis method," *J Optoelectron Adv Mater,* Vol. 9, pp 1414-1417, 2007.

[234].   Liu, Y., Li, Y., Li, W., Han, S., and Liu, C., "Photo electrochemical properties andphotocatalytic activity of nitrogen-doped nanoporous WO_3 photoelectrodesunder visible light," *J. Appl. Surf. Sci.,* Vol. 258, No. 12, pp 5038-5045, 2012.

[235].   Patil, P. R., and Patil, P. S., "Preparation of mixed oxide MoO_3-WO_3 thin films by spray pyrolysis technique and their characterization," *J. Thin Solid Films,* Vol. 382, pp 13-22, 2001.

[236].   Woodward, P. M., Sleight, A. W., and Vogt, T., "Structure refinement of triclinic tungsten trioxide," *J. Phys Chem Solids*, Vol. 56, No. 10, pp 1305-315, 1995.

[237].   Moulzolf, S. C., Legore, L. J., and Lad, R. J., "Heteroepitaxial growth of tungsten oxide films on sapphire for chemical gas sensors," *J. Thin Solid Films* Vol. 400, pp 56-63, 2001.

[238].   Cornell, R. M., and Schwertmann, U., "The Iron Oxides: Structure, Properties, Reactions, Occurrences and Uses," *2nd ed., Wiley-VCH, Verlag GmbH & Co,* 2003.

[239].   Han, N., Chai, L., Wang, Q., Tian, Y., Deng, P., and Chen, Y., "Evaluating the doping effect of Fe, Ti and Sn on gas sensing property of ZnO," *Sens Actuate B: Chem,* Vol. 147, pp 525-530, 2010.

[240].   Wang, F. D., Valentin, C., and Pacchioni, G., "Doping of WO_3 for photo catalytic water splitting: hints from density functional theory," *J. Phys. Chem. C,* Vol. 116 pp 8901-8909, 2012.

[241].   Zook, J. D., "Effects of grain boundaries in polycrystalline solar cells," *Appl Phys Lett,* Vol. 37, No. 2, pp 223-326, 1980.

[242].   Tauc, J., "Amorphous and liquid semiconductors," Plenum Press, London, 1974.

[243].   Moshfegh, A. Z., Azimirad, R., and Akhavan, O., "Optical properties and surface morphology of evaporated WO_3-Fe_2O_3 thin films," *J. Thin Solid Films,* Vol. 484 pp 124-131, 2005.

[244]. Fedorov, D. V., Zahn, P., and Mertig, I., "Size Effects and conductivity of ultrathin Cu films," *J. Thin Solid Films,* 2005, Vol. 473, pp 346-350.

[245]. Lethe, K. J., Been, D., Pillai, V. P. M., and Ganesan, V., "Band gap renormalization in Titania modified nanostructured Tungsten oxide thin films prepared by pulsed laser deposition," *J. Phys. Chem. C,* Vol. 120 pp 7909, 2010.

[246]. Patil, P. S., Mujawar, S. H., Inamdar, A. I., Shinde, P. S., Deshmukh, H. P., and Sadale, S. B., "Structural, electrical and optical properties of TiO_2 doped WO_3 thin films," *J. Appl. Surf. Sci.,* Vol. 252, pp 1643-1650, 2005.

[247]. Kofstad, P., " Nonstoichiometry, diffusion, and electrical conductivity in binary metal oxides," *Wiley, New York,* Vol. 20, 1972.

[248]. Niederberger, M., Garnweitner, G., "Organic Reaction Pathways in the Nonaqueous Synthesis of Metal Oxide Nanoparticles," *J. Chem A,* Vol. 12, No. 28, pp 7282-7302, 2006.

[249]. Ghasemi, L. Jafari, H., " Morphological characterization of tungsten trioxide nanopowders synthesized by sol-gel modified pechini's method"., *J. Mate Research.* Vol. 20, No. 6, pp 1713-1721, 2017.

[250]. Liu, H., Peng, T., Ke, D., Peng, Z., Yan, C., " Preparation and photocatalytic activity of dysprosium doped tungsten trioxide nanoparticles," *J. Mat. Chem. Phys.* Vol. 104, pp 377-383, 2007.

[251]. Wang, H. Y., Xu, P., Wang, T. M., "Doping of Nb_2O_5 in photocatalytic nanocrystalline/ nanoporous WO_3 films," *J. Thin Solid Films,* Vol. 388, pp 68-72, 2001.

[252]. Arfaoui, A., Ouni, B., Touihri, S., Mannoubi, T., "Investigation into the optoelectrical properties of tungsten oxide thin films annealed in an oxygen air," *J. Mater. Res. Bull.* Vol. 60, pp 719-729, 2014.

[253]. Vinodkumar, R., Navas, I., Porsezian, K. P., Unnikrishnan, N. V., and Mahadevan pillai, V. P., " Spectrochim. Acta A: Mol," *J. Biomol. Spectrosc.* Vol. 118, No. 24, pp 724, 2014.

[254]. Zhang, T. S., Huang, P., Huang, H. T., and Kilner, J., *J Mater. Sci.* Vol. 37 pp 997, 2002.

[255]. Zhang, Z, L., Han, D., Wei, S. J., and Zhang, Y. X., "Determination of active site densities and mechanisms for soot combustion with O_2 on Fe-doped CeO_2 mixed oxides," *J. Catal.* Vol. 276, pp 16-23, 2010.

[256]. Khare, A., Choudhary, R. J., Bapna, K., Phase, D. M. and Sanyal, S. P., " Resonance photoemission studies of (111) oriented CeO_2 thin film grown on Si (100) substrate by pulsed laser deposition," *J. Appl. Phys.* Vol. 108, pp 1–5 , 2010.

[257]. Thurber, A., Reddy, K. M., Shutthanandan,V., Engelhard, M. H., Wang, C., Hays, J., and Punnoose, "Ferromagnetism in chemically synthesized CeO_2 nanoparticles by Ni doping," *J. Phys. Rev. B*, Vol. 76, No. 16, pp 165206, 2007.

[258]. Ge, M. Y., Wang, H., Liu, E. Z., Liu, J. Z., Jiang, J. Z., Li, Y. K., Xu, Z. A., and Li, H. Y., "On theorigin of ferromagnetism in CeO2 nanocubes," *J. Appl. Phys. Lett,* Vol. 93, pp 062505, 2008.

[259]. Sundaresan, A., Bhargavi, R., Rangarajan, N., Siddesh, U., and Rao, C. N. R., "Ferromagnetism as a universal feature of nanoparticles of the otherwise nonmagnetic oxides", *J. Phys. Rev. B,* Vol. 74, No. 16, pp 161306(R), 2006.

[260]. Samiee, S., and Goharshadi E. K., *J. Mater. Res. Bull.* Vol. 47, pp 1089, 2012.

[261]. Hernandez-Alonso, M. D., Hungria,A. B., Martinez-Arias, A., Coronado, J. M., Conesa, J. C., Soria, J., and Fernandez-Garcia, M., *J. Phys. Chem. Chem. Phys.* Vol. 6, pp 3524, 2004.

[262]. Chen H. I., and Chang, H. Y., *J. Solid. State. Commun.* Vol. 133, pp 593, 2005.

[263]. Lu, X. H., Huang, X., Xie, S. L., Zheng, D. Z., Liu, Z. Q., Liang, C. L., and Tong Langmuir, Y. X., Vol. 26, pp 7569, 2010.

[264]. Colis, S., Bouaine, A., Schmerber,G., Ulhaq-bouillet, C., Dinia, A., and Choua, S., "High temperature ferromagnetism in Co-doped CeO₂ synthesized by the co-precipitation technique," *J. Phys. Chem. Chem. Phys.* Vol.14, pp 7256–7263, 2012.

[265]. Tsunekawa, S., Fukuda, T., and Kasuya, *J. A. Surf. Sci.* Vol. 457, pp L437, 2000.

[266]. Yue, L., and Zhang, X. M., "Structural characterization and photocatalytic behaviors of doped CeO₂ nanoparticles," *J. Alloys Compd.* Vol. 475, pp 702, 2009.

[267]. Boonprakob, N., "Enhanced visible-light photocatalytic activity of g-C3N4/ TiO₂ films," *J. Colloid. Interf. Sci.* Vol. 417, pp 402-409,2014.

[268]. Zhou, K. B., Wang, X., Sun, X. M., Peng, Q., Li, Y. D., "Enhanced catalytic activity of ceria nanorods from well-defined reactive crystal planes," *J. Catal.* Vol. 229, pp 206-212, 2005.

[269]. Khan, M. A. M., Kumar, S., Ahamed, M., "Structural, electrical and optical properties of nanocrystalline silicon thin films deposited by pulsed laser ablation," *J. Mater. Sci. Semi Cond. Process,* Vol. 30, pp 169, 2015.

[270]. Hammad, T. M., Salem, J. K., Kuhn, S., Saarlandes, U., and Saarlandes, U., " Optical properties of Cu²⁺ and Fe²⁺ doped ZnS semiconductor nanoparticles synthesized by coprecipitation method," *J. Mater Sci Mater Electron.* Vol. 26, pp 5495, 2015.

[271]. Baloach, Q., "A robust, enzyme-free glucose sensor based on lysine-assisted CuO nanostructures," *J. Sensors,* Vol. 16, pp 1878, 2016.

[272]. Zhang, M., "Highly sensitive glucose sensors based on enzyme-modified whole-graphene solution-gated transistors," *J. Sci. Rep.* Vol. 5, pp 8311, 2015.

[273]. Wang, Y., Bai, W., Nie, F., and Zheng, J., "A non-enzymatic glucose sensor based on Ni/ MnO₂ nano composite modified glassy carbon electrode," *J. Electro Analyses,* Vol. 27, pp 2399-2405, 2015.

[274]. Meng, Z., Sheng, Q., and Zheng, J., "A Sensitive non-enzymatic glucose sensor in alkaline media based on Cu/MnO₂-modified glassy carbon electrode," *J. Iran. Chem. Soc.* Vol. 9, pp1007-1014, 2012.

[275].   Yuan, H., "Preparation of $NiCo_2O_4$ and $NiCo_2S_4$ micro-onions for electrochemical sensing of glucose," *J. Appl. Phys. A,*   Vol. 125, pp 61, 2019.

[276].   M. M. Rahman, M. M., "A comprehensive review of glucose biosensors based on nanostructured metal-oxides," *J. Sensors*, Vol. 10, pp 4855-4886, 2010

[277].   Gorsley, G. J.,   "Continuous blood glucose monitoring with a thin-film optical sensor," *J. Clinical Chem,* Vol. 53, pp 1820-1826, 2007.

[278].   Hartono, A., Sanjaya, E., and Ramli, R., "Glucose sensing using capacitive biosensor based on polyvinylidene fluoride thin film," *J. Biosens*, Vol. 8, pp 12, 2018.

[279].   Kondo, T., "Amperometric sensing of H_2O_2 and glucose using wet-chemically deposited MnO_2 thin films," *J. Ceram Soci of Japan,* Vol. 126, pp260-262, 2018.

APPENDICES

Appendices

➢ **List of published/ communicated paper related to Ph.D research work**

1. **Muslima Zahan** and Jiban Podder, "Surface morphology, optical properties and Urbach tail of spray deposited Co_3O_4 thin films", Journal of Materials Science: Materials in Electronics; *Springer nature*; https://doi.org/10.1007/s10854-019-00717-2, Published online:, vol. 30, No 4, pp 4259-4269., 14 January, 2019.

2. **Muslima Zahan**. Jiban Podder, "Structural, optical and electrical properties of Cu: MnO_2 nanostructured thin films for glucose sensitivity measurements," Journal of SN Applied Sciences, *Springer nature;* https://doi.org/10.1007/s42452-020-2191-8; Vol. 2, pp 385., 12 February 2020.

3. **Muslima Zahan**, Jiban Podder, "Role of Fe doping on structural and electrical properties of MnO_2 nanostructured thin films for glucose sensing performance," Journal of Materials Science in Semiconductor Processing ; *Elsevier*, https://doi.org/10.1016/j.mssp.2020.105109 ; Vol. 117 , pp 105109, 12 May 2020.

4. **M. Zahan** and J. Podder, " Fe doped MnO_2 nanostructured thin films: synthesis and characterization for biosensor applications; Bangladesh Journal of Physics **;** Vol. 27, Issue 1, pp. 1−12, 28 July, 2020.

5. **M Zahan**, J Podder, "An investigation of spray pyrolysed Cu doped Co_3O_4 nanostructured thin films for glucose sensor applications**,"** Journal of Applied Physics A. (Communicated).

➢ **List of paper/ poster presentation related to Ph.D research work**

1. **M. Zahan** and J. Podder, "Effect of Substrate Temperature on the Characteristics of Co_3O_4 Thin Films Deposited by a Low Cost Spray Pyrolysis Technique." International Conference on Physics, 05-07 January, 2017 Dhaka-Bangladesh

2. **Muslima Zahan** and Jiban Podder "Synthesis of Spray pyrolysed nanocrystalline α-MnO_2 thin films and study their morphological, structural, optical and electrical properties" International Conference on Nanotechnology and Condensed Matter Physics, January 11-12, 2018, BUET, Dhaka, Bangladesh

3. **M Zahan,** M Sharmin and J Podder, "Effect of Cu Doping on Morphological, Structural, Optical and Electrical Properties of MnO_2 Thin Films Deposited by Spray Pyrolysis Method" The 4th International Conference On Structure, Processing and Properties of Materials, 1- 3 March 2018, BUET, Dhaka, Bangladesh.

4. Mehnaz Sharmin, **M Zahan** and J Podder, Investigation of Structural, Morphological, Optical and Electrical Properties of Spray Synthesized Fe_2O_3 Thin Films for Optoelectronic Applications, The 4th International Conference On Structure, Processing and Properties of Materials, 1- 3 March 2018, BUET, Dhaka, Bangladesh.

5. **Muslima Zahan** and Jiban Podder " The study of size dependent structural and optical properties of spray deposited Cu doped MnO_2 nanocrystalline thin films" International Conference on Advances in Materials Science and Engineering for Societal Applications, 2 - 3, March 2018, Chennai, India.

6. **M. Zahan** and J. Podder, "Effect of Fe Concentrations on the Characteristics of α-MnO_2Thin Films Synthesized by a Low Cost Spray Pyrolysis Technique" International Conference on Physics, 08-10 March, 2018, Dhaka, Bangladesh.

7. **M. Zahan** and J. Podder, "Spray Deposited Cu Doped MnO_2 Thin Films for Bio Sensing Application" International Conference on Physics, 08-10 March, 2018, Dhaka, Bangladesh.

8. **Muslima Zahan** and Jiban Podder, "Morphological, Structural, Optical and Electrical Properties of Fe Doped MnO_2 Thin Films Deposited by Spray Pyrolysis Technique" Seminar, Ministry of Science and Technology, Government of the People's Republic of Bangladesh, 15 March, 2018, Dhaka-Bangladesh.

9. **M Zahan,** M Sharmin and J Podder, "Effect of Cu Doping on Morphological, Structural, Optical and Electrical Properties of MnO_2 Thin Films Deposited by Spray Pyrolysis Method" International Workshop on Recent Advances in Nanotechnology and Applications (RANA-2018), University of MALAYA, 7-8 Sep. 2018.

10. **Muslima Zahan** and Jiban Podder, "Effect of Cu Concentrations on the Characteristics of Co_3O_4 Thin Films Synthesized by Spray Pyrolysis Technique." National Conference on Physics, 07-09 February, 2019, Dhaka-Bangladesh.

11. Podder, Jiban; **Zahan, Muslima**," Synthesis, processing and characterization of Fe doped MnO_2 nanostructured thin films for bio sensing performance**,"** ISE-2019; 17th International Symposium on Electrets**;** 02-06 September 2019 University of Limerick, Ireland

➢ **Attendances**

1. Attended on **International Virtual Conference** on "Advanced Functional Nanomaterials and Their Applications" (ICAFNTA-2020), Jointly organized by Department of Chemistry, Universitas Islam Indonesia and Nanotechnology and Catalysis Research Center, University of Malaya, 9-10 July, 2020

2. Attended the **International Webinar on** " Nanostructured Metal Oxides thin films for Sensor Technology," Organized by Department of Physics, Saveetha Engineering College, Affiliated to Anna University, India, 16 July, 2020

3. Attended the **International Webinar on** " Nanomaterials -A Multidisciplinary Approach," Organized by Department of Physics, Saveetha Engineering College, Affiliated to Anna University, India, 20 July, 2020

4. Attended in **Webinar Series**: "Materials for Energy and Environment" Organized by the Department of Chemistry, Universitas Islam Indonesia. 29 August, 2020

5. Attended in workshop on the use of the CASR Proposal Submission Portal, by **IQAC, BUET**, Dhaka, 29 August 2020.